

# **ROLLING STONES ?**

**TRIGGERING AND FREQUENCY OF HILLSLOPE  
DEBRIS FLOWS IN THE BACHELARD VALLEY,  
SOUTHERN FRENCH ALPS**

cover design: Harry Blijenberg

ISBN 90-6266-161-0 (Thesis)  
ISBN 90-6809-268-5 (NGS)

Copyright © Faculteit Ruimtelijke Wetenschappen Universiteit Utrecht 1998

Niets in deze uitgave mag worden vermenigvuldigd en/of openbaar gemaakt door middel van druk, fotokopie of op welke andere wijze dan ook zonder voorafgaande schriftelijke toestemming van de uitgevers.

All rights reserved. No part of this publication may be reproduced in any form, by print or photoprint, microfilm or any other means, without written permission by the publishers.

## **ROLLING STONES ?**

**TRIGGERING AND FREQUENCY OF HILLSLOPE  
DEBRIS FLOWS IN THE BACHELARD VALLEY,  
SOUTHERN FRENCH ALPS**

## **STROMENDE STENEN**

**INITIATIE EN HERHALINGSFREQUENTIE VAN  
HELLINGPUINSTROMEN IN HET BACHELARD DAL,  
ZUIDELIJKE FRANSE ALPEN**

(MET EEN SAMENVATTING IN HET NEDERLANDS)

### **PROEFSCHRIFT**

TER VERKRIJGING VAN DE GRAAD VAN DOCTOR AAN DE  
UNIVERSITEIT UTRECHT, OP GEZAG VAN DE RECTOR  
MAGNIFICUS, PROF. DR. H.O. VOORMA, INGEVOLGE HET  
BESLUIT VAN HET COLLEGE VOOR PROMOTIES IN  
HET OPENBAAR TE VERDEDIGEN OP DONDERDAG  
22 OKTOBER 1998 DES NAMIDDAGS TE 2:30 UUR

DOOR

**HENRICUS MARINUS BLIJENBERG**

GEBOREN OP 11 MEI 1965 TE AMERSFOORT

PROMOTOR: PROF. DR. J.D. NIEUWENHUIS  
FACULTEIT RUIMTELIJKE WETENSCHAPPEN  
UNIVERSITEIT UTRECHT

JO-PROMOTOREN: DR. TH.W.J. VAN ASCH  
DR. H. VAN STEIJN  
FACULTEIT RUIMTELIJKE WETENSCHAPPEN  
UNIVERSITEIT UTRECHT

## VOORWOORD

Maart '91: uit de brief die op mijn deurmat lag, bleek ik te solliciteren (tenzij ik een tegenbericht stuurde) op de AIO-post 'Temporal Analysis of Debris Flows in an Alpine Environment'. Puinstro-men, bergen, Frankrijk ... drie ingrediënten die mij er van overtuigden om inderdaad géén tegenbericht te sturen. Twee maanden later begon ik aan dit project, dat 4 jaar later voltooid moest zijn (ja ja ...). De veldwerken in het Bachelarddal, één van de parels van Franse Alpen, zullen me altijd bijblijven.

Mijn copromotoren, *Dr. Henk van Steijn* en de "mathematische coprofessor" *Dr. Theo van Asch*, hebben mij vanaf het begin bijgestaan. Dankzij jullie kennis, ondersteuning en stimulerende discussies (bij voorkeur met een glas wijn op een terrasje in Zuid-Frankrijk, maar soms ook zwoegend bij een temperatuur van 30° op een helling van 40°!) en jullie waardevolle suggesties is dit project uiteindelijk geslaagd. In 1993 treedt *Prof. Dr. Jan Nieuwenhuis* aan als hoogleraar Grondmechanica bij de vakgroep Fysische Geografie, en wordt daarmee mijn promotor. Je bijdrage, vooral aan het einde van de rit, heeft zeker tot verbetering van dit proefschrift geleid. Gedrieën hebben jullie bovendien veel constructieve op- en aanmerkingen op de eerste versie van de tekst van dit proefschrift geleverd.

*Dr. Marcel van der Perk*, met wie ik al die jaren een kamer heb gedeeld in de laagbouw. Ook jij bent meegeweest in het veld en hebt daar aardig wat vrije tijd in gestoken. Maar je hebt er uiteindelijk wel een leuke poster aan over gehouden. Veel problemen die ik tegenkwam wist ik met jouw hulp op te lossen, en je hebt daarmee een grote bijdrage aan dit proefschrift geleverd. Ook aan de titel. Ik herinner mij onder andere de vele lange avonden die we hier op de Uithof doorbrachten om aan onze proefschriften te werken. En de "Italiano's dubbel belegd" die daar bij hoorden. Ook *Dr. Hans* (1× bellen is koffie) *Middelkoop* kreeg de smaak te pakken, zodat we gedrieën vaak bleven hangen tot de mededeling "Het is vijf voor tien. De portier gaat over vijf minuten sluiten ...".

De meetopstelling op een steile helling op 2000 m hoogte was er zeker niet gekomen zonder de inzet van *Ing. Theo Tiemissen*, *Ing. Bas van Dam* en *Jaap van Barneveld*, zowel bij het ontwerpen, het maken en het opbouwen in het veld. Jullie eerste reactie bij het zien van de meetlokatie, toen wij die aanwezen, was: "Geintje zeker", maar jullie hebben het toch mooi volgehouden om elke dag weer een half uur tegen die helling op te klimmen met een volle rugzak en zodoende de meetopstelling op te bouwen. Diverse collega's van de vakgroep (tegenwoordig aangeduid met het synoniem disciplinecluster) Fysische Geografie hebben altijd een levendige belangstelling getoond voor het onderzoek en daarnaast ook belangrijke bijdragen geleverd, zowel in het veld als bij de verwerking van gegevens. *Dr. Martin Hendriks*, je hebt me behoorlijk geholpen met de hydrologie, en *Dr. Ed Weiss*, zonder jouw hulp waren de boomring-dateringen zeker een stuk slechter geweest. Bedankt voor jullie aanzienlijke bijdragen. Het bezoek aan de meetopstelling kostte *Drs. Pim Beukenkamp* naast vele zweetdruppeltjes ook zijn broek.

La Vallée du Bachelard est située en grande partie dans le **Parc National du Mercantour**. Je veux bien remercier le directeur/la directrice du Parc National pour l'autorisation de faire des travaux à la parcelle expérimentale et d'aller au dehors des sentiers. De plus, les employés du division Ubaye m'ont aidé à retenir l'installation de la parcelle expérimentale et avec leurs observations de tout ce qui se passe dans le Parc. *M. Pascal Chondroyannis* de l'**Organisation National des Forêts** (ONF) nous a mis à la disposition des données climatiques de la région de l'Ubaye. *M. Maurice Meunier* de **CEMAGREF**-Grenoble nous a fourni de données sur la relation entre durée, intensité et fréquence des pluies. En plus, il a fait la peine de lire et juger le manuscrit de cette thèse. En 1992, *Pierre Badieu* m'a montré qu'il y a plus que seulement des laves boueuses dans la Vallée du Bachelard. Et *M. Aillaud* a toujours réussi à nous munir d'un appartement assez agréable, même en plein été.



Veel werk is voor mij gedaan door studenten die hun doktoraal- of bijvakveldwerk in het Bachelarddal hebben verricht. *Drs. Jan de Ruiter, Drs. Peter de Graaf en Drs. Anton van Tetering* hebben mij ingewijd in de "geheimen" van het Bachelarddal toen ik daar voor het eerst kwam kijken. Daarnaast herinner ik me jullie vooral als exporteurs van laatstehands auto's naar Frankrijk. Het afsluiten van een vervangend-vervoer verzekering pleit voor jullie inschattingsvermogen. *Drs. Jelle Buma*, die de pech had dat wekenlang de regen niet gesimuleerd werd. Je hebt toch doorgezet en daarmee een goed begin gemaakt met de hydrologische modellering. *Drs. Jeroen Overbeek en Drs. Jan Wiersma* hebben zich vooral op de datering van puinstroomafzettingen gestort. *Drs. Dinand Alkema, Drs. Eduard van Duffelen, Drs. Marco Duiker, Drs. Marc Hulst, Dra. Eva Kamphorst, Drs. Marnix Mosselman en Drs. Erik Nomden*: ook jullie zijn niet ontkomen aan het uitvoeren van regensimulaties.

Daarnaast bedank ik *Maarten Zeylmans van Emmichoven* van het FAD voor de vele hulp bij computerproblemen en bij het printen van dit proefschrift, *Wim Haak* en *Kees Klawer* voor hun tijd en medewerking en *Ing. Peter Mekenkamp* voor het beschikbaar van een theodoliet met afstandsmeter. En de vele nog niet genoemde (oud-)collega's bij Fysische Geografie / Ruimtelijke Wetenschappen die altijd voor een goede werksfeer hebben gezorgd, met name *Nathalie Asselman, Henk Berendsen, Stefan van Beurden, Marc Bierkens, Wladimir Bleuten, Thom Bogaard, Leo Brouwer, Alfred Coerts, Oscar van Dam, Simone van Dijk, Doesjka Ertsen, Pauline van Gaans, Hans Hartholt, Victor Jetten, Steven de Jong, Derc-Jan Karssen, Anmina Koopmans, Henk Kruse, Jaap Kwadijk, Bart Makaske, Hans Riezebos, Ad de Roo, Tijs Rooijaards, Celia Roovers, Torbjörn Törnqvist, Birgitta van de Wateren, Henk Weerts, Cees Wesseling, Nico Willemse, Anja de Wit, Marcel de Wit, Kathelijne Wijnberg en Felix Wolf*. *Wim Hoek* van de VU mag in deze rij niet ontbreken, temeer daar hij ook paranimf speelt.

De last van het promoveren kan soms wel eens zwaar op de schouders drukken. Gelukkig zijn er dan vrienden, vriendinnen en familie die je weer kunnen laten zien dat er ook nog wel iets anders in de wereld is dan alleen je proefschrift. Ik hoop jullie nu weer eens wat vaker te kunnen zien. Bedankt *Marcel, Ida, Jurrien, Maarten, Doesjka, Wim, Annewietske, Erik, Gea, Marijke, Najib, Marleen, Jaap, Gert, Anja, Raymond, Kitty, Helen, Sander, Jo, Henk, Hanneke, Michiel, Erik, Carien, Michiel, Ellen, Saskia, Bas, Bart en Ellen* voor jullie interesse, morele steun en humor. Ook het volksdansen bij *Garoon* heeft me veel plezier gedaan, niet in de laatste plaats vanwege de reisjes naar Polen en Oekraïne. *Joop en Martha van der Meij*, bij wie het altijd weer "effe bijkome" was in "villa Kakelbont".

Mijn ouders, *Jan en Ria Blijenberg*, ik wil jullie bedanken voor de belangstelling en de onvoorwaardelijke steun en vrijheid die jullie mij altijd hebben gegeven. Jullie hebben mij lang geleden voor het eerst meegenomen naar de bergen, en sindsdien ben ik er aan "verslaafd". Na de drukte rond dit proefschrift zullen jullie me weer wat vaker zien. *Annemarijke*, ik ben ook jou veel dank verschuldigd. Je steun in de afgelopen jaren was onontbeerlijk, nadat er in de zomer van 1992 in de Franse Alpen meer opbloeide dan alleen de edelweiss.

Tot slot eindig ik met de woorden die mij zowel doen denken aan de tijd en energie die ik in dit proefschrift heb geïnvesteerd als aan het verblijf in het appartement aan de Rue Cardinalis in Barcelonnette in de zomer van 1991: *Ça suffit !*

Buren, 25 augustus 1998

*HARRY Blijenberg*

## CONTENTS

LIST OF FIGURES	12
LIST OF TABLES	16
LIST OF SYMBOLS	17
1 INTRODUCTION	23
1.1 Background and problem definition	23
1.2 Framework and objectives	25
1.3 Methodology and thesis structure	27
2 A REVIEW OF DEBRIS FLOWS	29
2.1 Debris flows	29
2.1.1 Introduction	29
2.1.2 Characteristics of debris flows	32
2.1.3 Debris-flow risk prevention	36
2.1.4 Debris-flow triggering	37
2.1.5 Debris-flow movement	43
2.2 Hydrologic control of debris-flow triggering	48
2.2.1 Infiltration	48
2.2.2 Infiltration envelopes	52
2.2.3 Overland flow	53
2.3 Dating of debris-flow deposits	54
2.3.1 Introduction	54
2.3.2 Dendrogeomorphology	55
2.3.3 Lichenometry	59
3 STUDY AREA: THE BACHELARD VALLEY	67
3.1 Characteristics of the Bachelard Valley	67
3.1.1 Topography	67
3.1.2 Geology	67
3.1.3 Morphology	70
3.1.4 Climate, vegetation and human influence	70
3.2 Debris-flow trigger zones and debris flows in the Bachelard Valley	72
3.2.1 Location of debris-flow trigger zones	72
3.2.2 Characteristics of debris-flow trigger zones and debris flows	75
3.3 TCP: The Tête du Clot des Pastres debris-flow trigger zone	76
4 RESEARCH METHODS	81
4.1 Introduction	81
4.2 Parameters of the coarse debris	81
4.2.1 Porosity	81
4.2.2 Strength	81
4.3 Parameters of the fine-grained regolith	84
4.3.1 Density, porosity, field water content and water-retention curve	84
4.3.2 Grain-size distribution	84
4.3.3 Regolith depth	84

4.3.4	Infiltration characteristics: rainfall simulations	85	8.3.2	Logistic regression models for debris-flow triggering	13
4.4	Rainfall and discharge monitoring	86		Single-variable models	13
4.5	Preparation of base maps	89		Multiple-variable models	13
4.5.1	DEM: geodetic survey	89	8.3.3	Other models for debris-flow triggering	13
4.5.2	Other maps	90	8.4	Debris-flow frequency	14
4.6	Dating debris-flow deposits	90	8.4.1	The maximum 10-minute rainfall intensity frequency curve	14
4.6.1	Preparations	90	8.4.2	Debris-flow frequencies and return periods	14
4.6.2	Dendrochronology	90	8.5	Discussion and conclusions	14
4.6.3	Lichenometry	91	8.5.1	Debris-flow triggering	14
4.6.4	Regular field surveys: observations and photographs	92	8.5.2	Debris-flow frequency	14
4.7	Other methods	92	8.5.3	Performance of the discharge models	14
5	PHYSICAL QUANTIFICATION OF DEBRIS-FLOW TRIGGERING CONDITIONS	95	9	DEBRIS FLOWS IN THE BACHELARD VALLEY: DATING OF DEPOSITS	14
5.1	Physical modelling of debris-flow triggering in the Bachelard Valley	95	9.1	Introduction	14
5.2	Characteristics of the coarse debris	95	9.2	Preparation of deposit dates	15
5.2.1	Strength	95	9.2.1	Dendrogeomorphological data: the Split-Moving Window test	15
5.2.2	Density, porosity and hydraulic conductivity	99	9.2.2	Lichenometrical data: a <i>Rhizocarpon geographicum</i> s.l. growth curve	15
5.3	Characteristics of the fine-grained regolith material	100	9.3	Occurrence and frequency of debris flows	15
5.4	Discussion and conclusions	102	9.4	Temporal variation in debris-flow activity	15
5.4.1	Effect of input-parameter uncertainties in quantitative physical modelling of debris-flow triggering	102	9.5	Discussion and conclusions	16
5.4.2	Consequences for modelling debris-flow triggering	103	10	DEBRIS FLOWS IN THE BACHELARD VALLEY: ACTIVITY IN THE PERIOD 1991-1995	16
6	RAINFALL SIMULATIONS IN DEBRIS-FLOW TRIGGER ZONES	105	10.1	Introduction	16
6.1	Introduction	105	10.2	Occurrence of debris flows in the Bachelard Valley in the period 1991-1995	16
6.2	Infiltration parameters	106	10.3	Discussion	17
6.2.1	Constant-runoff (CR) tests	106	10.3.1	Temporal aspects	17
6.2.2	Infiltration-envelope (IE) tests	110	10.3.2	Spatial aspects	17
6.2.3	Comparison of the constant-runoff and infiltration-envelope tests	111	10.4	Comparison of debris-flow frequencies from regular surveys and from deposit dating	17
6.3	Boundary effects during rainfall simulations	112	10.5	Conclusions	18
6.4	Occurrence of micro-scale mass movements during rainfall simulations	112	11	SUMMARY AND MAIN CONCLUSIONS	18
6.5	Conclusions	114	11.1	Methodological considerations and the physical approach	18
7	MODELLING DEBRIS-FLOW TRIGGERING AND FREQUENCY: MODELS	115	11.2	Debris-flow occurrence: the empirical approach	18
7.1	Introduction	115	11.3	Debris-flow frequency	18
7.2	Input data for the models	115	11.4	General conclusions and recommendations for future research	18
7.3	The rainfall models	117	SAMENVATTING		18
7.4	The discharge models	118	REFERENCES		20
7.4.1	General description of the discharge models	118	APPENDICES		21
7.4.2	TANKFLOW	119	A1	Dendrochronological sampling data form	21
7.4.3	DINOFLOW	120	A2	Characteristics of rainstorms recorded at the TCP site in the period 1991-1994	21
7.4.4	Calibration of the discharge models	121	CURRICULUM VITAE		22
7.4.5	Stability of the discharge models	122			
7.4.6	Sensitivity of the discharge models	123			
7.4.7	Accuracy of the discharge models	125			
7.5	Discussion and conclusions	126			
8	MODELLING DEBRIS-FLOW TRIGGERING AND FREQUENCY: RESULTS	127			
8.1	Introduction	127			
8.2	Debris flows at Tête du Clot des Pastres site between June 1991 and June 1995	127			

## FIGURES

1.1	World map of debris-flow occurrence	23
1.2	Debris-flow triggering hypothesis based on Postma (1988)	26
1.3	General flow chart of the project	26
2.1	Rheological classification of flows	30
2.2	Classification of debris flows based on deposit volume	31
2.3	Morphogenetic classifications of debris flows	31
2.4	Typical morphology of a hillslope debris flow and debris-flow terminology	33
2.5	Cross section of a debris-flow levee along a debris-flow channel, showing the typical inverse grading of the deposits and the orientation of clasts within the deposits	33
2.6	Relation between water content and viscosity	35
2.7	Threshold curves for debris flows and landslides	38
2.8	Tank model from Kobashi and Suzuki	39
2.9	Static forces on an infinite slope	40
2.10	Characteristic shear-strength and shear-stress distributions in saturated debris	40
2.11	Flow through a saturated debris bed	42
2.12	Rheological behaviour of various materials	44
2.13	Shear-stress and velocity profiles for a Newtonian and a Bingham viscoplastic debris flow on an infinitely wide slope	44
2.14	Shear-stress and velocity profiles for a Bingham viscoplastic debris flow in a semi-circular channel	45
2.15	Tilt of debris-flow surface in a channel bend	46
2.16	Some debris-flow velocity profiles by Chen	47
2.17	Soil moisture distribution during infiltration according to Green and Ampt	49
2.18	Infiltration capacity functions of Green and Ampt, Philip and Horton	51
2.19	Relation between infiltration rate and the infiltration envelope	52
2.20	Complacent and sensitive trees	55
2.21	Cell structure in a cross section of a conifer	56
2.22	Cross dating of tree rings	56
2.23	Decrease of ring width with tree age	56
2.24	Tilting of a tree by mass movement followed by trunk curvature and eccentric growth of annual rings	57
2.25	Cross section through an injured tree showing partial cover of the scar by new callous margin growth	57
2.26	The effect of burial by a single debris flow on the growth of <i>Picea abies</i>	58
2.27	Main features of a crustose lichen thallus	60
2.28	Cross section of an areole	60
2.29	Classification of the genus <i>Rhizocarpon</i>	61
2.30	Growth curve models for <i>Rhizocarpon alpicola</i> and section <i>Rhizocarpon</i> , assuming delayed colonization by <i>Rhizocarpon alpicola</i>	61
2.31	Reported growth curves for <i>Rhizocarpon geographicum</i>	62
2.32	Relative growth rates of <i>Rhizocarpon alpicola</i> and section <i>Rhizocarpon</i> species on debris-flow deposits in Austerdalen, Norway	63
2.33	Lichen-growth envelope for <i>Rhizocarpon geographicum</i> obtained from measured thalli on surfaces of known age	64
2.34	Increasing largest-thallus size with increasing area searched	65
2.35	Longest and shortest thallus diameter	65
3.1	Location of the study area	67

3.2	Geological structure of the western Alps
3.3	Geological-lithological map of the Bachelard Valley
3.4	Lithostratigraphic sequences in the Bachelard Valley
3.5	Morphology dominated by glacial processes in the Sanguinière Valley
3.6	Morphology dominated by slope processes in the Tellière Valley
3.7	Average monthly temperature and precipitation in Barcelonnette - St. Pons (1140 m)
3.8	Effects of elevation and aspect on temperature in the French Alps
3.9	Debris-flow trigger zones in the Bachelard Valley
3.10	Relation between elevation and the occurrence of debris-flow trigger zones in the Bachelard Valley
3.11	A couloir-type debris-flow trigger zone
3.12	Two 'bowl'-type debris-flow trigger zones on the west-facing slope of the Tête du Clot des Pastres
3.13	Size distribution of debris-flow trigger zones in the Bachelard Valley
3.14	Location of the debris-flow trigger zone TCP near Bayasse
3.15	Contour map of the debris-flow trigger zone TCP
3.16	Debris-flow trigger zones on the west-facing slope of the Tête du Clot des Pastres and their relation to lithology
3.17	Lithological profile near the debris-flow trigger zone TCP
3.18	Deep and sharply-incised rills in the debris-flow trigger zone TCP
3.19	Solifluction deposits and absence of rills in the debris-flow trigger zone TCP
4.1	The test method for determination of static and kinetic internal-friction angles of coarse, cohesionless debris
4.2	The rainfall simulator
4.3	Calibration curve for the rainfall simulator
4.4	The hydrologic monitoring unit equipment in 1991
4.5	Part of the hydrologic monitoring unit in the debris-flow trigger zone TCP in 1991
4.6	The discharge flume with the grating and the sediment deposition tank in 1991
4.7	The Campbell CR10 data logger
4.8	The hydrologic monitoring unit equipment in 1992-1994
4.9	The hydrologic monitoring unit in the debris-flow trigger zone TCP in 1992-1994
4.10	The discharge measurement box
4.11	The increment borer used for tree-ring sampling
4.12	A tree-ring sample prepared for analysis
4.13	Debris-flow deposits on top of late-lying snow
4.14	Set-up for measurement of the hydraulic conductivity of coarse debris
5.1	Location of the debris-strength test sites
5.2	Distributions of kinetic internal-friction angles for five debris types
5.3	Sensitivity of Takahashi's debris-flow triggering model for its component variables
5.4	Clast shapes based on clast-axis ratios for five debris types
5.5	Grain-size distributions of fine-grained regolith material in the debris-flow trigger zones TCP and PBN
5.6	pF-curves of fine-grained regolith material in the debris-flow trigger zones TCP and CdM
5.7	Distribution of F-values from Takahashi's debris-flow triggering model
5.8	Three typical situations if a rock-fluid mixture reaches an accumulation of coarse debris
6.1	Location of rainfall simulation sites
6.2	Distribution of K-values from the constant-runoff method
6.3	Relation between K and rainfall intensity
6.4	Distribution of S-values from the constant-runoff 'direct' method (TCP and CdM)
6.5	Sorptivity determined from time-to-ponding versus Smith and Parlange factor plot

6.6	Sorptivity determined from square root of time-to-ponding versus square root of Smith and Parlange factor plot	109	8.9	Comparison of debris-flow triggering probability curves with Caine's debris-flow threshold	13
6.7	Relation between $K$ and $S$ (TCP)	110	8.10	Comparison of individual rainstorms with Caine's and Innes' debris-flow thresholds	14
6.8	Comparison of infiltration-envelope functions and curve-fitting methods (PBS)	110	8.11	Frequency distribution of maximum 10-minute rainfall intensities	14
6.9	Infiltration envelopes for series of plots series with uniform characteristics (TCP)	110	8.12	Frequency distribution and probability density distributions for maximum 10-minute rainfall intensities $>1.5$ mm/hr	14
6.10	Time-to-ponding as a function of rainfall intensity on rills and interrill areas (TCP 1991)	111	8.13	Gumbel distribution and 95% confidence limits of exceedance probabilities and return periods for 10-minute rainfall intensities	14
6.11	Time-to-ponding as a function of rainfall intensity and initial soil moisture (TCP)	111	8.14	Frequency distribution and probability density distributions for maximum 10-minute rainfall intensities $>6$ mm/hr	14
6.12	Infiltration during a rainfall simulation	112	8.15	Gumbel probability curve of maximum 10-minute rainfall intensity (for rainfall intensities $>6$ mm/hr) and debris-flow triggering probability curve as a function of 10-minute rainfall intensity (logarithmic logistic regression model) and the 95% confidence limits of these curves	14
6.13	Micro-scale debris flow during a rainfall simulation	113	8.16	Relative occurrence of debris flows as a function of maximum 10-minute rainfall intensity	14
6.14	Threshold conditions for the occurrence of micro-scale mass movements during rainfall simulations	113	8.17	Distribution of simulated debris-flow frequencies for the period June 1991 - June 1995 obtained from the combination of 1000 pairs of debris-flow probability curves and maximum 10-minute rainfall intensity-frequency curves (method 4)	14
7.1	General overview of the rainfall and discharge models in this chapter	115	9.1	Location of debris-flow systems with dated deposits	14
7.2	Differences in rainfall recorded by two raingauges at the TCP site	116	9.2	The Split-Moving Window (SMW) test	15
7.3	Obstruction of the discharge flume with sediment	116	9.3	<i>Rhizocarpon geographicum</i> s.l. growth curves for the Bachelard Valley and the Aosta Valley	15
7.4	Map of the monitored gully in the debris-flow trigger zone TCP	117	9.4	Relation between longest and shortest diameters of section <i>Rhizocarpon</i> thalli at Storbreen, south Norway	15
7.5	Maximum error in calculated rainfall intensities caused by discrete, 0.2 mm resolution tipping-bucket raingauge registrations	117	9.5	Debris-flow deposits from the debris-flow systems TCP, TCP-N1, TG (TGE and TGW) and TdP	154-15
7.6	Basic structure of the discharge models	118	9.6	Temporal distribution of debris flows obtained from lichenometry and/or dendrogeomorphology	15
7.7	Downstream distribution of overland flow from a cell in DINOFLOW	120	9.7	Relation between size of trigger zone and activity of debris-flow systems	15
7.8	Relation between rainfall intensity and viscosity in DINOFLOW for different values of $\alpha_n$ and $\eta_{max}$	121	9.8	Spatial patterns of activity within debris-flow deposition zones	15
7.9	Measured and calculated discharges for the three calibration rainstorms	122	9.9	Periodicity of debris-flow activity in the investigated debris-flow systems	15
7.10	Numerical stability of the discharge models	123	9.10	Periodicity of debris-flow activity in the Bachelard Valley (all five debris-flow systems)	16
7.11	Effect of timestep length on TANKFLOW 'lumped' discharge at low, intermediate and high discharges	124	9.11	11-year periodicity of debris-flow activity in the Bachelard Valley obtained through dendrogeomorphology	16
7.12	Effect of timestep length on DINOFLOW discharge at low, intermediate and high discharges	124	10.1	Regions in the Bachelard Valley	16
7.13	Sensitivity of TANKFLOW discharge at low and high discharges	125	10.2	Debris flows in the Bachelard Valley in the period 1991-1995	167-17
7.14	Sensitivity of DINOFLOW discharge at low, intermediate and high discharges	125	10.3	Debris flow on the west-facing slope of the Tête de Peynier (autumn 1992)	17
8.1	Debris-flow tracks originating from the debris-flow trigger zone TCP from June 1991 until June 1995	127	10.4	Debris flows in the Grande Cayolle Valley (autumn 1994)	17
8.2	Logistic-regression relations between maximum 5-minute rainfall intensity $i_{5s}$ and debris-flow probability for different curve-fitting methods	129	10.5	Local, high-intensity rainfall cell in a rainstorm	17
8.3	Flow chart of the identification of 'debris-flow triggering likeliness' categories for rainstorms at TCP	129	10.6	Debris-flow activity in the Bachelard Valley between July 1992 and October 1994	17
8.4	Logistic regression relations between TANKFLOW maximum discharge (rill-interrill variant, accounting for antecedent precipitation) and debris-flow probability for different curve-fitting methods	130	10.7	Relation between debris-flow activity and debris-flow trigger-zone density	17
8.5	Probability of debris-flow triggering in relation to hydrological factors (linear models): maximum 1-, 2-, 3-, 5-, 10-, 15-, 30-minute, 1-, 2- and 24-hour rainfall intensities, total rainstorm rainfall and total daily rainfall, TANKFLOW and DINOFLOW maximum discharges and antecedent precipitation indexes obtained from single-parameter regression and from 2-parameter models	133	10.8	Small debris flow originating from the transformation of a small, surficial landslide in the Grand Talon Valley (Autumn 1994)	17
8.6	Probability of debris-flow triggering in relation to hydrological factors (logarithmic models): maximum 2-, 3-, 5-, 10-, 15- and 30-minute rainfall intensities and TANKFLOW and DINOFLOW maximum discharges	134	10.9	Location of debris-flow systems for which data are available on debris-flow occurrence from regular field visits as well as from dendrogeomorphology and lichenometry	18
8.7	Relation between debris-flow triggering and hydrological factors: debris-flow triggering-probability contour plots for 2-parameter models	137	11.1	Revised debris-flow triggering hypothesis	18
8.8	Comparison of Caine's and Innes' debris-flow thresholds with debris-flow triggering-probability curves	139			

# TABLES

1.1	Debris flows reported from various countries	24
2.1	Terms describing debris flows	31
2.2	Phenomena closely related to debris flow	32
2.3	Physical properties of debris flows	35
2.4	Typical values of Manning's roughness coefficient	54
2.5	Classification of the <i>Rhizocarpon</i> subgenus	60
2.6	Reported growth rates for <i>Rhizocarpon</i>	62
2.7	Environmental factors affecting lichen growth	63
4.1	Methods used in the field and in the laboratory	82
5.1	Kinetic internal-friction angles of five coarse, cohesionless debris types	96
5.2	Significance of differences in average kinetic internal-friction angles for five debris types	
5.3	Definition of debris parameters	97
5.4	Debris-parameter values for five debris types	98
5.5	Correlations between kinetic internal-friction angle and debris parameters	98
5.6	Porosity of coarse debris	99
5.7	Porosity and field water content of fine-grained regolith material	101
6.1	Steady-state infiltration capacities (mm/hr) obtained from rainfall simulations	106
6.2	Significance levels for differences in log-average <i>K</i> -values ( <i>K</i> -values from the <i>constant-runoff</i> method)	107
6.3	Sorptivities (cm/ $\sqrt{\text{min}}$ ) obtained from rainfall simulations using different calculation methods	108
6.4	Significance levels for differences in average <i>S</i> -values ( <i>S</i> -values from the <i>constant-runoff</i> 'direct' method)	109
7.1	Calibrated values of TANKFLOW model parameters	122
7.2	Calibrated values of DINOFLOW model parameters	123
8.1	Rainstorms triggering debris flows at the TCP site in the period June 1991 - June 1995	127
8.2	A priori probabilities allocated to debris-flow likeliness categories	130
8.3	Number of debris flows predicted for data set by logistic relations between probability of debris-flow occurrence and rainfall intensity $i_{r,s}$	131
8.4	Hydrological factors and debris-flow triggering: single-variable models	132
8.5	Rainfall intensity, antecedent precipitation index and debris-flow triggering	134
8.6	Hydrological factors and debris-flow triggering: multiple-variable models	135
8.7	Akaike's (1973) Information Criterion <i>AIC</i> for logistic-regression models	136
8.8	Debris-flow frequencies and return periods for four different methods	144
9.1	Number of debris-flow deposits and debris flows dated by lichenometry and dendrogeomorphology	152
9.2	Dated debris-flow deposits	152
9.3	Activity of five debris-flow systems in the period 1940-1994	157
9.4	Possibly matching debris-flow deposits of dated debris-flow systems in the Bachelard Valley	157
10.1	Field surveys for mapping 'fresh' debris flows in the Bachelard Valley in the period 1991-1995	165
10.2	Extreme rainstorms between June 1991 and September 1994 in the Bachelard Valley	166
10.3	Comparison of debris-flow frequencies obtained from field visits with frequencies obtained from dendrogeomorphology and lichenometry	179

# SYMBOLS

Symbol	Description	Dimension
$a$	coefficient	[-]
$a_B$	constant in Bagnold's dispersive stress ( $\approx 0.042$ )	[-]
$a_p, a_x$	constants ( $x = 1, 2, 3, \dots$ )	[-]
$a_K$	correction factor for <i>K</i> -values obtained from rainfall simulations	[-]
$a_r$	radial acceleration	[L·T <sup>-2</sup> ]
$a_S$	correction factor for <i>S</i> -values obtained from rainfall simulations	[-]
$a_\eta$	power coefficient in eq. 7.21	[-]
$A$	area	[L <sup>2</sup> ]
$A_{dfo}$	total surface area occupied by debris-flow trigger zones	[L <sup>2</sup> ]
$A_{ir}$	interrill surface area	[L <sup>2</sup> ]
$A_r$	rill surface area	[L <sup>2</sup> ]
$A_{rip}$	surface area of rainfall simulation plot	[L <sup>2</sup> ]
$A_{total}$	total surface area	[L <sup>2</sup> ]
$API$	antecedent precipitation index	[L]
$API_t$	antecedent precipitation index at time <i>t</i>	[L]
$b$	coefficient (1.0 for laminar flow; 2.0 for fully turbulent flow)	[-]
$B$	'intrinsic' viscosity ( $\approx 2.5$ for mono-sized rigid spheres)	[-]
$c'$	effective cohesion	[M·L <sup>-1</sup> ·T <sup>-2</sup> ]
$c_c$	volumetric clay content	[-]
$c_s$	volumetric solids content of debris	[-]
$c_s$	volumetric solids content of static debris ( $= 1 - \theta_s$ )	[-]
$cv$	coefficient of variation = standard deviation divided by average	[-]
$cv_a$	major clast axis length sorting	[-]
$cv_b$	intermediate clast axis length sorting	[-]
$cv_c$	minor clast axis length sorting	[-]
$cv_V$	clast volume sorting	[-]
$cv_{b/a}$	clast shape sorting based on ratio of intermediate to major clast axis	[-]
$cv_{c/a}$	clast shape sorting based on ratio of minor to major clast axis	[-]
$cv_{c/b}$	clast shape sorting based on ratio of minor to intermediate clast axis	[-]
$cv_{VVc}$	clast shape sorting based on ratio of clast volume to volume of cube with axes <i>a</i> , <i>b</i> , and <i>c</i>	[-]
$C_E$	Euler's constant = 0.57721566490...	[-]
$d$	grain size	[L]
$d_{ch}$	characteristic grain diameter	[L]
$d_{max}$	diameter of single largest lichen	[L]
$d_{max,5}$	average diameter of 5 largest lichen thalli	[L]
$d_{25}$	25-percentile grain diameter	[L]
$d_{75}$	75-percentile grain diameter	[L]
$df$	degrees of freedom	[-]
$D$	diffusivity	[L <sup>2</sup> ·T <sup>-2</sup> ]
$D^2$	generalized distance	varies
$DF_{min}$	minimum value of factor having triggered a debris flow	varies
$E_j$	ring width eccentricity of ring <i>j</i>	[-]
$ER_j$	Event-Response index for year <i>j</i>	[-]
$f$	function	varies

$f_{df}$	debris-flow frequency	[T <sup>-1</sup> ]	$K_t$	hydraulic conductivity of the transmission zone	[L·T <sup>-1</sup> ]
$f_{df,reg}$	debris-flow frequency obtained from regular field visits	[T <sup>-1</sup> ]	$K_s$	saturated hydraulic conductivity	[L·T <sup>-1</sup> ]
$f_{df,dll}$	debris-flow frequency obtained from dendrochronology and lichenometry	[T <sup>-1</sup> ]	$l$	length	[L]
$F$	safety factor	[-]	$m$	relative groundwater level (0 = dry, 1 = saturated)	[-]
$F_{SP}$	Smith & Parlange factor	[L <sup>2</sup> ·T <sup>2</sup> ]	$m_a$	average major clast axis length	[L]
$g$	gravitational acceleration ( $\approx 9.81 \text{ m·s}^{-2}$ )	[L·T <sup>-2</sup> ]	$m_b$	average intermediate clast axis length	[L]
	Fisher's test statistic	[-]	$m_c$	average minor clast axis length	[L]
$g_{p,cr}$	Critical value of Fisher's test statistic for a probability level $p$	[-]	$m_v$	average clast volume	[L <sup>3</sup> ]
$PDF$	Gumbel Type I probability density function	[-]	$m_{b/a}$	average ratio of intermediate to major clast axis	[-]
$CDF$	Gumbel Type I cumulative (probability) distribution function	[-]	$m_{c/a}$	average ratio of minor to major clast axis	[-]
$h$	pressure head	[L]	$m_{c/b}$	average ratio of minor to intermediate clast axis	[-]
$h_0$	depth of water layer at the soil surface; pressure head at the soil surface	[L]	$m_{v/vc}$	average ratio of clast volume to volume of cube with axes $a$ , $b$ , and $c$	[-]
$h_w$	pressure head at the wetting front	[L]	$M$	mobility index	[-]
$H$	total hydraulic head	[L]		rank (chapter 8)	[-]
$i$	infiltration rate; infiltration capacity	[L·T <sup>-1</sup> ]		mullion size (chapter 9)	varies
$i_0$	initial infiltration rate; initial infiltration capacity	[L·T <sup>-1</sup> ]	$n$	Manning's roughness coefficient	[-]
$i_{10}$	10-minute infiltration rate	[L·T <sup>-1</sup> ]	$N$	number of data, measurements or observations; sample size	[-]
$i_{\infty}$	final infiltration rate; final infiltration capacity	[L·T <sup>-1</sup> ]	$N_{df}$	number of debris flows	[-]
$i_{of}$	overland flow intensity	[L·T <sup>-1</sup> ]	$N_{df,c}$	number of 'certain' debris flows in the period late July 1992 - mid-October 1994	[-]
$i_r$	rainfall intensity	[L·T <sup>-1</sup> ]	$N_{df,p}$	number of 'probable' debris flows in the period late July 1992 - mid-October 1994	[-]
$i_{r,c}$	critical rainfall intensity	[L·T <sup>-1</sup> ]	$N_{df,so}$	number of debris-flow trigger zones	[-]
$i_{r,max}$	maximum rainfall intensity in eq. 7.21 ( $= 2.0 \text{ mm/min}$ )	[L·T <sup>-1</sup> ]	$N_j$	total number of trees sampled in year $j$	[-]
$i_{r,min}$	minimum rainfall intensity in eq. 7.21 ( $= 0.1 \text{ mm/min}$ )	[L·T <sup>-1</sup> ]	$N_{r,j}$	total number of trees sampled in year $j$ which show a response	[-]
$i_{r,t}$	rainfall intensity at time $t$	[L·T <sup>-1</sup> ]	$NDF_{max}$	maximum value of factor not having triggered a debris flow	varies
$i_{r,x}$	$i_{r,x,t}$ x-minute rainfall intensity ( $x = 1, 2, 3, 5, 10, 15, 20, 30, 60, 120, 1440$ ) and	[L·T <sup>-1</sup> ]	$OFC$	overland flow concentration factor	[-]
	x-minute rainfall intensity at time $t$	[L·T <sup>-1</sup> ]	$p$	probability	[-]
$i_s$	splash loss intensity	[L·T <sup>-1</sup> ]	$pF$	$-^{10}\log(-h)$ ( $h$ in m)	[-]
$I$	total amount of infiltration	[L]	$q$	flux density	[L·T <sup>-1</sup> ]
$I_b$	brittleness index	[-]	$q_{10}$	10-minute specific discharge	[L <sup>2</sup> ·T <sup>-1</sup> ]
$I_{inj,cap,t}$	potential total amount of infiltration capacity-limited infiltration at time $t$	[L]	$q_f$	muddy fluid discharge per unit width	[L <sup>2</sup> ·T <sup>-1</sup> ]
$I_{of}$	total amount of overland flow at time $t$	[L]	$Q$	discharge	[L <sup>3</sup> ·T <sup>-1</sup> ]
$I_{of,in,t}$	total amount of incoming overland flow at time $t$	[L]	$Q_{of}$	overland flow discharge from rainfall simulation plot	[L <sup>3</sup> ·T <sup>-1</sup> ]
$I_{of,r,t}$	total amount of overland flow from interrills at time $t$	[L]	$Q_w$	water discharge	[L <sup>3</sup> ·T <sup>-1</sup> ]
$I_{of,out,t}$	total amount of outgoing overland flow at time $t$	[L·T <sup>-1</sup> ]	$r$	radial distance perpendicular to flow	[L]
$I_{r,c}$	cumulative rainfall amount	[L]	$r^2$	correlation coefficient, explained variance	[-]
$I_{r,cr}$	critical rainfall amount	[L]	$r_0$	radius of rigid plug	[L]
$I_{r,daily}$	total amount of daily rainfall	[L]	$r_{Aj}, r_{Bj}, r_{Cj}$	tree-ring widths for ring $j$ in downslope, upslope and slope-parallel directions	[L]
$I_{r,eff}$	effective amount of rainfall	[L]	$r_b$	radius of channel bend	[L]
$I_{r,rs}$	total amount of rainstorm rainfall	[L]	$r_d$	radius of flow perpendicular to flow	[L]
$I_{r,t}$	total amount of rainfall at time $t$	[L]	$r_h$	hydraulic radius of (channel) flow	[L]
$I_{r,x}$	x-minute rainfall amount	[L]	$R$	viscous resistance	[M <sup>-1</sup> ·T]
$I_{reg,t}$	surface storage at time $t$	[L]	$R_j$	amplitude of $j^{\text{th}}$ harmonic	[-]
$I_s$	$I_{s,t}$ total amount of surface storage; total amount of surface storage at time $t$	[L]	$Re$	Reynolds number	[-]
$I_{storage,t}$	potential total amount of regolith storage capacity-limited infiltration at time $t$	[L]	$Re_{lam}$	Reynolds number from laminar flow velocity equation (eq. 2.89)	[-]
$I_{supply,t}$	potential total amount of supply-limited infiltration at time $t$	[L]	$Re_{tur}$	Reynolds number from turbulent flow velocity equation (eq. 2.90)	[-]
$I_t$	total amount of infiltration at time $t$	[L]	$s$	distance in direction of flow or slope	[L]
$j$	index counter	[-]		standard deviation	varies
$K$	hydraulic conductivity; steady state infiltration capacity	[L·T <sup>-1</sup> ]	$s_X$	sample standard deviation of variable X	varies
$K'$	corrected hydraulic conductivity; corrected steady state infiltration capacity	[L·T <sup>-1</sup> ]	$se$	standard error	varies
$K_j$	hydraulic conductivity of coarse debris for muddy fluid	[L·T <sup>-1</sup> ]	$S$	sorptivity	[L·T <sup>-1/2</sup> ]

$S'$	corrected sorptivity	$[L \cdot T^{-1/2}]$
$S$	sensitivity index; strength ratio	$[-]$
$SO_T$	Trask sorting coefficient $= (d_{75}/d_{25})^{1/4}$	$[-]$
$STO_{reg}$	regolith storage capacity	$[L]$
$t$	time	$[T]$
	Student's t-statistic	$[-]$
$t_p$	time-to-ponding	$[T]$
$t_r$	rainfall duration	$[T]$
$t_{rs}$	rainstorm duration	$[T]$
$t_s$	time where under ponded infiltration the same total amount of infiltration is reached as at time $t_p$ under non-ponded, constant infiltration	$[T]$
$T$	return period	$[T]$
$u$	flow velocity	$[L \cdot T^{-1}]$
$u_1, u_2$	flow velocity in points 1 and 2	$[L \cdot T^{-1}]$
$u_f$	velocity of debris-flow front	$[L \cdot T^{-1}]$
$u_m$	average flow velocity	$[L \cdot T^{-1}]$
$u_{max}$	maximum flow velocity	$[L \cdot T^{-1}]$
$u_{of,lam}$	laminar flow velocity of overland flow	$[L \cdot T^{-1}]$
$u_{of,tr}$	transitional flow velocity of overland flow	$[L \cdot T^{-1}]$
$u_{of,tur}$	turbulent flow velocity of overland flow	$[L \cdot T^{-1}]$
$U$	instantaneous unit hydrograph	$[L^2]$
$V$	volume	$[L^3]$
$V_{of}$	collected volume of overland flow from rainfall simulation plot	$[L^3]$
$x$	horizontal coordinate; horizontal distance	$[L]$
	variable; variable value	varies
$X$	variable	varies
$\bar{x}$	sample average of variable $X$	varies
$y$	distance perpendicular to flow; distance perpendicular to slope	$[L]$
$y_0$	depth of rigid plug (raft)	$[L]$
$y_f$	failure depth	$[L]$
$y_d$	depth of flow perpendicular to flow	$[L]$
$y_m$	average depth of flow perpendicular to flow	$[L]$
$Y$	discriminant function (Sengo 1980)	$[L]$
	discriminant function (Okuda et al. 1981, Okunishi & Suwa 1985)	$[L \cdot T^{-1}]$
$z$	vertical coordinate; depth	$[L]$
$z_f$	vertical coordinate of fluid surface; depth of failure plane	$[L]$
$z_h$	gravity head	$[L]$
$z_{of}$	depth of overland flow	$[L]$
$z_{reg}$	depth of regolith	$[L]$
$z_w$	depth of flow; depth of water flow above weir outflow base (m)	$[L]$
$z_{wf}$	depth of the wetting front	$[L]$
$\alpha$	recession coefficient, outflow constant, decrease coefficient	$[T^{-1}]$
	significance level	$[-]$
$\beta$	slope angle	$[\alpha]$
$\beta_f$	slope angle of failure plane	$[\alpha]$
$\beta_{min}$	threshold slope angle	$[\alpha]$
$\partial$	partial derivative	
$\delta$	parameter in standard error of estimate of Gumbel distribution (eq. 8.16)	$[-]$
$\delta_b$	surface tilt angle in channel bend	$[\alpha]$
$\Delta t$	time step length	$[T]$

$\Delta t_{fp}$	time period covered by the surveys (in years)	$[T]$
$\Delta t_{dl}$	time period covered by the lichenometrically and dendrogeomorphologically dated deposits (in years)	$[T]$
$\Delta t_{tr}$	time step on interrills	$[T]$
$\Delta t_r$	time step on rills (in seconds)	$[T]$
$\varepsilon$	random term with standard normal distribution (average 0; standard deviation 1)	$[-]$
$\eta_B$	Bingham viscosity	$[M \cdot L^{-1} \cdot T^{-1}]$
$\eta_C$	Coulomb viscosity	$[M \cdot L^{-1} \cdot T^{-1}]$
$\eta_f$	viscosity of interstitial fluid	$[M \cdot L^{-1} \cdot T^{-1}]$
$\eta_{max}$	maximum viscosity of overland flow in eq. 7.21	$[M \cdot L^{-1} \cdot T^{-1}]$
$\eta_N$	Newtonian viscosity	$[M \cdot L^{-1} \cdot T^{-1}]$
$\eta_{of}$	viscosity of overland flow	$[M \cdot L^{-1} \cdot T^{-1}]$
$\eta_w$	viscosity of water at 20°C (= 0.001 Pa·s)	$[M \cdot L^{-1} \cdot T^{-1}]$
$\theta$	volumetric water content	$[-]$
$\theta_f$	volumetric field water content	$[-]$
$\theta_i$	initial volumetric water content	$[-]$
$\theta_m$	volumetric water content at failure	$[-]$
$\theta_s$	saturated volumetric water content, porosity (= 1-c.)	$[-]$
$\theta_t$	volumetric water content of the transmission zone	$[-]$
$\kappa$	coefficient (constant) in Takahashi's debris-flow models	$[-]$
$\lambda$	linear concentration	$[-]$
$\rho_b$	bulk density of debris	$[M \cdot L^{-3}]$
$\rho_{dry}$	bulk density of dry debris	$[M \cdot L^{-3}]$
$\rho_f$	density of fluid	$[M \cdot L^{-3}]$
$\rho_m$	density of debris-flow matrix material	$[M \cdot L^{-3}]$
$\rho_{of}$	density of overland flow	$[M \cdot L^{-3}]$
$\rho_s$	density of solids	$[M \cdot L^{-3}]$
$\rho_{sat}$	bulk density of saturated debris	$[M \cdot L^{-3}]$
$\rho_u$	bulk density of unsaturated debris	$[M \cdot L^{-3}]$
$\rho_w$	density of water	$[M \cdot L^{-3}]$
$\sigma$	normal stress	$[M \cdot L^{-1} \cdot T^{-2}]$
$\sigma'$	effective normal stress	$[M \cdot L^{-1} \cdot T^{-2}]$
$\sigma_d$	dispersive stress	$[M \cdot L^{-1} \cdot T^{-2}]$
$\sigma_f$	pore pressure of fluid	$[M \cdot L^{-1} \cdot T^{-2}]$
$\sigma_{f1}, \sigma_{f2}$	pore pressure of fluid in points 1 and 2	$[M \cdot L^{-1} \cdot T^{-2}]$
$\tau$	shear stress	$[M \cdot L^{-1} \cdot T^{-2}]$
$\tau_0$	yield strength	$[M \cdot L^{-1} \cdot T^{-2}]$
$\tau_f$	maximum shear resistance; shear resistance at failure	$[M \cdot L^{-1} \cdot T^{-2}]$
$\tau_r$	residual shear resistance	$[M \cdot L^{-1} \cdot T^{-2}]$
$\varphi$	internal-friction angle	$[\alpha]$
$\varphi'$	effective internal-friction angle	$[\alpha]$
$\varphi'_s$	effective static internal-friction angle	$[\alpha]$
$\varphi'_k$	effective kinetic internal-friction angle	$[\alpha]$
$\varphi$	grain size = $^{-2} \log(\text{grainsize in mm})$	$[-]$
$\varphi_j$	phase of $j$ th harmonic	$[T]$
$\varphi^2$	strength of relation (= $\chi^2/N$ )	$[-]$
$\chi^2$	Chi-square statistic	$[-]$
$\omega$	frequency	$[T^{-1}]$
$\omega_j$	component frequency	$[T^{-1}]$

### 1.1 Background and problem definition

Mass movements, movements of rock and soil induced by gravity, are a major denudational process in steeply sloping terrains (Mulder 1991). Although most mass movements are relatively small and cause little damage, their widespread occurrence is still the cause of considerable economic losses. These losses may result from damage to buildings, infrastructure and arable land (Rapp and Strömquist 1976, Reid et al. 1991, Wohl and Pearthree 1991) and from blocking of roads and railways (Harp et al. 1995, Rebetez et al. 1997, Sasahara and Tsunaki 1994). Indirect damage may result from the sediment delivered to rivers (Jordan and Slaymaker 1991) and the damming of rivers with subsequent breaching and flooding (Evans 1986, Evans and Brooks 1991). Only few mass movements are dangerous enough to cause casualties: most mass movements are slides and flows moving at speeds of no more than millimeters to meters per day.

Debris flows are one of the more dangerous types of mass movement. They are rapid mass movements consisting of granular solids, water and air, moving as a viscous flow (Varnes 1978). The movement type of debris flows, gravity flow, differs on the one hand from landslides, in which a more or less rigid mass slides along a distinct shear surface. On the other hand, the movement type also differs from streamflow, where the material is transported by the shear forces exerted by the water flow, rather than by gravity. Debris flows are a well known phenomenon in mountainous areas all over the world (fig. 1.1; table 1.1). Their relatively high velocities, usually in the order of several meters per second, are the main cause for the comparatively high economic losses and high number of casualties induced by debris flows. In particular this applies to debris flows occurring in densely populated areas. In Japan alone, about 1000 people have been killed by debris flows between 1967 and 1980 (Takahashi 1981b). Examples of debris flows causing casualties are known from Brazil (Ogura et Filho 1991), Canada

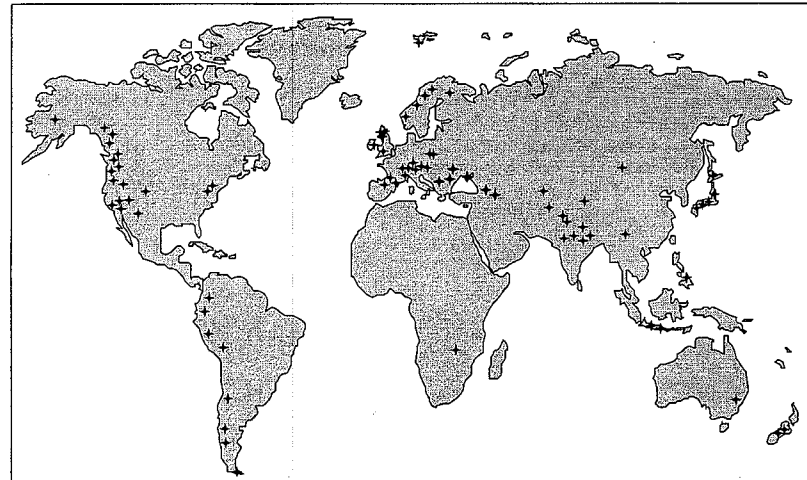


Figure 1.1 World map of debris-flow occurrence (after Innes 1983a).



Table 1.1 Debris flows reported from various countries (partly based on Innes 1983a).

Country	Author
Afghanistan	Kaszowski 1984
Argentina	Gallart et al. 1994
Atlantic Ocean	Masson et al. 1992
Austria	Aulitzky 1994, Aulitzky et al. 1994
Brazil	Jones 1973, Ogura and Filho 1991
Canada	Bovis and Dagg 1987, 1988, Gardner 1989, Owens 1973, 1974
Chile	Winchester and Harrison 1994
China	Brand 1993, Lehmkuhl and Liu Shijian 1994, Kang Zicheng and Li Jing 1987, Lehmkuhl and Pörtge 1991, Li 1994, Li Lie 1985, Li and Luo 1981, Renlin 1992, Tang Bangxing et al. 1994, Zeng et al. 1992
Colombia	Martinez et al. 1995, Thouret and Laforge 1994
Costa Rica	Mora et al. 1993
Ecuador	Peltre 1994
France	Azimi and Desvarreux 1974, Blijenberg 1993b, De Graaf et al. 1993, Evin 1990, Gispert 1993, Hovius 1990, Meunier 1991, Nieuwenhuijzen and Van Steijn 1990, Van Asch and Van Steijn 1991, Van Steijn 1988, 1991, Van Steijn et al. 1988b
Germany	Strunk 1991
Great Britain	Baird and Lewis 1957, Ballantyne 1981, 1991, Innes 1989, Kotarba 1984b, Luckman 1992
India	Owen et al. 1995, Starkel 1972
Indonesia	Camus et al. 1992, Chida and Hariyono 1995, Lavigne and Thouret 1994, Scrivenor 1929
Ireland	Prior et al. 1968
Italy	Engelen 1967, Marchi et al. 1993, Strunk 1988, 1989, 1991
Japan	Ikeya 1981, Kobashi and Suzuki 1987, Marui et al. 1997, Nakada 1992, Okuda 1989, Okuda et al. 1980, Sasahara and Tsunaki 1994, Sassa et al. 1997, Suwa and Okuda 1980, 1988, Suzuki and Furuya 1992, Takahashi 1981b, Takahashi et al. 1981
Kazakhstan	Khegai et al. 1992
Mongolia	Kowalkowski and Starkel 1984
Nepal	Saijo 1991, Yoshimatsu 1994
New Zealand	Pierson 1980, 1981
Norway	André 1995, Rapp 1963, Rapp and Strömquist 1976, Sulebak 1969
Pakistan	Hewitt 1993, Owen 1991, Wasson 1978
Peru	Plafker and Erickson 1978
Philippines	Arboleda and Punongbayan 1991, Arguden and Rodolfo 1990, Pierson 1992
Poland	Jonasson et al. 1991, Kotarba 1984a, 1989, 1992, 1997, Krzemiński 1988
Romania	Balteanu 1976
Russia	Gagoshidze 1969, Goldin and Lyubashevskiy 1966, Niyazov and Degovetz 1975
Slovakia	Midriak 1984
Spain	García-Ruiz et al. 1988
Sweden	Niessen et al. 1992, Rapp and Nyberg 1981, Rapp and Strömquist 1976, Schlyter et al. 1993
Switzerland	Haeblerli et al. 1990, 1991, Kienholz and Mani 1994, Kienholz et al. 1991, Rickenmann 1990, Rickenmann and Zimmermann 1993, Rösli and Schindler 1990, Zimmermann 1990
United States	Benda 1990, Benda and Dunne 1987, Campbell 1974, 1975, Cenderelli and Kite 1998, Coe et al. 1997, Cummins 1981, DeGraff 1994, Fleming et al. 1989, Harp et al. 1995, Harris and Gustafson 1993, Johnson and Rodine 1984, Reid et al. 1991, Walder and Driedger 1994, Wohl and Pearthree 1991

(Bovis 1993), China (Brand 1993, Zeng et al. 1992), Colombia (Martinez et al. 1995) and Nepal (Yoshimatsu 1994). The most devastating example in recent history is the catastrophic debris flow caused by an eruption of the Nevado del Ruiz volcano in Colombia in 1988. It buried the village of Armero, killing over 30,000 people.

However, most debris flows are quite small and occur unnoticed in remote, sparsely inhabited or uninhabited areas. Usually such small debris flows are triggered by heavy rainfall (Blijenberg 1993b, Kobashi and Suzuki 1987, Rapp and Nyberg 1981). Trigger zones of debris flows are often difficult to access. Other geomorphological processes such as rock fall are often highly active in these zones, and therefore research in such areas involves some risk. Thus it is not surprising that debris flows have

received much less attention in literature than landslides. Most of the research has concentrated on the 'safer' aspects of debris flows: laboratory simulations (Bagnold 1954, Phillips and Davies 1991, Van Steijn and Coutard 1989, Van Steijn et al. 1988a) and model development dealing mainly with the triggering and movement mechanisms (Bovis and Dagg 1987, 1988, Fleming et al. 1989, Johnson 1965, 1970, Johnson and Rahn 1970, Johnson and Rodine 1984, Postma 1988, Takahashi 1978, 1980, 1981a, 1981b); debris-flow deposit studies dealing with their morphological and sedimentological characteristics (Nieuwenhuijzen and Van Steijn 1990, Van Steijn et al. 1988b) or the dating of old deposits (De Redelijkheid 1988, Innes 1982a, 1983b, 1985b, Strunk 1989, 1991); or case studies of debris flows which have occurred during extreme meteorological situations (Campbell 1974, 1975, Haeblerli et al. 1990, 1991, Hovius 1990, Zimmermann 1990). The last type of research may be biased toward the description of larger debris flows, as such debris flows are more likely to draw attention. With the increasing use of natural resources even in high mountain areas, the economic damage by debris flows is likely to increase, especially in densely populated areas like the Alps. In order to reduce the risk caused by debris flows, both spatial and temporal aspects of debris-flow hazard should be known. Moreover, the risk associated with debris flows may well change if rainfall regimes change as a part of a general climate change. If debris-flow hazards and risks are to be assessed quantitatively, models must be available describing the triggering, movement and deposition of debris flows. Also, the values of all the factors in these models must be known. In case of an assessment of the effect of climatic change on debris-flow hazards, the amount of change in rainfall parameters relevant to debris-flow triggering must be known and the sensitivity of debris-flow occurrence to those parameters. Of course this implies that such parameters must be known. At present, the generation of precipitation scenarios by the present climate models (GCM's) is still problematic (Kwadijk 1991, 1993, World Meteorological Organization 1987). They generate inaccurate, low resolution time-averaged precipitation values, so that changes in specific rainfall parameters are difficult or impossible to quantify for future climatic change (Gates 1985). Apart from the models describing triggering, movement and deposition of debris flows, the aspects mentioned have received little attention in the past.

## 1.2 Framework and objectives

In 1991 the project 'The Temporal Analysis of Debris Flows in an Alpine Environment' (the *Debris Flow project*) was started at the Department of Physical Geography of Utrecht University, where it was embedded in the research cluster GEOPRO II (GEOMorphological PROCesses). It was part of the project 'Temporal Occurrence and Forecasting of Landsliding in the European Community', financed by EPOCH (European Programme on Climatology and Natural Hazards). The coordination of this project was carried out by the CERG, the European Center of Geomorphological Hazards. Central themes of this EPOCH project were the temporal aspects of instability and of the factors causing instability (Flageollet 1993a, 1993b, European Commission 1994).

The present project is a continuation of research on debris flows and landslides carried out since the early eighties by the Department of Physical Geography in the region around Barcelonnette in the southern French Alps (e.g. Salomé and Beukenkamp 1989, Braam et al. 1987a, 1987b, Caris and Van Asch 1991, De Redelijkheid 1988, Hovius 1990, Miltenburg 1986, Mulder 1991, Mulder and Van Asch 1987, 1988a, 1988b, 1988c, 1988d, Mulder et al. 1987, Postma 1988, Nieuwenhuijzen and Van Steijn 1990, Van Asch and Buma 1997, Van Asch and Van Steijn 1991, Van Asch et al. 1989, Van Steijn 1989, 1991, 1996, Van Steijn et al. 1988b). Preceding work on debris flows had mainly concentrated on morphological and sedimentological properties of the deposits in relation to the movement mechanisms (Nieuwenhuijzen and Van Steijn 1990, Van Steijn and Coutard 1989, Van Steijn et al. 1988a, 1988b) and on dating of deposits (De Redelijkheid 1988, Van Steijn 1991). Debris

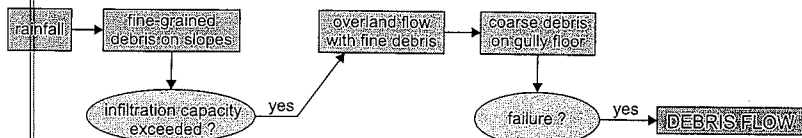


Figure 1.2 Debris-flow triggering hypothesis according to Postma (1988).

flows in the Ubaye Valley and its tributaries are usually <100 m<sup>3</sup> to several 1000 m<sup>3</sup> (small-scale to medium-scale), <100 m to over 1000 m long and they hardly ever continue to move when they reach the valley floor (hillslope debris flows).

The field experiences of these workers has led to the following hypothesis of debris-flow triggering in this part of the French Alps (Postma 1988; fig. 1.2):

*Small-scale hillslope debris flows in the Bachelard Valley are mainly triggered during short-duration rainstorms with high rainfall intensities. During such rainstorms, Hortonian overland flow occurs in the debris-flow trigger zones and incorporates fine-grained debris. This muddy overland flow concentrates towards a central gully in a trigger zone, where it meets and enters an accumulation of loose, cohesionless, coarse debris. Depending on the fluid pressure exerted by the muddy fluid, the coarse debris may or may not be destabilized and move downslope as a debris flow.*

The final aim of the Debris Flow project is to forecast the triggering and frequency of debris flows, based on precipitation characteristics on the one hand, and on morphological and hydrological characteristics of debris flow trigger zones on the other hand (fig. 1.3). The relation between debris-flow magnitude and frequency will be ignored in this project. Using the above hypothesis, the following research objectives were formulated:

With respect to modelling debris-flow triggering:

- quantify all the factors in an appropriate (physical) debris-flow triggering model.
- find the most important morphological and hydrological characteristics of debris-flow trigger zones controlling debris-flow triggering; preferably characteristics that can be easily obtained from a survey or from aerial photographs.

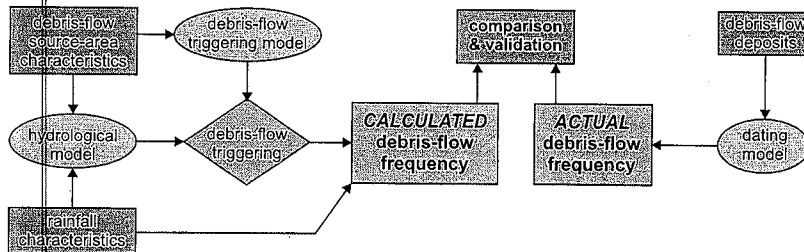


Figure 1.3 General flow chart of the project.

With respect to the specific role of water in debris-flow triggering:

- quantify the amount of water necessary to trigger a debris flow (threshold values of rainfall and/or runoff).
- identify the relevant rainfall characteristics involved in debris-flow triggering.
- find the optimal hydrological model with regard to its ability to discriminate between conditions triggering debris flows and those not triggering debris flows.
- determine the characteristics of the muddy runoff fluid.

With respect to debris-flow activity in the Bachelard Valley:

- quantify the frequency of debris flows by combining rainfall intensity-duration-frequency characteristics with debris-flow threshold values obtained from the triggering model.
- check this debris-flow frequency with the frequency obtained from deposit dating methods.
- forecast the triggering and frequency of debris flows on the basis of morphological and hydrological characteristics of debris-flow trigger zones and of precipitation characteristics.
- investigate the temporal and spatial variability of debris-flow activity in the Bachelard Valley.

### 1.3 Methodology and thesis structure

In order to meet the research objectives, a number of different approaches have been used. The Tête du Clot des Pastres debris-flow trigger zone, representative for debris-flow trigger zones in the Bachelard Valley, was chosen for detailed measurements. In this catchment a hydrological measurement station was installed. This station consisted of two raingauges, a discharge gauge, a flume with sediment removal, and a video camera, all connected to a data logger which was installed at the end of spring and removed in autumn (chapter 4). Erosion plots and erosion markers were installed and a DEM was produced from a geodetic survey. Finally, debris-flow deposits originating from this site have been dated with dendrogeomorphology and lichenometry in order to reconstruct past debris-flow activity (chapter 9).

For this site, several hydrological models with different degrees of complexity were developed (chapter 7). This was done to predict the amount of overland flow for any particular rainstorm and the threshold runoff necessary to trigger a debris flow (chapter 8). Two of these models used an infiltration module for which the infiltration parameters were determined from in-situ rainfall simulations on the fine-grained regolith material (chapter 6). The models were tested to find the best models with regard to their ability to discriminate between conditions that trigger debris flows and conditions that do not. These debris-flow triggering conditions are compared with rainfall characteristics, which leads to a prediction of debris-flow frequency (chapter 8).

Debris parameters were determined for use in the debris-flow triggering model and the hydrologic models for this site (chapters 5 and 6): density, porosity, grain-size distribution, grain shape, hydraulic conductivity and strength of the coarse debris; density, porosity, grain-size distribution, water-retention curves, infiltration characteristics (sorption, steady-state infiltration capacity) of the fine-grained regolith material and the regolith depth. Also an attempt was made to investigate the relation between sediment content, density and viscosity of the runoff fluid on the one hand and the relation between sediment content and rainfall (excess) intensity on the other hand. With these data it should be possible to predict the runoff fluid characteristics and the fluid level in the coarse debris during a rainstorm (chapter 5).

For all other debris-flow trigger zones in the Bachelard Valley, less data have been gathered. At a few other sites, some of the measurements mentioned for the Tête du Clot des Pastres site have also been carried out, for instance debris strength determinations (chapter 5), rainfall simulations (chapter 6), deposit dating (chapter 9) or geodetic surveys.

Besides these 'extended' measurements for a few sites, an inventory has been made of all debris-flow trigger zones in the Bachelard Valley (chapter 3). Regular surveys have been carried out twice a year to search for newly formed debris-flow deposits (chapter 10), revealing the spatial and temporal variability of debris-flow activity. For most of the debris-flow trigger zones in the Bachelard Valley, an attempt was made to make an inventory of their topographical, morphological, hydrological and lithological characteristics and to relate these to their activity (chapters 3 and 10).

A detailed account of the methods used in this study is given in chapter 4. Further, this thesis contains a general introduction to debris flows (chapter 2) and a description of the study area in the southern French Alps (chapter 3). Finally, chapter 11 summarizes the results and presents the main conclusions, which are compared with the research objectives stated in section 1.2.

## 2.1 Debris flows

### 2.1.1 Introduction

Apart from some isolated studies (Bailey et al. 1934, Blackwelder 1928, Bonney 1902, Conway 1893, 1894, Penck 1924, Rickmers 1913, Scrivenor 1929, Walther 1924), the study of debris flows is still young. This can be attributed to the difficulties involved in debris-flow research. Laboratory equipment for determination of debris-flow rheology must be large enough to test coarse, heterogeneous materials, such as the 2 m large rheometer described by Phillips and Davies (1991) or the 95 m long, 2 m wide debris-flow flume of Iverson et al. (1993). Difficult terrain circumstances make direct measurement of debris-flow properties problematic. In the past decades however, an increasing number of studies concerning debris flows have been carried out. The increasing interest in debris flows is largely caused by the growing need to understand the hazards of high mountain areas, which pose increasing risks as human pressure on high mountain environments steadily expands (Bovis 1993). On the other hand, the recognition of debris flows as important mechanisms of sediment transport and sediment supply to rivers in mountain areas has also led to an increase of debris-flow research (Bovis 1993, Evans and Brooks 1991).

A debris flow has been defined by Varnes (1978) as a rapid mass movement of granular solids, water and air, moving as a viscous flow. Johnson (1970) defined a debris flow as a gravity-induced mass movement intermediate between landsliding and water flooding, with mechanical characteristics different from either of these two processes. In landslides, a more or less rigid mass slides along a distinct shear surface. On the other hand, in streamflow the sediment transport is caused by shear forces exerted on the sediment by the streaming water. In debris flows, the movement of the debris is caused by its own mass, and the shear deformation is distributed over a large part of the flow depth. This type of flow is called gravity flow. Within the continuum from pure streamflow to dry landslides, no sharp division can be made between (hyperconcentrated) streamflow and debris flow, or between landslides and debris flows. For the flow part of the continuum, the rheological classification given by Pierson and Costa (1987) discriminates between debris flow and other types of flow (fig. 2.1). Here the groups of slurry flows and granular flows add up to form the group of gravity flows. In granular flows, water content is less than in slurry flows, and the behaviour is dominated by grain interactions. In debris flows, viscous water effects, grain-grain and water-grain interactions play an essential role. Water content and grain-size composition determine the relative influence of these three effects on debris flow behaviour.

The variety of terms used to describe debris flows in the past (see table 2.1) has been quite confusing, as pointed out by Brunsten (1979). Partly, this is the result of debris flows being part of a continuum of processes without sharply defined transitions. Terms such as *slide*, *avalanche*, *solifluction* or *torrent* indicate other movement mechanisms than gravity flow and should not be used for debris flows, although Innes (1983a) includes debris avalanches in the term debris flow. *Mudflow* and *earthflow* are nowadays usually applied to slow, periodically active debris mass movements (Prior et al. 1971), whereas debris flows occur as single events. Table 2.2 lists some phenomena which are closely related to debris flow. The term *lahar* is reserved for debris flows related to volcanic activity.

Debris flows can be classified according to various criteria. Innes (1983a) proposed a subdivision of debris flows based on deposit volume (fig. 2.2). The class limits are rather arbitrary. In the former Soviet Union a distinction was made between structural (containing little water) and turbulent (containing much water) debris flows (Gol'din and Lyubashevskiy 1966, Syanozhetsky et al. 1973).

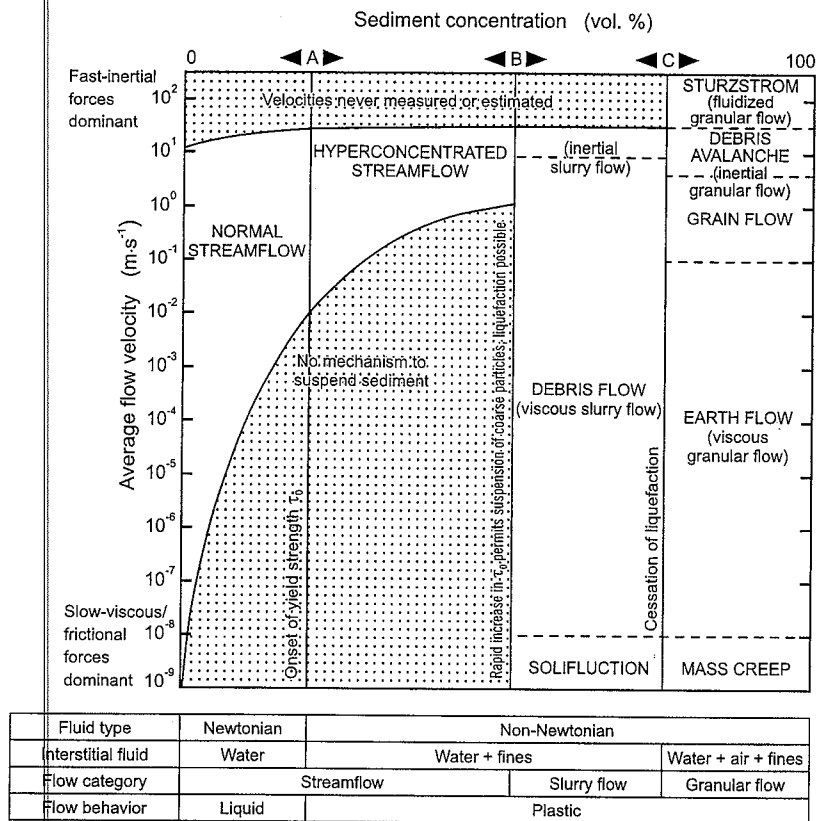


Figure 2.1 Rheological classification of flows proposed by Pierson and Costa (1987). The vertical boundaries A, B and C are rheological thresholds related to sediment composition; their positions in this figure are shown for a coarse, poorly sorted mixture. For coarser sediments the boundaries move to the right, for fine-grained sediments they move to the left. Shaded zones indicate conditions not known in nature (after Selby 1993).

This subdivision was based on the effect of water content on debris-flow movement. Varnes (1978) proposes a velocity-based classification of debris flows: debris avalanches, debris flows and mudflows. However, the terms debris avalanche and mudflow both indicate other types of mass movement, and should not be used merely to indicate velocity differences. Brunsden (1979) proposed the classification shown in figure 2.3a. Hillslope flows are those flows that occur on hillslopes and usually do not continue their movement once they reach the valley floor. On the contrary, valley-confined flows can have long run-out distances in narrow valleys, only to deposit their sediment on fans at the mouth of the valley. Once again, no sharp distinction exists between catastrophic flows, hillslope flows and valley-confined flows. This classification was extended by

Table 2.1 Terms describing debris flows (partly based on Innes 1983a).

Name	Author
English	
Alpine mudflow	Slaymaker and McPherson 1977
Debris avalanche	Williams and Guy 1973
Debris slide	Bogucki 1977, Rapp 1963
Debris torrent	Bovis 1993, Swanston and Swanson 1976
Lahar	Neall 1976, Scrivenor 1929
Mud avalanche	Conway 1893, 1894
Mudflow	Blackwelder 1928, Owens 1973, 1974
Mudrock flow	Bailey et al. 1934
Mudspate	Rickmers 1913
Mudstream	Bonney 1902, Scrivenor 1929
Summer solifluction	Baird and Lewis 1957
French	
Boue torrentielle	Lefebvre in Meunier 1991
Coulée boueuse	Caillex and Tricart 1950, Van Vliet-Lanoë and Valladas 1992
Coulée de débris	Van Steijn et al. 1988a
Coulée de débris canalisée	Sauret in Meunier 1991
Coulée de laves	Van Steijn et al. 1988a
Flot de débris	Bertran and Texier 1994, Chamley 1977, Héty et al. 1995
Lave boueuse	Héty et al. 1995
Lave de ruissellement	Van Steijn et al. 1988a
Lave torrentielle	Tricart 1957
German	
Mure	Rickmers 1913
Murgang	Haerberli et al. 1991
Murschub	Strunk 1988
Sandbrei	Walther 1924
Schlammstrom	Penck 1924
Other languages	
Blockig slamström	Rapp and Nyberg 1981
Puinestroom	De Graaf et al. 1993, Hovius 1990, Van Steijn 1989
Sjel	Gontscharev 1962

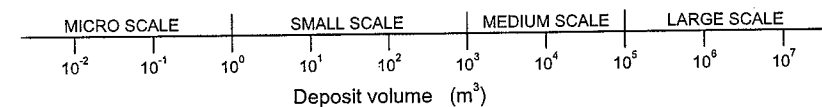


Figure 2.2 Classification of debris flows based on deposit volume (after Innes 1983a).

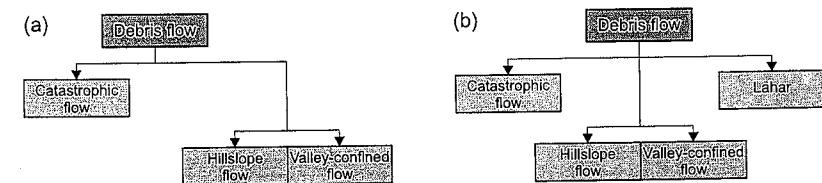


Figure 2.3 Morphogenetic classification of debris flows: (a) original classification (Brunsden 1979); (b) revised classification (Innes 1983a).

Table 2.2 Phenomena closely related to debris flow (partly based on Innes 1983a).

Process	Difference with debris flow
Debris avalanche	Very fast, inertial granular flow with little or no interstitial fluid
Debris slide	Slide mechanism
Dry grain flow	Dry, inertial, granular flow with no or little interstitial fluid
Frost-coated clast flow (Héty et al. 1994)	Dry, inertial, granular flow with ice-covered particles
Hyperconcentrated flow, debris torrent	Streamflow transportation
Mudflow, earthflow	Slow, viscous, granular flow
Peat soilflow (Gallart et al. 1994)	Mixture of water and peat
Pyroclastic flow	Inertial granular flow of hot volcanic ash and gas
Slush avalanche (Buli et al. 1995)	Mixture of water, snow and ice; large-scale event
Slush flow (Elder and Kattelmann 1993)	Mixture of water, snow and ice; small-scale event
Slush stream (Gude and Scherer 1995)	Mixture of water, snow and ice; small-scale event
Slush torrent (André 1995, Gude and Scherer 1995)	Mixture of water, snow and ice; large-scale event
Solifluction	Very slow viscous flow
Sturzstrom (Hstü 1975)	Extremely fast (up to 100 m s <sup>-1</sup> ), dry, fluidized, granular flow with no or little interstitial fluid
Turbidity current	Submarine density current
Waterflood	Very dilute streamflow transportation

Innes (1983a) to give the essentially morphogenetic classification of figure 2.3b. Other classifications can be made, based on for example composition (silty debris flow, sandy debris flow), parent material (tillflow, peatflow), morphology or triggering mechanism. Selby (1993) points out that there is still a lot of confusion concerning the subdivision of debris flows.

## 2.1.2 Characteristics of debris flows

Debris flows have rarely been observed by trained professionals (Johnson and Rodine 1984, Khegai et al. 1992, Morton and Campbell 1974, Pierson 1980, Sharp and Nobles 1953, Wasson 1978), but in more recent years video cameras have proven useful for debris-flow observation (Blijenberg 1993a, 1993b, Okuda et al. 1980, Okunishi and Suwa 1985). From such observations, debris flows often appear to occur as a series of waves or surges (Li and Luo 1981, Pierson 1980). The surges typically have a steep front which contains the largest boulders transported by the debris flow. Between the surges, phases of more fluid, watery, turbulent flow with a high sediment content but with fewer boulders may occur. Another feature sometimes observed is an apparent *rigid plug* in the centre of flow, which seems to float as a raft on the flowing debris (Johnson 1970, Wasson 1978). A rigid plug is not always observed; sometimes the flow character is very turbulent, with boulders jostling and jumping at the surface (Okuda et al. 1980, Pierson 1980, 1981).

Debris flows show a very distinct morphology (fig. 2.4). The length of a debris flow is usually much larger than its width; frequently reported length:width ratio's are usually over 10:1 and can be 50:1 or more (Van Steijn 1988). Usually three different zones can be distinguished (Van Steijn 1989): a source area or trigger zone, a transport zone, and a deposition zone. Debris flows originate in the trigger zone, where sediment removal by debris flows dominates over deposition. Usually this trigger zone is a steep, little vegetated area, with sufficient debris present at the surface. The trigger zone can be a landslide complex, a steep couloir above a scree slope, or a bare, often spoon-shaped or funnel-shaped erosion zone on a slope. Downslope, the trigger zone changes into the transport zone, where erosion and deposition by debris flows are more or less balanced. This transport zone usually consists of a channel, either or not bordered by lateral levees. The channel can be situated on the valley floor, in a gully, or it can be a shallow channel on a scree slope.

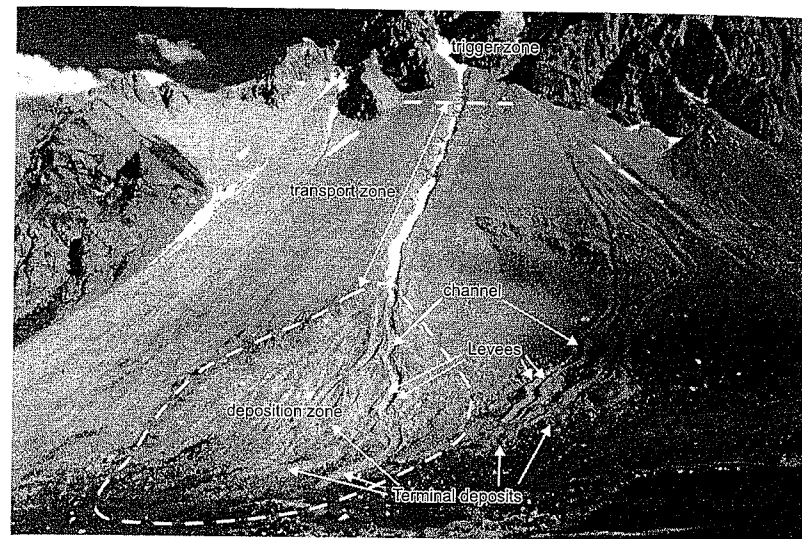


Figure 2.4 Typical morphology of a hillslope debris flow and debris-flow terminology.

Further downslope, the transport zone gradually changes into the deposition zone, where deposition dominates over erosion. In the upper part, the deposition zone often consists of a channel bordered by levees, which can be difficult to distinguish from the lower part of the transport zone. The lateral levees have steep sides, and they often show inverse grading: the coarsest particles can be found on top of the levees and on the outside. Figure 2.5 shows a cross-section through a debris-flow channel and levee. The levees meet downslope in a terminal or frontal lobe. This lobe has a steep front and may also show inverse grading. If the flow consists of relatively fine material and the deposition takes place on relatively flat terrain, the deposit can have a sheet-like character. Debris-flow deposits within the channel are called medial deposits (Johnson and Rodine 1984). Debris-flow deposits can be found on talus slopes, on alluvial fans and on debris fans. They may also occupy large parts of valley floors. Very often the debris-flow deposits are not the only type of deposits found at such locations. On scree slopes deposits formed by processes such as rockfall, dry grainflow or snow avalanches may be present beside debris-flow deposits. On alluvial fans and valley floors they alternate with alluvial deposits. The distinction between alluvial fans and debris fans is based on the relative influence of debris-flow and streamflow processes on the formation and morphology of the fans: on alluvial fans, torrent deposits dominate, whereas on the steeper debris fans debris-flow deposits dominate (Rapp and Nyberg 1981).

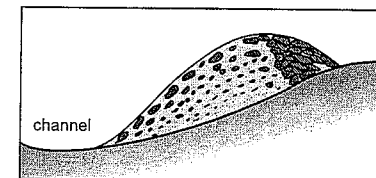


Figure 2.5 Cross-section of a debris-flow levee along a debris flow channel, showing the typical inverse grading of the deposits and the orientation of clasts (b-axis) within the deposits (after Nieuwenhuijzen and Van Steijn 1990).

A phenomenon which is sometimes mistaken for a debris-flow levee is the so-called boulder berm. Although boulder berms are morphologically similar to debris flows, and also show inverse grading, they do not contain fine-grained matrix material (Carling 1987, Costa 1984). Boulder berms are thought to be deposited as bedload by debris torrents (Carling 1987, Miles and Kellerhals 1981). Clasts within debris-flow deposits can show strong orientation. Owen (1991) found that clast a-b planes tend to be oriented more or less parallel to shear planes. Innes (1983a) and Van Steijn (1988) used a-axis data. For the outside of levees, they observed orientation of the stones in directions between the general slope direction and the local levee surface slope direction. Nieuwenhuijzen and Van Steijn (1990) and Van Steijn (1988) reported that a-axes of stones tend to be oriented parallel to the flow direction on the inner side of levees. The orientation of clasts in the frontal lobes usually shows much weaker orientation (Van Steijn 1988, Van Steijn and Coutard 1989).

Debris-flow material usually shows a wide range of grain sizes from clay-sized material to cobbles and boulders. Sometimes boulders as large as several metres can be transported by debris flows. Usually a small, but significant amount of clay-sized material is present. Several workers have mentioned clay contents of only a few percent. Van Steijn (1989) reports a bi-modal grain-size distribution with peaks in the fine fraction (< 1 mm) and in the coarse gravel fraction. The material of the debris-flow deposits often closely resembles the material in the trigger zones. Organic material can also be incorporated in the debris-flow material. The most common types of material favourable for debris-flow triggering reported in literature are:

- in-situ regolith (Johnson and Rodine 1984, Rapp and Strömquist 1976, Tricart 1957)
- glacial sediments (Addison 1987, Bovis and Dagg 1987, 1988)
- fluvial sediments (Bovis and Dagg 1987, 1988, Pierson 1980)
- volcanic sediments (Arguden and Rodolfo 1990, Okunishi et al. 1988)

Table 2.3 summarizes some values of physical properties of debris flows mentioned by debris-flow researchers. The wide grain-size distribution is essential for the high densities and the high concentrations of solids reported for debris-flow material. From a computer model for packing of multi-sized spheres, Rodine and Johnson (1976) concluded, that a mixture of three different sizes of spheres can have a solids concentration as high as 0.98. In a moving fluid, interlocking of particles will occur above a certain concentration. According to Rodine and Johnson (1976), this causes an increase in both the apparent angle of internal friction and the apparent cohesion of the fluid. Johnson and Rodine (1984) give an example of a pebbly-silty material, where a 1.5% increase in water content from 14% to 16.5% resulted in a strength decrease by nearly an order of magnitude. For the mixture of three sizes of spheres (Rodine and Johnson 1976), interlocking might be negligible up to a solids concentration of 0.89, and the strength of the flowing material will essentially be determined by the interstitial fluid. For realistic debris flows, they state that the solids concentration might be as high as 0.95 without significant interlocking.

The solids concentration also influences the viscosity of the debris-flow material. Einstein (1956) gives the following relation between solids concentration and Newtonian viscosity for a suspension at low solids concentrations:

$$\eta_N = \eta_{if}(1 + Bc_s) \quad 2.1$$

where:  $\eta_N$  = Newtonian viscosity;  $\eta_{if}$  = viscosity of interstitial fluid;  $c_s$  = volumetric solids content of debris. According to Chen (1988a),  $B$  represents an *intrinsic viscosity* of the fluid and  $B=2.5$  for mono-sized rigid spheres. Many other formulas relating viscosity to solids concentration have been developed, for example Mooney (1951), Roscoe (1952), Rutgers (1962) and Thomas (1965). The following equation is based on Krieger and Dougherty (1959); it shows good agreement with viscometric data (Chen 1986) at high concentrations:

Table 2.3 Physical properties of debris flows (partly based on Hovius 1990).

Property	Notation	Minimum	Maximum	Unit
Average grain size	$\phi$	-1.8	1.5	$\phi$
Trask grain-size sorting coefficient	$So_T$	2.6	25	-
Debris-flow material density (bulk)	$\rho_b$	1.4	2.6	$Mg \cdot m^{-3}$
Debris-flow material density (matrix)	$\rho_m$	1.5	2.0	$Mg \cdot m^{-3}$
Volumetric solids content (bulk)	$c_s$	0.25	0.86	-
Volumetric solids content (matrix)	$c_r$	0.40	0.60	-
Volumetric clay content	$c_c$	0.005	0.20	-
Strength	$\tau_r$	$0.3^a$	$5.0 \cdot 10^4$	Pa
Newtonian viscosity	$\eta_N$	$10^b$	$8.0 \cdot 10^3$	Pa·s
Bingham viscosity	$\eta_b$	$0.01^c$	700	Pa·s
Average flow velocity	$u_m$	0.1	$30^d$	$m \cdot s^{-1}$
Length	$l$	0.2	$1.2 \cdot 10^5$ to $6.0 \cdot 10^7$	m
Volume	$V$	$1 \cdot 10^{-3}$	$1 \cdot 10^{12}$	$m^3$

<sup>a</sup> Li and Luo (1981)

<sup>b</sup> Morton and Campbell (1974)

<sup>c</sup> Zhang et al. (1985)

<sup>d</sup> Zeng et al. (1992)

<sup>e</sup> Martinez et al. (1995)

<sup>f</sup> subaqueous debris flows described by Masson et al. (1992)

$$\eta_N = \eta_{if} \left( 1 - \frac{c_s}{c_c} \right)^{-Bc_s} \quad 2.2$$

where:  $c_s$  = volumetric solids content of static debris. Relations such as equation 2.2 can account for the very large apparent viscosities mentioned in table 2.3, as reported by Curry (1966), Pierson (1980) and Sharp and Nobles (1953). Costa (1984) observed a sharp transition from Newtonian to non-Newtonian flow behaviour at  $\rho_b = 1.5-1.8 \cdot 10^3 \text{ kg} \cdot m^{-3}$ , which he attributes to a critical sediment concentration. Figure 2.6 shows the relation between viscosity and water content found by Bentley (1979).

A third effect of the wide grain-size distribution is the very slow dissipation of excess pore pressures from the debris. In a mixture of solid particles and fluid, a part of the weight of the solid particles is carried by the fluid through buoyancy. The fluid pressure increases with the fraction of the load supported by the interstitial fluid, creating an excess pore pressure in addition to the hydrostatic pore pressure. The excess pore pressures dissipate as the solids settle out. In a mixture containing a wide variety of grain sizes, the pores between larger grains are occupied by smaller grains and interstitial fluid. This occurs at a variety of scales, and only the pores between the smallest grains are occupied by interstitial fluid only. Thus the connections between these pores (pore necks) are very small. Moreover, the interstitial fluid often contains some clay, making it more viscous. The net effect is a very slow flow of the interstitial fluid through the pores, and thus a slow dissipation of the excess pore pressure. The experiments conducted by Pierson (1981) showed that excess pore pressures could persist for several hours in a static mixture of debris and water. The mixture was composed of 4% clay, 5% silt, 19% sand and 72% gravel with a volumetric concentration of solids of 0.66. According to Pierson (1981), the interstitial fluid consisted of water and suspended clay and silt.

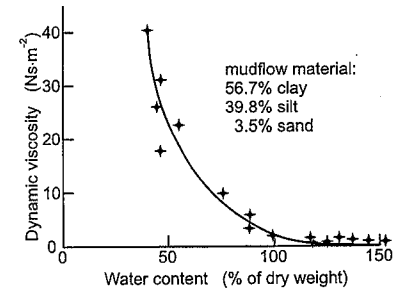


Figure 2.6 Relation between water content and viscosity (source: Selby 1993).

### 2.1.3 Debris-flow risk prevention

In order to avoid damage to structures and loss of lives by debris flows, a wide variety of countermeasures can be taken. These measures can be classified from *soft* to *hard*. Soft countermeasures include all measures which attempt to reduce damage by avoiding endangered areas or by evacuating endangered areas either definitively or temporarily. Hard measures attempt to control directly the triggering, the flow path or the sedimentation of debris flows. Differentiation must be made between debris-flow hazard and debris-flow risk (Hansen 1984, Selby 1993, Varnes 1984). Debris-flow hazard concerns the probability, frequency, magnitude and areal extent of debris-flow occurrence, whereas debris-flow risk concerns the potential damage by debris flows to people and structures (the *threat*). In uninhabited high-mountain areas, debris flows are a natural hazard, but they do not pose a serious risk to people and structures, so countermeasures will not be necessary.

Soft countermeasures rely on the recognition of areas endangered by debris flow. These can be presented as debris-flow hazard maps, where a distinction may be made between hazard areas with regard to triggering, transport and deposition. They may be based on calculations of debris-flow hazard from topographical information, climatic and meteorologic data and a set of equations describing debris-flow triggering (section 2.1.4), flow (section 2.1.5) and deposition (e.g. Takahashi 1981a, 1981b). With this approach, debris-flow deposition patterns at the mouth of a tributary valley were calculated by Ikeya (1981), Takahashi (1981b) and Takahashi et al. (1981). Hazard maps can also be derived from qualitative data: topographical, geological and geomorphological maps, aerial photos and field investigations (Bovis 1993, Chida and Hariyono 1995, Gispert 1993, Jackson et al. 1987, Suzuki and Furuya 1992). Supplemental data may come from (magnitude-)frequency analysis of debris-flow deposits (Van Steijn 1996). An analysis of the material in debris-flow trigger zones may also contribute to the evaluation of debris-flow hazards. This may be done for instance by determining material composition, structure, sensitivity, brittleness or mobility (see section 2.1.5, eqs. 2.27-2.29). On the basis of such hazard maps, actions can be taken, such as the permanent evacuation of hazardous zones or other measures to ensure the safety of people and structures. Hung et al. (1984) followed a different approach by trying to estimate the largest probable debris flow originating from steep channel systems in the Canadian Rockies and found that debris volume correlated best with channel length.

Short-term soft countermeasures can be taken if the debris-flow hazard areas are known. Some of these measures are based on the recognition of critical values of debris-flow triggers and on the ability to forecast the occurrence of such critical situations. The critical situations may be rainfall (Brand 1993, Caine 1980, Innes 1983a, Kobashi and Suzuki 1987, Okuda et al. 1981, Okunishi and Suwa 1985, Sengo 1980), rainfall type (Rapp and Nyberg 1981, 1988), snowmelt, discharge (Kobashi and Suzuki 1987), earthquakes or volcanic activity. Based on the expected exceedance of the critical value, warnings may be issued and evacuation of endangered areas may be ordered (Brand 1993). More direct warning systems may also be used. Video cameras and trip wires (Chida and Hariyono 1995, Costa 1984, Okuda et al. 1980) have been used to detect debris flows. However, such systems are expensive and usually leave little time between the detection of the debris flow and its arrival in the area to be evacuated. Therefore, they are only used when debris flows pose a serious threat in densely populated areas. Together with the warning systems, efficient evacuation procedures must be established to ensure the avoidance or mitigation of a disaster.

Hard countermeasures can also be taken (Marui et al. 1997). Bare trigger zones may be reforested to diminish erosion. Water may be drained from landslides to demobilize them and thereby prevent them from transforming into debris flows. When debris flows do occur, they may be diverted to areas where they cause less damage, or they may be captured in sedimentation basins. One way to stop debris flows is to increase their strength and viscosity by draining the interstitial fluid from the debris flow. This may be achieved by installing gratings in the flow path of the debris flow, although drainage can be

difficult (Pierson 1981). The opposite may also work: by adding water to the debris flow, its viscosity and mobility are greatly increased. The debris flow may then continue its way as a hyperconcentrated flow or as a normal streamflow, from which the coarsest particles may settle. Intermediate between hard and soft measures are control measures such as modified land use and careful planning and execution of human activities. Generally a combination of the different types of measures gives the best results with regard to the avoidance or mitigation of debris-flow hazards.

### 2.1.4 Debris-flow triggering

Prerequisites for the occurrence of debris flows are steep slopes, available debris, high pore pressures and a loss of consistency of the material after initial movement. When these conditions are met, debris flows can be triggered in many different ways. Landslides can transform into debris flows by dilatancy or liquefaction during movement, as described by Arboleda and Punongbayan (1991), Campbell (1974, 1975), Fleming et al. (1989), Johnson (1970), Johnson and Rahn (1970), Johnson and Rodine (1984) and Reid et al. (1991). Takahashi (1978, 1980, 1981a, 1981b) and Takahashi et al. (1981, 1992) describe the spontaneous triggering of a debris flow by dilatancy when a water film of a certain thickness appears at the surface of a saturated body of debris in a channel. Dilatancy is the increase of bulk volume which causes the incorporation of additional water. Liquefaction is the loss of strength caused by a (sudden) increase of pore pressure. Other possible mechanisms include spontaneous liquefaction, damming of water behind debris dams with subsequent breaching (Costa 1984, Mora et al. 1993, Pierson 1992), undrained loading (Marui et al. 1997, Sassa et al. 1997) or the *firehose effect* caused by the impact of a high-speed stream of water (Johnson and Rodine 1984).

External forces can trigger the movement: vibrations caused by earthquakes (Martinez et al. 1995), passing debris flows or volcanic eruptions (Pierson 1992), and impact or loading forces by snow avalanches or mass movements (Bovis and Dagg 1987, Marui et al. 1995, Sassa 1985, Sassa et al. 1997, Selby 1993). Usually however an increase of pore pressures caused by a supply of water to the material provides the trigger for triggering of movement. Water can be supplied by rainfall, snowmelt (Owen 1991) or a combination of both (Azimi and Desvarreux 1974). Less frequent water supplies include drainage of (crater) lakes (Pierson 1992), rapid snow and ice melt during volcanic eruptions, glacial outburst floods and stream diversions. Although less frequent, such water supply mechanisms cause the most catastrophic debris flows.

Long-duration rainfall of moderate intensity will cause a rise of both the groundwater level and the water content in the soil, resulting in an increase in pore pressures. If the soil becomes saturated, this causes the occurrence of saturation overland flow. Both effects are favourable for the triggering of debris flows (Campbell 1974, Kobashi and Suzuki 1987, Luckman 1992, Pierson 1980, Wohl and Pearthree 1991, Zimmermann 1990). For these situations the rainfall history, which may be expressed as an antecedent precipitation index API, is of importance. Short-duration rainfall with high intensities can also trigger debris flows (Kotarba 1989, Okuda et al. 1980, Okunishi and Suwa 1985, Okunishi et al. 1988, Zimmermann 1990). In the southern French Alps, debris flows are mostly triggered by short-duration rainstorms with high rainfall intensities. Hovius (1990) and Van Asch and Van Steijn (1991) mention eye-witness observations of 50-100 mm/hr rainfall during 5-10 minutes causing debris-flow triggering. In this area long-duration low-intensity rainfall and snowmelt hardly produce debris flows.

Clearly, a minimum amount of water is necessary to trigger a debris flow. For rainfall-triggered debris flows, a logical first step will be the determination of the characteristics of the triggering rainstorm. The most simple approach is to give the total amount of rainfall or the mean rainfall intensity (Bovis and Dagg 1988, Cenderelli and Kite 1998, Johnson and Rodine 1984, Luckman 1992, Ogura and Filho 1991, Pierson 1980, Zimmermann 1990). The peak intensity of rainfall related to the triggering of the

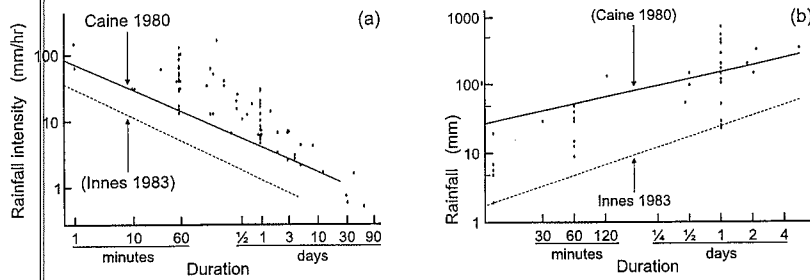


Figure 2.7 Threshold curves for debris flows and landslides from Caine (1980) and Innes (1983a). Data: (a) Caine (1980); (b) Innes (1983a).

debris flow and the corresponding peak rainfall duration are more difficult to obtain, as most rainfall gauging stations do not measure rainfall intensities on very short (< 1 hr) time scales, and often no gauging station is located close to the debris flow trigger zone. Still, many workers have reported short-duration peak rainfall intensities from continuous raingauges related to debris-flow triggering or severe erosion (Blijenberg 1993b, Campbell 1974, Carling 1986, Chida and Hariyono 1995, Coe et al. 1997, De Graaf et al. 1993, Kotarba 1992, Okuda et al. 1980, Olyphant et al. 1991, Zimmermann 1990).

The next step is to deduce the critical combination of amount of rainfall, rainfall intensity and rainfall duration. From a literature survey, Caine (1980) has found a threshold curve for the occurrence of debris flows and shallow landslides. This critical rainfall intensity is a function of rainfall duration:

$$i_{r,cr} = 14.82 t_r^{-0.39} \quad 2.3$$

where  $i_{r,cr}$  = critical rainfall intensity (mm/hr);  $t_r$  = rainfall duration (hr). Debris flows are unlikely if the critical rainfall intensity exceeds the actual rainfall intensity. This threshold can also be expressed in terms of total amount of rainfall and rainfall duration:

$$I_{r,cr} = 14.82 t_r^{0.61} \quad 2.4$$

where  $I_{r,cr}$  = critical rainfall amount (mm). Again, debris flows are unlikely if the critical rainfall amount exceeds the actual rainfall amount. Innes (1983a) also gives a threshold curve for the occurrence of debris flows, which differs considerably from Caine's (1980) curve (fig. 2.7):

$$I_{r,cr} = 4.9355 t_r^{0.5041} \quad 2.5$$

Sengo (1980) gives a discriminant function for the occurrence of debris flows for the Kami-kamihori Valley in north Japan:

$$Y = 0.692 I_{r,20} + 0.0230 I_{r,c} - 7.42 \quad 2.6$$

where  $I_{r,20}$  = total amount of rainfall in 20 minutes (mm);  $I_{r,c}$  = cumulative rainfall amount (mm).  $Y$  becomes positive if rainfall conditions are favourable for debris-flow occurrence. In this relation, both the antecedent rainfall and the instantaneous (20-minute) rainfall intensity are represented. Okuda et al. (1981) and Okunishi and Suwa (1985) propose a discriminant function based on the time series of 10-minute rainfall:

$$Y_t = \sum_j a_j i_{r,10,t-j} + const \quad 2.7$$

where  $t$  = time;  $j$  = counter;  $a_j$  = weight coefficient for rainfall at time  $t-j$ ;  $i_{r,10,t-j}$  = 10-minute rainfall intensity at time  $t-j$ . This function considers more explicitly the decreasing influence of antecedent rainfall with increasing time delay between rainfall occurrence and the moment under consideration. Kobashi and Suzuki (1987) found a critical effective rainfall of 55 mm in the Rokko mountains in Japan from:

$$I_{r,eff,t} = \sum_{j=0}^n a^{j+1} i_{r,t-j} \quad 2.8$$

where  $I_{r,eff,t}$  = effective rainfall amount at time  $t$ ;  $a$  = decrease coefficient;  $i_{r,t-j}$  = rainfall intensity at time  $t-j$  (mm). This function coincides with the general antecedent precipitation index function  $API$  if the decrease function has the form  $f(t) = e^{-\alpha t}$  ( $\alpha$  = decrease coefficient):

$$API_{t_0} = \int_0^t i_{r,t_0-\tau} f(\tau) d\tau \quad 2.9$$

where  $API$  = antecedent precipitation index.

From the 10-minute rainfall series, a 10-minute discharge series can be obtained:

$$q_{10,t} = \sum_j U_j (i_{r,10,t-j} - i_{10}) \quad 2.10$$

where:  $q_{10,t}$  = 10-minute specific discharge at time  $t$ ;  $U_j$  = instantaneous unit hydrograph;  $i_{10}$  = infiltration capacity over 10 minutes. Okunishi and Suwa (1985) and Okunishi et al. (1988) found that the values of the instantaneous unit hydrograph  $U_j$  in this equation closely resemble the values of  $a_j$  in equation 2.7. The critical discharge for debris-flow occurrence in the Kami-kamihori Valley appeared to be about 1200 m<sup>3</sup>/hr. Kobashi and Suzuki (1987) have investigated critical conditions for debris-flow triggering using a tank model composed of three tanks. Their critical values are water levels in the top and middle tanks and runoff. They give a danger index (water levels 35 mm in the top tank and 50 mm in the middle tank, 10 mm/hr runoff), and a warning index (water levels 25 in the top tank and 35 mm in the middle tank) indicating 1-2 hours left before disaster (see fig. 2.8).

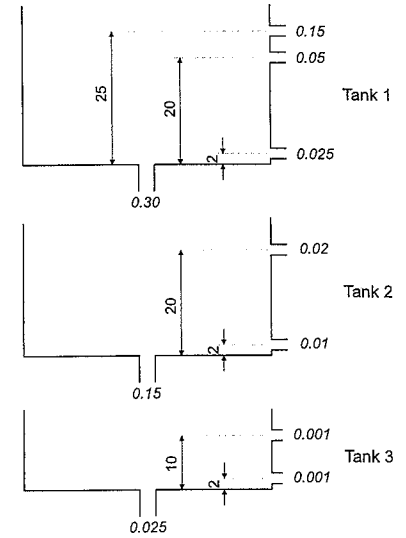


Figure 2.8 Tank model from Kobashi and Suzuki (1987). Figures shown are outflow levels (in mm) and outflow constants (in hr<sup>-1</sup>; in italics).

Besides these empirical measures for debris-flow triggering, physical models have been developed, based on force equilibrium. These models also indicate a critical (ground)water level, but they do not indicate under what rainfall conditions the critical level will be reached. For surficial landslides transforming into debris flows, Johnson (1965, 1970) and Johnson and Rodine (1984) have developed a model describing the triggering conditions. As the debris flow originates from a landslide, the limiting equilibrium conditions for triggering are essentially the same as those for the triggering of the translational landslide on an infinite slope (fig. 2.9):

$$F = \frac{\text{shear resistance } \tau_f}{\text{shear stress } \tau} = \frac{c' + (1-m)\rho_u + m(\rho_{sat} - \rho_w)g y \cos\beta \tan\phi'_s}{(1-m)\rho_u + m\rho_{sat}g y \sin\beta} \quad 2.11$$

where:  $F$  = safety factor;  $c'$  = effective cohesion;  $m$  = relative groundwater level (0 = dry; 1 = saturated);  $\rho_u$  = bulk density of unsaturated debris;  $\rho_{sat}$  = bulk density of saturated debris;  $\rho_w$  = density of water;  $g$  = gravitational acceleration (9.81 m/s<sup>2</sup>);  $y$  = distance perpendicular to slope;  $\beta$  = slope angle;  $\phi'_s$  = effective angle of static internal friction. If  $F = 1$ , the mass is at the point of failure; for  $F < 1$  failure will occur and the mass will start sliding. The subsequent



transformation to a debris flow is caused by either dilatancy or liquefaction during movement. Dry, coarse debris with little or no matrix material has a negligible cohesion. The strength of such debris is essentially determined by its internal friction angle. This makes the limiting equilibrium conditions easier to model. For cohesionless ( $c' = 0$ ), dry ( $m = 0$ ) debris, equation 2.11 simplifies to:

$$F = \frac{\tan \phi'_s}{\tan \beta} \quad 2.12$$

This shows, that dry, coarse, cohesionless debris will fail if the slope angle exceeds the effective angle of static internal friction, which may occur as a result of undercutting or accumulation of debris

According to Takahashi (1978, 1980, 1981a, 1981b) and Takahashi et al. (1981, 1992) an accumulation of debris on a gully floor may spontaneously transform into a debris flow. This happens by dilatancy as soon as a water film of a certain thickness  $h_0$  appears at the surface of a saturated body of debris. Figure 2.10 gives three different situations distinguished by Takahashi. The equilibrium model used by Takahashi is also based on an infinite slope situation. The shear stress  $\tau$  at depth  $y$  is given by:

$$\tau = (c_s(\rho_s - \rho_f)y + \rho_f(y + h_0))g \sin \beta \quad 2.13$$

and the maximum shear resistance  $\tau_f$  by:

$$\tau_f = c_s(\rho_s - \rho_f)gy \cos \beta \tan \phi'_s \quad 2.14$$

where:  $c_s$  = volumetric concentration of solids;  $\rho_s$  = solids density;  $\rho_f$  = fluid density;  $h_0$  = depth of surface water layer. Situation 1 in figure 2.10 shows the non-stationary bed situation, where shear stress increases faster with depth than shear resistance:

$$\frac{d\tau}{dy} > \frac{d\tau_f}{dy} \quad 2.15$$

In this situation the whole bed of debris will start to move. The combination of equations 2.13 and 2.14 yields the critical slope angle:

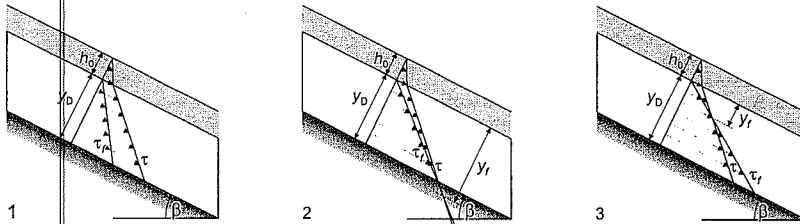


Figure 2.10 Characteristic shear-strength and shear-stress distributions in saturated debris (after Takahashi 1978, 1980).

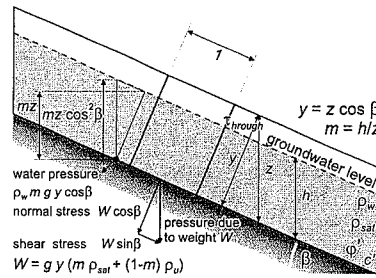


Figure 2.9 Static forces on an infinite slope.

$$\tan \beta \geq \left( \frac{c_s(\rho_s - \rho_f)}{c_s(\rho_s - \rho_f) + \rho_f} \right) \tan \phi'_s \quad 2.16$$

If  $h_0 = 0$  or the body of debris is not fully saturated, failure may still occur. However, in this situation there is not enough water available for the debris to dilate and lose consistency, so a landslide is formed rather than a debris flow.

In the second and third situations in figure 2.10 the shear resistance of the debris increases faster with depth than the shear stress:

$$\frac{d\tau}{dy} < \frac{d\tau_f}{dy} \quad 2.17$$

For this situation failure can only occur if  $h_0 > 0$ . At a certain depth  $y_f$  the shear stress and the shear resistance are equal and up to this depth failure will occur. In situation two, where  $y_f$  is deeper than the base of the debris accumulation, the limit of moving and stable material is formed by the gully floor. In the third situation, not all of the debris mass will move. This is the (quasi)-stationary bed situation. Takahashi gives an additional boundary condition for this case:

$$y_f \geq d_{ch} \quad 2.18$$

where:  $d_{ch}$  = characteristic grain diameter. If  $y_f < d_{ch}$ , no debris flow can take place, only transport by streamflow. The following equation gives the condition under which a debris flow may occur:

$$\frac{c_s(\rho_s - \rho_f)}{c_s(\rho_s - \rho_f) + \rho_f \left( 1 + \frac{h_0}{d_{ch}} \right)} \tan \phi'_s \leq \tan \beta < \frac{c_s(\rho_s - \rho_f)}{c_s(\rho_s - \rho_f) + \rho_f} \tan \phi'_s \quad 2.19$$

One more boundary condition is introduced by Takahashi to exclude situations in which there is too much water for the debris to be uniformly dispersed throughout the depth of flow:

$$y_f \geq \kappa h_0 \quad 2.20$$

Usually  $\kappa \approx 1$ . Combination of equations 2.19 and 2.20 gives the critical slope angle for the occurrence of debris flows:

$$\tan \beta = \frac{c_s(\rho_s - \rho_f)}{c_s(\rho_s - \rho_f) + \rho_f \left( 1 + \frac{1}{\kappa} \right)} \tan \phi'_s \quad 2.21$$

This equation can also be presented in a form similar to equation 2.11. For fully saturated, cohesionless materials (Blijenberg 1995):

$$F = \frac{c_s(\rho_s - \rho_f)}{c_s(\rho_s - \rho_f) + \rho_f \left( 1 + \frac{1}{\kappa} \right)} \frac{\tan \phi'_s}{\tan \beta} \quad 2.22$$

For realistic values ( $c_s = 0.7$ ;  $\rho_s = 2600 \text{ kg}\cdot\text{m}^{-3}$ ;  $\rho_f = 1000 \text{ kg}\cdot\text{m}^{-3}$ ;  $\kappa = 0.75$ ;  $\tan \phi'_s = 0.8$ ) debris flows may occur on slopes between  $14.5^\circ$  and  $22.9^\circ$ . On steeper slopes, landslides occur rather than debris flows.

Bovis and Dagg (1988) have emphasized the importance of the hydraulic conductivity of the debris bed. The conductivity is not a constant, but changes in time as a result of selective removal of finer material by streamflow. As mean pore size increases, the conductivity will increase as well. Equation 2.23 is the empirical relationship given by Bovis and Dagg (1988) to calculate the hydraulic conductivity:

$$K_s = \frac{u_m \theta_s}{\left(\frac{dH}{ds}\right)^b} \quad 2.23$$

where:  $K_s$  = saturated hydraulic conductivity;  $u_m$  = mean flow velocity;  $\theta_s$  = volumetric water content at saturation;  $H$  = total hydraulic head;  $s$  = distance in flow direction;  $b$  = coefficient (1.0 for laminar flow; 2.0 for turbulent flow). The increase of conductivity causes an increase of the stability of the debris mass as the discharge needed to reach a critical groundwater level in the mass is increased. The increase in hydraulic conductivity can be many orders of magnitude. Bovis and Dagg (1988) give an example in which conductivity may have increased by a factor  $10^3$ . Besides the large increase of conductivity, the angle of internal friction may increase slightly as fine material is washed out. According to Bovis and Dagg (1988) the increase may be about  $2^\circ$  from  $37^\circ$  for hillslope colluvium to  $39^\circ$  for coarse channel deposits.

Debris-flow research by the Department of Physical Geography of Utrecht University in the 1980's has shown that none of the above-mentioned triggering mechanisms was realistic enough for the study area. On gully floors coarse, cohesionless debris was present, whereas on the side slopes much fine-grained material was present. A hypothesis was formulated by Postma (1988) and Hovius (1990) that during high-intensity rainstorms overland flow occurs which entrains much of the fine material present on the side slopes. This muddy runoff fluid has both a higher density and a higher viscosity than pure water. When it encounters an accumulation of coarse debris on the gully floor, it enters into the pores and destabilizes this coarse debris. The mixed material then continues to move as a debris flow. Figure 1.2 presents the flow chart of this hypothesis. The hypothesis differs from Takahashi's (1978, 1980, 1981a, 1981b) model on several points:

- Takahashi assumes the presence of all grain-size fractions in the gully, whereas in this hypothesis a separation exists between coarse debris on the gully floors and the relatively fine-grained material on the side-slopes.
- Instead of water, the fluid entering the pores of the coarse debris is a mixture of water and fine debris with higher density and higher viscosity than water.
- Fluid is not only supplied from upstream through the gully, as assumed by Takahashi, but also from the side slopes of the gully.

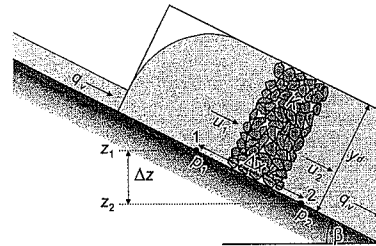


Figure 2.11 Flow through a saturated debris bed (after Postma 1988).

Postma (1988) has given a mathematical formulation of the hypothesis. She assumed that instability of the debris mass will occur as soon as it is fully saturated with the muddy fluid (see fig. 2.11), i.e. when the discharge of fluid into the coarse debris equals the maximum discharge that can flow through the debris. For laminar flow conditions Bernoulli's law can be used to calculate the discharge  $q_f$  through the coarse debris between points 1 and 2 from:

$$\frac{\Delta\sigma_f}{\rho_f g} + \frac{\Delta(u^2)}{2g} + \Delta z = \frac{\sigma_{f2} - \sigma_{f1}}{\rho_f g} + \frac{u_2^2 - u_1^2}{2g} + z_2 - z_1 = R q_f \quad 2.24$$

where:  $\sigma_f$  = pore pressure of fluid;  $u$  = flow velocity;  $z$  = vertical height;  $\rho_f$  = fluid density;  $R$  = viscous resistance. The viscous resistance can be obtained from:

$$R = \frac{\Delta s}{y_d K_f} \quad 2.25$$

where  $s$  = distance in flow direction;  $y_d$  = depth of flow perpendicular to slope;  $K_f$  = hydraulic conductivity of coarse debris with respect to muddy runoff fluid. As can be derived from figure 2.11, fluid stress as well as flow velocity are equal in points 1 and 2, resulting in the well-known Darcy flow equation:

$$q_f = y_d K_f \sin \beta \quad 2.26$$

From equation 2.26 it follows that the critical supply of muddy fluid depends on slope angle, debris depth and debris hydraulic conductivity. It is difficult to determine the hydraulic conductivity  $K$  of coarse debris for a muddy fluid, and even more difficult for fluids consisting of a mixture of water and fine-grained material (see chapter 5).

### 2.1.5 Debris-flow movement

Once a debris flow has started, a continuation of the movement is only possible if the moving mass is able to retain its water, or even take up more water. A loss of consistency and strength after initial failure will also favour the continued movement of the debris flow. The relative loss of strength can be expressed by the strength ratio or sensitivity index  $S_r$ , which is normally used for clays (Skempton and Northey 1952):

$$S_r = \frac{\text{undisturbed, undrained strength}}{\text{remoulded, undrained strength}} = \frac{\tau_f}{\tau_r} \quad 2.27$$

or by the brittleness index  $I_b$  (Bishop 1973, Statham 1977):

$$I_b = \frac{\tau_f - \tau_r}{\tau_r} \cdot 100\% \quad 2.28$$

Buchanan and De Savigny (1990) give strength ratios of 1.62-3.05 for debris flows in the Smith Creek basin (Washington, USA). The strength decrease after initial failure is caused partly by the decrease of the friction angle of the material from its static value  $\phi_s'$  to its residual or kinetic value  $\phi_k'$  and partly by the decrease of cohesion.

Another measure that can be used to evaluate the possibility that a debris flow may continue its movement is the mobility index  $M$  (Johnson and Rodine 1984):

$$M = \frac{\theta_s}{\theta_m} \quad 2.29$$

where:  $\theta_m$  = volumetric water content at failure. For  $M \geq 1$ , the saturated water content is sufficient to assure continued debris-flow movement without additional water (Fleming et al. 1989). Mobility can also be described by the effective coefficient of friction, defined by  $\Delta z / \Delta x$  where  $\Delta z$  and  $\Delta x$  are the total vertical and horizontal distances travelled by the debris flow (Bovis 1993, Scheidegger 1973).

Debris-flow movement has been described using different rheological models. Some of these models are the Newtonian viscous fluid model (linear viscous model), the Bingham and Coulomb viscoplastic models and the dilatant-fluid model. The simplest model for debris-flow movement is the Newtonian fluid model or the linear viscous model. From figure 2.12 it can be seen that a Newtonian fluid is governed by:

$$\tau = \eta_N \left| \frac{du}{dy} \right| \quad 2.30$$

From figure 2.13, the shear stress can be derived, so that for steady, fully developed, laminar flow on an infinitely wide and long slope:

$$\rho_b g y \sin \beta = -\eta_B \frac{du}{dy} \quad 2.31$$

where:  $\rho_b$  = bulk density of debris. Integrating with  $u=0$  at  $y=y_d$  gives the velocity profile for a Newtonian fluid:

$$u = \frac{\rho_b g \sin \beta}{2\eta} (y_d^2 - y^2) \quad 2.32$$

In this parabolic curve, maximum velocity occurs at the surface and is given by:

$$u_{\max} = \frac{\rho_b g \sin \beta}{2\eta} y_d^2 \quad 2.33$$

The Newtonian fluid model has some severe disadvantages: it explains neither the formation of levees and lobes on relatively steep slopes ( $>10^\circ$ ) nor the observed rigid plug in the centre of some flows nor the inverse grading of the deposits. For this reason, other models have been developed, which can account better for debris-flow behaviour. Still, the simplicity of this model has led several workers to continue using this model for debris flows (Hunt 1994, Rickenmann 1990).

Johnson (1965, 1970) and Yano and Daido (1965) have used viscoplastic models to explain debris-flow movement. For a homogeneous Bingham viscoplastic, flow will occur if the shear stress exceeds the yield strength  $\tau_0$  (see fig. 2.13):

$$\tau = \tau_0 + \eta_B \left| \frac{du}{dy} \right| \quad 2.34$$

The yield stress level will be reached at a depth  $y_0$ :

$$y_0 = \frac{\tau_0}{\rho_b g \sin \beta} \quad 2.35$$

and, again deriving shear stress from figure 2.13, the velocity profile for flow of a Bingham-viscoplastic material on an infinite slope is given by:

$$u = \frac{1}{\eta_B} \left[ \frac{\rho_b g \sin \beta}{2} (y_d^2 - y^2) - \tau_0 (y_d - y) \right] \quad 2.36$$

Which describes a parabolic velocity profile between depths  $y_0$  and  $y_d$ . Above  $y_0$  the yield strength is not exceeded, and the material moves with a uniform velocity without internal deformation. The velocity  $u_{\max}$  of this rigid plug can be found by substituting  $y_0$  for  $y$  in equation 2.36:

$$u_{\max} = \frac{\rho_b g \sin \beta}{2\eta_B} (y_d - y_0)^2 \quad \text{for } 0 \leq y \leq y_0 \quad 2.37$$

Johnson (1965, 1970) also derived the velocity profile for debris flow in a semi-circular channel of radius  $r_d$  (see fig. 2.14) with a rigid plug of radius  $r_0$ :

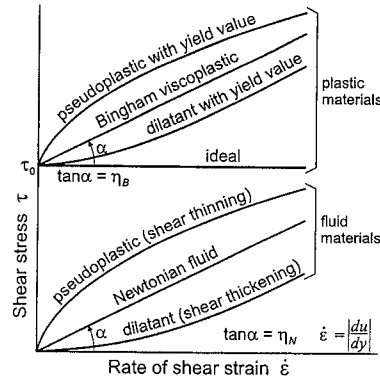


Figure 2.12 Rheological behavior of various materials.

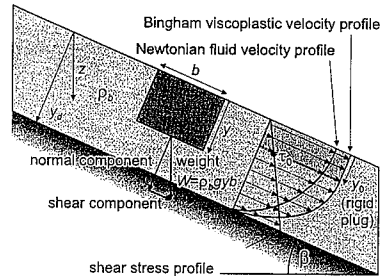


Figure 2.13 Shear stress and velocity profiles for a Newtonian and a Bingham viscoplastic debris flow on an infinitely wide slope (after Johnson 1970 and Johnson and Rodine 1984).

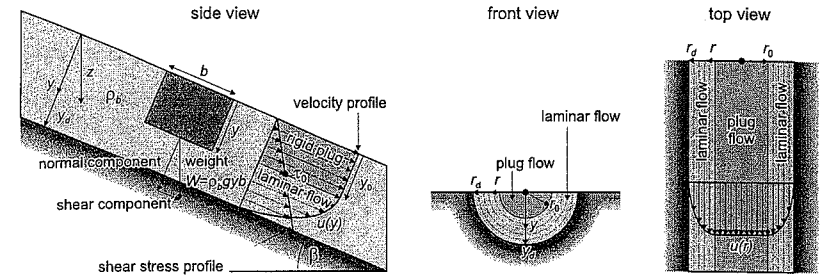


Figure 2.14 Shear stress and velocity profiles for a Bingham viscoplastic debris flow in a semi-circular channel (after Johnson 1970 and Johnson and Rodine 1984).

$$u = \frac{1}{\eta_B} \left[ \frac{\rho_b g \sin \beta}{4} (r_d^2 - r^2) - \tau_0 (r_d - r) \right] \quad \text{for } r_0 \leq r \leq r_d \quad 2.38$$

where:  $r$  = radial distance perpendicular to flow direction. Again the velocity of the rigid plug can be obtained by substituting  $r_0$  for  $r$  in equation 2.38. The rigid plug in the centre of flow has a radius:

$$r_0 = \frac{2\tau_0}{\rho_b g \sin \beta} \quad 2.39$$

For homogeneous Coulomb-viscoplastic materials, Johnson and Rodine (1984) have developed models similar to those for Bingham viscoplastic materials. The main difference is the dependence of the yield strength on normal stress:

$$\tau = \tau_0 + \eta_C \left| \frac{du}{dy} \right| = c' + \sigma' \tan \phi' + \eta_C \left| \frac{du}{dy} \right| \quad 2.40$$

where  $\eta_C$  = Coulomb viscosity;  $c'$  = effective cohesion;  $\phi'$  = effective angle of internal friction, with  $\phi' = \phi_s$  for  $\tau \leq \tau_0$  and  $\phi' = \phi_k$  for  $\tau > \tau_0$ ;  $\phi_s$  = effective angle of static internal friction;  $\phi_k$  = effective angle of kinetic internal friction. The yield stress level will be reached at a depth  $y_0$ :

$$y_0 = \frac{c'}{\rho_b g \sin \beta} + \frac{\tan \phi'_s}{\tan \beta} \quad 2.41$$

Integration of equation 2.40 results in the following velocity profile for flow of a Coulomb-viscoplastic material on an infinite slope:

$$u = \frac{1}{\eta_C} \left[ \frac{\rho_b g \cos \beta}{2} (\tan \beta - \tan \phi'_k) (y_d^2 - y^2) - c' (y_d - y) \right] \quad \text{for } y_0 \leq y \leq y_d \quad 2.42$$

Again, between depths  $y_0$  and  $y_d$  the curve is parabolic, and above  $y_0$  a rigid plug exists with a uniform velocity  $u_{\max}$ :

$$u_{\max} = \frac{1}{\eta_C} \left[ \frac{\rho_b g \cos \beta}{2} (\tan \beta - \tan \phi'_k) (y_d^2 - y_0^2) - c' (y_d - y_0) \right] \quad \text{for } 0 \leq y \leq y_0 \quad 2.43$$

The debris-flow movement models based on Bingham viscoplastic or Coulomb viscoplastic behaviour can explain some specific features of debris flows. The models give a good explanation for the

apparent high viscosities. Buoyancy, together with the yield strength caused by cohesion, can explain the ability of debris flows to carry large particles. Strength also explains the existence of a rigid plug in the centre of the flow, a phenomenon which has been observed in natural and experimental flows. Also, the formation of levees and lobes on relatively steep slopes can be explained in terms of strength of the material: once the flow thins out to a critical minimum thickness  $y_0$ , the flow will stop. This characteristic is used to calculate the strength  $\tau_0$  of the debris-flow material from field deposits. For Bingham viscoplastic behaviour, the strength can be obtained from equation 2.35 for flow on an infinite slope and from equation 2.39 for flow in a semicircular channel.

The average flow velocity of a debris flow can also be estimated from the deposits in channel bends (Johnson and Rodine 1984). In bends, the outer levees are generally higher than the inner levees as a result of the tilt of the flow surface in a bend (fig. 2.15). The tilt is caused by the radial acceleration  $a_r$ :

$$\tan \delta_b = \frac{a_r}{g \cos \beta} = \frac{u_m^2}{r_b g \cos \beta} \quad 2.44$$

where:  $\delta_b$  = flow surface tilt angle in channel bend;  $u_m$  = average flow velocity;  $r_b$  = radius of channel bend;  $\beta$  = slope angle. The average flow velocity can be obtained easily from equation 2.44:

$$u_m = \sqrt{g r_b \cos \beta \tan \delta_b} \quad 2.45$$

A shortcoming of the Newtonian viscous and the Bingham and Coulomb viscoplastic rheological models is the absence of grain-grain interactions in these models. Takahashi (1978, 1980, 1981a) has formulated a debris-flow movement model based on the concept of dispersive pressure (or Weissenberg effect) caused by grain collisions at high concentrations, which was introduced by Bagnold (1954, 1956). Both the magnitude and frequency of momentum exchange by grain collisions vary in direct proportion to the shear rate in the material, so the stress is proportional to the square of the shear rate and acts normal to the shear planes. The magnitude of the resulting stresses has been analysed by Bagnold (1954):

$$\sigma_d = a_B \rho_s (\lambda d)^2 \left( -\frac{du}{dy} \right)^2 \cos \phi'_k \quad 2.46$$

and

$$\tau = \sigma_d \tan \phi'_k = a_B \rho_s (\lambda d)^2 \left( -\frac{du}{dy} \right)^2 \sin \phi'_k \quad 2.47$$

where:  $\sigma_d$  = dispersive stress for grains of size  $d$ ;  $a_B$  = constant ( $= 0.042$ );  $\lambda$  = linear concentration of grains;  $d$  = grain size. The linear grain concentration  $\lambda$  is related to volumetric grain concentration by:

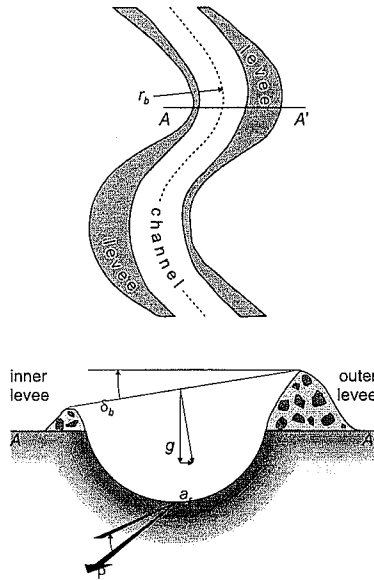


Figure 2.15 Tilt of debris flow surface in a channel bend (after Johnson and Rodine 1984).

$$\lambda = \left( \sqrt[3]{\frac{c_s}{c_s} - 1} \right)^{-1} \quad 2.48$$

Takahashi assumes that the grains are uniformly dispersed throughout the depth of flow  $y_d$  and he neglects the shear due to distortion of the intergranular fluid, so that normal and shear stresses may be derived from figure 2.15. For flow in an open channel in the fully inertial range, this results in:

$$\sigma_d = a_i \rho_s (\lambda d)^2 \left( -\frac{du}{dy} \right)^2 \cos \phi'_k = c_s (\rho_s - \rho_f) g y \cos \beta \quad 2.49$$

and

$$\tau = a_i \rho_s (\lambda d)^2 \left( -\frac{du}{dy} \right)^2 \sin \phi'_k = (c_s (\rho_s - \rho_f) + \rho_f) g y \sin \beta \quad 2.50$$

Integration of equation 2.50 with  $u = 0$  at  $y = y_d$  gives the velocity profile:

$$u = \left[ \frac{4 g \sin \beta}{9 a_i d^2 \sin \phi'_k} \left( c_s + (1 - c_s) \frac{\rho_f}{\rho_s} \right) \right]^{\frac{1}{2}} \left[ \left( \frac{c_s}{c_s} \right)^{\frac{1}{3}} - 1 \right] \left( y_d^{\frac{3}{2}} - y^{\frac{3}{2}} \right) \quad 2.51$$

According to Takahashi, uniform and steady debris flow can only occur if:

$$\tan \phi'_k \leq \left( \frac{c_s (\rho_s - \rho_f) + \rho_f}{c_s (\rho_s - \rho_f)} \right) \tan \beta \leq \tan \phi'_s \quad 2.52$$

Takahashi's debris-flow model can explain the observed accumulation of the larger particles at the surface (inverse grading) and at the snout of the debris flow. The accumulation of larger particles at the surface is caused by the concave velocity profile: large particles at the bottom will have a higher mean velocity than smaller particles because they project further into the flow. Also, the dispersive stress is highest on the largest particles and near the bottom of the flow, where the sharpest velocity gradient occurs. As a result, they will tend to 'climb' over the smaller particles towards the region of lower shear gradient near the surface. Once the larger particles are located at the surface, they will be transported to the front, because at the surface the velocity is maximal. Once arrived at the front, the larger particles will be re-entrained by the flow or pushed aside, where they can form the levees. The model also accounts for the observed jostling and jumping of particles at the flow surface.

More recently, Chen (1986, 1988a, 1988b) has extended Takahashi's model to account for Coulomb yield strength, non-uniform grain sizes and non-uniform grain dispersal. His generalized viscoplastic fluid (GVF) model can give various velocity profiles (see fig. 2.16), and shows good agreement with experimental data from Takahashi (1980) and Tsubaku et al. (1982). Iverson and Denlinger (1987) have reviewed some of the modern concepts regarding debris-flow movement. New concepts have come from studies on dry granular flows (Drake and Shreve 1986, Savage 1984) and often use the concepts of statistical thermodynamics (Lun et al. 1984). Others have studied solid-fluid interactions (Davis et al. 1986, Iverson and Lahusen 1986). Iverson and Denlinger (1987) report two other mechanisms which can cause inverse grading: kinetic sieving of particles which have velocity fluctuations in the presence of a gravity field and differences in angular momentum between diffe-

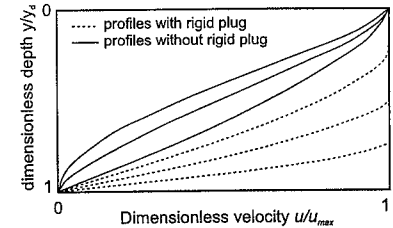


Figure 2.16 Some debris-flow velocity profiles by Chen (1988a, 1988b).

rent-sized particles in a grain-size mixture under shear. According to Innes (1983a), the clay content of a debris flow largely determines which model is most appropriate to describe debris-flow behaviour. At higher clay contents, the Bingham-viscoplastic and Coulomb-viscoplastic models apply, whereas at lower clay contents Newtonian fluid models, with or without grain interactions, are more appropriate.

It is well-known that debris flows can transport large boulders (Innes 1983a, Takahashi 1981a). The models described in this section all have one or more mechanisms for the suspension of solids and for the transport of boulders. These mechanisms are:

- cohesion (provided mainly by the clay-water slurry)
- internal friction
- buoyancy (caused by the displacement of the fluid)
- structural support (by static grain-to-grain contacts)

and if the debris flow is in motion, two more factors can be involved:

- dispersive pressure (by grain collisions)
- turbulence

Average flow velocities for debris flow can be derived from the physical models presented by averaging the velocity over the depth of flow (eqs. 2.32, 2.36+2.37, 2.42+2.43 and 2.51). For Johnson's (1965, 1970) model of debris flow in a semicircular channel, the velocity must be averaged over the flow cross sectional area. Empirical hydraulic formulas have also been used to calculate average debris-flow velocity. Some Russian hydrologists (Shamova and Sribniy, both in Gofdin and Lyubashevskiy 1966, Kherkheulidze 1967) have used Chezy-type formulas of the form:

$$u_m = a_1 y_m^{a_2} (\tan \beta)^{a_3} \quad 2.53$$

where:  $y_m$  = average flow depth perpendicular to slope. Others have also presented formulas for the velocity of the debris-flow front (Li Jian et al. 1983, Syanozhetsky et al. 1973). Tsubaku et al. 1982 give the following formula:

$$u_f = 2.5 (g y_m \sin \beta)^{0.5} \quad 2.54$$

where:  $u_f$  = velocity of debris-flow front.

## 2.2 Hydrologic control of debris-flow triggering

### 2.2.1 Infiltration

As mentioned in section 2.1.4, debris flows in the southern French Alps are usually triggered by short-duration rainstorms with high rainfall intensities (Blijenberg 1993b, De Graaf et al. 1993, Hovius 1990, Van Asch and Van Steijn 1991, Van Steijn 1991). In this area long-duration low-intensity rainfall and snowmelt hardly produce debris flows. From these observations it may be inferred, that overland flow is generated as infiltration-excess overland flow (Hortonian overland flow) rather than saturation overland flow (Dunne overland flow) or subsurface flow. The amount of overland flow triggering debris flows can be calculated if rainfall supply and infiltration into the ground are known. Usually the water-supply rate is known and the infiltration rate can be calculated.

Flow in and into the soil or another porous medium, is governed by two basic equations. The first is the continuity equation or the mass conservation equation, which in the case of one-dimensional flow in vertical direction is:

$$\frac{\partial \theta}{\partial t} + \frac{\partial q}{\partial z} = 0 \quad 2.55$$

where:  $\theta$  = volumetric water content;  $q$  = flux density;  $t$  = time;  $z$  = depth;  $\partial$  refers to partial derivatives. The second equation is Darcy's law, describing the flow intensity or discharge as a function of both the conductivity of the porous material and the hydraulic gradient. For vertical flow:

$$q = -K \frac{\partial H}{\partial z} = -K \left( \frac{\partial h}{\partial z} + \frac{\partial z_h}{\partial z} \right) = -K \left( \frac{\partial h}{\partial z} - 1 \right) \quad 2.56$$

where:  $K$  = hydraulic conductivity;  $H$  = total hydraulic head;  $h$  = pressure head;  $z_h$  = gravity head. The combination of these equations results in the Richard equation for one-dimensional, unsteady, unsaturated vertical flow in a porous medium:

$$\frac{\partial \theta}{\partial t} = \frac{\partial}{\partial z} \left( D \frac{\partial \theta}{\partial z} + K \right) \quad 2.57$$

where:

$$D = K \frac{\partial h}{\partial \theta} \quad 2.58$$

is the diffusivity.

One of the first major attempts to model infiltration of water into a soil was made by Green and Ampt (1911). They developed an analytical solution for infiltration based on the decrease of the hydraulic gradient with time during infiltration. The resulting water-content profile is shown in figure 2.17. Their assumptions were:

- The initial water content,  $\theta_i$ , is constant throughout the non-infiltrated zone.
- Throughout the infiltrated zone the volume fraction of water,  $\theta$ , is uniform and constant with time.
- The change of  $\theta_i$  to  $\theta$ , at the wetting front takes place in a layer of negligible thickness.
- The pressure head at the wetting front,  $h_{wf}$ , is constant and independent of the depth of the wetting front,  $z_{wf}$ .

These assumptions are realistic for infiltration into coarse-textured soils with low initial water content, such as the regolith cover on slopes in debris-flow trigger zones in the study area. From the second assumption it follows that throughout the transmission zone the hydraulic conductivity of the transmission zone,  $K_t$ , is constant. Also, the flux density is uniform throughout the transmission zone. Using the latter two assumptions and the assumption that the ponded water layer at the soil surface has a negligible thickness ( $h_0 = 0$  at  $z = 0$ ), Darcy's law can be rewritten for vertical, downward flow:

$$i = q = -K_t \left( \frac{\partial h}{\partial z} - 1 \right) = -K_t \left( \frac{h_{wf}}{z_{wf}} - 1 \right) \quad 2.59$$

where:  $i$  = infiltration capacity. From figure 2.17 the total amount of infiltrated water,  $I$ , can be obtained at any time  $t$ , because continuity demands that:

$$I = \int_{z=0}^{\infty} (\theta_i - \theta) dz = (\theta_i - \theta) z_{wf} \quad 2.60$$

so the infiltration capacity can also be written as:

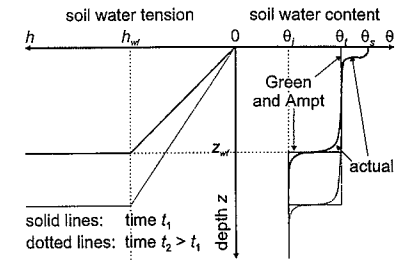


Figure 2.17 Soil moisture distribution during infiltration according to Green and Ampt (1911).

$$i = \frac{dI}{dt} = (\theta_i - \theta_i) \frac{dz_{wf}}{dt} \quad 2.61$$

Combining equations 2.59 and 2.61 gives:

$$-K_t \left(1 - \frac{h_{wf}}{z_{wf}}\right) = (\theta_i - \theta_i) \frac{dz_{wf}}{dt} \quad 2.62$$

In the initial phase of infiltration, the pressure head gradient  $h_{wf}/z_{wf}$  exceeds the gravity head gradient by far and infiltration is dominated by the pressure head gradient. Therefore the gravity head may be neglected for the early phase of infiltration:

$$-K_t \frac{h_{wf}}{z_{wf}} = (\theta_i - \theta_i) \frac{dz_{wf}}{dt} \quad 2.63$$

Integration with the boundary condition  $z_{wf} = 0$  at  $t = 0$  gives:

$$z_{wf} = \left( \frac{-2K_t h_{wf}}{\theta_i - \theta_i} \right)^{1/2} t^{1/2} \quad 2.64$$

This shows that the depth of the wetting front is proportional with the square root of time for small  $t$ . Combining with equation 2.60 results in:

$$I = [-2K_t h_{wf} (\theta_i - \theta_i)]^{1/2} t^{1/2} = S t^{1/2} \quad 2.65$$

where  $S$  is the sorptivity, which physically represents the suction of water into a soil by the matric forces of the soil. The sorptivity depends on the hydraulic conductivity of the transmission zone, on the pressure head at the wetting front, and on the difference between initial and final water content of the soil:

$$S = [-2K_t h_{wf} (\theta_i - \theta_i)]^{1/2} \quad 2.66$$

For a given, homogeneous soil,  $K_t$  and  $\theta_i$  are constants, and only  $\theta_i$  and  $h_{wf}$  (which in turn is a function of  $\theta_i$ ) vary in time. Thus for a given soil the sorptivity only depends on the initial water content.

For larger  $t$ , the contribution of the pressure head to the infiltration process diminishes and gravity can no longer be neglected. Equation 2.62 can then be written as:

$$\frac{K_t}{\theta_i - \theta_i} dt = \frac{z_{wf}}{z_{wf} - h_{wf}} dz_{wf} \quad 2.67$$

Integration with boundary condition  $z_{wf} = 0$  at  $t = 0$  results in:

$$t = \frac{\theta_i - \theta_i}{K_t} \left[ z_{wf} + h_{wf} \ln \left( 1 - \frac{z_{wf}}{h_{wf}} \right) \right] \quad 2.68$$

The logarithmic term can be substituted by a power-series expansion of the form:

$$\ln(1-x) = \sum_{i=1}^N \frac{(-x)^i}{i} \quad 2.69$$

where:  $x = z_{wf}/h_{wf}$ . Substitution in equation 2.68 and rearranging gives  $z_{wf}$  as a function of  $t$ :

$$z_{wf} = a_1 t^{1/2} + a_2 t + a_3 t^{3/2} + \dots \quad 2.70$$

where:

$$a_1 = \left( \frac{-2K_t h_{wf}}{\theta_i - \theta_i} \right)^{1/2} \quad 2.71$$

$$a_2 = \frac{2K_t}{3(\theta_i - \theta_i)} \quad 2.72$$

$$a_3 = \left[ \frac{-K_t}{\theta_i - \theta_i} \right]^3 \cdot \frac{1}{18 h_{wf}} \quad 2.73$$

Combination with equations 2.60 and 2.66 results in a solution for the cumulative amount of infiltration:

$$I = A_1 t^{1/2} + \frac{2}{3} K_t t + A_3 t^{3/2} + \dots \quad 2.74$$

where:

$$A_1 = [-2K_t h_{wf} (\theta_i - \theta_i)]^{1/2} = S \quad 2.75$$

$$A_3 = \left( \frac{-K_t^3}{18 h_{wf} (\theta_i - \theta_i)} \right)^{1/2} \quad 2.76$$

Neglecting the third and higher terms, equation 2.74 becomes:

$$I = S t^{1/2} + \frac{2}{3} K_t t \quad 2.77$$

Philip (1957) obtained a similar power series expression for vertical, ponded infiltration:

$$I = S t^{1/2} + K t + a_4 t^{3/2} + a_5 t^2 + \dots \quad 2.78$$

For vertical infiltration, the first two terms are usually sufficient (Dunin 1976, Philip 1957), resulting in Philip's (1957) equation for cumulative infiltration, from which the infiltration rate of a soil under vertical, ponded infiltration can be derived:

$$i = \frac{1}{2} S t^{-1/2} + K \quad 2.79$$

Equations 2.77, 2.78 and 2.79 show that sorptivity is the dominant factor controlling infiltration in the early stage of infiltration, whereas hydraulic conductivity (steady state infiltration capacity) determines the later stages of infiltration (see fig. 2.18). Sometimes the saturated conductivity,  $K_s$ , is used instead of  $K$  or  $K_t$ . Usually however,  $K$  and  $K_t$  are less than  $K_s$ . This is caused by the entrapment of air bubbles during infiltration and by the fact that macropores only contribute to infiltration under saturated conditions. From equations 2.77 and 2.78 it can be seen that  $K \approx \frac{2}{3} K_t$ . According to Dunin (1976), for most soils the hydraulic conductivity meets the following criterion:

$$\frac{1}{3} < \frac{K}{K_s} < \frac{2}{3} \quad 2.80$$

Another infiltration equation is given by Horton (1933, 1939), who also observed that infiltration under ponded conditions decreases from an initial rate  $i_0$  until it reaches a constant rate  $i_\infty$  (fig. 2.18):

$$i = i_\infty + (i_0 - i_\infty) e^{-\alpha t} \quad 2.81$$

where:  $\alpha$  = decrease coefficient. In this equation,  $i_\infty$  is Horton's (1933, 1939) equivalent of  $K$ . Raudkivi (1979) showed that Horton's equation can be derived from the Richard equation. Assuming  $K$  and  $D$  to be constant, Richards equation reduces to a standard diffusion equation:

$$\frac{\partial \theta}{\partial t} = D \frac{\partial^2 \theta}{\partial z^2} \quad 2.82$$

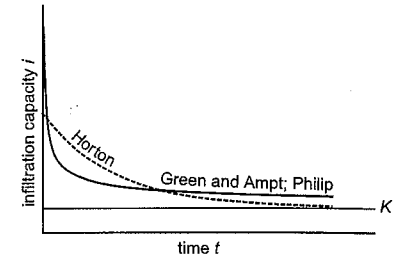


Figure 2.18 Infiltration capacity functions of Green and Ampt (1911), Philip (1957) and Horton (1933, 1939).

## 2.2.2 Infiltration envelopes

In nature, ponded infiltration rarely occurs immediately after the start of rainfall. When it does occur, it usually happens on impermeable surfaces such as solid bedrock. On a porous medium, surface ponding usually starts after a certain time has elapsed after the start of rainfall, or it may not take place at all. If the steady state infiltration capacity  $K$  exceeds the rainfall intensity, all the water supplied by rainfall will infiltrate. In this situation, no infiltration excess overland flow will take place, although saturation overland flow may take place once the storage capacity of the regolith is exceeded.

A different situation may occur if the rainfall intensity exceeds  $K$ . Initially, the infiltration rate will equal the rainfall intensity, and all water will infiltrate into the regolith. As rainfall continues, the amount of infiltrated water in the regolith increases, and therefore the infiltration capacity decreases. At a certain moment it will be equal to the rainfall intensity. After this moment, called the time-to-ponding  $t_p$ , the rainfall intensity exceeds the infiltration capacity and surface ponding occurs. The value of  $t_p$  depends on the rainfall intensity:  $t_p$  increases with decreasing rainfall intensity. For rainfall intensities approaching  $K$ ,  $t_p$  tends toward infinity. The curve describing this relationship between rainfall intensity and time-to-ponding is called the infiltration envelope. The infiltration envelope and its relationship to the infiltration curve are shown in figure 2.19.

Using Philip's (1957) equations 2.78 and 2.79, for the infiltration envelope can be derived. The following assumptions are used:

- The infiltration capacity,  $i$ , depends on the total amount of infiltrated water,  $I (= t_p i_r)$ .
- Under non-ponded conditions, infiltration takes place with a constant rate,  $i$ , which is equal to the rainfall intensity,  $i_r$ :  $i = i_r$  for  $0 \leq t \leq t_p$ .
- The rainfall intensity is constant.
- The rainfall intensity exceeds the steady state infiltration capacity:  $i_r > K$ .

From the first and second assumptions it follows that under conditions of ponded infiltration the criterion  $i = i_r$  will be attained sooner (at time  $t_*$ ) than under conditions of non-ponded infiltration (at time  $t_p$ ).  $t_*$  can be calculated from equation 2.79:

$$t_* = \frac{S^2}{4(i_r - K)^2} = \frac{S^2}{4(i_r - K)^2} \quad 2.83$$

Combining equations 2.83 and 2.78 with the second and third assumptions gives  $t_p$ :

$$t_p = \frac{I}{i_r} = \frac{S\sqrt{t_*} + Kt_*}{i_r} = \frac{S^2\left(i_r - \frac{K}{2}\right)}{2i_r(i_r - K)^2} \quad 2.84$$

is Philip's infiltration envelope function. For  $t \geq t_p$ , the infiltration capacity behaves according to equation 2.79, but with a shifted time coordinate  $t' = t - (t_p - t_*)$ . Using the same assumptions, Chow et al. (1988) give an equation for infiltration envelopes based on Horton's (1933, 1939) infiltration equation 2.81:

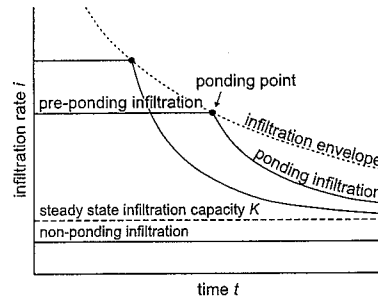


Figure 2.19 Relation between infiltration rate and the infiltration envelope.

$$t_p = \frac{1}{\alpha i_r} \left( i_0 - i_r + K \ln \left( \frac{i_0 - K}{i_r - K} \right) \right) \quad 2.85$$

where  $K$  is used instead of  $i_*$ . A third infiltration envelope function is given by Smith and Parlange (1978):

$$\int_0^{t_p} i_r dt = \frac{S^2}{2K} \ln \left( \frac{i_r}{i_r - K} \right) \quad 2.86$$

where:  $\int_0^{t_p} i_r dt$  = total amount of rainfall from start of rainfall until time-to-ponding.

## 2.2.3 Overland flow

On steep slopes there is little opportunity for actual ponding. The water that does not infiltrate into the soil will immediately start to flow down over the slope, thus generating overland flow. On interrill areas, a more or less uniform, sheet-like film of water will flow over the entire surface. In more detail, sheetflow shows small tracks where water is concentrated as a result of the effect of surface irregularities on the flow pattern. Blijenberg (1993b), Blijenberg et al. (1996) and De Graaf et al. (1993) called such preferential tracks *micro-rills*. Downslope, the amount of water increases and the flow begins to concentrate in rills and further downslope the rills join in gullies. Together with these changes in flow concentration and flow depth, the flow behaviour will change. In sheetflow, the flow character is assumed to be laminar, but in rills and gullies flow usually behaves turbulent. The Reynolds number,  $Re$ , indicates whether the flow is laminar or turbulent. For sheetflow:

$$Re = \frac{\rho_w u_m z_w}{\eta_w} \quad 2.87$$

and for open channel flow:

$$Re = \frac{\rho_w u_m r_h}{\eta_w} \quad 2.88$$

where:  $\rho_w$  = density of water;  $u_m$  = average flow velocity;  $z_w$  = flow depth;  $r_h$  = hydraulic radius of channel flow;  $\eta_w$  = viscosity of water ( $= 0.001 \text{ Pa s}$  at  $20^\circ\text{C}$ ). Flow is laminar if  $Re \leq 500$ , for  $Re \geq 2000$  the flow is turbulent and for  $500 < Re < 2000$  the flow is transitional between laminar and turbulent. The average velocity for uniform, laminar sheetflow on an inclined plane can be derived from equation 2.32 by averaging the velocity over the flow depth (Robertson and Crowe 1975):

$$u_m = \frac{\rho_w g z_w^2 \sin \beta}{3 \eta_w} \quad 2.89$$

and Manning's equation gives the velocity for fully turbulent flow:

$$u_m = \frac{r_h^{2/3} (\sin \beta)^{1/2}}{n} \quad 2.90$$

where:  $n$  = Manning's roughness coefficient. Table 2.4 presents some typical values for Manning's coefficient. The applicability of Manning's equation on very steep slopes remains uncertain.

Table 2.4 Typical values of Manning's roughness coefficient.

Terrain/material	Manning's $n$
Concrete	0.012-0.014
Gravel bottom with:	
concrete sides	0.020
mortared stone sides	0.023
riprap sides	0.033
Excavated channel in:	
earth	0.022
gravel	0.025
Mountain stream with cobbles/boulders	0.050
Natural stream channels:	
clean major stream	0.025
clean straight stream	0.030
clean winding stream	0.040
winding with weeds and pools	0.035-0.070
with heavy brush and timber	0.100
Flood plain with:	
pasture	0.035
field crops	0.040
light brush and weeds	0.050
dense brush	0.070
dense trees	0.100
Fallow land	0.08
Grassland	0.12
Woodland	0.15

Based on Chow et al. (1988), De Roo (1993) and Richards (1982).

On steep slopes, gravity eases the entrainment of material by the flow. This increases both the density and the viscosity of the overland flow fluid compared to pure water. As a result, the velocity and the Reynolds number decrease, so the entrained sediment will suppress fluid turbulence. The rainfall also has an effect: the impact of raindrops on the overland flow surface causes disturbance of the flow, increasing turbulence.

Catchment discharge can be calculated by routing the flow of water through the catchment using the flow equations presented. This can only be done accurately if a large amount of input data is available, but usually this is not so. A lumped model may then just as well be used to calculate catchment discharge. One discharge model is the tank model of Kobashi and Suzuki (1987) described in section 2.1.4 (fig. 2.9). Even simpler is the negative exponential model, giving a direct relation between the catchment discharge and the amount of water available in the catchment:

$$Q = \alpha V e^{-\alpha t} \quad 2.91$$

where:  $Q$  = discharge;  $V$  = total amount of water;  $\alpha$  = recession coefficient.

### 2.3.2 Dendrogeomorphology

Trees and shrubs that form annual growth rings, may respond in a variety of ways to changes in their environmental conditions and record these changes in their growth pattern. The term dendro-chronology refers to the general science of dating the annual growth layers in woody plants and the exploitation of associated environmental information (Shroder 1980). Dendrogeomorphology is a branch of dendrochronology that uses plant ecology and dendrochronological data to investigate the occurrence, intensity and chronology of geomorphologic phenomena (Alestalo 1971). Another branch is dendroclimatology, which extracts climatic information from tree data (Fritts 1976). Fritts (1976) mentioned some concepts vital to the use of dendrochronological information:

- *Uniformitarianism*. The present is the key to the past: Present day processes must be the same types of processes that acted in the past.
- *Growth limiting factors and sensitivity*. Only trees that are sensitive to changes in an environmental factor and also grow on a site actually affected by that environmental factor may yield information on that factor (fig. 2.20).
- *Cross dating*. In some years, trees grow more than one layer, or no layer at all. In order to accurately date the time of formation of any individual ring, such false or missing rings must be identified. This can be done by and comparing sufficient samples from multiple trees.
- *Replication*. Objective methods and criteria must be used when processing tree-ring data. This was also mentioned by Shroder (1980), who noted that the use of carefully researched statistical procedures was common practice in dendroclimatology, but not in dendrogeomorphology. More recently, Braam et al. (1987a, 1987b) have employed statistical tests to date mass movements from tree-ring data.

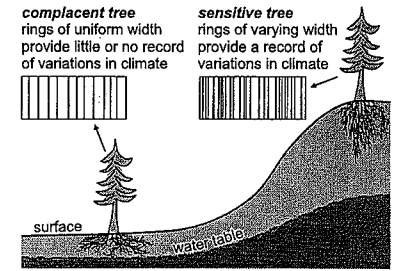


Figure 2.20 Complacent and sensitive trees.

## 2.3 Dating of debris-flow deposits

### 2.3.1 Introduction

When material is transported and deposited by a debris flow, it causes some small-scale changes in both the slope morphology and the environmental conditions. These changes serve as the basis for a dating of the debris-flow deposits. Obviously, the morphological changes formed by the track and the deposits of a debris flow may be recognized in the field and on (aerial) photographs. Thus time series of site visits or photographs may reveal information on the occurrence of debris flows within a certain time frame. Such information, however, is not readily available. Where it is available, the former often concerns a spatially limited area and the latter usually reveals the situation only at a few moments in time. Therefore, debris-flow activity in the past must be investigated through methods which require only a single field campaign. Several dating methods are available to this end. In more densely populated areas, archives can sometimes be a source of information. Finally, radiocarbon dating  $^{14}\text{C}$  has been used (Rapp and Nyberg 1981), but this method is surrounded with difficulties (Matthews 1980). Dendrogeomorphology and lichenometry are more common dating methods.

Physiological processes in a tree determine its growth. Hormones regulate the growth, which usually is strongest in a vertical, upward direction. The growth takes place in the cambium, a tissue situated immediately behind the bark where cells divide into phloem (inner bark) and xylem (wood) cells. Phloem conducts food and produces new bark. Xylem conducts water and produces the supporting tissue of the tree.

In mid and high latitudes, climatic seasonality causes trees to develop distinct layers of woody tissue: tree rings (see fig. 2.21). Growth starts in spring with the development of large, thin-walled cells forming the earlywood which makes up the inner part of the annual increment. Later in the year changes in external factors cause the formation of smaller, thicker and darker latewood. The transition of this latewood to next year's earlywood is usually marked by a sharp boundary. The new tissue formed every year roughly forms a cone of wood stacked upon previously formed cones. In a cross section through the stem, this shows up as a ring.

Usually the cone of new-formed wood is continuous and more or less uniform throughout the tree, but this is not always the case. Double or multiple rings may form if during the growth season the tree growth has been interrupted by periods of unfavourable weather or mechanical injury (Alestalo 1971, Glock and Agerter 1963; fig. 2.21). Also rings may be locally or completely absent, for instance if the growth season has been unfavourable altogether. Double, multiple and missing rings are a possible source of dating errors, so they must be identified by careful investigation of the cell structure (double rings usually do not show the sharp transition that characterizes the boundary between latewood and the succeeding earlywood) and by cross dating of tree-ring samples (figs. 2.21 and 2.22).



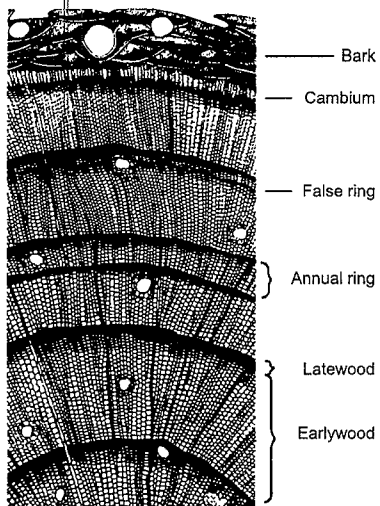


Figure 2.21 Cell structure in a cross section of a conifer (source: Bradley 1985).

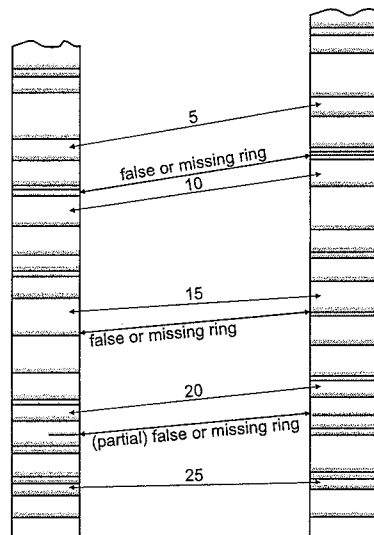


Figure 2.22 Cross dating of tree rings (after Bradley 1985).

Factors influencing tree (ring) growth are numerous. First of all, tree-ring width generally decreases with the age of the tree (fig. 2.23). Some climatic factors are sunshine, temperature, water availability, frost and wind. Other environmental factors are for instance slope angle, slope aspect, animal activity, human activity and geomorphic processes. According to Shroder (1978, 1980), a process produces a number of events affecting trees which respond in different ways to these events. The process-event-response system concept should be useful for handling large amounts of information (Shroder 1980). Processes may lead to one or more of the following events (Alestalo 1971, Shroder 1978, 1980):

- *Inclination*, or tilting of a tree,
- *Shear* of rootwood or stemwood,
- *Corrasion*, or removal of bark tissue and sometimes cambium and wood tissue as well,
- *Burial* of stemwood, caused by deposition of sediment around the tree,
- *Exposure* of rootwood, caused by erosion of the substrate on which the tree grows,
- *Inundation* or flooding by water, and
- *Nudation*, the formation of an unvegetated surface, either by the actual formation of new land or by the removal of existing vegetation.

And the resulting responses can be any of the following:

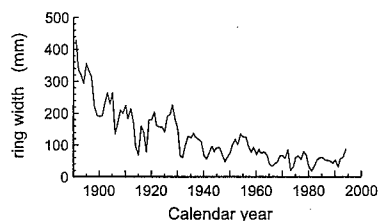


Figure 2.23 Decrease of ring width with tree age.

- *Reaction-wood growth*, generally the geotropic, or gravity-growth control, response of a tilted tree to return its growth to vertical and strengthen the lower part of the stem. In conifers, reaction-wood occurs as compression wood on the underside of the inclined tree. This compression wood consists of yellowish and reddish brown, short, thick walled dense cells. As a result, annual rings show eccentric growth with the fastest growth in the compression wood on the lower side of the tree and the slowest growth on the upper side. In deciduous trees, reaction wood is formed as yellowish to gray tension wood with long dense cells on the upper side of the inclined stem. Here the eccentric growth is greatest on the upper side of the stem. Inclination generally leads to reaction-wood growth (fig. 2.24), but other factors may also cause reaction-wood growth.

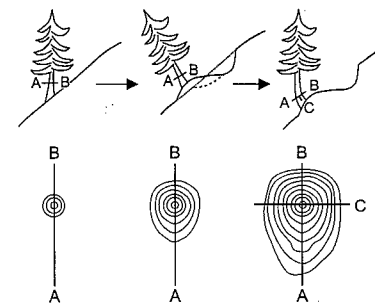


Figure 2.24 Tilting of a tree by mass movement followed by trunk curvature and eccentric growth of annual rings (after Braam et al. 1987b).

- *Growth suppression*, this is the general growth retardation of a tree which results in narrower tree rings. Burial, exposure and inundation generally lead to growth suppression. In severe cases, growth ceases altogether and the tree dies.
  - *Growth release*, which is the opposite of growth suppression and causes the formation of wider tree rings. This is generally the case after nudation, when a tree is left without competitors. Also short-term flooding of a generally dry location may lead to growth release.
  - *Ring termination and new callous growth*, which occurs as a result of shear or corrasion. The scars slowly become covered again with new callous margin, younger wood and bark. The new-formed tree rings meet the older, weathered rings at an angle, as can be seen in figure 2.25.
  - *Sprouting of new branches or roots*. After burial, new roots may develop in the freshly deposited layer of sediment.
  - *Succession*, which is the normal development series of plant communities leading to a state of relative stability (the climax). This is the normal reaction to nudation.
  - *Miscellaneous structural and morphological changes* in internal or external wood character.
- Bradley (1985) generalized these events and reactions into two groups yielding different types of dating information:
- *Providing minimum ages* for the substrate on which they are growing, corresponding to Shroder's (1978, 1980) nudation-succession (process)-event-response system, and
  - *Dating events which disrupted tree growth*, corresponding to the other event-response systems.



Figure 2.25 Cross section through an injured tree showing partial cover of the scar by new callous margin growth.

With regard to debris flows, possible events are: inclination, corrasion, burial of stemwood, exposure of rootwood and nudation. Inclination may occur if a debris flow hits the tree and pushes it downslope will lead to reaction-wood growth with eccentric tree rings (fig. 2.24). In the case of debris flows, nudation consists of the formation of a new surface caused by the deposition of sediment on which new trees may start to grow. The oldest trees on a debris-flow deposit may therefore provide information

on the minimum age of that surface. There are two possible sources of error associated with this type of information. Firstly, the oldest tree present does not necessarily have to be the first tree to have started growing on that surface and secondly, there may have been a considerable time between the nudation event and the invasion of the first trees, the so-called ecesis period (Sigafoos and Hendricks 1969). Shroder (1980) mentioned that ecesis periods can range from one to more than 100 years. Corrasion may occur by the debris flow itself if it still has considerable eroding capacity. Also, large stones separated from the flow may cause the damage. Some degree of growth suppression can be expected from this, as well as new callous growth and gradual disappearance of the scar. Exposure of roots may occur if the tree was standing in the flow channel of the debris flow. In this case, the roots are likely to be damaged, and severe growth suppression may be the result. Burial occurs when the debris-flow deposits sediments around the tree. These can be levee deposits as well as terminal deposits. The tree itself may be the trigger for the deposition of material. When burial occurs, corrasion of the tree is not very likely. Burial can cause growth suppression and sprouting of new, adventitious roots just below the new surface (Strunk 1989, 1991). Figure 2.26 shows that there is a critical depth of burying by a single event. The data were obtained by Strunk (1991) for burial of spruces (*Picea abies*) by debris flows on debris-flow cones in the Dolomites of Prags, Italian Alps. Often, an event attributed to a debris flow can be caused by another process just as well. For instance, corrasion may also occur by rockfall or by snow avalanches. Inclination may also be caused by other types of mass movement, by snow creep or by severe storms, and nudation may also be caused by

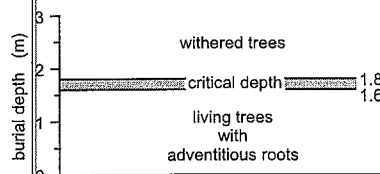


Figure 2.26 The effect of burial by a single debris flow on the growth of *Picea abies* (after Strunk 1991).

snow avalanches. Exposure of roots and burial of the stem are less likely to be erroneously attributed to the debris-flow process. This clearly is a potential source of error when dating debris-flow deposits with dendrogeomorphology. Another more potential source of error concerns the obtained date. If a debris flow causes an event in a tree, for example inclination, the reaction of the tree may be delayed. A delay of one year in recording of the event will certainly occur if the debris flow took place after the growing season: in this case the reaction cannot be recorded any sooner than the next growing season.

Shroder (1980) mentioned four possible types of samples that can be taken from a tree: cross-cut, longitudinal cut, or wedge-cut sections, and cores. Section type samples usually provide better and more reliable information, but also destroy the tree. Core samples hardly affect tree growth. Therefore, most studies rely on information derived from cores. The samples can be used for at least four types of dating methods: ring width measurement (Fritts 1976), ring density measurement (Schweingruber et al. 1978, 1988), D/H or  $^{18}\text{O}/^{16}\text{O}$  isotope variations (Epstein et al. 1976, Jacoby 1980), and event-response plotting (Shroder 1978). Ring width analysis is the simplest and most commonly used method.

The tree-ring width data can be analysed in three different ways. The first and simplest way is to count the number of rings to obtain the age of the tree. This is relatively straightforward. It is used in the case of nudation and (primary) succession, where only one sample is needed for each tree. The problems with this technique have already been mentioned. In the case of corrasion and the subsequent rehewed callous growth, two samples from the same tree must be compared, one taken through the wound and one taken in an undamaged part of the tree. The growth patterns in the period before the damage are the same in both samples, and these patterns must be synchronized. Such synchronization may be performed visually or statistically. The number of rings produced in the undamaged part of the tree since the infliction of the wound provides the date of corrasion.

The second method involves the overall reaction of tree-ring width growth, related to growth suppression and growth release. The last method involves the analysis of differences in ring width growth in different directions. To this end, the tree-ring eccentricities must be calculated. The eccentricity of the tree rings is given by Alestalo's (1971) formula (fig. 2.24):

$$E_j = \frac{r_{A_j}}{r_{A_j} + r_{B_j}} \quad 2.92$$

or by the more sensitive formula given by Braam et al. (1987a, 1987b) and Weiss (1988):

$$E_j = \frac{r_{A_j} - r_{C_j}}{r_{A_j} + r_{C_j}} \quad 2.93$$

where:  $E_j$  = eccentricity of ring  $j$ ;  $r_{A_j}$ ,  $r_{B_j}$  and  $r_{C_j}$  are the widths of ring  $j$  in the downslope, upslope and slope-parallel directions respectively. In analysing tree-ring widths and tree-ring eccentricities, it must be kept in mind that there are always slight variations occurring in these measures, which are caused by reactions to other factors than the one under investigation. Using a procedure known as the Split-Moving Window or SMW test (Braam et al. 1987b, Webster and Wong 1969), large, significant changes in one of these measures can be separated from small, insignificant changes. The SMW test is explained in more detail in chapter 9. Before the SMW test is used on ring widths, the ring widths should be standardized by correcting for the general decrease of ring width with age (Fritts 1971), although this is less important when searching for sudden changes in growth. Standardization is not necessary when working with tree-ring eccentricities.

Where more than one tree can be influenced by a particular process, for example on landslides, not all trees may show a reaction to activity of the process. For any year (or for any event), the Event-Response Index may be calculated from (Shroder 1978, Braam et al. 1987b, Weiss 1988):

$$ER_j = \frac{N_{r,j}}{N_j} \cdot 100\% \quad 2.94$$

where:  $ER_j$  = Event-Response Index for year  $j$ ,  $N_{r,j}$  = number of trees showing a response in year  $j$ , and  $N_j$  = total number of sampled trees alive in year  $j$ . Event-Response Index values depend on the distribution of the analysed trees in relation to the process.

### 2.3.3 Lichenometry

Lichenometry is based on the use of lichens to determine the age of the substrate on which these lichens are growing. The method may provide relative or absolute ages and has been widely adopted especially in environments where other dating methods cannot be used, such as arctic and alpine environments. Lichenometry is a relatively young method, effectively initiated by Beschel's (1950, 1961). Still a number of difficulties surrounding the method exist.

The main type of lichen used in lichenometric studies is the *Rhizocarpon* subgenus, a yellow-to-green crustose lichen common in arctic and alpine environments. As crustose lichens grow on rock surfaces, the use of lichenometry as a dating technique is limited to bedrock surfaces and coarse deposits. These include geomorphological features like moraines (Begét 1994, Bickerton and Matthews 1992, 1993, Evans et al. 1994, Haines-Young 1983, Mahaney and Spence 1989, McCarroll 1994, Rodbell 1992), rock glaciers (Hamilton and Whalley 1995), slush avalanches (André 1995, Bull et al. 1995), landslides (Bull et al. 1994), rockfalls (Bull et al. 1994, Ormelli and Porter 1983), debris flows (André 1995, De Redeljkheid 1988, Innes 1983b, 1985b, Kotarba 1989, Overbeek and Wiersma 1996, Rapp and Nyberg 1981, Van Steijn 1991, 1996) and periglacial phenomena (Cook-Talbot 1991, McCarroll 1994). Many other phenomena have also been dated using lichenometry. These include natural phenomena like earthquakes (Smirnova and Nikonov

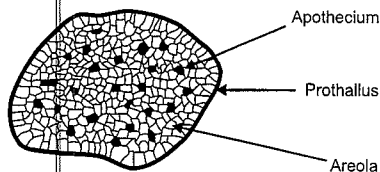


Figure 2.27 Main features of a crustose lichen thallus (after Innes 1985c).

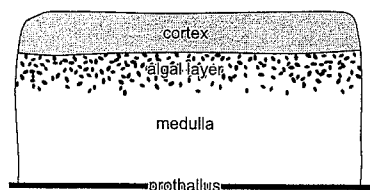


Figure 2.28 Cross section of an areole (after Benedict 1988).

1990), former snow cover extent (Benedict 1993) and river floods (Innes 1985c) and anthropogenic phenomena, for example the stone images on Easter Island (Follmann 1961).

Lichens are symbiotical communities of algae and fungus. The fungus provide a protective environment for the algae, which in turn provide carbohydrates by photosynthesis. An individual lichen is called a thallus. Foliose lichens form small bush-like thalli, whereas crustose lichens are flat disc-like forms growing so close to the rock surface as a crust that they are practically inseparable from the rock surface. Figure 2.27 shows the main features of a typical crustose lichen thallus, *Rhizocarpon*. It consists of a thin, black, fungal layer, the prothallus, upon which the areoles and apothecia are situated. Along the margins, only the prothallus is present. The apothecia are black spots producing spores. The areoles are the 'greenhouses' maintained by the fungus for the benefit of its algal food producers and the storehouses for food and water (Benedict 1988). Figure 2.28 shows an areole in cross section. The transparent top layer or cortex consists of interwoven fungal hyphae and protects the algal cells immediately beneath the cortex. Below the algal cells we find the medulla, which also consists of interwoven fungal hyphae and acts as the storage for food and water.

Taxonomic subdivision of lichens into species is based on the fungal component (Benedict 1988). The classification of lichens is extremely complex. Criteria for the subdivision of *Rhizocarpon* genus to subgenus, section, species and subspecies level is based on morphological and chemical features. The *Rhizocarpon* genus can be subdivided into the subgenus *Phaeothallus* and the subgenus *Rhizocarpon*, with the latter having a yellow-greenish colour caused by the presence of rhizocarpic acid (Innes 1985a). This subdivision is relatively easy to carry out in the field. According to Innes (1985b), field identification is often possible to section level, but further subdivision requires microscopic details and chemical tests and cannot be carried out easily in the field (Benedict 1988, Poelt 1988). Figure 2.29 shows the subdivision of the *Rhizocarpon* species to section level (Innes 1985a) and table 2.5 shows the subdivision to species level.

Table 2.5 Classification of the *Rhizocarpon* subgenus (after Innes 1983d and Poelt 1988).

Section	Species
<i>Alpicola</i>	<i>R. alpicola</i> , <i>R. eupetraeoides</i> , <i>R. inarense</i> .
<i>Rhizocarpon</i>	<i>R. atroflavescens</i> , <i>R. carpathicum</i> , <i>R. ferax</i> , <i>R. furax</i> , <i>R. geographicum</i> (L.) DC., <i>R. intermediellum</i> , <i>R. lecanorinum</i> , <i>R. macrosporum</i> , <i>R. pulverulentum</i> , <i>R. rapax</i> , <i>R. riparium</i> , <i>R. saanense</i> , <i>R. sphaerosporum</i> , <i>R. subclucidum</i> , <i>R. tavaresii</i> , <i>R. tinei</i> (s. str.).
<i>Superficiale</i>	<i>R. dispersum</i> , <i>R. effiguratum</i> , <i>R. norvegicum</i> , <i>R. parvum</i> , <i>R. pusillum</i> , <i>R. superficiale</i> .
<i>Viridiatrum</i>	<i>R. atrovirellum</i> , <i>R. dinohetes</i> , <i>R. kakurgon</i> , <i>R. lusitanicum</i> , <i>R. oportense</i> , <i>R. subtile</i> , <i>R. tetrasporum</i> , <i>R. viridiatrum</i> .

As classification of lichens is complex, many misinterpretations are probably present in the literature. Innes (1985a) reported seven different names involving *Rhizocarpon* and/or *geographicum*. For many of these cases, Innes suspected that only a yellow-green *Rhizocarpon* is being referred to which could be any number of species. Innes (1985a, 1985c) therefore recommends that the terms corresponding to the level of classification are used:

- Subgenus level, for the entire yellow-green *Rhizocarpon* subgenus,
- Section level, where identification to section level has been made; e.g. *Rhizocarpon* section *Alpicola*,
- Species level, where the actual species has been determined, for instance using the manual by Poelt (1988); e.g. *Rhizocarpon geographicum* (L.) DC.

Crustose lichens commonly show radial growth and for this reason they are the main type of lichens used in lichenometry. Figure 2.30 shows a sigmoidal growth curve, which is believed to be the appropriate growth model for *Rhizocarpon* species (e.g. Innes 1982b). Three features of the growth curve are apparent. Lichen growth starts with a period in which the growth rate steadily increases, the prelinear phase. During the first part of the prelinear phase, the thallus is not yet (macroscopically) visible. This period is called the colonization time. In the linear phase, the growth rate is highest. This is also known as the great period of growth (Beschel 1950). After the linear phase, the growth rate gradually decreases (the postlinear phase) and finally the lichen will start to show signs of mortality. The duration of the linear and postlinear phases appears to be size-dependent rather than age-dependent (Innes 1985c). For *Rhizocarpon* section *Rhizocarpon*, lichen diameters up to 150 mm may be safely used without effects of mortality (Innes 1985c).

The apparently linear relations between lichen size and age found by several authors (e.g. Gordon and Sharp 1983) probably represent only a small part of the actual growth curve. Hamilton and Whalley (1995) also constructed a linear growth curve for *Rhizocarpon geographicum* s.l. in northern Iceland using data from Caseldine (1990), Häberle (1990) and Kugelmann (1990). Semi-logarithmic growth curves for *Rhizocarpon* have been found by Orombelli and Porter (1983) and Bickerton and Matthews (1992) and log-log relations between lichen size and age have been used by Innes (1983b, 1985b). Growth rates are usually expressed in mm/century, which is also called the lichen factor. For the *Rhizocarpon* subgenus, a variety of growth rates has been reported, as shown in table 2.6. Figure 2.31 shows some reported growth curves for *Rhizocarpon geographicum*.

Lichen growth differs among *Rhizocarpon* species. In many studies, the terms *Rhizocarpon geographicum* s.l. or *Rhizocarpon geographicum* agg. are used to indicate that lichen determination has been carried out to subgenus level. In these studies it is assumed that only one species will actually be measured: the fastest growing species. According to Innes (1982b, 1983d), this assumption is

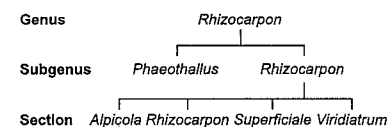


Figure 2.29 Classification of the genus *Rhizocarpon* (after Innes 1985a).

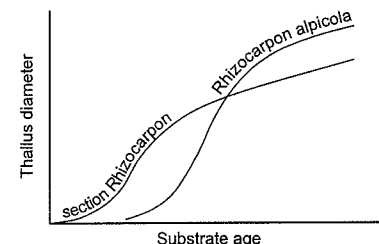


Figure 2.30 Growth curve models for *Rhizocarpon alpicola* and section *Rhizocarpon*, assuming delayed colonization by *Rhizocarpon alpicola* (after Innes 1982).

Table 2.6 Reported growth rates for *Rhizocarpon*.

Author	Location	Lichen factor or growth rate <sup>a</sup>		
		Linear phase	Postlinear phase	Undifferentiated
Andersen and Sollid (1971)	Nigardsbreen/Midtdalsbreen (Norway)			39-41
Andersen and Sollid (1971) <sup>b</sup>	Storbreen (Norway)			41
Andrews and Barnett (1979) <sup>c</sup>	North West Territories (Canada)			2.4-3.5
Benedict (1967) <sup>c</sup>	Colorado Front Range (USA)	14	3.3	
Bornfeldt and Österborg (1958) <sup>d</sup>	Jostedalsbreen (Norway)			44-55
Haines-Young (1983)	Storbreen (Norway)			20
	Nigardsbreen (Norway)			31
Hamilton and Whalley (1995)	Tröllaskagi (Iceland)			40
Innes (1985c)	general data			2-200
Jonasson et al. (1991)	Tatra Mountains (Poland)			44
Karlen (1975) <sup>c</sup>	Lapland (Sweden)	36	3.6	
Kotarba (1989)	subalpine zone (Poland)			38.1
	alpine meadow zone (Poland)			32.5
Matthews (1974) <sup>b</sup>	Storbreen (Norway)			46
Orombelli and Porter (1983)	Aosta valley (Italy)	43		27-33
Stork (1963)	Storglaciär (Sweden)			18-20
Stork (1963) <sup>b</sup>	Nigardsbreen (Norway)			46

<sup>a</sup> Growth rate in mm/century.

<sup>b</sup> In Haines-Young (1983).

<sup>c</sup> In Innes (1985c).

<sup>d</sup> In Stork (1963).

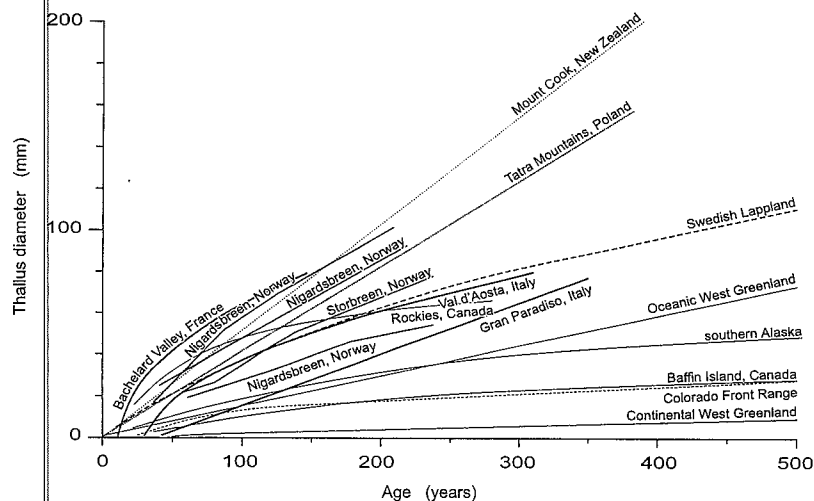


Figure 2.31 Reported growth curves for *Rhizocarpon geographicum* (after Bradley 1985, De Redeljkheid 1988, Haines-Young 1983, Innes 1985c, Jonasson et al. 1991 and Orombelli and Porter 1983).

incorrect. Figure 2.32 shows the largest *Rhizocarpon alpicola* and section *Rhizocarpon* lichen thalli growing on debris-flow deposits in Austerdalen, Norway (Innes 1983b). On young deposits, section *Rhizocarpon* thalli are generally larger than *Rhizocarpon alpicola* thalli, whereas on older deposits this is reversed. The reversal occurs at diameters of about 100 mm. The growth curve models that can account for this relation are shown in figure 2.30. This relation implies that if section *Rhizocarpon* or *Rhizocarpon geographicum* growth curves are used for dating, but field identification is carried out at subgenus level, deposit ages will be overestimated for deposits with thalli >100 mm if *Rhizocarpon alpicola* is present. At other locations, the relation between the largest thalli of both lichens differs slightly, which Innes (1985c) attributed to the narrower ecological range of *Rhizocarpon alpicola*. Lichen growth is affected by many environmental factors. Furthermore, different species of lichens respond differently to changes in environmental factors (e.g. Haines-Young 1983). Innes (1985c) presented a long list of factors affecting lichen growth (table 2.7). Substrate is important in two ways. The surface texture determines whether or not lichens can easily colonize the surface. Lichen establishment is inhibited on extremely smooth surfaces. Rapidly weathering rocks may also prevent lichen establishment. The chemical composition of the rock is also important. Many *Rhizocarpon* species are calcifugous. Another lichen species, the bright-orange *Xanthoria elegans*, grows preferably on limestone and other nutrient-rich substrates (De Redeljkheid 1988). Substrate stability influences lichen growth, because lichens can only start continuous growth after stabilization of a deposit. The effect of temperature is still relatively unknown, although Coxson and Kershaw (1983) have found maximum photosynthetic rates in *Rhizocarpon superficiale* at temperatures of 0-10 °C. Moisture availability is another key factor. Both too much and too little water may inhibit growth. Generally larger lichens are found along streams (Innes 1985d). Pollution components that may affect lichens are for example sulphur dioxide, heavy metals and dust. Competition between lichens becomes an issue in older deposits where lichens cover most of the surface. In this situation, lichens will compete for the available and occupied space, with some species being competitively superior to others. The other factors in table 2.7 mainly affect lichen growth indirectly. Of these, most attention has been given to the effect of snow cover on lichen growth (Benedict 1990, 1991, 1993, Innes 1985d).

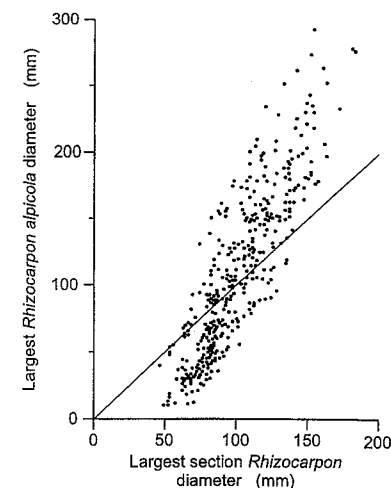


Figure 2.32 Relative growth rates of *Rhizocarpon alpicola* and section *Rhizocarpon* species on debris-flow deposits in Austerdalen, Norway (after Innes 1983d).

Table 2.7 Environmental factors affecting lichen growth (after Innes 1985c).

Factor	Indirect effect on growth through
1 Substrate lithology	
a Texture	
b Chemical composition	
2 Substrate stability	
3 Light intensity	
4 Temperature	
5 Moisture availability	
6 Wind exposure	4, 5, 7
7 Snow cover	3, 4, 5, 6
8 Elevation	3, 4, 5, 6, 7, 8, 10
9 Aspect	3, 4, 5, 6, 7, 10
10 Vegetation	3, 4, 5, 6, 7, 11
11 Competition	
12 Pollution	

Several methods have been used to construct lichen-growth curves. The curve can be established directly by measuring lichen growth of individual thalli of different sizes over a given time period, or indirectly by measuring lichen thalli diameters on surfaces of known age. Direct measurements can be performed using a ruler or a micrometer. The measurements can be performed directly on the thallus or on photographs of the thallus. The errors involved with this technique are often considerable, mainly because of the limited time periods between successive measurements and the slow growth of the lichens. Also, successive measurements must be carried out along exactly the same axes. According to Innes (1985c), the use of photographs is preferable for direct growth measurements. Photographs do not damage the thallus, an infinite number of axes can be measured from photographs at any time, measurements from photographs are generally more accurate, and finally photographs enable replication of measurements.

The use of direct measurements for the construction of lichen-growth curves generally involves the assumption of a uniform environment through time. However, in most studies involving lichenometry, the consequences of climatic changes are investigated or at least the assumption of a uniform environment through time may be questionable. For this reason, most lichenometrists rely on indirect measurements of lichen growth. By measuring the diameters of lichens on surfaces of known age, the actual growth over the whole period since colonization took place is recorded. Any climatic or other environmental changes causing lichen-growth fluctuations are implicitly accounted for in these measurements. The most often used surfaces with well-known dates of origin are gravestones (Innes 1983b, Orombelli and Porter 1983, Miltenburg 1986, De Redeljkheid 1988), but other anthropogenic surfaces such as bridges (Innes 1983c, De Redeljkheid 1988), stone walls (Benedict 1967, Miltenburg 1986) and abandoned farmsteads (Caseldine 1983) can also be used. However, the factors influencing lichen growth at these locations can be quite different from those in the area under investigation. Natural surfaces such as moraines (Innes 1986b, Bickerton and Matthews 1992), rock fall deposits (Orombelli and Porter 1983) and debris-flow deposits (Overbeek and Wiersma 1996) have also been used, when these surfaces could be dated independently by other means, such as archives (Andersen and Sollid 1971, Orombelli and Porter 1983), photographs (Pedersen 1976), dendrochronology (Overbeek and Wiersma 1996),  $^{14}\text{C}$  radiocarbon dating (Rapp and Nyberg 1981) or even other lichenometric techniques (De Redeljkheid 1988, Innes 1986b). Often, the surface of known age from which the largest thallus size has been derived, is relatively small. In this case, it is likely that the largest thallus on the surface does not correspond with the largest possible thallus on a surface of that age. Therefore the growth curves are generally drawn as envelopes around the largest measured thalli (fig. 2.33) and the ages predicted by the curve must be regarded as minimum ages (Innes 1985c). As the area of the surface searched for lichens increases

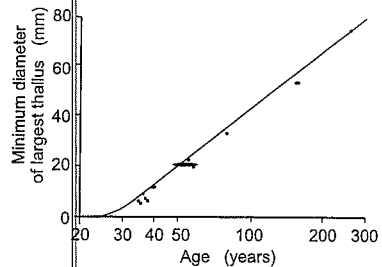


Figure 2.33 Lichen-growth envelope for *Rhizocarpon geographicum* obtained from measured thalli on surfaces of known age (after Orombelli and Porter 1983).

in size, the probability of including a lichen with a size close to the maximum lichen size also increases, as shown in figure 2.34. Whenever possible, the entire surface should be searched for the largest lichens (Innes 1985c). Different curves are obtained when different plotting systems (linear, semi-log or log-log) are used. Innes (1985c) recommends the use of a goodness-of-fit test to find the best curve.

Where indirect measurements are made for growth curve construction, a variety of slightly differing techniques have been used. Two different lichen size parameters have been used to construct the growth curve and to obtain dates (fig. 2.35). Several authors have measured the *largest inscribing circle* or *shortest diameter* of

individual thalli (e.g. Caseldine 1983, Orombelli and Porter 1983, De Redeljkheid 1988, Van Steijn 1991). Others have used the *longest diameter* or *smallest enveloping circle* (Haines-Young 1983, Innes 1983b, 1983c, 1986a, De Redeljkheid 1988, Kotarba 1989, Hamilton and Whalley 1995, Overbeek and Wiersma 1996). Some have even used both diameters. According to Innes (1985c), the longest diameter is the most suitable parameter to be used. The main risk of the use of the longest diameter is the inclusion of coalesced thalli. When multiple thalli grow together, they may appear as a single thallus. It is believed that such multiple thalli will often show up as non-circular thalli. For this reason, several authors have adopted criteria for rejection of irregular thalli, based on the ratio of smallest to largest diameter, for example Birkeland (1982) and Hamilton and Whalley (1995) have used a ratio of 0.75, and Overbeek and Wiersma (1996) have used a ratio of 0.67. However, single thalli also tend to become more irregular as they grow older and larger (Matthews 1974).

The number of lichens used for the construction of dating curves and for the dating has also differed among researchers. The single largest thallus can be used (Orombelli and Porter 1983, Bickerton and Matthews 1992, Hamilton and Whalley 1995) or the mean of several largest thalli (Innes 1985b, De Redeljkheid 1988, Bickerton and Matthews 1992, Overbeek and Wiersma 1996), usually 5 or 10. Innes (1984) and Locke et al. (1979) recommended using the mean of the 5 largest thalli.

When many more lichens are measured, at least 500-1000, the size-frequency technique may be applied. Its basic assumption is that lichen population characteristics may provide a better indication of age than a measure based on the largest thalli only. Both Locke et al. (1979) and Innes (1986a) used the *1 in 1000 thallus* derived from size-frequency distributions as indicators of deposit age, although Innes (1983c) had earlier rejected this parameter as a suitable age indicator. The *1-in-1000 thallus* represents the thallus size that is exceeded by 0.1% of all thalli. Recently, a new, promising technique of lichenometry has been developed by Bull et al. (1994, 1995) and McCarroll (1994). By measuring a large number of largest thalli on individual plots or (stone) surfaces, a normal size distribution of these largest thalli is obtained. In the case of surfaces that have been formed as a result of periodic activity, such as block fields that are affected by periodic rockfall as a result of earthquakes (Bull et al. 1994), talus slopes (McCarroll 1994) or debris fans that experience periodic slush avalanching (Bull et al. 1995), the dates of individual events appear as individual peaks within an overall uneven, multi-peaked distribution of largest thalli sizes. The

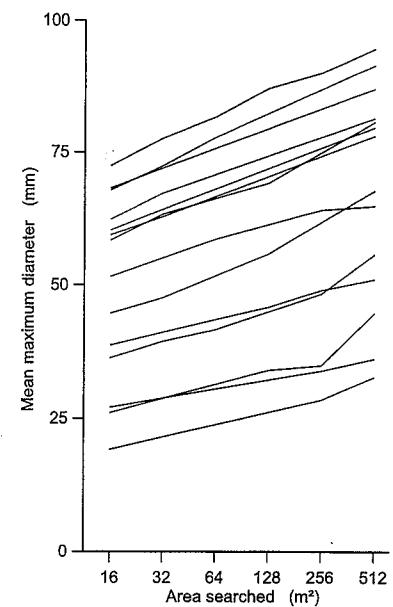


Figure 2.34 Increasing largest-thallus size with increasing area searched (after Innes 1985c).

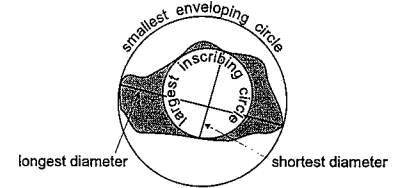


Figure 2.35 Longest and shortest thallus diameter.

technique has a high temporal resolution of less than 10 years in most cases. Also, confidence limits can be given for individual size-distribution peaks and the method is not sensitive to anomalously large thalli caused by incorporation of pre-existing lichens or by coalesced thalli.

Problem with thallus sizes is the occurrence of anomalous thalli. Sometimes lichens may have survived transport and deposition, so they are older than the substrate. Also, stones containing lichens may have been deposited onto an already existing substrate. The lichens introduced to the substrate in such ways are often larger than lichens that have colonized the substrate after its original position. In order to account for such anomalously large thalli, Rapp and Nyberg (1981) rejected the largest thalli which were more than 10 mm larger than the second largest thallus. Calkin and Ellis (1980) rejected the largest thallus if it was over 20% larger than the second largest thallus, and Innes (1984) rejected the largest thallus if:

$$d_{\max,5} < 0.76d_{\max} - 0.0006566d_{\max}^2 \quad 2.95$$

where:  $d_{\max,5}$  = mean diameter of 5 largest lichens (mm) and  $d_{\max}$  = diameter of single largest lichen.

One more lichenometric technique is worth mentioning, the percentage cover measurement technique originally developed by Locke et al. (1979). It builds upon the assumption that the growth of lichens on a substrate will result in a gradual increase of the surface area covered by lichens on the substrate. It has been used mainly as a relative dating technique. It appears to be less suitable for absolute dating, as a number of difficulties still surround the method: the subjective measurements involved and the sensitivity of percentage cover to environmental variations make it prone to errors (Innes 1986b).

One of the techniques described can be considered to be the best. Depending on the availability of lichens on surfaces of known age, on the size of the surface or deposits to be dated and available, the most suitable technique can be chosen. No firm guidelines for the techniques (e.g. size-frequency distributions, the parameters (e.g. the largest thallus diameter) and the criteria (e.g. for rejection of anomalously large thalli) to use exist. When a growth curve is available for the area under investigation, the choice will often be a practical one: to use the same method as the one that is used to obtain the growth curve.

## 3 STUDY AREA: THE BACHELARD VALLEY

### 3.1 Characteristics of the Bachelard Valley

#### 3.1.1 Topography

The study area is situated in the southern French Alps in the department Alpes-de-Haute-Provence (fig. 3.1). The study has been carried out mainly in the catchment of the Bachelard River. The Bachelard Valley is largely situated within the borders of the Mercantour National Parc. Most of the summits surrounding the valley reach up to 2600-2900 m. The highest summits are the Mont Pelat (3050 m) and the Cimet (3020) in the southeast of the study area. From east to west the study area measures 21 km, from north to south 5-10 km. The Bachelard River springs from a small lake at 2500 m elevation near the Col de la Cayolle in the southeast of the Bachelard Valley. From there it runs north towards the village of Bayasse, turns west towards Morjuan where it passes through a gorge, then turns north again until it flows into the Ubaye River near Barcelonnette at 1120 m elevation.

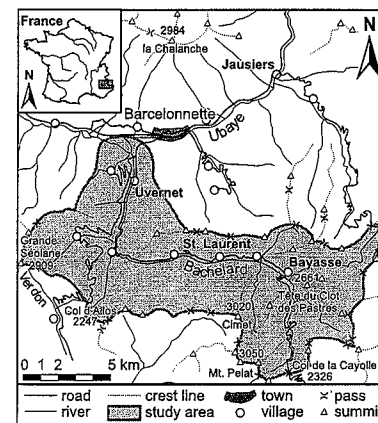


Figure 3.1 Location of the study area.

#### 3.1.2 Geology

The Bachelard Valley is situated in the transition zone between the internal and external zones of the Western Alps (Debelmas 1983, Kerckhove 1979; fig. 3.2). From east to west, the internal zone comprises the zones Piemontaise, Briançonnaise and Subbriançonnaise. The internal zone is characterized by the occurrence of large-scale nappes. In the western, external zone only autochthonous material is present. The oldest rocks in the study area date from the Mesozoic Era. At that time the area was occupied by the sea and limestones and marls were deposited. At the end of the Cretaceous period the Alpine orogenesis showed its first signs of activity. The area started to uplift and contract in an east-west direction. The uplift and contraction of the Alpine region continued during the Tertiary and east-west oriented folds were formed. As a result of stronger uplift in the east, a large mass of flysch deposits, the Autapie nappe, moved westward from the Piemontaise zone, overriding the autochthonous rocks. In the Miocene another nappe arrived from the east, the Parpaillon nappe, dragging along at its base large rock fragments torn from the overridden rocks. (BRGM 1972, Debelmas 1987, Kerckhove 1979, Pairis 1968). During the Quaternary, the uplift continued at a slower rate: according to Lemoine et al. (1988), the Alps have uplifted another 10 m since Hannibal's elephants have passed the Alps. Figures 3.3 and 3.4 show the lithology of the study area and the main lithological sequences. The main rock types are limestones, sandstones, conglomerates, flysch (repetitive regular alternations of limestone, sandstone and argillaceous beds) and marls. In the east and southeast of the study area

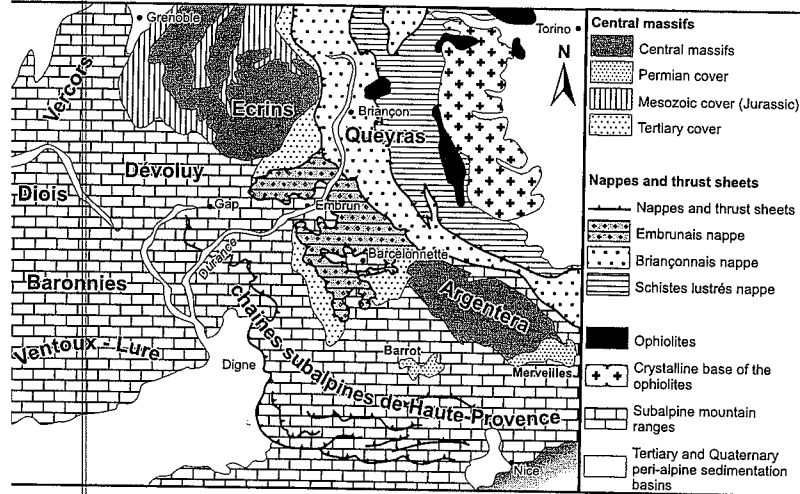


figure 3.2 Geological structure of the western Alps (after Debeltas 1987).

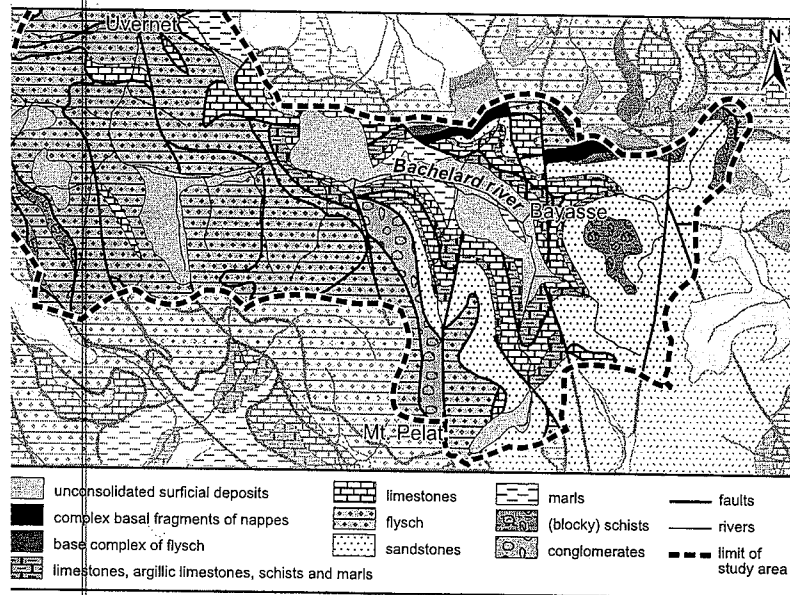


figure 3.3 Geological-lithological map of the Bachelard Valley.

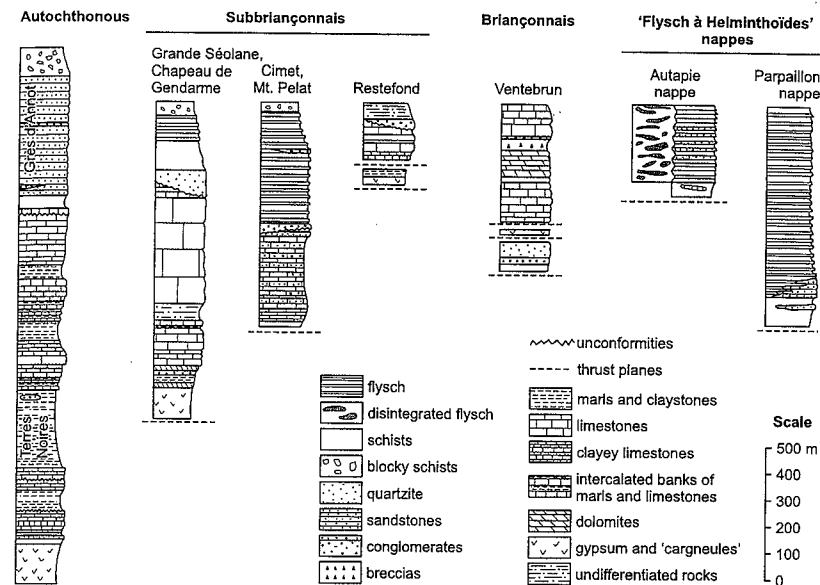


Figure 3.4 Lithostratigraphic sequences in the Bachelard Valley (based on geological map Barcelonnette 1:50.000).

autochthonous rocks dominate. The oldest autochthonous rocks can be found near Bayasse and near the mouth of the Bachelard River: erosion-sensitive dark marls called *Terres Noires* from the late Jurassic. The marls are overlain by hard Jurassic limestones (calcaire à silex) which outcrop south of Bayasse. On top of the limestones are early-mid Cretaceous limestones and marls and late Cretaceous to Eocene limestones, calcareous marls and schists. These are overlain by late Eocene to Oligocene massive sandstones, the Grès d'Annot, which in turn are covered by Oligocene schists. In the western part of the Bachelard Valley and on the mountain range south of the Bachelard River, autochthonous rocks are overlain by late Cretaceous flysch deposits of the Autapie nappe. These flysch deposits originated from turbidites deposited in a deep-sea basin (Debeltas 1987, Debeltas et al. 1989, Lemoine and Tricart 1988). Together with related Subbriançonnais flysch deposits this nappe covers the largest part of the west of the study area. Flysch deposits belonging to the Parpaillon nappe can be found in the mountains north of the Bachelard River. At the base of the nappe there are large rock fragments, mainly heavily fractured limestones, that were dragged along during its westward movement (Pairis 1968).

Weathering produces large massive blocks of several centimeters up to one meter diameter in sandstones and limestones. On further disintegration, a sandy regolith is produced, but limestones can also generate a loamy regolith. Flysch produces both large, massive plates and smaller, less massive plates, further disintegrating to a sandy or loamy regolith and marls produce small platelets which may alter to a silty or clayey regolith. In the Bachelard Valley the marls usually produce a silty regolith, with only a few percent the clay fraction.



During the Pleistocene cold periods alternated with warmer periods. In the Würm period, and probably in earlier cold periods as well, a glacier occupied the Bachelard Valley, uniting with the Ubaye glacier near Barcelonnette (Beaujeu-Garnier 1972, Kerckhove 1979). The valley was deepened and widened, especially near Bayasse, where Terres Noires marls favoured erosion. A large part of the upper and middle Bachelard Valley still has the characteristic U-shape of glacially scoured valleys. Glacially-scoured basins and steps can be found in the upper part of the valley and in some tributary valleys. In the east of the study area some tributary valleys are hanging at 2200-2400 m, about 300 m above the main valley. Other abundant glacial erosion forms include cirques, roches moutonnées, polished surfaces and striations (fig. 3.5). Morainic deposits dating from the Würm glaciation can be found near Bayasse, in the Agneliers Valley and on the slopes surrounding Uvernet.

Holocene forms are also abundant. In the Grande Cayolle Valley a rock glacier can be found at 2700 m elevation, which seems to be active. Rivers and torrents occupy the valley floors and have either eroded the valley floors or deposited fluvial sediments. At the mouth of several tributary valleys in the upper and middle part of the Bachelard Valley, torrential cones have formed. In the lower part of the valley, the Bachelard River has deeply eroded into the rock to form a gorge. Probably this gorge has formed subglacially. Many of the glacial basins have been filled with peat, fluvial sediments, and probably debris-flow deposits as well. A few of these basins are still occupied by lakes. The disappearance of the Würm glaciers has also resulted in the activation of large landslides through the removal of valley-side support. By now these are probably inactive, but small-scale, active landslides are widespread throughout the study area. Many are triggered by fluvial erosion at the toe. Scree slopes have developed in many places underneath rock cliffs. Single-particle rockfall supplies most of the material on scree slopes. The scree slope deposits have often been affected by dry grain flows or by debris flows. Figure 3.6 shows a scree slope affected by such processes. Debris flows are also a widespread and frequent phenomenon in the Bachelard Valley. The abundance of rock cliffs overhanging scree slopes and steep slopes covered with loose materials seem to be factors promoting debris-flow activity in the study area.

#### 3.1.4 Climate, vegetation and human influence

The present climate of the Bachelard Valley shows mediterranean and oceanic influences. Due to orographic influences, the amount of precipitation generally increases with elevation (Givone 1990). Maximum precipitation occurs in autumn, a secondary maximum occurs in June. Average annual precipitation amounts to 763 mm in St. Pons near Barcelonnette at 1140 m elevation (ONF data; fig. 3.7) and to 977 mm in Fours-St. Laurent (1660 m). Summer precipitation often occurs as short-duration high-intensity rainstorms. Such rainstorms are mostly local phenomena. In winter a large part of the precipitation falls down as snow. Figure 3.7 also shows the seasonal temperature fluctuations in Barcelonnette. Average annual temperature in Barcelonnette is 7.5 °C, average January temperature is -2.0 °C. As the Bachelard Valley is situated higher than Barcelonnette, average temperatures will be lower. In the Queyras, 50 km north of the study area, the 0 °C-isotherm is near 2400 m (Evin and Assier 1983). This isotherm marks the lower limit of sporadic permafrost. According to the same authors, the lower limit of discontinuous permafrost can be found near 2700 m. In the Bachelard Valley the 0 °C-isotherm is probably situated at 2400-2500 m.

Local climate is strongly influenced by slope gradient and slope aspect and general relief, determining the amounts of rainfall, radiation and wind. According to Douguédroit and De Saintignon (1970), in the southern French Alps the differences in average annual temperature between sun-exposed slopes and valley floors at 2000 m elevation are 3.4 °C, 1.6 °C and 0.2 °C for respectively minimum, average and maximum temperatures (fig. 3.8).



Figure 3.5 Morphology dominated by glacial processes in the Sanguinière Valley.

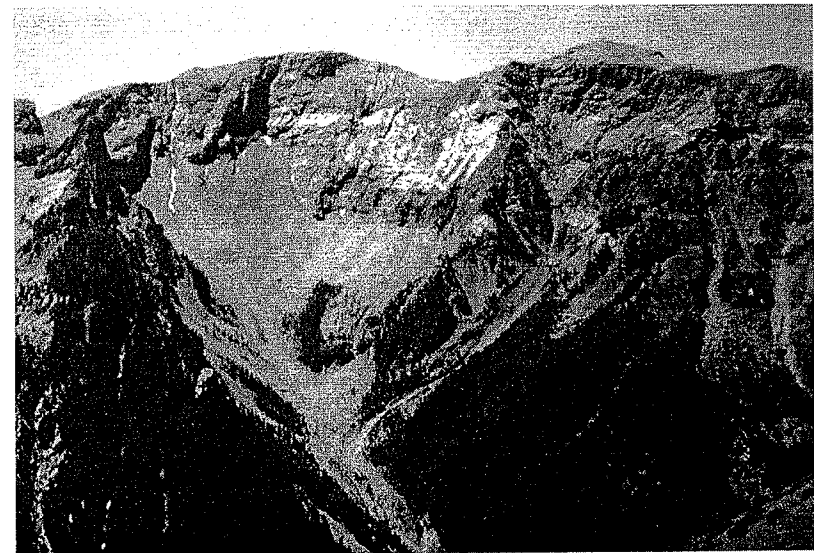


Figure 3.6 Morphology dominated by slope processes in the Tellière Valley.



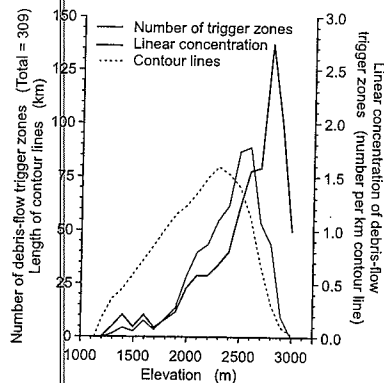


Figure 3.10 Relation between elevation and the occurrence of debris-flow trigger zones in the Bachelard Valley.

represent a band of constant width. However, this assumption does not hold if contour lines show mutual differences in short-distance 'ruggedness' or if average slope gradients differ between the altitudinal zones. Neither does the assumption hold for the highest contour lines (2900 and 3000 m), leading to an overestimation of the area represented by these contours. The decrease of debris-flow trigger zone concentration above 2800 m in figure 3.10 may well be the result of this overestimation. The second pattern is related to vegetation. Figure 3.9 shows that few debris-flow trigger zones are located in forested areas, which occupy the larger part of the study area below 2100 m. It seems likely that forest vegetation protects the underlying material against the eroding forces of raindrop impact and overland flow. On the other hand, once a debris-flow trigger zone has formed, vegetation has little opportunity of regenerating in an actively eroding environment on a steep slope. Unfavourable climatic conditions above 2000 m also hamper vegetation growth, making the surface more sensitive to erosion.

A third distinct pattern is visible as well. Many debris-flow trigger zones are grouped in distinct clusters, each of which is situated around an individual summit. Large clusters are located around the Ventebrun-Chevalier, the Trou de l'Aigle, the Cimet and the Petit Cheval de Bois. In these large clusters, many of the larger debris-flow trigger zones can be found. Smaller clusters can be found around the Crête de la Pierre Éclatée, the Tête de Glaudon and the Chapeau de Gendarme. Three out of the four large clusters are located in flysch deposits: Trou de l'Aigle, Cimet, Petit Cheval de Bois. The smaller cluster at the Tête de Glaudon is located in sandstones and schists, which, together with limestones, are also found in the cluster around the Crête de la Pierre Éclatée. The two remaining clusters, Chapeau de Gendarme and Ventebrun-Chevalier, are located in highly fractured zones near the base of the Parpaillon nappe, where many different rock types are found (limestones, sandstones, flysch, schists and marls). Many of the remaining debris-flow trigger zones are located in flysch deposits, some in sandstones (Vallon de Restefond, Vallon de Sanguinière). Very few trigger zones have developed mainly in other rock types, such as the trigger zones in Terres Noires marls near Uvernet. However, in many trigger zones other rock types may be present besides the dominant rock type. The general conclusion seems to be that the development of debris-flow trigger zones is greatly promoted by the presence of rapidly alternating rock types and highly fractured rocks.

### 3.2.2

#### Characteristics of debris-flow trigger zones and debris flows

Two main types of debris-flow trigger zones can be distinguished in the Bachelard Valley. The first type usually consists of a steep couloir in bedrock located above a scree slope (fig. 3.11). This *couloir* type trigger zone is usually found in resistant rocks such as limestones, sandstones or flysch. The couloir type effectively shows a separation between the part supplying water and the part supplying debris during debris-flow triggering. Debris is continuously being supplied from the bedrock cliffs to the scree slope. Even though some debris may be present in the couloir, the couloir mainly acts as a catchment supplying water to the scree slope. The actual debris-flow triggering takes place at the top of the scree slope. As couloirs are very steep, the water may flow with a very high velocity and mobilize the scree-slope material by the fire-hose mechanism mentioned by Johnson and Rodine (1984). This generally leads to incision at the top of the scree slope.

The second type is a cavity on a slope, usually bowl- or funnel-shaped. Within this *bowl* type debris flow there is no sharp distinction between parts supplying water and parts supplying debris during debris-flow triggering. Usually a large part of the surface is covered with unconsolidated material and often the bowl type shows a separation between parts where mainly fine-grained material (clay, silt, sand) is present and parts with mainly coarse debris at the surface (fig. 3.12). The occurrence of this type of debris-flow trigger zone is favoured by the presence of both resistant and erodible rocks,

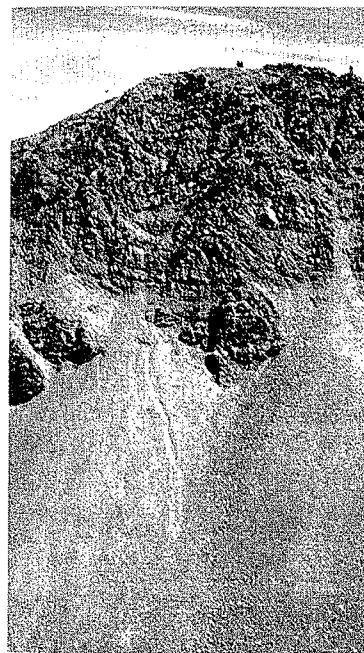


Figure 3.11 A couloir-type debris-flow trigger zone.

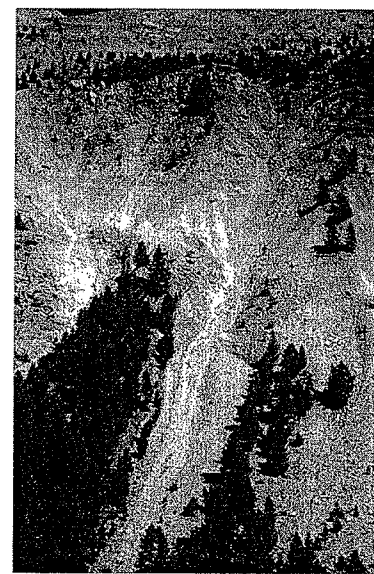


Figure 3.12 Two 'bowl'-type debris-flow trigger zones on the west-facing slope of the Tête du Clot des Pastres: on the right TCP (Tête du Clot des Pastres), on the left TCP-N1 (TCP North 1).

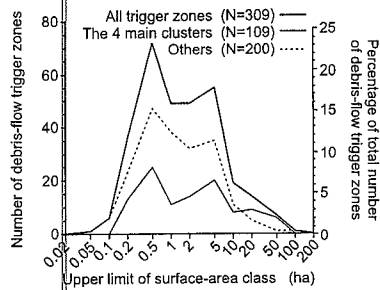


Figure 3.13 Size distribution of debris-flow trigger zones in the Bachelard Valley.

mainly in summer and autumn during high-intensity rainstorms. Small slides may also mobilize the fine-grained material. The thickness of fine-grained material within the trigger zone can vary widely even over very short distances.

Many debris-flow trigger zones, especially the larger ones, show characteristics of both trigger zone types. The average size of debris-flow trigger zones in the Bachelard Valley is  $0.030 \text{ km}^2$  (fig. 3.13). The four large clusters contain comparatively large trigger zones: the average size in these four clusters is  $0.048 \text{ km}^2$ , whereas the average size of the remaining debris-flow trigger zones is only  $0.017 \text{ km}^2$ . Hovius (1990) and Van Steijn (1991) describe some other characteristics of typical bowl-type debris-flow trigger zones in the Bachelard Valley. Vegetation consists mainly of grasses and herbs and covers less than 10% of the trigger zone. Average minimum slope angles within typical trigger zones are  $33^\circ$ , average slope angles are  $38^\circ$ , and drainage channels have gradients of at least  $30^\circ$ . Many trigger zones have parts with much steeper slope angles, especially the couloir-type ones.

Most debris-flow deposits are found between 1700 and 2400 m. Debris-flow tracks are usually several hundreds to over 1000 m long (see also Van Steijn 1996). Most of the debris flows in the study area are small-scale flows ( $1\text{--}10^3 \text{ m}^3$ ) according to the classification by Innes (1983a; fig. 2.2). There are only a few medium-scale debris flows ( $10^3\text{--}10^5 \text{ m}^3$ ). Van Steijn (1988) and Van Steijn et al. (1988b) back-calculated debris-flow velocities of 1–10 m/s from the difference in height between the inner and the outer levee in debris-flow track bends (section 2.1.5, eq. 2.45).

### 3.3 TCP: The Tête du Clot des Pastres debris-flow trigger zone

One of the bowl-type debris-flow trigger zones on the west-facing slopes of the Tête du Clot des Pastres was selected as a key site for detailed investigations. The main reasons for selecting this site were its representability for bowl type trigger zones and for practical reasons, its good accessibility (30 minutes from Bayasse) and relative safety. With regard to safety, both the risk of rockfall and the risk of falling down were considered acceptable for this site. This site (fig. 3.12), which will be referred to as TCP, is situated 1 km southeast of Bayasse at an elevation of 1975–2150 m (fig. 3.14). The TCP site is 280 m long and up to 75 m wide (fig. 3.15). In the main channel slope angles range from  $35^\circ$  to  $38^\circ$ , on the side slopes they can be as high as  $45^\circ\text{--}50^\circ$ . It is one of a series of debris-flow trigger zones stretching along the slope, which are strongly related to the lithological structure, as figure 3.16 clearly shows.

which respectively supply the coarse and the fine-grained material. At the bottom, bowl type trigger zones are often confined by an outcrop of resistant bedrock. Sometimes this layer is the only source of coarse debris. The trigger zone drains through a narrow passage in this bedrock.

Coarse debris is found on the floors of channels and gullies. It is usually supplied by rockfall from rock cliffs. The fine-grained material is often a regolith formed in situ by weathering of marls or marly limestones. Slope deposits that had formed before the trigger zone started to develop can also act as a source of fine-grained material. The regolith is often dissected by rills and gullies. This indicates active erosion by overland flow, which seems to occur

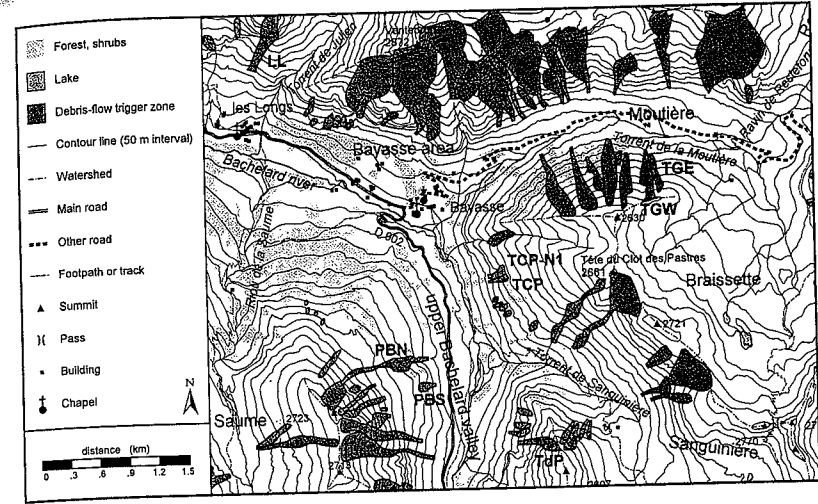


Figure 3.14 Location of the debris-flow trigger zone TCP (Tête du Clot des Pastres) near Bayasse.

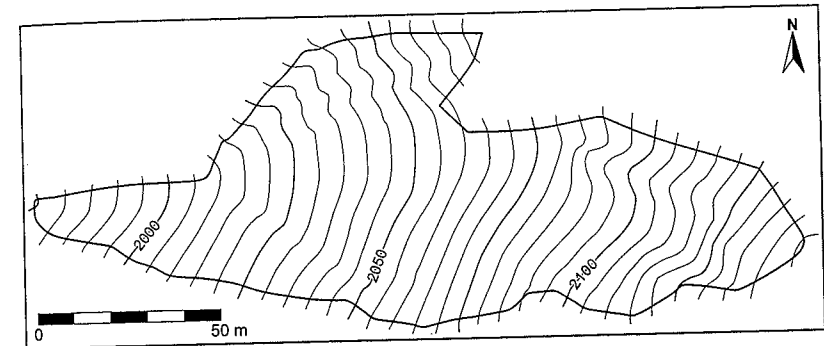


Figure 3.15 Contour map of the debris-flow trigger zone TCP.

Three rock types outcrop in the TCP trigger zone (fig. 3.17). Above 2060 m Grès d'Annot sandstones are present. Between 2015 and 2060 m Cretaceous marls are found. Within the marls an alternation exists of more calcareous and more silty-argillaceous bands. Near the top of the marls a several metres thick limestone bank shows up. A Cretaceous limestone formation forms the lower boundary of the trigger zone. Below these limestones, bedrock is covered with slope deposits.

The marls are covered with regolith which consists mainly of sand and up to a few cm large stones. In dry periods, the top of the regolith desiccates and forms a strong crust, cemented by lime. On wetting, this crust quickly softens and during wet periods the crust is absent. The regolith is very sensitive to



Figure 3.16 Debris-flow trigger zones on the west-facing slope of the Tête du Clot des Pastres and their relation to lithology.

erosion by overland flow, which has resulted in the formation of sharply incised gullies, especially north of the main channel. These gullies have average slope angles of about  $42^\circ$  and their side slopes have slope angles of  $39\text{--}50^\circ$ . In summer and in autumn, Hortonian overland flow produced by heavy rainstorms deepens existing rills and gullies and forms new rills. In autumn these rills and gullies are sharply incised and can be up to 20 cm deep and wide (fig. 3.18). The eroded material is transported down towards the main channel. During erosional rainstorms the sediment concentration in the runoff is usually high and sometimes the flow character changes into debris flow. At the end of spring, after the snow has melted, rills and gullies are often blurred or masked (fig. 3.19). The main reason for this seems to be solifluction caused by persistent wet conditions during the snow-melt period. On the gully floors a thick accumulation of these solifluction masses may be present after the snowmelt period. These seasonal fluctuations could also be seen clearly from erosion marker data. Throughout the year, small debris slides of several dm long and wide can also occur under wet conditions. The vegetation cover of the marls south of the main channel is about 2–10%, north of the main channel it is less than 1%. Above the marls, the sandstone outcrops are partly covered by a thin layer of regolith. Here the main channel gradually becomes narrower. At 2090 m into two narrow, shallow channels join to form the main channel. In these two channels little debris has accumulated, as they have minimum slope angles of  $40^\circ$ . On the side slopes some vegetation is present, with a cover of up to 20%. The vegetation consists mainly of grasses and herbs, but also some larch trees stand here.

The main channel is a shallow, 20 m wide channel. The channel floor is covered with an up to 1 m thick deposit of coarse, cohesionless debris. This debris is mainly supplied from the sandstone cliffs above by single particle rockfall. Individual stones are up to 2 m long, but the sizes of 1–25 cm dominate. The accumulated debris shows signs of secondary transport processes within the trigger zone. Tracks of material, differing from the surrounding material in average grain size or in grain-sorting pattern, can be recognized. They are caused by processes such as dry grain flow and debris flow. The occurrence of dry grain flows is favoured by the small difference between the slope angle and the static internal friction angle of the debris. No vegetation exists in the main channel.

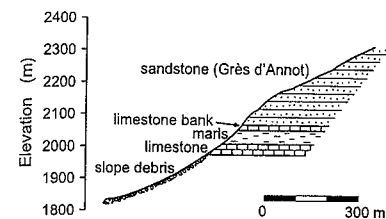


Figure 3.17 Lithological profile near the debris-flow trigger zone TCP.

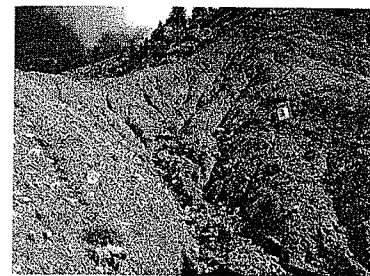


Figure 3.18 Deep and sharply-incised rills in the debris-flow trigger zone TCP.



Figure 3.19 Solifluction deposits and absence of rills in the debris-flow trigger zone TCP.

In the Cretaceous limestone formation below the marls, the trigger zone and the main channel are only a few metres wide and the channel is filled with a 1–2 m thick accumulation of coarse debris. Beneath this narrow passage debris-flow deposits can be found all the way down to the Bachelard River at 1820 m. The debris-flow deposits found here are coarse grained (10–50 cm stones) and filled with a finer-grained matrix.

#### 4.1 Introduction

In order to meet the research objectives stated in section 1.2, data had to be collected. Data to be collected concerned debris-flow trigger-zone characteristics, all of the factors in a debris-flow triggering model (based on Takahashi 1978, 1980, 1981a, 1981b), rainfall and runoff characteristics and thresholds concerning debris-flow triggering, the frequency of such critical conditions and past and present debris-flow activity. Table 4.1 lists the methods used in this study. Data collection in the field was strongly determined by the difficult terrain conditions accompanying debris-flow trigger zones. Therefore, practical considerations played an important role in deciding on which methods to use.

#### 4.2 Parameters of the coarse debris

##### 4.2.1 Porosity

Coarse-debris porosity has been measured by filling a bucket of known volume with coarse debris (containing little or no sand, silt or clay-sized material) and then fill the pores with water. Porosity is then simply calculated by dividing the volume of water in the bucket by the total volume of the bucket. The porosity measurements were done for different average grain sizes, sorting and packing. Loose packing was obtained by carefully putting material into the bucket. Dense packing was obtained by shaking and beating the bucket. Boundary effects caused by the bottom and sides of the bucket in these tests were tested by measuring porosity at different levels of filling. Coarse-debris porosity is necessary rainstorms.

##### 4.2.2 Strength

The strength of coarse debris is an important factor in a debris-flow triggering model (see chapters 2 and 5). It can be determined by taking samples to the laboratory or by performing field tests. Justo (1991) mentions that in-situ strength tests are preferred for coarse materials, as large amounts of material are needed to eliminate boundary effects caused by a small ratio of particle size to sample size. In order to determine the static and kinetic internal-friction angles of the coarse, cohesionless debris in the field, a new test method was designed. This test takes advantage of naturally occurring accumulations of coarse debris at slope angles approaching the kinetic internal-friction angle of the debris. Such locations can be found at the top of scree slopes and in some steep gullies, at slope angles of 35° or more (fig. 3.6). The method is also described in Blijenberg (1995).

The test starts by digging a cut in the debris on a slope. The material above the cut has a steeper local slope and will fail if too much material is dug away (fig. 4.1a). The failure plane is steeper than the average surface slope. Ideally, a straight failure plane starts at downslope point 1 and emerges at upslope point 2. If the locations of points 1 (at depth  $z_1$ ) and 2 (at distance  $s$ ) and the average surface-slope angle,  $\beta$ , are known, the angle of the failure plane,  $\beta_p$ , can be calculated for a vertical cut:

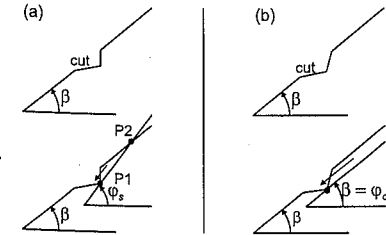


Figure 4.1 The test method for determination of static (a) and kinetic (b) internal-friction angles of coarse, cohesionless debris.

Table 4.1 Methods used in the field and in the laboratory.

Target data	Field methods	Laboratory or office methods
Coarse debris		
Density and porosity	Measuring water levels in a bucket filled with coarse debris	
Internal-friction angle	Strength test in coarse debris on steep slopes	
Fine-grained debris		
Density, porosity and water content	Taking 100 cm <sup>3</sup> cylindrical regolith samples	Saturating, drying and weighing regolith samples
Grain-size distribution	Taking regolith samples	Mechanical sieving and fall velocity
<i>p</i> / <i>F</i> -curves (water content - matrix suction)	Taking 100 cm <sup>3</sup> cylindrical regolith samples	Subject samples to matrix suctions in sand/kaolinite box
Regolith-depth distribution	Driving a rod into the regolith	
Infiltration parameters <i>K</i> and <i>S</i>	Rainfall simulations	Hydrologic simulations
Rainfall and runoff		
Rainfall time series	Automatic rainfall registration: rain gauges	
Discharge time series	Automatic discharge registration: discharge measurements	Hydrologic simulations
Reliability of discharge measurements	Video camera, field observations	Comparison of video-camera images with discharge records
Discharge characteristics	Video camera, rainfall simulations, field observations	
Fluid viscosity as a function of sediment content	Flume experiments with fine-grained debris mud	Flume experiments
Base maps		
Digital terrain model of debris-flow source areas	Geodetic survey	Interpolation of field data to regularly-spaced grid
Topographical map of the Bachelard Valley		Digitizing
Geological map of the Bachelard Valley		Digitizing
Spatial distribution of debris-flow source areas	Field survey	
Debris-flow occurrence		
Debris-flow deposit ages, debris-flow frequency	Tree-ring sampling	Tree-ring pattern analysis
Debris-flow deposit ages, debris-flow frequency	Lichen-size measurement	
Spatial distribution of debris-flow occurrence	Regular field surveys, photographs	Comparison of photographs, digitizing
Temporal distribution of debris-flow occurrence	Regular field surveys, photographs	Comparison of photographs, digitizing
Occurrence of debris flows at TCP	Video camera, regular field visits	
Other data		
Annual and seasonal erosion	Erosion markers	
Storm-event erosion	Erosion plots	
Morphological changes	Video camera, photographs, erosion markers	Comparison of photographs

$$\tan \beta_f = \frac{z_f + s \sin \beta}{s \cos \beta}$$

4.1

The angle of the failure plane equals the static internal-friction angle  $\phi_s'$  of the debris according to equation 2.12, provided the mass that starts sliding is large enough. However, if the mass that slides is small, boundary effects caused by single-particle interactions may play an important role.

When more material is dug away, a larger mass will slide. This mass may continue to move downslope over some distance along a failure plane more or less parallel to the slope surface (fig. 4.2b). If it slides with a low, uniform velocity, the force necessary to overcome friction equals the downslope component of the weight of the mass. In that case the sliding mass is in dynamic equilibrium ( $F \approx 1$ ) and if single-particle effects and boundary effects are absent,  $\phi_s'$  should equal  $\beta$  according to equation 2.12. The surface-slope angle of the sliding mass,  $\beta$ , was measured by placing a 2 m long bar on the surface and measuring its inclination. The maximum error for individual measurements was estimated to be about 2°.

If the dimensions of the sliding mass are small compared to individual stones, single-particle effects may prevail. Friction at the sides may occur if the depth of the sliding mass is large compared to its width. Arching, the formation of a structural bridge of individual particles between the stationary boundaries of the sliding mass (like in a Roman arch), is a special kind of single-particle effect which is more likely to occur in narrow sliding masses (compared to individual stones) than in wide ones. When arching occurs, the strength to overcome is that of the rock material constituting the particles, not the friction between the particles. Therefore, the sliding mass should be large compared to the individual stones in the mass. In 1969 however, Lambe and Whitman noticed that guidelines for testing cohesionless materials coarser than sands were still lacking. More recently, Charles (1991) has given some guidelines for sample sizes to be used in triaxial tests and direct-shear tests. To avoid single-particle effects, sample height in direct-shear tests should be at least ten times the maximum grain size, equivalent to an average depth of the failure plane of at least five times the maximum grain size.

It seems justifiable that the criteria used in our field tests were less stringent than those for the confined direct-shear tests: single-particle effects are less likely to occur in unconfined conditions. To avoid single-particle and side-friction effects, in this test the sliding mass had to be at least 2 m long and at least 90% of the stones had to be smaller than 10 cm. The width of the mass had to be at least ten times average (estimated) stone size and the depth of the failure plane had to be at least three times average (estimated) stone size.

Internal friction-angle tests were done 50 times at each test location. Besides describing the rock type(s) constituting the debris, at each location 100 stones were randomly picked and their principal axes were measured for a characterization of the debris. These principal-axis measurements served to derive other parameters of stone size, stone shape and stone-size distribution which may be related to the static and kinetic angle of internal friction.

It turned out that the test did not work well for the determination of the static internal-friction angle. Once a small debris mass started to move, it immediately triggered failure of more upslope material, which made it impossible to find point 2. On the other hand, the method seems to have worked quite well for the determination of the kinetic internal-friction angle. Usually the boundary conditions mentioned above were amply fulfilled. Typically the sliding mass was 3-6 m long, 50-200 cm wide and 10-50 cm deep, with estimated sliding velocities of 1-10 cm/s.

The simplicity, the low cost, the modest equipment and the abundance of coarse debris on scree slopes and in some steep gullies are clear advantages of this test method over laboratory measurements, as well as the large number of tests that can be carried out in a short time. The test seems practicable for testing undisturbed, natural debris with average stone sizes of up to 15-20 cm. However, there are some disadvantages. Suitable locations can be difficult to find, as the slope angle must be near the kinetic internal-friction angle of the material. Also, such locations are often difficult to reach and hazardous: debris is usually supplied to these locations by single-particle rockfall.

Debris characteristics like stone size, sorting or rock type can hardly be controlled, making it difficult to single out the influence of such parameters on  $\phi_k'$ . Finally, a large number of tests is necessary to eliminate measurement errors from individual tests.

#### 4.3 Parameters of the fine-grained regolith

##### 4.3.1 Density, porosity, field water content and water-retention curve

100 cm<sup>3</sup> cylindrical samples were taken to determine bulk density and solid density of the fine-grained regolith material in several debris-flow trigger zones. Also, porosity and volumetric field water content were determined, both of which play a role in the infiltration process (cf. eqs. 2.65 and 2.74). In the laboratory the samples were weighed (field weight), then placed for about 24 hours in a water-filled box and weighed again (saturated weight). Then the samples were oven-dried for 24 hours at 105°C and weighed again to determine the dry weight. Cylindrical soil samples were also taken during rainfall simulations. In that case samples were taken before and after the rainfall simulation, providing a better understanding of the change in water content during the simulation. Two important problems were encountered with these cylindrical samples. The most important one was disturbance of the regolith material during sampling. The presence of stones in the regolith made it very difficult to push the ring into the regolith without disturbance. Another problem was caused by some swelling and shrinking of the samples during respectively wetting and drying.

In 1992 100 cm<sup>3</sup> cylindrical samples were taken to the laboratory to determine *water-retention curves* (pF-curves). At different matric-suction levels, the water content was determined by weighing. The matric suction was imposed on the sample by placing it in close contact with the sand surface in a box with adjustable matric suction (pF = 1.0, 1.3, 1.7 and 2.0). At pF = 2.3 and 2.7, the same procedure was repeated in a kaolinite-filled box.

##### 4.3.2 Grain-size distribution

Grain-size distributions have been obtained using the standard sieving method for grain sizes 50µm-2mm, and the fall-velocity method in a water-filled cylinder for grain sizes <50µm. One major problem was encountered. The standard procedure demands that samples are treated with acid to remove calcareous bonds between particles. However, in the material concerned, the particles are themselves composed of limestone; also, our primary interest is on the distribution of particles transported by overland flow or by (micro-scale) debris flows, which may be individual grains or strongly-cemented water-resistant aggregates. As a treatment with acid would drastically alter the grain-size distribution, it was decided not to treat the specimens with acid.

##### 4.3.3 Regolith depth

Regolith depth and porosity determine the maximum storage of water in the ground. The depth of the regolith layer covering the side slopes in the marls of the Tête du Clot des Pastres debris-flow trigger zone (TCP) has been measured on interrill areas and on the gully floor of the monitored gully. This was done by driving a 6 mm metal rod into the ground until it struck on the underlying bedrock and could not be driven deeper into the ground. The regolith quickly increases in stoniness with depth, and many times a single stone was struck rather than the actual bedrock. In order to account for this, multiple determinations were done at each location. The ones suspected to have struck stones in the regolith were rejected. The difference between striking a stone in the regolith or the bedrock was striking: hitting a stone generally produced a 'dull' sound, but the bedrock produced a much 'clearer' sound. Very deep penetrations were also rejected: these were suspected to be joints in the bedrock.

#### 4.3.4 Infiltration characteristics: rainfall simulations

Rainfall simulations were carried out in several debris-flow trigger zones to assess the infiltration characteristics of these areas. The infiltration characteristics to be measured were the steady-state infiltration capacity,  $K$ , and the sorptivity,  $S$ . A rainfall simulator (fig. 4.2) was used because it had a large sample size, it caused little or no damage to the regolith, and it was more practical.

The rainfall simulator covers a test surface with a horizontal length and width of 24.5±0.5 cm, making up a horizontal, square surface area,  $A_{\text{rps}}$  of 0.060±0.002 m<sup>2</sup>, so 1 liter of water produces an equivalent rainfall depth of 16.7±0.5 mm. The simulator is placed horizontally in a frame connected to four rods. Rain is produced from 49 dripholes on a square grid with 3.5 cm interhole distance (fig. 4.2b). The fall height of the raindrops is 1.00-1.20 m. Drop size has not been measured, but is estimated to be 3-4 mm.

The rainfall intensity of the simulator can be changed by adjusting the level of an air-entry tube in the simulator. At the base of the air-entry tube the water pressure equals atmospheric pressure. Water-pressure height at the top of the dripholes equals the height difference  $\Delta h$  between the top of the holes and the base of the air-entry tube. Although calibration showed a linear relation between rainfall intensity and air-entry tube height (De Graaf et al. 1993; fig. 4.3), it appeared that reading the water-level in the rainfall simulator regularly during a simulation provided a more reliable way to calculate rainfall intensity.

In 1990 the simulator was used in its standard form. It could produce rainfall intensities from about 130 mm/hr upward. However, it was expected that actual rainfall intensities in the study area would not exceed 130 mm/hr, so the simulator was modified in 1991. By narrowing the air-entry tube, air entry becomes more difficult and water pressure at the base of the air-entry tube is then less than atmospheric pressure. The modified simulator allowed testing at rainfall intensities down to 30 mm/hr.

With each simulation, average slope gradient, surface type (rill or interrill) and initial wetness of the testplot were noted and rainfall intensity,  $i_r$ , and time-to-ponding,  $t_p$ , were measured. Initial wetness was sometimes measured using cylindrical soil



Figure 4.2 The rainfall simulator: (a) set-up for a simulation; (b) detail of the drop-former plate.

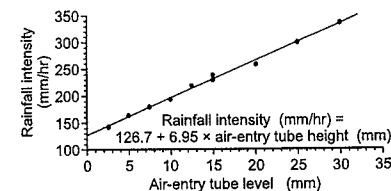


Figure 4.3 Calibration curve for the rainfall simulator.



samples (section 4.3.1), but most of the time it was done subjectively by touch and sight. Rainfall intensity was kept constant during a simulation. A detailed description of the rainfall simulator and its operation is given by De Graaf et al. (1993).

Two different evaluation methods were used. With the *infiltration envelope* or *IE* method infiltration envelopes were constructed by plotting time-to-ponding as a function of rainfall intensity (Imeson and Kwaad 1982; see also section 2.2.2). From figure 2.19 it can be seen that for  $t \rightarrow \infty$  the infiltration capacity will approach  $K$ . In the *constant runoff* or *CR* method the simulation was continued until overland flow discharge from the plot,  $Q_{of}$ , became constant and steady-state infiltration capacity  $K$ -values were calculated from:

$$K = i_r - i_{of} = i_r - \frac{Q_{of}}{A_{rsp}} = i_r - \frac{V_{of}}{A_{rsp} \Delta t} \quad 4.2$$

where:  $i_{of}$  = overland flow intensity [L/T];  $V_{of}$  = collected volume of overland flow from the rainfall simulation plot in time step  $\Delta t$ . This  $K$  is assumed to be equal to  $K$  in Philip's (1957) infiltration equation (eq. 2.79).  $S$  can then be calculated in several ways (see section 6.2.1). The CR method involves more actions in the field, making it more sensitive to operational errors than the IE method, where only time-to-ponding and rainfall intensity have to be measured. Other disadvantages of the CR method are the larger amount of water needed for each test and the larger loss of water by splash. On the other hand, with the CR method  $K$  and  $S$  values are obtained from each test making it possible to obtain  $K$  and  $S$  distributions, whereas with the IE method at least about 10 tests are needed to obtain a single  $K$ - $S$  pair. Thus the CR method seems preferable.

The rainfall simulator has some disadvantages: a small test surface, a small fall distance and a uniform, large raindrop size. The small test surface causes relatively large boundary effects, as the test plot is not confined in a lateral sense. The small fall distance causes raindrops to have less kinetic energy at impact than raindrops falling at final velocity. Besides, the uniform and large raindrops produced do not coincide with drop-size distributions occurring in natural rainfall.

Imeson (1977) improved his simulations by using a rainfall simulator with a larger fall distance to increase impact velocity, and with a wire-netting to get a more realistic drop-size distribution. However, in natural high-intensity rainstorms large raindrops have the major part of the kinetic energy, so the absence of smaller raindrops in our tests may have been of minor importance. Also, for practical reasons the simulator had to be kept as simple and small as possible.

#### 4.4 Rainfall and discharge monitoring

In 1991 a hydrologic monitoring unit was installed in the debris-flow trigger zone TCP at an elevation of 2028 m. It measured rainfall and discharge from a  $\pm 30$  m long gully, which was chosen as the 'key' gully for this study. The monitoring unit is shown in figures 4.4 and 4.5. Rainfall was recorded by two tipping-bucket raingauges. These collect the rain until 0.2 mm of rain has fallen. Then the weight of the water causes the tipping bucket to tip over and give an electric signal to a datalogger counting the number of signals given by each raingauge every minute. The tipping-bucket raingauges were supplemented by a simple handheld raingauge that was read out on every visit to the site.

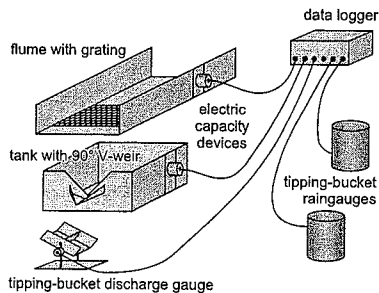


Figure 4.4 The hydrologic monitoring unit equipment in 1991.

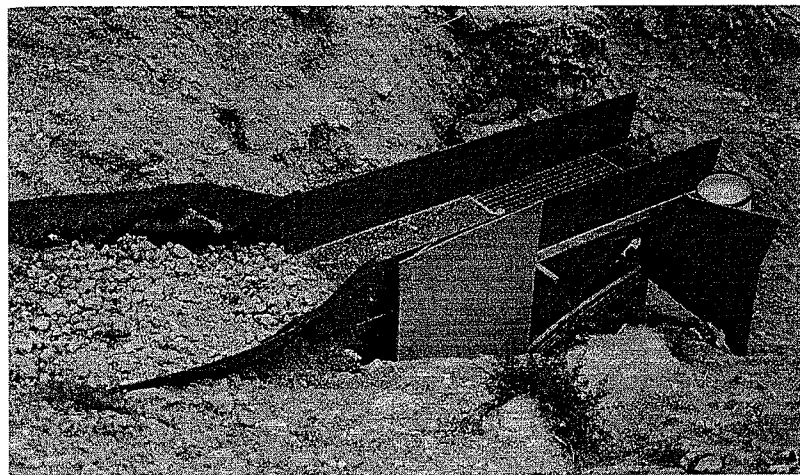


Figure 4.5 Part of the hydrologic monitoring unit in the debris-flow trigger zone TCP in 1991.



Figure 4.6 The discharge flume with the grating and the sediment deposition tank in 1991.

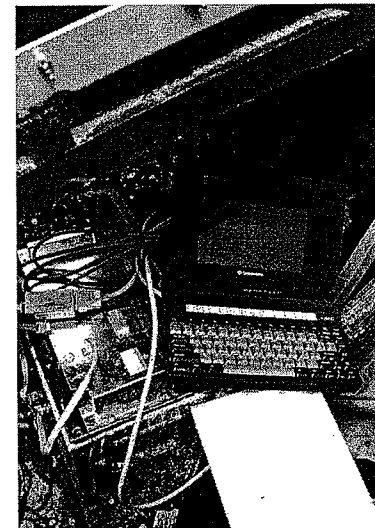


Figure 4.7 The Campbell CR10 data logger.

If overland flow occurred during a rainstorm, it was forced to flow through a flume (fig. 4.6). This flume was 200 cm long, 50 cm wide and 28 cm high, sloping 16°. In the flume a grating was mounted with 2\*2 cm² meshes retaining the coarsest sediment which should leave the flume at the front. Water level in the flume was measured by an electric-capacity device fixed at one side of the flume. Finer-grained sediments and water could fall through the grating into a tank, where most of the finer sediment settled. On one of the sides of the tank the water level in the tank was measured by another electric-capacity device. As water level rose, it could reach the outlet of the tank, a 90° V-shaped weir. The water flowing out of the tank passed through a tipping-bucket discharge gauge, sensitive to 0.5 l. This discharge gauge was designed to give reliable discharge measurements up to about 12 l/min. Higher discharges had to be calculated from an empirical relationship for a 90° V-shaped weir:

$$Q_w = 1.40 z_w^{2.5}$$

4.3

where:  $Q_w$  = water discharge (m³/s);  $z_w$  = depth of water flow above weir outflow base (m). The tipping-bucket raingauges, the electric-capacity devices and the tipping-bucket discharge gauge were connected to a Campbell CR10 datalogger (fig. 4.7). Once either of the two raingauges tipped, the logger started storing rainfall, discharge and electric capacity (water level) until rainfall had ceased for 30 minutes.

It appeared that monitoring unit did not work satisfactory. Once overland flow with a high amount of debris entered the flume, its velocity decreased as a result of the sudden decrease in slope angle from 30° in the gully to 16° in the flume. Coarse debris often settled in the flume, blocking the way for other material reaching the flume. The effect was enhanced by the rough surface of the grating and the removal of water through the grating. Once the flume was filled up with sediment, new material reaching the flume would flow over the edges of the flume and remain unregistered. The electric-capacity device in the flume broke down after a few weeks and could not be repaired. Sediment entering the tank also settled, filling up the tank. In these conditions, the electric-capacity device in the tank measured capillary water in the sediment rather than a water level related to discharge. Therefore most of the registrations from this device were useless. However, qualitative results could be obtained or some events. Once the tank was full, sediment flowed out of the tank and blocked the tipping bucket discharge gauge.

To overcome these problems, the unit was changed in 1992 (figs. 4.8 and 4.9). Both electric-capacity devices were removed. To reduce friction in the flume, the grating with square meshes was replaced by a grating made of bars 2 cm apart pointing in downslope direction. A second sediment-removing wire-netting with 4 mm wide mazes was fixed under the grating, removing even more debris. Water and finer sediment fell into a new tank with a fine maze, where most of the remaining debris was removed. The finest material (fine sand, silt, clay) and water were conducted from this tank to a box.

In this box the discharge was first measured by the tipping bucket gauge and then led through a conventional household water-discharge meter (fig. 4.10). This discharge meter could measure discharges > 12 l/min more reliably than the tipping bucket. A video camera was added to the installation to show the motion of debris through the flume and the reliability of the discharge measurements. The camera was only activated at high rainfall intensities. In 1993 and 1994 the camera was used to record the occurrence of overland flow and debris-flow-like surges in the debris-flow trigger zone TCP.

Although the renewed installation worked better than the 1991 configuration, the grating still

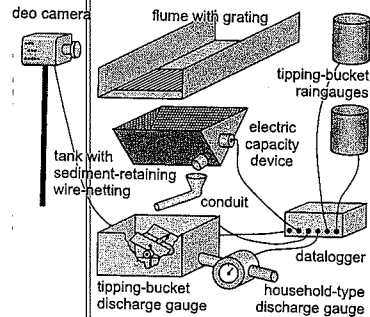


Figure 4.8 The hydrologic monitoring unit equipment in 1992-1994.

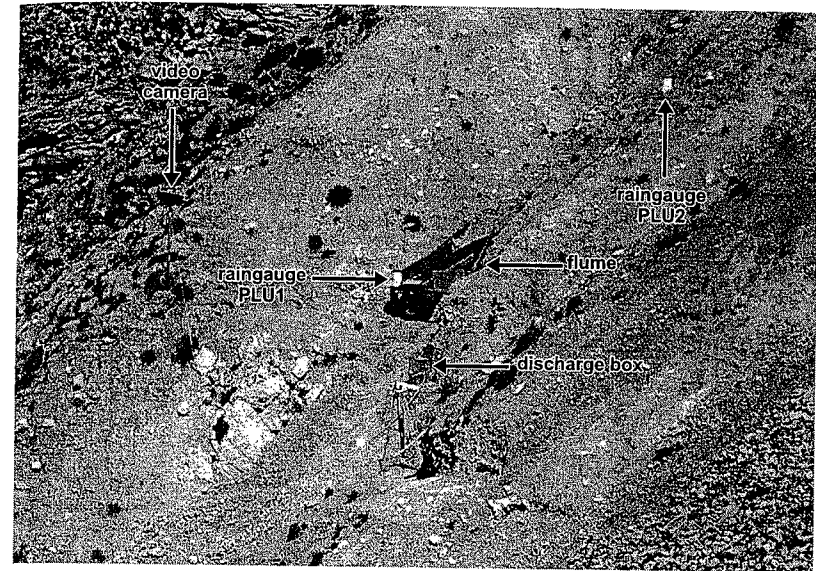


Figure 4.9 The hydrologic monitoring unit in the debris-flow trigger zone TCP in 1992-1994.

became blocked when debris moved in. The video camera recordings clearly showed that once the grating was blocked by debris, additional debris arriving at the flume piled up behind the blockage until finally water and sediment would flow over the edges of the flume.

## 4.5 Preparation of base maps

### 4.5.1 DEM: geodetic survey

In order to run hydrologic simulations of a debris-flow trigger zone, a digital elevation model (DEM) of the area was needed. In 1991 and 1992 the TCP debris-flow trigger zone was accurately surveyed, with the 'key' gully in high detail. This was done with a Wild T2 theodolite sensitive to 0.0001 degree and a Wild Distomat D3 infrared distance meter sensitive to 0.001 m. The accuracy of any measured point is estimated at ±0.05 m in all directions.

Measurement points were as much as possible chosen along characteristic lines like ridges, gullies and rills, making their positions accurately known. Every series of measurement points along one characteristic line was called a 'measurement series'. The slope surface connecting any two adjacent points within a measurement series is straight, so more 'known' points could be generated along these series by linear interpolation. About 300 points were measured and about the same number generated along the characteristic lines by linear interpolation. These irregular-spaced datapoints were interpolated to a regular grid using a kriging-based interpolation technique of the GRID v4.06 module of the SURFER software package. This DEM was converted to PC-Raster (Wesseling et al. 1996) and DINOFLOW formats, and in these programs it was used for hydrologic simulations. Also, the DEM was used to produce contour maps of the debris-flow trigger zones.



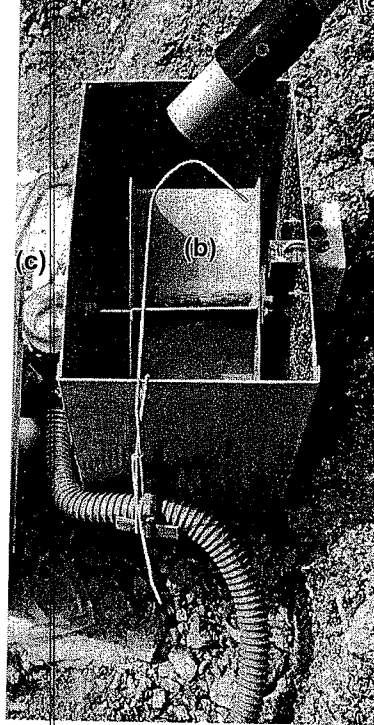


Figure 4.10 The discharge-measurement box with conduit (a) and tipping-bucket (b) and household-type (c) discharge gauges.

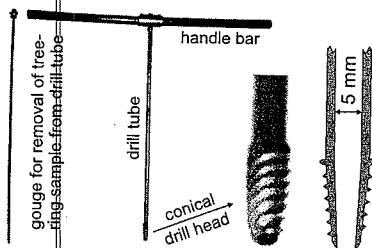


Figure 4.11 The increment borer used for tree-ring sampling.

A topographical base map of the Bachelard Valley was obtained by digitizing the IGN 1:25,000 topographical maps (sheets 3539E Jausiers / Le Sauze, 3539O Barcelonnette / Pra-Loup and 3540-est Entraunes / Col de la Cayolle). A geological base map was derived from the BRGM geological maps 1:50,000 (sheets XXXV-39/895 Barcelonnette and XXXV-40 / 919 Allos) and 1:250,000 (sheet 35 Gap). In 1993, a survey has been carried which resulted in a map with a complete inventory of debris-flow trigger zones in the Bachelard Valley.

#### 4.6 Dating debris-flow deposits

##### 4.6.1 Preparations

Debris-flow deposits originating from five different debris-flow trigger zones have been dated using several methods. The first step for each of the five sites consisted of delineating the deposit zones belonging to each of these trigger zones. Next, individual debris-flow deposits within the deposit zones were identified and mapped, discriminating as much as possible between channels, levees and terminal deposits. A preliminary relative dating of the deposits was performed by investigating their positions relative to each other. Finally, each of the deposits was searched for possible dating material: lichens and affected trees. Some of the deposits lacked both lichens and trees, making dating by these means impossible. For each deposit, several environmental variables that might have influenced the growth of the investigated trees or lichens were investigated as well.

##### 4.6.2 Dendrochronology

Tree-ring samples were usually taken at breast height using a stainless-steel incremental bore (fig. 4.11). After sampling the sampling hole in the tree was sealed with a balm to prevent infections. Data concerning sampling location, tree and samples were recorded on a standard form (appendix A1). The tree-ring samples of 0.5 cm wide and up to 30 cm long were dried to prevent rot. In the laboratory the tree-ring samples were glued to grooved sticks for support (fig. 4.12) and a fresh-cut surface was prepared along the sample using a knife or



Figure 4.12 A tree-ring sample prepared for analysis.

sandpaper. Next the tree-ring widths were measured using a microscope with cross-wire connected to a hand-driven pulse generator which produced 250 pulses per mm (1 pulse every 4  $\mu$ m). After measuring tree-ring widths, multiple samples from each tree were cross-correlated to identify false and missing rings. However, no cross-correlation between trees was executed and therefore it was assumed that no missing rings were present in any of the samples, so that only false rings had to be removed. This was done by visual inspection of the ring-width diagrams and the tree-ring samples. In a sample that would actually have a missing ring, the procedure would thus lead to the erroneous removal of a fictional false ring from the other sample from the same tree.

Different sampling techniques were used for trees which had been subjected to different events. These events include corrosion, partial burying and inclination. Also, trees that were thought to have started growing on top of the deposits after deposition had taken place were sampled (*minimum-age* trees). In trees with corroded bark, two samples have been taken: one sample in the scar tissue, another sample in an undamaged part of the tree.

Partially buried trees, inclined trees and minimum-age trees were usually sampled at breast height (about 1.40 m above the surface) at the downslope side of the tree and in a direction perpendicular to it (Weiss 1988). For some buried trees, a sample has also been taken in the buried part of the stem. By taking samples at breast height (about 1.40 m), the age of a minimum-age tree cannot be derived from the tree-ring sample alone (Alestalo 1971). Clearly, the tree must have grown for some years before reaching a height of 1.40 m. In the study area, 1.40 m high trees appeared to be 6-8 years old, so 7 years were added to the ages indicated by the tree-ring samples of all minimum-age trees or a proportional number of years if sampling had taken place at another height. For the other categories of trees, such corrections were not necessary. Another problem with minimum-age trees occurred. Not all tree-ring samples contained the central, innermost tree rings. Hence a correction was made by estimating the number rings to the center of the tree not present in the sample.

Further analysis of the samples involved simple visual analysis of the tree-ring pattern for the corroded tree and the minimum-age trees. A statistical analysis was necessary for buried and inclined trees. The Split-Moving Window test, described in more detail in chapter 9, was used to analyze the ring-width pattern of buried trees and the ring-width eccentricity pattern of inclined trees.

##### 4.6.3 Lichenometry

Lichenometrical dating of debris-flow deposits was performed using the species *Xanthoria elegans* and *Rhizocarpon geographicum* s.l. Each deposit was searched for the five largest lichens growing on the deposit. Of each of these lichens, the *largest diameter* or *smallest enveloping circle* was measured using a circle-template or a ruler which were read to the nearest 1 mm. The deposits were searched from bottom to top to prevent disturbance of that part that still had to be investigated. Irregular thalli were discarded from the data set if the largest diameter exceeded the smallest diameter (or largest inscribing circle) by more than 50%, a criterion also used by Locke et al. (1979). Lichens growing on exceptionally large stones and on stones within the debris-flow channels were discarded, as it is likely that such stones have been transported by processes other than debris flow. Innes' (1984) criterion was used to check if the largest lichen found on a deposit actually belonged to the lichen population on the deposit (eq. 2.95).

From regular surveys and photographs taken in the years 1991-1995, 'fresh' debris flows have been mapped. Most of the photographs used for this purpose were taken in 1992 and later. The photographs are not complete for all parts of the Bachelard Valley. The term 'fresh' refers to deposits that have originated since the preceding visit to the study area. A combination of investigation of field characteristics of the deposits, comparison of photographs taken at different times, and memory was used to identify fresh deposits. At the TCP site, a video camera supplied additional images of debris-flow triggering within that trigger zone. Field characteristics used were:



Figure 4.13 Debris-flow deposits on top of late-lying snow.

- vegetation cover on the deposits (very recent deposits are not vegetated),
- vegetation buried by the deposits (broken or severely damaged vegetation in a debris-flow track that still looks fresh is probably less than a week old),
- presence of very fine material on stones at the surface (very fine material tends to be washed away from stones at the surface after only a few rainstorms),
- deposits covering or cutting a road (if the past state of that road is also known),
- presence of snow under or on top of deposits (then snow has fallen before respectively after the debris flow took place: fig. 4.13),
- steepness and stability of levee sides and lobe fronts (steep and unstable in fresh deposits; secondary processes lead to stabilization and flattening),
- wetness and packing of the deposits (fresh deposits are very wet and loosely packed; subsequently drainage and compaction),
- presence of stones in the debris-flow channel (recently used debris-flow channels are often swept free of stones; subsequently there is an accumulation of stones falling from the side levees or from other sources),
- colour.

#### Other methods

Several other methods have also been applied or attempted. Erosion in the 'key' gully was measured on a seasonal basis from late summer 1992 until late spring 1995 using three rows of erosion markers perpendicular to the gully (51 markers all together). This was done to get some idea of the annual amount of material removed from the TCP site. Although mass movements and severe gully incision have caused problems with the markers, good and reasonably detailed results were obtained. In summer 1994, t-based erosion was measured from 0.5 m wide and 0.5, 1.0 and 1.5 m long erosion plots installed in debris-flow trigger zones. However, only few rainstorms occurred during the period that the plots were installed and during one of these (26 June), several tanks were completely filled with sediment and other plots were destroyed by falling stones. The results from the erosion measurements are not discussed in this thesis.

Some methods have completely or largely failed. An attempt to inventory and characterize the debris-flow trigger zones, by measuring or estimating parameters describing their topographic, morphologic and hydrologic characteristics, was largely unsuccessful due to the inaccessibility of many debris-flow trigger zones. Among the characteristics checked were trigger-zone dimension, steepness, aspect and shape, number and dimensions of gullies, presence of rills, vegetation cover, rock types, regolith material and debris presence. Attempts to measure the hydraulic conductivity of the coarse debris by means of the salt-dilution method (Benischke and Harum 1990, Gees 1990) with the setup shown in figure 4.14 have also failed. The same box has been used to determine pore-size characteristics of the coarse debris by filling the pores with a hardening foam, but this has also failed. Finally, flume tests for the determination of overland-flow viscosity and density as a function of sediment content has also failed.

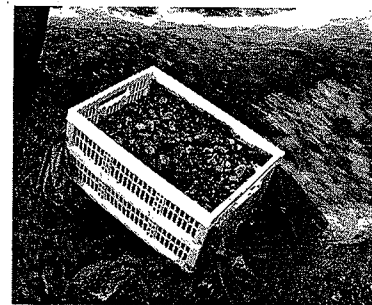


Figure 4.14 Set-up for measurement of the hydraulic conductivity of coarse debris.

## 5.1

## Physical modelling of debris-flow triggering in the Bachelard Valley

The initial quantification of the conditions leading to debris-flow triggering in the Bachelard Valley was based on Takahashi's (1978, 1980, 1981a, 1981b) physical model of debris-flow triggering (eq. 2.22). This model uses the strength parameters effective cohesion  $c'$  and effective static internal-friction angle  $\phi_s'$ ; solid density  $\rho_s$ , solid concentration  $c$ , and surface-slope angle  $\beta$  of the coarse debris and the density  $\rho_f$  of the fluid flowing through the pores of the coarse debris.

In order to quantify the level of fluid flowing through the coarse debris, the conductivity of the coarse debris must be determined. The conductivity depends on the porosity and the pore-size distribution of the coarse debris, as noticed by Bovis and Dagg (1988; eq. 2.23) and on the characteristics of the fluid flowing through the debris. In many debris-flow trigger zones in the Bachelard Valley, Hortonian overland flow is produced during high-intensity rainstorms on slopes covered with fine-grained regolith. Such runoff usually contains a lot of fine-grained sediment (cf. Postma 1988, Hovius 1990), so it will have a high density and viscosity compared to pure water. Sometimes the sediment content is high enough to classify the runoff fluid as a debris flow. The high viscosity slows down the flow through the pores and suppresses turbulence. When the fluid contains stones, these may get stuck in the pores of the coarse debris and block the flow path. Especially the sizes of the pore necks (the narrow connections between adjacent wider spaces, the pores) in the coarse debris will determine whether or not this will occur. Thus both the runoff-fluid characteristics and the pore-size characteristics of the coarse debris should be incorporated in any models of debris-flow triggering in the Bachelard Valley.

## 5.2

## Characteristics of the coarse debris

## 5.2.1 Strength

The strength of the coarse, cohesionless ( $c' = 0$ ) debris in debris-flow trigger zones is determined by its static angle of internal friction  $\phi_s'$ . The test described in section 4.2.2 was used to determine kinetic internal-friction angles (Blijenberg 1995), although the trigger model uses the static internal-friction angle. As explained in section 4.2.2, it was impossible to correctly determine the static internal-friction angles, but the tests were continued with the idea to later try and find a relation between static and kinetic internal-friction angles in the literature. The rock type constituting the debris determined the choice of the five test locations (fig. 5.1). Rock-type compositions tested were sandstone, flysch, limestone and two mixtures, mix1 consisting of sandstone, limestone and some marl, and mix2 consisting of sandstone and limestone. These rock-type compositions are characteristic of debris on scree slopes in the study area.

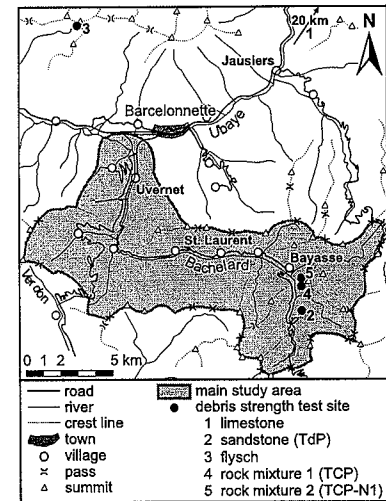


Figure 5.1 Location of debris-strength test sites.

Table 5.1 Kinetic internal-friction angles of five coarse, cohesionless debris types.

Debris type	All data					Outliers rejected									
	N <sup>c</sup>	Average <sup>d</sup> $\sigma$	Min	Max		High-low rejection <sup>a</sup>					Stepwise rejection <sup>b</sup>				
						N <sup>c</sup>	Average <sup>d</sup> $\sigma$	Min	Max		Average <sup>d</sup> $\sigma$	Min	Max		
All data	250	37.5±0.6	2.1	31	43	248	37.5±0.6	2	33	43	37.5±0.6	2	33	43	
Limestone	50	36.0±0.4	1.3	34	40	48	36.0±0.3	1.1	34	38	35.9±0.3	1.1	34	38	
Mixture 1 <sup>e</sup>	50	36.6±0.5	1.8	31	40	48	36.7±0.5	1.6	33	40	36.8±0.5	1.6	34	40	
Sandstone	50	37.7±0.6	2.2	33	43	48	37.7±0.6	2	34	42	37.7±0.6	2	34	42	
Flysch	50	38.3±0.5	1.8	34	42	48	38.4±0.5	1.7	34	42	38.5±0.5	1.6	35	42	
Mixture 2 <sup>f</sup>	50	38.7±0.6	2	36	43	48	38.7±0.5	1.9	36	43	38.5±0.5	1.8	36	42	

All values (average,  $\sigma$ , min, max) are in (°).

Outliers are the highest and the lowest values of the sample.

Outliers are the two values with the largest difference from the sample average, one removed at a time.

Number of samples.

Values given are the average and the 95% confidence interval of the average.

Composed of sandstone, limestone and some marl.

Composed of sandstone and limestone.

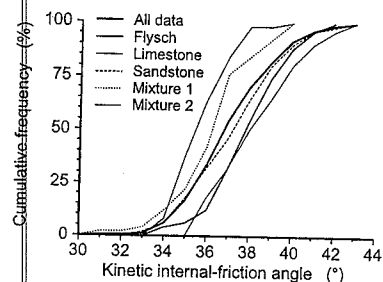


Figure 5.2 Distributions of kinetic internal-friction angles for five debris types.

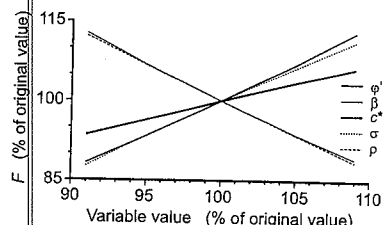


Figure 5.3 Sensitivity of Takahashi's (1978, 1980, 1981a, 1981b) debris-flow triggering model for its component variables.

average was rejected and in the second step this procedure was repeated with the reduced subset to remove a second outlier. It appears that the influence of outliers on average  $\phi_k'$  values is small: with 2 outliers removed, the maximum change is 0.2° (0.5%). Naturally, the removal of outliers has more

Measured kinetic internal-friction angles  $\phi_k'$  range from 31–43° for 250 individual tests. The  $\phi_k'$ -distributions of the overall data set and five different location subsets are shown in figure 5.2. Average  $\phi_k'$  values for each of the five subsets are given in table 5.1. The average  $\phi_k'$  values range from 36.0° for limestone to 38.7° for a mixture of limestone and sandstone. Standard deviations are about 2°, but smaller for limestone. The width of the range of measured values is the result of both natural variation and measurement errors. The last doesn't seem to be very large: measurement errors are estimated to be generally less than 2°. A Kolmogorov-Smirnov test showed that each of the five location data sets has a normal  $\phi_k'$ -distribution at a 95% confidence level.

Even small differences in internal-friction angle have a marked influence on the potential triggering of debris flows, as shown in the sensitivity analysis of Takahashi's (1978, 1980, 1981a, 1981b) debris-flow triggering model (fig. 5.3). Therefore the influence of outliers in the data on the  $\phi_k'$ -distributions was examined by rejecting two outliers from each data subset (table 5.1). In the high-low-rejection method outliers were defined as the highest and lowest values in the subset. The stepwise-rejection method consisted of a two-step procedure of rejecting the outliers. In the first step the  $\phi_k'$  value with the largest difference from the

Table 5.2 Significance of differences<sup>a</sup> in average kinetic internal-friction angles for five debris types.

Debris type	Mixture 2	Flysch	Sandstone	Mixture 1
Limestone	0.000 <sup>b</sup>	0	0	0.061
Mixture 1	0	0	0.009	
Sandstone	0.018	0.106		
Flysch	0.352			

<sup>a</sup> Values indicate the probability that samples belong to the same population.

<sup>b</sup> Bold value indicates significant difference between sample averages at the 95% confidence level.

influence on the standard deviation, which then decreases by 0.09–0.24° (5–13%). Our primary interest is on average  $\phi_k'$  values, and as the influence of the outliers on these values is small, the complete data subsets have been used for further analysis.

The range of average  $\phi_k'$  values in this study is in accordance with results obtained by others. Martins (1991) reported static internal-friction angles  $\phi_s' = 38–41°$  for angular fragments of crushed rock of 30–80 mm. Kinetic angles of internal friction can then be expected to be somewhat smaller, perhaps 0–3° (Martins 1991). The average clast size in his experiments is well comparable to the one in this study (50–95 mm), but the size range in this study is wider: 5 to 200 mm. Charles (1991) mentioned results from Gallacher (1972, 1988), who has performed field tests on unconsolidated gravel at Megget Dam in Scotland yielding  $\phi_s' = 37.5°$ . Kenney (1984) reported  $\phi_k'$  values of 37° for well-graded, crushed, angular sandstone and slate with average grain sizes of about 5–40 mm and Statham (1977) found kinetic internal-friction angles of 38–42° for angular gravel and talus, slightly higher than in this study. For loosely-packed, well-sorted, 38–53 mm pebbles, Kjellman and Jakobson (1955, in Farouki and Winterkorn 1964) have determined a static internal-friction angle  $\phi_s' = 37.1°$ . If, as suggested by the term 'pebbles', this concerns smooth, rounded clasts,  $\phi_s'$  may be expected to be higher for angular, rough-surfaced material.

Average  $\phi_k'$  values from the data subsets were compared using difference-of-means tests. Table 5.2 shows that in most cases the differences in average  $\phi_k'$  values between the data sets are statistically significant at the 95% confidence level. This seems to suggest a relation between the rock-type composition of the debris and  $\phi_k'$ . However, the large difference in  $\phi_k'$  between the two mixtures, mix 1 and mix 2, urges for caution. Of course, the large difference in  $\phi_k'$  between the two rock-mixture subsets might actually be related to the presence of a small (5–10%) marl fraction in mix 1. On the other hand, factors such as clast size, size sorting, clast shape or clast roughness, which themselves may be influenced by rock-type, could equally well be the cause of the difference. Therefore, average  $\phi_k'$  values were compared to several other debris-characterizing parameters describing clast size, shape and sorting (tables 5.3 and 5.4). Table 5.5 shows that the clast-size sorting parameters have high, positive correlations with  $\phi_k'$  (table 5.5). The sorting parameter used here is the coefficient of variation (= standard deviation / average) which gives low values for well-sorted materials (narrow grain-size range) and high values for poorly-sorted materials (wide grain-size range). From these sorting parameters, the one based on clast volume,  $cv_v$ , has the best correlation with  $\phi_k'$  (71% explained variance, significant at the 95% confidence level):

$$\phi_k' = 34.50 + 0.993 cv_v$$

5.1

This agrees with Lambe and Whitman (1969), Statham (1977) and Hansen and Lundgren (1960), who also mentioned higher (static ?) internal-friction angles with wider grain-size distributions. The sorting parameters  $cv_v$  and  $cv_s$  can also explain the  $\phi_k'$ -variation well, but the small number of subsets prevents statistical significance of their correlations with  $\phi_k'$  at the 95% confidence level.

Average clast-size parameters do not have statistically significant relations with  $\phi_k'$ . This absence of a relation may be caused by the small range of clast sizes in this study (average b-axis length

Table 5.3 Definition of debris parameters.

Parameter type	Parameter	Description
<b>Average</b>		
Clast size	$m_a$	clast long-axis length: $a$ (mm)
	$m_b$	clast intermediate-axis length: $b$ (mm)
	$m_c$	clast short-axis length: $c$ (mm)
	$m_V$	clast volume: $V = a \cdot b \cdot c$ (cm <sup>3</sup> )
Clast shape		dimensionless clast-size ratios based on:
	$m_{b/a}$	intermediate to long clast-axis length: $b/a$
	$m_{c/a}$	short to long clast-axis length: $c/a$
	$m_{c/b}$	short to intermediate clast-axis length: $c/b$
	$m_{V/V_c}$	Volumetric coefficient (Joisel 1948, Lee et al. 1983): ratio of volumes of ellipsoid with axes $a, b, c$ to volume of sphere with axes $a: V/V_c = b \cdot c/a^2$
<b>Sorting (coefficient of variation)</b>		
Clast size		variation in stone sizes based on:
	$CV_a$	clast long-axis length
	$CV_b$	clast intermediate-axis length
	$CV_c$	clast short-axis length
	$CV_V$	clast volume
Clast shape		variation in stone shapes based on:
	$CV_{b/a}$	$b/a$ ratio
	$CV_{c/a}$	$c/a$ ratio
	$CV_{c/b}$	$c/b$ ratio
	$CV_{V/V_c}$	$V/V_c$ ratio

Table 5.4 Debris-parameter values for five debris types.

Debris type	Average								Sorting							
	Clast size				Clast shape				Clast size				Clast shape			
	$m_a$	$m_b$	$m_c$	$m_V$	$m_{b/a}$	$m_{c/a}$	$m_{c/b}$	$m_{V/V_c}$	$CV_a$	$CV_b$	$CV_c$	$CV_V$	$CV_{b/a}$	$CV_{c/a}$	$CV_{c/b}$	$CV_{V/V_c}$
Limestone	51	33	20	71	0.66	0.39	0.61	0.26	0.57	0.6	0.66	2	0.24	0.31	0.3	0.46
Mixture 1	79	51	29	30	0.67	0.38	0.57	0.26	0.78	0.7	0.81	3	0.23	0.38	0.36	0.51
Sandstone	70	42	27	19	0.62	0.4	0.66	0.26	0.66	0.63	0.61	3	0.22	0.25	0.24	0.39
Flysch	95	50	21	34	0.56	0.25	0.45	0.15	0.86	0.78	0.84	3	0.3	0.51	0.48	0.68
Mixture 2	65	42	28	35	0.67	0.45	0.68	0.31	0.84	0.8	0.84	5	0.2	0.3	0.27	0.42

Table 5.5 Correlations between kinetic internal-friction angle and debris parameters.

	Average								Sorting							
	Clast size				Clast shape				Clast size				Clast shape			
	$m_a$	$m_b$	$m_c$	$m_V$	$m_{b/a}$	$m_{c/a}$	$m_{c/b}$	$m_{V/V_c}$	$CV_a$	$CV_b$	$CV_c$	$CV_V$	$CV_{b/a}$	$CV_{c/a}$	$CV_{c/b}$	$CV_{V/V_c}$
Regression $r^a$	0.92	0.68	0.44	1.36	0.8	0.17	0	0.24	1.87	2.28	0.87	2.73 <sup>b</sup>	0.1	0.27	0.19	0.25
Relation <sup>c</sup>	+	+	+	-	-	-	-	-	+	+	+	++	-	-	-	-
1 variable <sup>d</sup>	22	13	6	38	18	1	0	2	54	63	20	71	0	2	1	2
2 variables <sup>e</sup>	83	73	78	71	99	88	81	91	74	74	0	-	87	79	81	82

<sup>a</sup> Regression with 1 independent variable. Critical  $t = 2.35$ : 1-tailed test, 3 degrees of freedom, 95% confidence level

<sup>b</sup> Regression with 1 independent variable. **Bold** value is significant.

<sup>c</sup> -, + and ++ indicate respectively weak negative, weak positive and strong (significant) positive relations with  $\phi_k'$ .

<sup>d</sup> Variation in  $\phi_k'$  explained by variable (%).

<sup>e</sup> Variation in  $\phi_k'$  explained by 2 variables of which one is  $CV_V$  (%).

33–50 mm), but still seems to agree with results from others, who have found either no relation at all (Bishop 1948), or a slightly positive (Martins 1991) or negative relation (Lambe and Whitman 1969, Kenney 1984). A literature survey and theoretical considerations led Farouki and Winterkorn (1964) and Statham (1977) to the conclusion that internal-friction angles should be independent of average grain size. It seems reasonable to assume that this applies to both  $\phi_k'$  and  $\phi_k''$ , which would make it acceptable to apply the  $\phi_k'$  values from this study to coarser debris as well.

At first glance clast shape and clast-shape sorting seem to have little influence on  $\phi_k'$ . However, clast shape, especially with  $m_{b/a}$ , correlates well with  $\phi_k'$  in a multiple regression with  $CV_V$  as the second independent variable. Together,  $CV_V$  and  $m_{b/a}$  explain more than 99% of the  $\phi_k'$ -variation (statistically significant even at the 99% confidence level):

$$\phi_k' = 42.81 + 1.062 CV_V - 13.4 m_{b/a} \quad 5.2$$

The effect of clast shape found here is difficult to compare with results from other researchers, who have generally used shape factors based on clast angularity or clast-surface roughness. These factors are based on relatively small irregularities on the clast surface. Positive relations are mentioned for these shape factors (Hansen and Lundgren 1960, Kézdi 1974, Statham 1977, Kenney 1984, Martins 1991). Kenney (1984) reported that grain angularity influences  $\phi_k'$  more than grain-size sorting. All tests in this study have been performed on equally rough, angular material; only the limestone may have been a bit less rough. In contrast, this study uses an *overall clast shape* factor based on clast axis ratios (fig. 5.4) and giving the same values for example for spheres and cubes.

## 5.2.2 Density, porosity and hydraulic conductivity

The density of the coarse debris depends on its rock-type composition and porosity. Sandstone and flysch have solid densities  $\rho_s = 2.4\text{--}2.7 \cdot 10^3 \text{ kg}\cdot\text{m}^{-3}$ , limestone is slightly less dense with  $\rho_s = 2.2\text{--}2.5 \cdot 10^3 \text{ kg}\cdot\text{m}^{-3}$ . Porosity determinations (table 5.6) did not yield unexpected results. Average

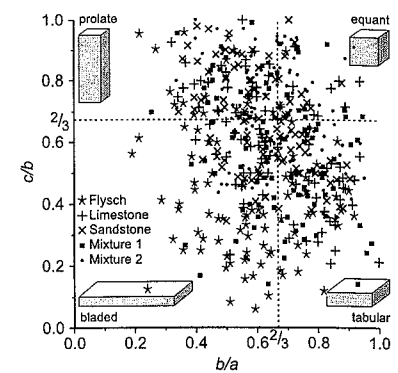


Figure 5.4 Clast shapes based on clast-axis ratios for five debris types.

Table 5.6 Porosity of coarse debris.

Debris parameter	Subset	N <sup>a</sup>	Porosity				Difference-of-means test (95% confidence level)		
			Average	$\sigma$	Min	Max	Tested samples	Different	1 / 2 tailed test
Packing	All samples	110	0.45	0.05	0.33	0.59			
	Dense	47	0.43	0.04	0.33	0.50	Dense - Loose	Yes	1
	Loose	57	0.48	0.04	0.40	0.59			
Average grain size	10–25 mm	36	0.44	0.05	0.33	0.50	Fine - Coarse	No	2
	30–50 mm	74	0.46	0.05	0.34	0.59			
Grain-size sorting	Good	58	0.48	0.04	0.41	0.59	Good - Quite poor	Yes	1
	Quite poor	10	0.44	0.01	0.43	0.46	Quite poor - Poor	Yes	1
	Poor	37	0.42	0.04	0.34	0.50	Poor - Very poor	Yes	1
	Very poor	5	0.37	0.04	0.33	0.43			

<sup>a</sup> Number of samples.

porosity is 0.45. The porosity is independent of the average stone size, but shows a strong relation with packing and stone-size sorting. For densely-packed samples, porosity is 5% less than for loosely packed ones. Stone-size sorting was determined visually in the field and divided into the following 4 classes with increasingly wide stone-size distributions: *good*, *quite poor*, *poor* and *very poor*. From *good* to *very poor*, each of the sorting categories has a significantly lower porosity than its predecessor, with an 11% difference in porosity between the two extreme categories. Field observations revealed that the coarse debris in trigger zones usually falls into one of the categories *good*, *quite poor* or *poor*. Figure 4.14 shows the setup which was used to measure the hydraulic conductivity by means of the salt-dilution method, as a function of porosity and grain-size distribution of the debris. Two problems were encountered. First, the measurement of the pore geometry using hardening foam was problematic. It was impossible to define exactly what formed pores (the 'wider spaces' between stones) and what formed a pore necks (the 'narrow connections' between adjacent pores). Also, the flow of water through the coarse debris is probably turbulent. However, with regard to debris-flow triggering in the Bachelard Valley, the fluid flowing through the coarse debris is not pure water but sediment-rich runoff with a high viscosity. Under such conditions, the flow may well be laminar. Also, stones in the runoff fluid can block the pores of the coarse debris, effectively decreasing its conductivity. Because of these problems, the hydraulic-conductivity measurements were abandoned.

### 5.3 Characteristics of the fine-grained regolith material

Most of the determinations concerning the fine-grained regolith material have been done in the Tête du Clot des Pastres debris-flow trigger zone, where the regolith has developed in marls. The solid density is  $2.51 \pm 0.55 \cdot 10^3 \text{ m}^3$  and the dry bulk density,  $\rho_{dry}$ , is  $1.65 \pm 0.31 \cdot 10^3 \text{ m}^3$ . Grain-size distributions from the TCP and PBN trigger zones are shown in figure 5.5 for the fraction  $\leq 2000 \mu\text{m}$ . At TCP and PBN, the regolith has developed in the same parent material, so it is not surprising that the samples from both trigger zones are well comparable. The regolith material is mainly composed of sand-sized (35-80%) or coarser (20-65%; small stones of up to several cm) material. The very low amount of clay and silt (0.1-1.2% fraction  $\leq 53 \mu\text{m}$ ) is surprising, because a small but significant amount of clay (and silt) is usually thought to play a crucial role in the mobility of debris flows (Innes 1983a, Pierson 1981; section 2.1.2). Here the non-standard grain-size analysis procedure (section 4.3.2) may have played a role: lime bonds between individual particles have not been destroyed, so many small particles may have been coagulated into aggregates. The particle-size distribution thus resembles an aggregate-size distribution rather than a grain-size distribution. On the other hand, Innes (1982a) has also recorded clay contents as low as 0.01%.

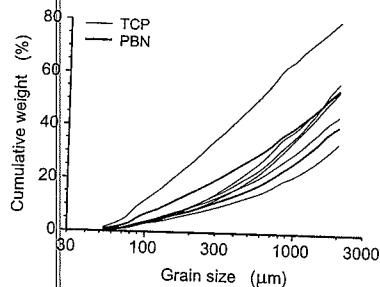


Figure 5.5 Grain-size distributions of fine-grained regolith material in the debris-flow trigger zones TCP and PBN.

Table 5.7 presents the porosities and field water contents of fine-grained regolith material. The samples have been taken in the TCP and CdM (Combal du Menon; location see fig. 6.1) debris-flow trigger zones. Average porosities for samples from TCP are about 29% on a volume basis. The 1991 samples taken in dry material have about 8% higher porosities than samples from 1991 and 1992 taken in wet material. This might be caused by sampling disturbance. During sampling, wet material is likely to be somewhat compacted. On the contrary, dry and crusted material is likely to break up during sampling which may result in an increased porosity of the sample compared to the

Table 5.7 Porosity and field water content of fine-grained regolith material.

Location	Subset	Porosity				Field water content					
		N <sup>a</sup>	Average	σ	Min	Max	N <sup>a</sup>	Average	σ	Min	Max
TCP	All samples	151	0.289	0.067	0.166	0.76	148	0.083	0.046	0.01	0.44
	1991	41	0.342	0.055	0.173	0.45	40	0.083	0.037	0.01	0.17
	1992	110	0.269	0.06	0.166	0.76	111	0.084	0.051	0.01	0.44
	1991 dry surface	38	0.347	0.054	0.173	0.45	37	0.077	0.03	0.01	0.17
	1991 wet surface	3	0.248	0.018	0.269	0.3	3	0.161	0.01	0.154	0.17
	1992 dry period	31	0.271	0.035	0.22	0.35	31	0.052	0.03	0.01	0.11
	1992 wet period	79	0.269	0.068	0.166	0.76	80	0.097	0.052	0.041	0.44
CdM		12	0.335	0.038	0.281	0.41	12	0.06	0.016	0.039	0.1

<sup>a</sup> Number of samples.

undisturbed parent material. As far as field water contents are concerned, the table confirms that these are higher in wet situations than in dry situations. Although the water contents of samples immediately taken after rainfall simulations are higher (16%) than those of the other samples taken on wet surfaces (10%), they are still far from saturation (25-35%). The 7-8% higher porosities of the 1991 dry surface samples compared to the 1992 dry period samples might be explained by surface conditions: the 1991 samples were all taken in a hard, crusted surface, but in 1992 the dry period samples were taken only a few days after a period of prolonged rainfall in a surface that had not yet been desiccated. However, if this explanation were valid, the 1991 samples could be expected to have lower measured field water contents than the 1992 samples. As table 5.7 shows the opposite to be true, it must be concluded that there is no satisfactory explanation for the differences in both porosity and field water content between the 1991 dry surface and the 1992 dry period samples.

In addition to porosity and field water content, pF-curves were determined for several samples taken in the wet period of 1992 from TCP and CdM (fig. 5.6). The average water content of the TCP samples at  $pF \approx 0$  (0.249) agrees well with the porosities from the 1992 samples and the 1991 wet-surface samples. The initial water contents of the 1992 samples taken from wet surfaces (0.097) agree with field capacity of the regolith ( $pF = 2-2.5$ ). The difference between the pF-curves from TCP and CdM is due to the different parent materials from which the regoliths have developed: marls at TCP and flysch at CdM. Comparison of the samples taken immediately after rainfall simulations with the pF-curve shows that such samples are at  $pF \approx 1.4$  ( $\approx 25 \text{ cm}$  matric suction). This indicates that only a thin layer at the surface is saturated when runoff occurs during rainfall simulations. It must be remembered that the cylindrical samples used for sampling are 5 cm long.

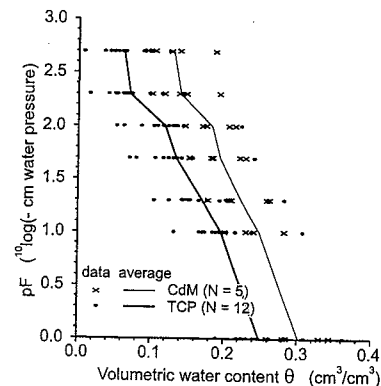


Figure 5.6 pF-curves of fine-grained regolith material in the debris-flow trigger zones TCP and CdM.

## 5.4.1 Effect of input-parameter uncertainties in quantitative physical modelling of debris-flow triggering

When the results obtained in the previous sections are compared with the triggering model of equation 2.22, two observations can be made. First, the parameters that could be measured all have a distribution around their respective averages due to natural variations and measurement errors. Second, some parameters could not be determined, such as the fluid density  $\rho_f$  and the static internal-friction angle  $\phi_s'$ . No clear relation between  $\phi_s'$  and  $\phi_k'$  has been found in literature. This makes it difficult to use the measured  $\phi_k'$  values in the debris-flow triggering models, although Martins (1991) reports  $\phi_k'$  values to be 0.3° less than  $\phi_s'$ . These differences are as large as the total variation in  $\phi_k'$  values caused by debris composition found in this study. Besides, it is not known whether the difference between  $\phi_s'$  and  $\phi_k'$  is also related to the parameters in table 5.3. A preliminary, rough estimate of  $\phi_s'$  values would be about 40–42°.

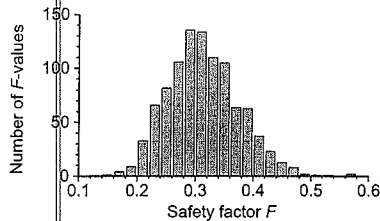


Figure 5.7 Distribution of  $F$ -values from Takahashi's (1978, 1980, 1981a, 1981b) debris-flow triggering model.

standard deviation of 0.06. Although the slope angle used here is smaller than slope angles in debris-flow trigger zones in the Bachelard Valley, this has no effect on the relative range of  $F$ -values.

Besides the variation in  $F$ -values resulting from uncertainties in the input values of the triggering model, other uncertainties arise from the lack of knowledge of the fluid flow through the pores of the coarse debris. Such uncertainties arise from the strong effect of water content on the viscosity of the interstitial fluid in fluids with high sediment concentration, as found by Bentley (1979) and Chen (1986) (see section 2.1.2). The viscosity can easily vary by an order of magnitude for only a few percent change in water content. Also, the size of the pore necks of the coarse debris has a strong effect on the hydraulic conductivity. Suppose the pore (necks) can be represented as small tubes in the debris mass. The flow velocity through a tube is proportional to the square of its radius  $r_d$  and can be derived from equation 2.38 for  $\tau_0=0$  and using  $\eta_N$  instead of  $\eta_b$ . According to Poiseuille's Law, the discharge through a tube is proportional to the 4<sup>th</sup> power of the tube radius:

$$Q_{tube} = \int_{r=0}^{r_d} u dA = \int_{r=0}^{r_d} \frac{\rho_f g}{4\eta_N} \frac{-dH}{ds} (r_d^2 - r^2) \pi r dr = \frac{\pi r_d^4}{8\eta_N} \quad 5.3$$

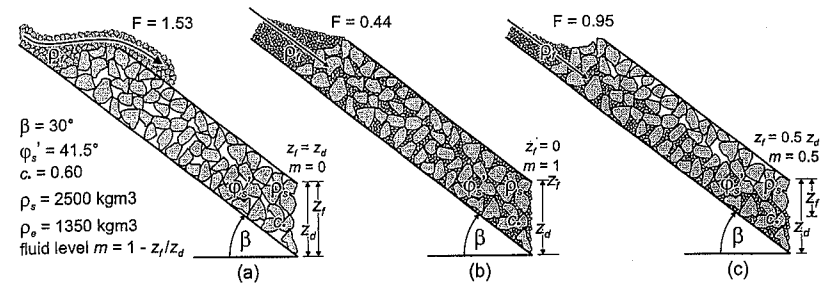


Figure 5.8 Three typical situations if a rock-fluid mixture reaches an accumulation of coarse debris.

For two debris masses 1 and 2 differing in average grain size ( $d_1$  and  $d_2$ ), but with identical coefficients of variation of grain size ( $cv$ ) and porosities  $\theta_s$ , the ratio of average grain sizes  $d_1/d_2$  will also be the ratio of the average pore sizes. The ratio of the number of pores per unit area increases inversely proportional to the square of the average pore size, so the ratio of the number of pores of the two debris masses will be  $d_2^2/d_1^2$ . Now the ratio of the hydraulic conductivities can also be determined. With the hydraulic conductivity expressed as the number of pores per unit area  $\times$  conductivity of a pore, the hydraulic conductivities will have the ratio  $(d_2^2/d_1^2) \cdot (d_1^4/d_2^4) = d_1^2/d_2^2$ . So the hydraulic conductivity of the coarse debris varies with the square of the pore (neck) sizes of the debris. The probability that stones in the runoff fluid may block the pores of the coarse debris also depends strongly on the pore-neck sizes.

In figure 5.8 three situations are depicted when runoff from the fine-grained regolith in a debris-flow trigger zone reaches the coarse-debris accumulation on the channel floor. From left to right the viscosity decreases. For each of these situations, the value of the stability factor  $F$  is calculated from equation 2.11 using  $\beta = 30^\circ$ ,  $\phi_s' = 41.5^\circ$ ,  $c = 0.60$ ,  $\rho_s = 2500 \text{ kg m}^{-3}$  and  $\rho_f = 1350 \text{ kg m}^{-3}$ . The leftmost situation represents the immediate and complete blocking of the pores by stones from a highly-viscous runoff. The debris mass remains completely unsaturated and the runoff will mainly flow over the surface of the coarse debris (fig. 5.8a). This results in  $F = 1.53$  (stable). The middle situation occurs at a medium viscosity and a lower stone content. Now the fluid flows through the pores of the coarse debris, completely saturating it (fig. 5.8b) giving  $F = 0.44$  (failure!). Finally, the rightmost situation is for a low-viscosity fluid flowing through the coarse debris, saturating only the lower half of the debris (fig. 5.8c) and resulting in  $F = 0.95$  (failure imminent). It can be seen that the  $F$ -values from these situations vary by a factor 3.5. In situation b failure would occur, in situation a all is stable. For situation b, Takahashi's triggering model (1978, 1980, 1981a, 1981b; eq. 2.22) with  $\kappa = 1$  yields even less stable conditions:  $F = 0.32$ .

## 5.4.2 Consequences for modelling debris-flow triggering

From figures 5.7 and 5.8 it must be concluded that the use of a quantitative, physical model for debris-flow triggering only makes sense if the factors playing a role in the triggering can be quantified accurately. Considering the available data and, moreover, the missing data, further use of such a model in this study seems absurd. After abandoning the quantitative, physical approach, the question remains whether or not another approach can still be followed. The most promising direction seems to be an empirical approach using rainfall and runoff data on the one hand and actual, recorded occurrences of debris flows. The combination of these data should result in the determination of threshold values of rainfall (such as duration or intensity) and discharge with regard to the triggering of debris flows.

## 6.1

## Introduction

In the previous chapter it was concluded, that a quantitative, fully-physical modelling of debris-flow triggering was impossible. A more promising, indirect approach was chosen based on available data in order to find the critical amounts of rainfall and discharge triggering debris flows. Discharges can be calculated by performing simulations with a hydrologic model (chapter 7). The hydrologic model divides water inputs at the surface (rainfall, runoff) into infiltrating and non-infiltrating portions. In order to perform this division, the infiltration process must be described, preferably by a simple function (see section 2.2.1, eqs. 2.77-2.79 and 2.81). In this study, the Philip infiltration function was used (eq. 2.79), which uses 2 parameters to describe the infiltration process: the steady state infiltration capacity  $K$  and the sorptivity  $S$ . These parameters were determined by means of rainfall simulations (see section 4.3.4; also Blijenberg et al. 1996).

Altogether 351 rainfall simulations have been carried out in at six locations (fig. 6.1): Tête du Clot des Pastres (further called TCP: 252 simulations), Pra Bouréou North (PBN: 10 simulations), Pra Bouréou South (PBS: 36), Les Longs (LL: 6), Bayasse/Bachelard (BB: 14) and Combal du Menon (CdM: 33). The rainfall simulations at TCP and PBN were carried out in regolith developed from calcareous sandy-silty marls; at LL the simulations tests were performed in slope deposits consisting of sandstone, limestone and flysch debris and at CdM in slope debris originating from flysch. BB is located in the highly erodible Terres Noires marls; it is not a debris-flow trigger zone, but its material characteristics are representative for debris-flow trigger zones developed in Terres Noires. The simulations were carried out in 1990, 1991 and 1992 on test plots with slope angles of 27-54°. Rainfall intensities in the simulations varied from 28-291 mm/hr. After a simulation, the wetting front had usually penetrated less than 10 cm deep into the regolith, and the saturated zone never extended deeper than a few cm.

During the rainfall simulations, some of the processes occurring in debris-flow trigger zones during rainfall have been observed (see section 3.3). The initially dry regolith surface is usually irregular, showing a more or less pronounced micro-relief formed by small lumps and fissures. After a dry period, the desiccated top layer of the regolith often forms a crust cemented by lime. When rainfall starts, the crust softens very quickly, usually within seconds. Raindrops falling on the surface cause splash, which transports material downslope. The splashed water and sediment often disappears from the testplot, causing a net loss of water (estimated up to 30% water loss). After some time ponding occurs. The steep slopes offer little opportunity for surface storage, so overland flow starts quickly. The overland flow immediately concentrates in micro-rills of only a few millimetres wide and deep.

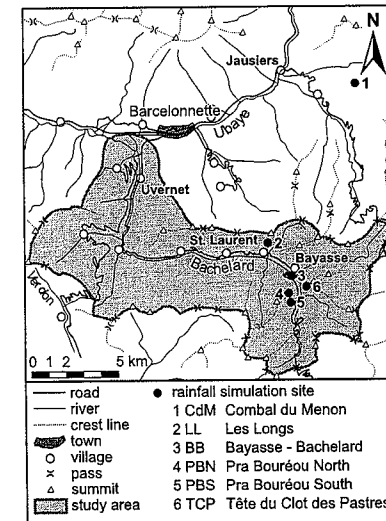


Figure 6.1 Location of rainfall simulation sites.



## 1 Constant-runoff (CR) tests

constant-runoff or CR method was used in 154 rainfall simulations at TCP, PBN, LL and CdM. The angles of test plots ranged from 27-52°, and rainfall intensities were 55-230 mm/hr.  $K$ -values range from 7-128 mm/hr and are log-normally distributed (fig. 6.2). Average  $K$ -values from the log-transformed  $K$ -distributions are presented in table 6.1 for homogeneous subsets based on location, test-plot, lithology or other criteria. Homogeneous subsets were mutually tested for differences in log-average  $K$ -values with a difference-of-means test (Student's  $t$ -test). Table 6.2 presents the significance levels for differences in log-average  $K$ -values between different locations and between different years. Bold values indicate significant differences at a 95% confidence level (probability  $p \leq 0.05$ ).

as assumed that the different parent materials in table 6.1 would have produced different regoliths and that these would show different infiltration characteristics. Table 6.2 shows that this is the case, with the highest  $K$ -values in the sandstone-limestone-flysch material at LL (88 mm/hr) the lowest values in the flysch debris at CdM (35 mm/hr). The regolith developed in calcareous ls at TCP is intermediate between those two with 43 mm/hr. Values from the TCP-site in 1990 show a significant difference from those of 1991 and 1992 (table 6.2). This is probably caused by the high rainfall intensities used in the 1990 simulations, as  $K$ -values

6.1 Steady-state infiltration capacities (mm/hr) obtained from rainfall simulations.

subset ion	Lithology	Other criteria	Test method		Infiltration Envelope	
			Constant Runoff			
			$N^a$	$K^b$	$N^a$	$K^b$
-PBS+TCP			154	42		
		1990	16	68		
		1991	17	42		
		1992	126	40		
	Terres Noires marls	series 8			14	40.2
	flysch		30	35	30	47.9
	sandstone, flysch, limestone		3	88	5	131
	calcareous marls		121	43	267	52.4
			2	53	10	127.1
					36	51.7
		series 5			12	67.9
		series 6			12	57.4
		series 7			12	42.5
	(calcareous marls)		119	43	221	55.9
		1990	6	66	30	- <sup>c</sup>
		1991	17	42	82	53
		1992	96	42	109	71.2
		1990+1991	23	47	112	45.7
		1991+1992	113	42	191	52.3
		series 1			14	29.9
		series 2			11	45.7
		series 3			14	45.9
		series 4			14	9.8
		test plot		3	42	

ber of samples.

n/hr.

id, negative value obtained.

appear to be influenced by rainfall intensity  $i_r$  (fig. 6.3). The average rainfall intensity used in 1990 was 144 mm/hr, whereas in 1991 and 1992 it was about 105 mm/hr. The testplot data from figure 6.3 were obtained by testing one plot with three different rainfall intensities. It shows a clear linear increase of  $K$  with  $i_r$ , which could have several causes:

1 The runoff intensity ( $i_{of}$ , expressed as a depth-per-time, equivalent to rainfall intensity) increases with rainfall intensity, causing a greater depth of the water film at the surface and an increased hydraulic head between the surface and the wetting front. For example, if the hydraulic head at the wetting front is -100 cm, an increase of the water-film depth at the surface from 1 to 2 mm results in a 0.1% higher hydraulic gradient between the surface and the wetting front. Therefore, the effect is virtually negligible.

2 However, a greater depth of the water layer at the surface must also result in a greater depth of the saturated zone in the regolith immediately below the surface. When the depth of the saturated zone increases, more (macro)pores are filled with water and  $K$  increases. This means that  $K$  is not a constant, but a function of rainfall intensity. This effect is probably much stronger than the effect mentioned in the preceding point.

3 A part of the overland flow was not captured due to the imperfect contact of the collection funnel and the regolith surface, causing a loss of runoff water that was not measured. This means that measured  $K$ -values are overestimated. It seems likely that this overland flow loss will increase with increasing overland flow intensity, and thus with increasing rainfall intensity.

4 Splash loss is a significant factor in the apparent relation between  $K$  and  $i_r$ . Under natural rainfall the net loss by splash is zero, but due to the small size of the test plots a fraction of the rainfall splashes outside the plot in simulations. If each raindrop causes a constant fraction,  $a$ , to splash outside the testplot, the splash loss intensity,  $i_s$  (also expressed as a depth-per-time, equivalent to rainfall intensity), increases linearly with rainfall intensity. Corrected  $K$ -values,  $K'$ , can then be calculated from:

$$K' = (i_r - i_s) - i_{of} = (i_r - i_{of}) - i_s = K - ai_r \quad 6.1$$

Table 6.2

Significance levels for differences in log-average  $K$ -values ( $K$ -values from the constant-runoff method).

Data subset	$N^a$				
A: year (TCP)	1990-1991	1992	1991	1990	
1990+1991	23	0.294	0.318	0.397	0.11
1990	6	<b>0.016<sup>b</sup></b>	<b>0.019</b>	<b>0.029</b>	
1991	17	0.906	0.892		
1992	96	0.969			
1990-1992	119				
B: lithology	CdM		LL		
TCP	119	<b>0.01</b>	0		
LL	3	0			
CdM	30				

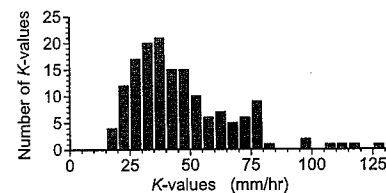
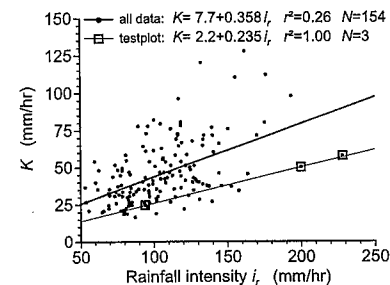
<sup>a</sup> Number of samples.<sup>b</sup> Bold value indicates significant difference between sample averages at the 95% confidence level.Figure 6.2 Distribution of  $K$ -values from the constant-runoff method.Figure 6.3 Relation between  $K$  and rainfall intensity.

Table 6.3 Sorptivities (cm/ $\sqrt{\text{min}}$ ) obtained from rainfall simulations using different calculation methods.

Data subset	Location	Lithology	Other criteria	Test method				Infiltration envelope		
				CR						
				Direct	$t_p - F_{SEP}$ plot		$\sqrt{t_p} - \sqrt{F_{SEP}}$ plot		Philip	Smith & Parlange
					All data	Outliers rejected	All data	Outliers rejected		
All data				0.194	0.183	0.169	0.181	0.176		
-			1990	0.224	0.21	0.21	0.213	0.213		
-			1991	0.206	0.2	0.162	0.195	0.171		
-			1992	0.19	0.174	0.17	0.177	0.175		
BB		Terres Noires marls	series 8							
CdM		flysch		0.226	0.207	0.207	0.215	0.215	0.25	0.32
LL		sandstone, flysch, limestone		0.327					0.17	0.21
TCP+PBN		calcareous marls		0.183	0.178	0.159	0.173	0.165	0.15	0.22
PBN				0.189						
PBS										
-			series 5						0.2	0.27
-			series 6						0.2	0.31
-			series 7						0.21	0.28
TCP		(calcareous marls)							0.2	0.25
			1990	0.183	0.178	0.16	0.173	0.165	0.14	0.2
			1991	0.196	0.204	0.204	0.201	0.201		
			1992	0.206	0.2	0.162	0.195	0.171	0.15	0.21
			1990+1991	0.179	0.162	0.158	0.166	0.163	0.14	0.2
			1991+1992	0.203	0.2	0.164	0.195	0.174	0.17	0.23
			series 1	0.183	0.178	0.159	0.172	0.164	0.16	0.21
			series 2						0.17	0.23
			series 3						0.2	0.28
			series 4						0.17	0.24
									0.18	0.23

Assuming that splash loss is the dominant factor determining the relation between  $K$  and  $i_r$ , equation 6.1 can be used to assess the amount of splash loss and to correct measured rainfall intensities and  $K$ -values. For the testplot data in figure 6.3,  $a$  is nearly 25% and the correction decreases the log-average  $K$ -value from 41.5 mm/hr (at  $i_r = 167$  mm/hr) to  $K' = 2.2$  mm/hr (at  $i_r = 0$  mm/hr). In some cases, this correction of individual  $K$ -values resulted in negative  $K$ -values. Thus splash cannot be the only factor involved in the  $K$ - $i_r$  relation. Also, the assumption that splash loss increases linearly with rainfall intensity may be wrong.

As the quantitative effect of each of these factors involved is unknown, the  $K$ -values have not been corrected for the effect of rainfall intensity.

Table 6.3 presents the results of the sorptivity determinations. In the *direct* method, sorptivities were calculated for each CR test using the Smith and Parlange (1978) equation (eq. 2.86).  $S$  varies from 0.19 to 0.33 cm/ $\sqrt{\text{min}}$ . Sorptivities have normal distributions, as can be seen in figure 6.4 for TCP and CdM. Average sorptivities for different parent materials show significant differences. The  $S$ -values at flysch (0.23 cm/ $\sqrt{\text{min}}$ ) are the highest; 0.33 cm/ $\sqrt{\text{min}}$ . Average sorptivities at CdM (0.21 cm/ $\sqrt{\text{min}}$ ) are significantly higher than sorptivities at TCP (calcareous marls; 0.18 cm/ $\sqrt{\text{min}}$ ), as can be seen in table 6.4. No differences were found between measurements from different years.

Two other methods based on Smith and Parlange (1978) were also used to calculate average sorptivities for the CR method. Assuming a constant rainfall intensity, equation 2.86 can be written as:

$$t_p = S^2 F_{S\&P} \quad 6.2$$

or

$$\sqrt{t_p} = S \sqrt{F_{S\&P}} \quad 6.3$$

with:

$$F_{S\&P} = \frac{\ln\left(\frac{i_r}{i_r - K}\right)}{2i_r K} \quad 6.4$$

where:  $F_{S\&P}$  = Smith and Parlange factor in  $[\text{T}^2\text{L}^{-2}]$ ;  $t_p$  is time-to-ponding. When  $t_p$  is plotted as a function of  $F_{S\&P}$ , the average sorptivity is the square root of the tangent of the regression line of the data set (fig. 6.5). For  $\sqrt{t_p}$  plotted against  $\sqrt{F_{S\&P}}$ , average sorptivity is the tangent of the regression line (fig. 6.6). Both methods produce very similar  $S$ -values but give on average 4-5% smaller  $S$ -values (-10% to +4%) than the *direct* method (table 6.3). Outliers have little effect on average  $S$ -values from the CR *direct* method. Data from CdM show no outliers, and rejection of the three outliers at the TCP site will decrease the average  $S$ -value with only 3% from 0.183 cm/ $\sqrt{\text{min}}$  to 0.178 cm/ $\sqrt{\text{min}}$ .

+	1991	$t_p = 0.0398 F_{S\&P}$	$r^2 = 0.65$	$N = 15$
+	1992	$t_p = 0.0264 F_{S\&P}$	$r^2 = 0.61$	$N = 83$
+	outliers rejected:			
+	1991	$t_p = 0.0263 F_{S\&P}$	$r^2 = 0.84$	$N = 13$
+	1992	$t_p = 0.0249 F_{S\&P}$	$r^2 = 0.70$	$N = 82$
+	outliers			

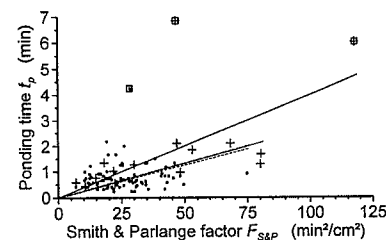


Figure 6.5 Sorptivity determined from time-to-ponding versus Smith and Parlange factor plot.

Table 6.4 Significance levels for differences in average  $S$ -values ( $S$ -values from the constant-runoff 'direct' method).

Data subset	$N^a$				
A: lithology		CdM	LL		
TCP	103	0.001 <sup>b</sup>	0		
LL	2	0.002			
CdM	27				
B: year (TCP)		1990-1992	1992	1991	1990
1990+1991	20	0.172	0.094	0.908	0.8
1990	5	0.645	0.519	0.76	
1991	15	0.178	0.104		
1992	83	0.58			
C: year		1992		1991	
All data	134	0.6		0.487	
1990	9	0.107		0.554	
1991	15	0.336			
1992	110				

<sup>a</sup> Number of samples.

<sup>b</sup> Bold value indicates significant difference between sample averages at the 95% confidence level.

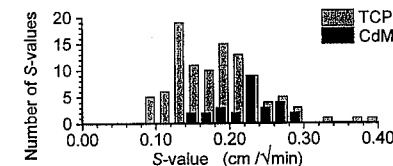


Figure 6.4 Distribution of  $S$ -values from the constant-runoff 'direct' method (TCP and CdM).

+	1991	$\sqrt{t_p} = 0.195 \sqrt{F_{S\&P}}$	$r^2 = 0.90$	$N = 15$
+	1992	$\sqrt{t_p} = 0.166 \sqrt{F_{S\&P}}$	$r^2 = 0.90$	$N = 83$
+	outliers rejected:			
+	1991	$\sqrt{t_p} = 0.171 \sqrt{F_{S\&P}}$	$r^2 = 0.95$	$N = 13$
+	1992	$\sqrt{t_p} = 0.163 \sqrt{F_{S\&P}}$	$r^2 = 0.91$	$N = 82$
+	outliers			

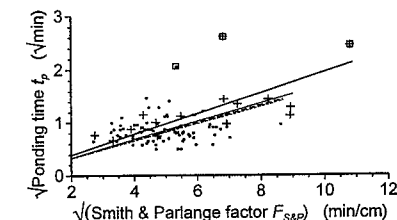


Figure 6.6 Sorptivity determined from square root of time-to-ponding versus square root of Smith and Parlange factor plot.

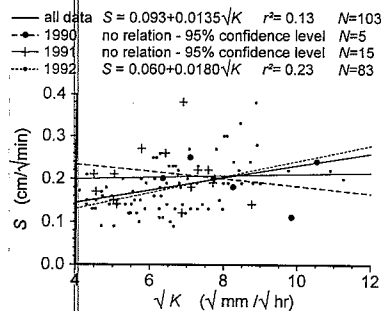


Figure 6.7 Relation between  $K$  and  $S$  (TCP).

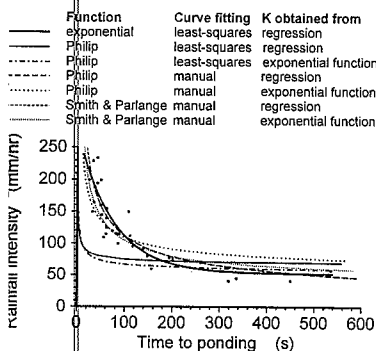


Figure 6.8 Comparison of infiltration-envelope functions and curve-fitting methods (PBS).

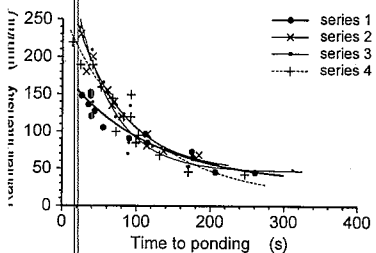


Figure 6.9 Infiltration envelopes for series of plots with uniform characteristics (TCP).

(range -6% to 0%). The  $\sqrt{t_p} - \sqrt{F_{SEP}}$  method (fig. 6.6) is slightly more sensitive to a rejection of outliers with an average decrease of 4% (-12% to 0%). The  $t_p - F_{SEP}$  method (fig. 6.5) reacts even more strongly with an average decrease of 8% (-19% to 0%). According to Green and Ampt (1911), sorptivity is linearly related to the square root of the steady state infiltration capacity (eq. 2.66). Figure 6.7 shows the relation between  $K$  and  $S$  for TCP. The relation is weak (all data, 1992 data) or not significant at a 95% confidence level (1990 data, 1991 data). For the overall TCP data set, only 13% of the variation in  $S$  is explained by  $K$ . If  $S$  is plotted against the square root of  $K$ , the significance and the explained variation of the relations are nearly the same.

## 6.2.2 Infiltration-envelope (IE) tests

316 infiltration-envelope or IE tests were performed at TCP, PBN, PBS, LL, BB and CdM. Slope angles of testplots ranged from 27-54° and rainfall intensities from 28-291 mm/hr. Figure 6.8 shows that it was not possible to use least-squares fitting for the Philip (1957) and Smith and Parlange (1978) equations (eqs. 2.84 and 2.86). These equations cannot be written in the form  $i_r = f(t_p)$ , only in the form  $t_p = f(i_r)$ , so a least-squares regression minimizes the sum-of-squares of the  $t_p$ -deviations from the infiltration envelope rather than the sum-of-squares of  $i_r$ -deviations. Manual fitting of these functions usually resulted in a good fit only for near-zero or negative values of  $K$ . A negative-exponential function appeared to fit the data better:

$$i_r = K + e^{a_1 + a_2 t_p} \quad 6.5$$

The negative-exponential function is the only function that produces realistic  $K$ -values with least-squares fitting. As the physical meaning of the constants  $a$  and  $b$  in this function is not clear, this function is only used to obtain  $K$ -values (table 6.1). This function explains as much as 87-96% of the variation in  $i_r$  for datasets from testplots with similar characteristics (slope angle, regolith type, initial soil wetness, surface type), as shown in figure 6.9, where a 'series' refers to a group of

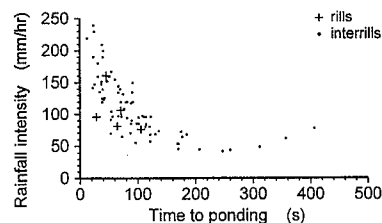


Figure 6.10 Time-to-ponding as a function of rainfall intensity on rills and interrill areas (TCP 1991).

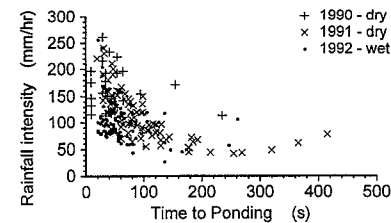


Figure 6.11 Time-to-ponding as a function of rainfall intensity and initial soil moisture (TCP).

rainfall simulations on mutually similar plots. The explained variation decreases for less uniform datasets. For data grouped by test location (regolith type) the explained variation is 23-92%. Here the high values of explained variation, 82% at PBS and 92% at BB, are again for datasets from testplots which are also similar in other characteristics.  $K$ -values from the IE method shows the same pattern as for the CR method: LL (sandstone-limestone-flysch) has the highest value (131 mm/hr), CdM (flysch) the lowest (48 mm/hr) and TCP (calcareous marls) is intermediate (56 mm/hr). To calculate sorptivities, the  $K$ -values obtained from the negative-exponential function were used in the Smith and Parlange (1978) and Philip (1957) infiltration-envelope functions. Table 6.3 presents the results. The Philip (1957) function gives on average nearly 30% lower values than the Smith and Parlange (1978) function. For manually-fitted curves, the Smith and Parlange (1978) function seems to fit the data slightly better than the Philip (1957) function (fig. 6.8). When different lithologies are compared, TCP and CdM do not differ much in their sorptivities, but the sorptivity at BB (Terres Noires marls) is much higher (table 6.3). Figure 6.10 shows that rills and interrill areas seem to have the same time-to-ponding at comparable rainfall intensities, and therefore they seem to have the same sorptivities. However, hard conclusions cannot be drawn, because rills never occupied more than 30-50% of a rainfall simulation plot. Figure 6.11 shows that time-to-ponding is generally shorter on moist or wet surfaces than on dry surfaces as a result of a smaller sorptivity on wet surfaces (cf. eq. 2.66). In this figure the 1992 data are from a wet period and the 1990 and 1991 data from a dry period.

## 6.2.3 Comparison of the constant-runoff and infiltration-envelope tests

Table 6.1 shows that the CR method gives on average 22% lower  $K$ -values than the IE method (excluding the LL and PBN data because of the small number of tests at these sites). However, a direct comparison poses some difficulties. When fitting an infiltration envelope, the datapoints with large time-to-ponding have far more influence on the value of  $K$  than the datapoints at smaller time-to-ponding. This results from the importance of  $K$  relative to  $S$  in the infiltration-envelope functions, which increases with increasing time-to-ponding. As mentioned before, the CR method probably overestimates  $K$ -values. It then follows that the IE method overestimates  $K$ -values even more. Where sorptivities are concerned, the IE Smith and Parlange method gives the highest values. They are on average 10% higher than values from the CR direct method. The IE Philip method gives the lowest values, on average 21% lower than from the CR direct method. The three CR methods give well-comparable results.

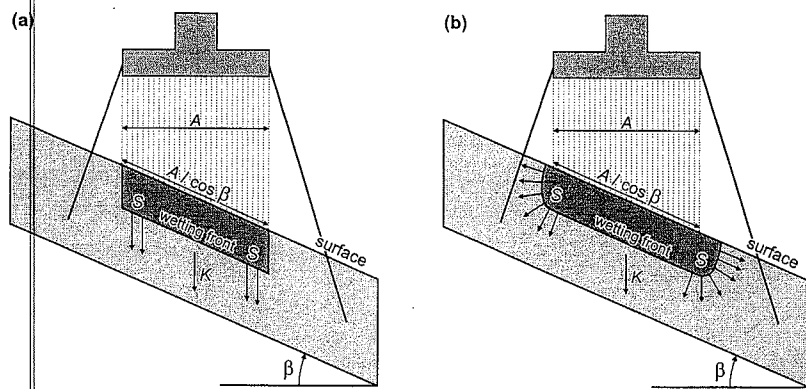


Figure 6.12 Infiltration during a rainfall simulation: (a) the 'ideal' situation with laterally-confined infiltration; (b) the actual field situation with laterally-unconfined infiltration.

### 6.3 Boundary effects during rainfall simulations

The plots that are tested during rainfall simulations are not clearly defined in a lateral sense. In the calculations a confined situation is assumed where only vertical flow occurs in a soil column below the testplot surface as a result of gravity and matric forces: the *ideal* situation shown figure 6.12a. In reality the situation is unconfined and matric forces will also cause lateral flow from this column (fig. 6.12b). As water is removed from the column, the wetting front will move downward slower than in the ideal situation, so  $t_p$  will increase compared to the ideal situation. Horizontal flow from the column also implies that at any moment the infiltration rate at the surface is larger than for the ideal situation. Thus for  $t \rightarrow \infty$  the apparent infiltration capacity is also larger than for the ideal situation and therefore the measured value of  $K$  overestimates the actual value. At small  $t$ , the horizontal flow from the soil column implies that the apparent, measured  $S$ -values also exceed the actual values. One approach to correct for such boundary effects is to quantify the lateral flow of water from the regolith column. Such quantitative relations between measured and the actual values of  $t_p$ ,  $K$  and  $S$  have not been found, so no corrections could be made. In the next chapter, their actual values are estimated from a calibration of runoff models on measured discharges in the TCP debris-flow trigger zone.

### 6.4 Occurrence of micro-scale mass movements during rainfall simulations

At high rainfall intensities, a remarkable phenomenon sometimes occurred. Within the first few minutes after the start of ponding, the top layer of the regolith failed and a micro-scale mass movement was triggered with dimensions of up to 10 cm long and wide and a few centimetres deep. This usually occurred on a local steepening of the microrelief. During downslope movement the slide disintegrated and might transform into a micro-scale debris flow which could move well outside the testplot. Figure 6.13 shows such a micro-scale debris flow. These mass movements only occurred on steep slopes at high rainfall intensities, when overland flow was present. On the other hand, no

more mass movements occurred during the later phases of a simulation, when the surface became smoothed by runoff and splash. It therefore seems likely that, besides the overall slope angle and the rainfall intensity, the surface microrelief plays an important role in the occurrence of these micro-scale mass movements. An attempt was made to define the threshold conditions for their occurrence as a function of both slope angle and rainfall intensity. Figure 6.14 seems to suggest a minimum slope angle of about  $34-36^\circ$  at very high rainfall intensities, and a minimum rainfall intensity (not corrected for splash loss) of about 60-70 mm/hr at slope angles of  $55^\circ$  or more. This minimum rainfall intensity must exceed the steady-state infiltration capacity, as the occurrence of runoff also seems to be an important factor involved in the occurrence of the micro-scale mass movements. The threshold function in figure 6.14 is given by:

$$\beta_{min} = 32 + \frac{600}{i_{r,min} - 47} \quad 6.6$$

where:  $\beta_{min}$  = minimum slope angle ( $^\circ$ );  $i_{r,min}$  = minimum rainfall intensity (mm/hr). The threshold function is valid for  $i_r$  between 60-70 and 200-250 mm/hr. Bearing in mind that splash loss does not occur during normal rainfall, and that the splash loss during the rainfall simulations may be in the order of 25% of the imposed rainfall intensity (see section 6.2.1, fig. 6.3), the actual minimum rainfall intensity for the occurrence of these micro-scale debris flows could be about 75% of the uncorrected rainfall intensity used in equation 6.6. This implies that micro-scale debris flows might be triggered on slopes of at least  $39-44^\circ$  for actual rainfall intensities of 70-100 mm/hr. Eye-witness accounts state that debris flows in the Bachelard Valley usually occur within 5-10 minutes after the start of high-intensity (50-100 mm/hr) rainfall (Hovius 1990, Van Asch and Van Steijn 1991), so the occurrence of these micro-scale mass movements seems to be an important link between the occurrence of overland flow and the actual triggering of debris flows. The link is probably established through the deliverance of high amounts of sediment to the overland flow, which causes an increase in density, viscosity and flow depth of the overland flow, resulting in a higher capacity to mobilize coarse material such as stones.

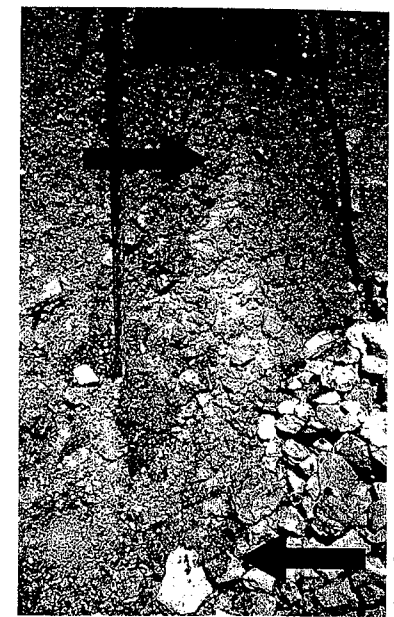


Figure 6.13 Micro-scale debris flow during a rainfall simulation. Arrows indicate the upper and lower ends of the flow; total length of the flow is about 1 m.

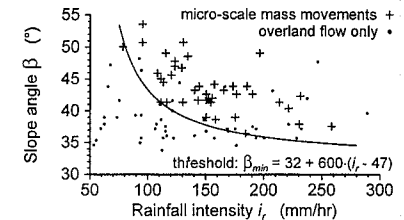


Figure 6.14 Threshold conditions for the occurrence of micro-scale mass movements during rainfall simulations.

In spite of the disadvantages of the rainfall simulations, the method seems to offer good possibilities for use in difficult terrain circumstances. The main advantages are testing on undisturbed material and the relatively quick testing procedure. The main disadvantages are the boundary effects in the soil, water loss by splash, the small fall distance and the large, uniform raindrops. The CR and IE methods both have their advantages and disadvantages. In spite of the larger operational efforts and measurement errors the CR method seems preferable. K and S values are easily calculated and for each CR test a K and an S value are obtained, making it possible to construct K and S distributions from multiple CR tests. For the TCP debris-flow trigger zone, K-values from the CR method were generally in the order of 20-80 mm/hr, and S-values were generally 0.12-0.28 cm/vmin. For the IE method, K-values were generally 40-55 mm/hr and S-values 0.15-0.17 cm/vmin (Philip function) or 0.20-0.24 cm/vmin (Smith and Parlange function). Both methods overestimate the actual values of K and S. Taking into consideration this overestimation, which probably exceeds the (estimated) 25% overestimation of rainfall intensity, Hortonian overland flow is indeed likely to occur during high-intensity rainfall of 50-100 mm/hr which is believed to trigger debris flows in the Bachelard Valley. The occurrence of micro-scale mass movements on steep slopes at high rainfall intensities (at least 39-44° at rainfall intensities of 70-100 mm/hr) could be a key factor in debris-flow triggering. These micro-scale mass movements are likely to deliver high amounts of relatively fine sediment to the overland flow. Such sediment-rich overland flow has different hydraulic properties from pure water and has a higher capacity to mobilize coarse material.

## 7.1 Introduction

For the Bachelard Valley, eye-witness accounts state that most debris flows occur within 10-15 minutes after the start of high-intensity rainfall (Hovius 1990, Van Asch and Van Steijn 1991), so rainfall intensity and probably Hortonian overland flow (see section 6.5) seem to be key factors in the triggering of debris flows. Therefore the empirical quantification of debris-flow triggering conditions must be based on the comparison of recorded debris flows on the one hand and on rainfall or discharge characteristics on the other hand. In this chapter, the models that were used to calculate rainfall and discharge characteristics will be presented. Figure 7.1 shows the general characteristics in terms of input and output of these models. The models based on rainfall data only are described in section 7.3 and the discharge models based on both rainfall and infiltration characteristics, are described in section 7.4. In the next chapter, these models will be used to quantify debris-flow triggering thresholds.

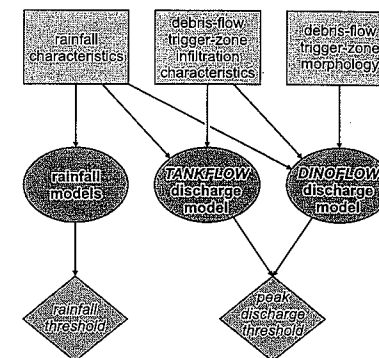


Figure 7.1 General overview of the rainfall and discharge models in this chapter.

## 7.2 Input data for the models

The input data necessary for such models were only available for the TCP debris-flow trigger zone. For this site detailed rainfall and discharge records and debris-flow occurrence dates for four consecutive summers (1991-1994) were available, as well as data on regolith characteristics. For the rainfall models, described in section 7.3, only rainfall data are needed. The discharge models (see section 7.4) use data on rainfall and regolith characteristics to calculate infiltration and discharge; these models can be calibrated by comparing calculated discharges with measured ones.

The rainfall records were obtained from discrete tipping-bucket raingauges which registered every 0.2 mm of rainfall. As the first recorded tip of a bucket in any minute may have been caused by rainfall which had mostly fallen in the preceding minute, the maximum error in the value recorded rainfall for any minute is 0.2 mm. This means that rainfall totals also have an uncertainty of 0.2 mm. Besides the error introduced by the moment of the tip, the rainfall records for the two different raingauges also show differences. The 1991 rainfall records for instance show that non-systematic differences between the two raingauges were often 5-10% and could be as high as 20%, even though the raingauges were less than 10 m apart (see fig. 7.2). In 1992, 1993 and 1994 only one of the raingauges functioned reliably. For most of the 1991 rainstorms, data from both raingauges were averaged, as neither of the two raingauges showed any obvious malfunction.

A major problem was the lack of rainstorms with reliable discharge records. Inspection of the discharge records, video camera recordings and field observations have all shown that on many occasions discharge had occurred, but it was hardly, or not at all, recorded. This could be caused by an internal malfunction of the equipment, as happened in 1993. A more frequent cause was the obstruction of the

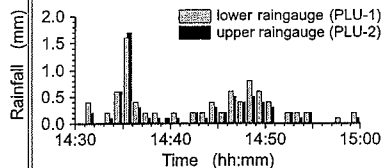


Figure 7.2 Differences in rainfall recorded by two raingauges at the TCP site.

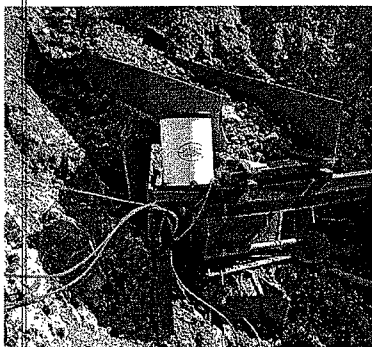


Figure 7.3 Obstruction of the discharge flume with sediment.

$$\theta_s = 0.313 + 0.060\varepsilon \quad 7.2$$

$$\theta_f = 0.007 + 0.187\theta_s + 0.017\varepsilon \quad 7.3$$

where:  $\varepsilon$  = a random term with the standard normal distribution (average = 0, standard deviation = 1).

Regolith depth (normal) distributions were obtained from 100 measurements in gullies and larger rills and from over 200 measurements on interrill areas. The  $K$ -distribution (log-normal) was obtained from the constant-runoff method and the  $S$ -distribution (normal) from the 'constant-runoff direct' method (see section 6.2.1). The  $S$ -distribution also takes the weak relation between  $S$  and  $K$  into account. For the interrills the data distributions are given by:

$$K = 10^{1.559 + 0.194\varepsilon} = 36.2 \times 1.563^\varepsilon \quad 7.4$$

$$S = 0.1018 + 0.001864K + 0.05118\varepsilon \quad 7.5$$

$$z_{reg} = 0.423 + 0.283\varepsilon \quad 7.6$$

and for the rills by:

$$K = 10^{1.658 + 0.070\varepsilon} = 45.5 \times 1.175^\varepsilon \quad 7.7$$

$$S = 0.1302 + 0.001004K + 0.05050\varepsilon \quad 7.8$$

$$z_{reg} = 0.250 + 0.139\varepsilon \quad 7.9$$

discharge flume with sediment, as shown in figure 7.3. This made most of the 1994 measurements and a large part of the 1991 and 1992 measurements useless. All events with high discharges have caused obstruction of the flume, and the flume could only be cleaned during the field campaigns. Thus only a few events which had occurred before the flume was obstructed and which had low or moderate discharges, less than 20-30 l/min, were reasonably reliable. These occurred in June and July 1991 and in June and July 1992.

The discharge models also need regolith and surface characteristics. These are the infiltration parameters  $K$  (steady-state infiltration capacity) and  $S$  (sorptivity; see chapter 6) and the regolith storage capacity, expressed as an equivalent depth, which was calculated from:

$$STO = z_{reg}(\theta_s - \theta_f) \quad 7.1$$

where:  $STO$  = regolith storage capacity in (m);  $z_{reg}$  = regolith depth in (m);  $\theta_s$  = porosity and  $\theta_f$  = field water content, both dimensionless. For porosity and field water content the (normal) distributions are based on TCP data for dry conditions (the subsets '1991 dry surface' and '1992 dry period' in table 5.7,  $N = 67$ ). The  $\theta_f$ -distribution also takes into account the very weak relation between  $\theta_s$  and  $\theta_f$  for this data set. However the data did not allow to make a distinction between interrills and rills:

with:  $K$  in (mm/hr),  $S$  in (cm/vmin) and  $z_{reg}$  in (m). Finally, the TCP catchment was mapped from a geodetic survey. Figure 7.4 shows the contour map of the monitored catchment with the position of the equipment. From this map the surface area was derived: total area  $A_{total} = 213 \text{ m}^2$ , rill area  $A_r = 13 \text{ m}^2$  and interrill area  $A_{ir} = 200 \text{ m}^2$ . Also the pattern of gullies and larger rills was mapped.

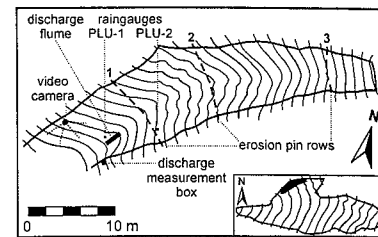


Figure 7.4 Map of the monitored gully in the debris-flow trigger zone TCP.

### 7.3 The rainfall models

The rainfall models are based on rainfall data only. The following parameters could be derived for each rainstorm recorded at TCP: total rainstorm precipitation  $I_{r,rs}$ , rainstorm duration  $t_{rs}$ , maximum rainstorm rainfall intensity over an  $x$ -minute interval  $i_{r,x}$  ( $x = 1, 2, 3, 5, 10, 15, 30, 60, 120$  and 1440 minutes) and rainstorm antecedent precipitation index  $API$ . Also, total daily precipitation  $I_{r,day}$  was calculated. The  $API$  was calculated using the discrete form of the general antecedent precipitation index function (eq. 2.9):

$$API_t = \sum_{N=0}^{\infty} i_{r,t-N\Delta t} \Delta t e^{-\alpha N\Delta t} \quad 7.10$$

where:  $API_t$  =  $API$  at time  $t$  in (mm);  $N$  = counter;  $i_{r,t-N\Delta t}$  = amount of rain fallen during time step  $t-N\Delta t$  in (mm);  $\Delta t$  = time step length in (days), in this study  $\Delta t = 1 \text{ minute} = 1/1440 \text{ day}$ ;  $\alpha$  = decrease coefficient in (days<sup>-1</sup>);  $e^{-\alpha N\Delta t}$  = weighting factor for rain fallen  $N\Delta t$  days before time  $t$  ( $\leq 1$ ; dimensionless).

With these parameters, several models were made. The simplest models use only one parameter: this is either an  $x$ -minute rainfall intensity, a total rainfall amount or the rainfall history. The other models use two, three or four parameters. One of these uses total rainstorm precipitation and rainstorm duration, which will enable to make a comparison with equations 2.4 and 2.5, the threshold curves for debris-flow triggering based on Caine (1980) and by Innes (1983a). The other multiple parameter models use a maximum rainfall intensity parameter  $i_{r,x}$  and one or more of the parameters  $t_{rs}$ ,  $I_{r,rs}$  and  $API$ ; one of these uses  $i_{r,x}$  and  $t_{rs}$ , which will therefore enable a comparison with Caine's (1980) original debris-flow threshold curve (eq. 2.3).

Some remarks can be made on the uncertainties in the rainfall models. All rainfall totals, rainfall intensities and rainfall histories have uncertainties of about 10%, resulting from the uncertainty in the rainfall records. The effect of the discrete, 0.2 mm tips of the tipping-bucket raingauges causes an uncertainty in the rainfall totals of 0.2 mm. With rainfall intensities, it causes an extra uncertainty which can amount to  $\pm 12 \text{ mm/hr}$  for the 1-minute maximum rainfall intensity (fig. 7.5).

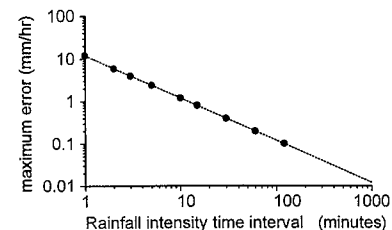


Figure 7.5 Maximum error in calculated rainfall intensities caused by discrete, 0.2 mm resolution tipping-bucket rain gauge registrations.

## 7.4.1 General description of the discharge models

The models that were used to simulate discharges are single-event models, appropriate for modelling discharges for short-duration rainstorms lasting a few hours or less. Each of the discharge models treats either the whole catchment or a part of the catchment as a tank with several compartments for storing water (fig. 7.6). It was expected that for short-duration events subsurface flow would contribute very little to the discharge, especially to peak discharge, so subsurface flow is not taken into account. Also, the rocks beneath the regolith are assumed to be impervious, so no deep percolation can occur. Infiltration into the regolith is based on Philip's (1957) equation (eq. 2.78). In the calculations, every time step one of three situations may occur:

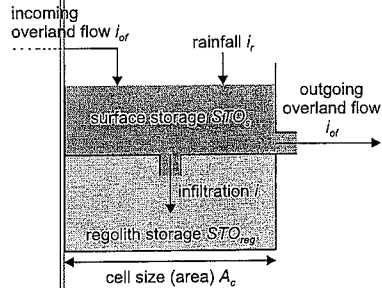


Figure 7.6 Basic structure of the discharge models.

If the situation is not supply-limited, a certain amount of water will remain ponded at the surface, the surface storage  $I_s$ . From this surface storage, a part will flow out of the tank as overland flow. Also, overland flow coming from upstream may flow into the tank.

In order to calculate the actual amount of infiltrated water at time  $t$ , three 'virtual' amounts of infiltration are calculated which represent the maximum amounts of cumulative infiltration for each of the three limiting situations. The amounts are called 'virtual' because only one of the three situations can actually occur at a time: this is the minimum of these three virtual amounts of infiltration and determines the actual amount of infiltration. For the *storage-limited situation*, this virtual amount is simply the maximum amount of water that can be stored in the regolith, the regolith storage capacity  $STO$  (in mm). For the *supply-limited situation*, this virtual amount consists of the total amount of water stored in  $(I_{s,t-\Delta t})$  and on  $(I_{s,t-\Delta t})$  the regolith at the end of the previous time step  $(t-\Delta t)$ , adding the incoming of water from rainfall  $(I_{r,t})$  and overland flow  $(I_{of,in,t})$  during time step  $t$  and subtracting the amount of overland flow  $(I_{of,out,t})$  leaving the tank at time  $t$ :

$$I_{supply,t} = I_{t-\Delta t} + I_{s,t-\Delta t} + I_{of,in,t} - I_{of,out,t} + I_{r,t} \quad 7.11$$

where all terms are equivalent depths in (m). For the *infiltration capacity limited situation* the virtual amount,  $I_{inf, cap,t}$ , is calculated from the Philip (1957) cumulative infiltration capacity function (eq. 2.78, discarding the third and higher terms). The maximum amount of water infiltrating at time  $t$  depends on the infiltration parameters  $K$  and  $S$ , as well as on the total amount of infiltrated water at the end of the previous time step,  $(I_{t-\Delta t})$ :

- 1 The regolith may become saturated and no more water will infiltrate, resulting in saturation overland flow. This is the *storage-limited situation*. Once this is true, the regolith will remain saturated for the remainder of the rainstorm, as no subsurface flow or deep percolation occur.
- 2 The amount of rainfall and ponded water may exceed the infiltration capacity of the regolith, resulting in Hortonian overland flow. Now the situation is *infiltration-capacity limited*.
- 3 If neither of the above situations apply, all water will infiltrate and overland flow will not take place. This is the *supply-limited situation*.

$$I_{inf, cap,t} = I_{t-\Delta t} + \int_{t-\Delta t}^t i dt = K(t_* + \Delta t) + S(t_* + \Delta t)^{3/4} \quad 7.12$$

with:  $t_*$  in (min);  $K$  in (m/min);  $S$  in (m/min).  $t_*$  is a 'corrected' time corresponding to the time needed under conditions of continuously-ponded infiltration ('Philip' conditions) to obtain an amount of infiltration equal to  $I_{t-\Delta t}$  and it can be calculated by solving the Philip cumulative infiltration equation for  $t_*$ :

$$t_* = \left\{ \frac{-S + \sqrt{S^2 + K I_{t-\Delta t}}}{2K} \right\}^2 \quad 7.13$$

The models use correction factors for  $K$  and  $S$ ,  $a_K$  and  $a_S$  respectively ( $0 \leq a_K, a_S \leq 1$ ). These have been introduced because the measured values of  $K$  and  $S$  overestimate the actual values of these parameters, as was concluded in chapter 6. The corrected values used in the calculations are therefore  $K' = a_K \cdot K$  and  $S' = a_S \cdot S$ . The correction factors were obtained from calibration of the discharge models.

## 7.4.2 TANKFLOW

TANKFLOW is a simple rainfall-runoff model. The catchment is reduced to one tank in the *lumped* variant. TANKFLOW can also be run as a two-tank *rill-interrill* variant, allowing a distinction between rills and interrills. No explicit spatial information is used other than the total catchment area or the total rill and interrill surface areas. For the lumped variant and for the interrills in the rill-interrill variant, there is no overland flow coming in, so that equation 7.11 becomes:

$$I_{supply,t} = I_{t-\Delta t} + I_{s,t-\Delta t} + I_{r,t} \quad 7.14$$

For the rills in the rill-interrill variant, all overland flow coming from the interrills is added to the surface storage of the rills before the infiltration is calculated for the rills:

$$I_{supply,t} = I_{t-\Delta t} + I_{s,t-\Delta t} + \frac{A_{ir}}{A_r} I_{of,ir,t} + I_{r,t} \quad 7.15$$

where:  $I_{of,ir,t}$  = amount of overland flow coming in from the interrills in (m);  $A_{ir}$ ,  $A_r$  are the surface areas of respectively the interrills and rills in (m<sup>2</sup>). If the situation is not supply-limited (see section 7.4.1), water will be retained at the surface and a part will leave the tank as overland flow. The outflow is linearly related to the amount of water 'stored' at the surface, so surface storage decreases exponentially with time:

$$I_{s,t+\Delta t} = I_{s,t} e^{-\alpha \Delta t} \quad 7.16$$

and the amount of overland flow can be calculated from:

$$I_{of,t} = I_{s,t} (1 - e^{-\alpha \Delta t}) \quad 7.17$$

where:  $I_{of,t}$  = amount of overland flow in (m);  $\alpha$  = outflow constant in (min<sup>-1</sup>). Input for TANKFLOW includes rainfall, the regolith parameters  $K$ ,  $S$  and  $STO$  with the correction factors  $a_K$  and  $a_S$ , the catchment parameters surface area  $A$  ( $= A_{total}$ ,  $A_{ir}$  or  $A_r$ ) and the catchment outflow constant  $\alpha$ . In the lumped variant,  $A = A_{total}$ . In the rill-interrill variant,  $K$ ,  $S$ ,  $STO$ ,  $a_K$ ,  $a_S$ ,  $A$  and  $\alpha$  must be given for both rills and interrills ( $A = A_{ir}$  or  $A_r$ ). In the calibration runs for the rill-interrill variant, it was assumed that  $a_K$  and  $a_S$  were the same for interrills and rills.

In contrast to TANKFLOW, DINOFLOW (Distributed Infiltration and Overland FLOW model) uses grid-based spatial data to calculate infiltration and overland flow and to route overland flow through a catchment. For TCP,  $0.5 \times 0.5 \text{ m}^2$  cells (tanks) were used. Each cell in the grid is either rill or interrill. In order to calculate the amount of overland flow from a cell to its neighbour cells, the surface water layer is treated as a square, rigid layer. During a time step  $\Delta t$  this square moves downslope in the direction of the steepest dip of the slope (the *drainage direction*) over a distance depending on the flow velocity. Next, the square is divided over the source cell and its neighbours in proportion to the areas of these cells covered by the displaced square of water, as indicated in figure 7.7. Thus the amount of overland flow flowing from one cell to another during a time step  $\Delta t$  depends on the time step duration, the water layer depth, the flow velocity and the drainage direction. If the source cell is a rill, overland flow will only move to the downslope neighbour rill cell, not to downslope interrill cells.

At the start of each time step, flow velocities for both laminar and turbulent conditions are calculated:

$$u_{of,lam} = \frac{\rho_{of} g (OFC z_{of})^2 \sin \beta}{3 \eta_{of}} \quad 7.18$$

$$u_{of,tur} = \frac{(OFC z_{of})^{2/3} (\sin \beta)^{1/2}}{n} \quad 7.19$$

where:  $u_{of,lam}$  = overland flow velocity for laminar conditions in (m/s);  $u_{of,tur}$  = overland flow velocity for turbulent conditions in (m/s);  $\rho_{of}$  = density of overland flow in ( $\text{kg/m}^3$ );  $z_{of}$  = cell-averaged depth of surface water layer in (m);  $OFC$  = overland-flow concentration factor (dimensionless;  $OFC \geq 1$ );  $\eta_{of}$  = viscosity of overland flow fluid in (Pa·s);  $\beta$  = slope angle in ( $^\circ$ );  $n$  = Manning's roughness coefficient (dimensionless). The overland-flow concentration factor,  $OFC$ , is introduced because overland flow is never evenly distributed throughout a cell. By concentration of the flow along preferential paths, the actual depth of overland flow is increased. The  $OFC$  is the ratio of the actual flow depth in these paths to the cell-averaged flow depth.

Next, the Reynolds number,  $Re$ , is calculated from equation 2.87 using both the laminar and turbulent overland flow velocities. This results in two  $Re$  values:  $Re_{lam}$  and  $Re_{tur}$ . The Reynolds number determines whether flow conditions are laminar ( $Re_{lam} \leq 500$ ), turbulent ( $Re_{tur} \geq 2000$ ) or transitional ( $Re_{lam} > 500$  and  $Re_{tur} < 2000$ ). Now for laminar conditions, the flow velocity is calculated from equation 7.18 and for turbulent conditions from equation 7.19. For transitional flow conditions, the low velocity,  $u_{of,ir}$ , is interpolated between the laminar and turbulent velocities:

$$u_{of,ir} = \frac{(2000 - Re_{lam})u_{of,lam} + (Re_{tur} - 500)u_{of,tur}}{(2000 - Re_{lam}) + (Re_{tur} - 500)} \quad 7.20$$

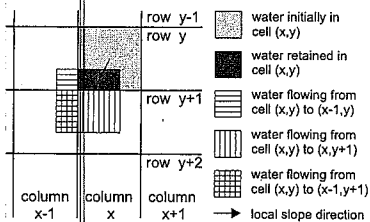


Figure 7.7 Downstream distribution of overland flow from a cell in DINOFLOW.

DINOFLOW also attempts to include the effects of entrained sediment on the overland flow. On the steep slopes in debris-flow trigger zones, overland flow often contains high amounts of sediment. This increases the density and strongly increases the viscosity of the overland flow compared to pure water (see section 2.1.2). As the amount of sediment transported depends on the overland flow intensity, viscosity is modelled in DINOFLOW as a function of rainfall intensity:

$$\eta_{of} = \begin{cases} \eta_w & \text{for } i_r \leq i_{r,min} \\ \eta_w + (\eta_{max} - \eta_w) \left( \frac{i_r^{a_n} - i_{r,min}^{a_n}}{i_{r,max}^{a_n} - i_{r,min}^{a_n}} \right) & \text{for } i_{r,min} < i_r < i_{r,max} \\ \eta_{max} & \text{for } i_r \geq i_{r,max} \end{cases} \quad 7.21$$

where:  $\eta_w$  = viscosity of pure water in (Pa·s; 0.001 Pa·s at  $20^\circ\text{C}$ );  $\eta_{max}$  = maximum viscosity of overland flow fluid in (Pa·s);  $i_{r,min}$  = minimum rainfall intensity needed for sediment entrainment in (mm/min; fixed at 0.1 mm/min);  $i_{r,max}$  = maximum rainfall intensity in (mm/min; fixed at 2.0 mm/min);  $a_n$  = power constant (dimensionless). The power constant  $a_n$  and the maximum viscosity  $\eta_{max}$  must be measured or calibrated. Figure 7.8 shows some of the possible relations between rainfall intensity and viscosity from equation 7.21.

Input for DINOFLOW consists of maps of slope angle, slope aspect, rill pattern,  $K$ ,  $S$ ,  $STO$  and outflow point. Also, the correction factors  $a_K$  and  $a_S$ , the overland flow concentration factor  $OFC$ , the overland flow density  $\rho_{of}$ , the maximum viscosity  $\eta_{max}$ , the power constant in the viscosity function  $a_n$ , Manning's  $n$  and the minute-to-minute rainfall are needed.

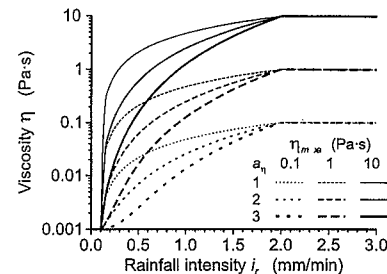


Figure 7.8 Relation between rainfall intensity and viscosity in DINOFLOW for different values of  $a_n$  and  $\eta_{max}$ .

#### 7.4.4 Calibration of the discharge models

A major problem in the calibration of TANKFLOW and DINOFLOW was the lack of rainstorms with reliable discharge records. Only the events in June and July of 1991 and 1992 had reasonably reliable discharge records. The June 1992 events were dismissed for calibration purposes, because the initial water contents for these events were always high, near saturation. In such conditions, saturation overland flow is likely to be the dominant type of overland flow, but neither TANKFLOW nor DINOFLOW were specifically developed to simulate saturation overland flow. Finally only three acceptable rainstorms were left for calibration. These occurred on 23 July 1991 and on 4 and 5 July 1992. Of these three events, the first was considered to be the most important one for calibration, as interest would be mainly on high discharge events. Calibration was performed for a single parameter at a time. Model results were interpreted by visual comparison of measured and calculated discharges, with emphasis on peak discharge.

With TANKFLOW, in order to account for the variability of  $K$ ,  $S$  and  $STO$ , a Monte Carlo simulation was performed with each Monte Carlo simulation consisting of 500 TANKFLOW runs. For each TANKFLOW run, new values were drawn randomly from the distributions of the parameters  $K$ ,  $S$ ,  $\theta_r$ ,  $\theta_s$  and  $z_{veg}$  according to equations 7.2 - 7.9. Using these input data, the correction parameters  $a_K$ ,  $a_S$  and the outflow constant  $a$  were calibrated, in the rill-interrill variant for both the rills and the interrills. In order to reduce the wide range of parameter combinations giving acceptable results, two additional assumptions were made for the rill-interrill variant. The correction factors  $a_K$  and  $a_S$  were assumed to be the same for rills and for interrills and the outflow constant  $a$  for the interrills was expected to be slightly smaller than for the rills.

The results are given in table 7.1 and figure 7.9 shows the measured and calculated runoff for the three rainstorms used in the calibration. It is conspicuous that the first calculated discharge peaks of the



23 July 1991 event do not appear in the discharge measurement records. This is caused by the fact that overland flow first had to fill up a sediment-removal basin which withheld the first 80-90 l of water and sediment. With DINFLOW, the variability of the input data was accounted for by both the construction of the input maps and by performing a Monte Carlo simulation with each simulation consisting of 10 DINFLOW runs. For each run, maps of  $K$ ,  $S$  and  $STO$  were generated by assigning random values to each cell using equations 7.2-7.9. DINFLOW was calibrated for seven parameters: the correction factors  $a_K$  and  $a_S$ , the overland flow concentration factor  $OFC$ , the overland flow density  $\rho_{of}$ , the maximum viscosity  $\eta_{max}$ , the power constant in the viscosity function  $a_\eta$  and Manning's  $n$  (table 7.2). The same rainstorms were used for the calibration. Figure 7.9 shows the measured and calculated runoff for these rainstorms.

#### 7.4.5 Stability of the discharge models

The numerical stability of the models was investigated by running them with an imaginary rainstorm of 900 minutes duration with a constant rainfall intensity of 1 mm/min, followed by 100 minutes of no rainfall. Such a rainstorm should give a monotonically and slowly rising discharge curve of decreasing steepness, followed at the end of the rainfall by a monotonically and quickly falling discharge curve of decreasing steepness. For DINFLOW, five runs were carried out. Figure 7.10 shows that both TANKFLOW and DINFLOW produce such curves without any apparent numerical instabilities.

Table 7.1 Calibrated values of TANKFLOW model parameters.

Variant	$a_K$		$a_S$		$\alpha$ (min <sup>-1</sup> )	
	Best guess	Acceptable range	Best guess	Acceptable range	Best guess	Acceptable range
lumped	0.45	0.35-0.55	0.5	0.40-0.60	0.4	0.25-0.60
rill-interrill:						
- interrill	0.35	0.25-0.45	0.5	0.40-0.60	0.4	0.25-0.60
- rill	id.	id.	id.	id.	0.6	0.40-0.90

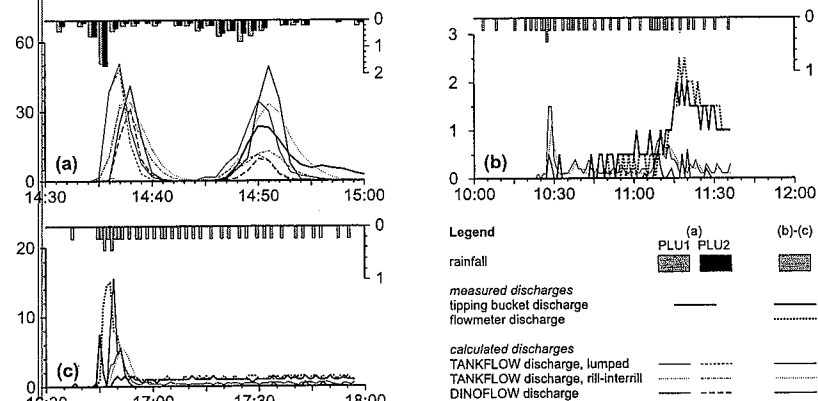


Figure 7.9 Measured and calculated discharges for three calibration rainstorms: (a) 23 July 1991; (b) 4 July 1992; (c) 5 July 1992. Horizontal axis: time; left axis: discharge (l/min); right axis: rainfall (mm).

Table 7.2 Calibrated values of DINFLOW model parameters.

Model parameter	Calibration		Physically or logically acceptable range	Units
	Best guess	Acceptable range		
$a_K$	0.4	0.25 - 0.55	>0 - 1	-
$a_S$	0.45	0.25 - 0.60	>0 - 1	-
$a_\eta$	3	<1 - »4	>1 ?	-
$\eta_{max}$	0.3	«0.03 - »3	0.001 - ~10	Pa·s
$\rho_{of}$	1200	«1000 - »2400	1000 - ~2000	kg·m <sup>3</sup>
$OFC$	1.5	<1 - »2.5	≥1	-
$n$	0.1	«0.03 - »0.25	0.05 - 0.15 ?	-

The effect of time step length on discharge was investigated for three different rainstorms, with low (1 July 1993 at 19:23), intermediate (6 June 1993 at 18:06) and high (5 August 1993 at 14:15) discharges. Figure 7.11 shows the effect of time step length on discharge for the TANKFLOW lumped variant. The TANKFLOW rill-interrill variant shows a similar response. All time steps up to 20 seconds give nearly the same discharge curves, so the time step for the calculations was fixed at  $\Delta t = 2$  seconds. From figure 7.12 it appears that a time step of 0.5-1 seconds would be optimal for DINFLOW, especially at high discharges. In order to reduce computation time, the time steps were fixed at  $\Delta t_r = 2$  seconds for interrills and at  $\Delta t_r = 1$  second for rills.

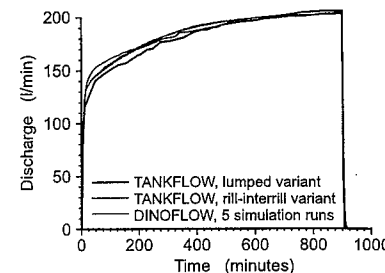


Figure 7.10 Numerical stability of the discharge models.

#### 7.4.6 Sensitivity of the discharge models

Sensitivity analyses were also carried out for the three rainstorms with low, intermediate and high discharges mentioned in the previous section. They were carried out to investigate the influence of changes in model parameter values on peak discharge for the hydrologic models. The sensitivity in figures 7.13 and 7.14 is given here by the relative value of the peak discharge as a function of the relative value of an input parameter, where 100% refers to the calibrated values of the input parameters and the corresponding peak discharges.

Figure 7.13 shows the sensitivity of TANKFLOW peak discharge for the parameters  $a_K$ ,  $a_S$  and  $\alpha$ . The lumped variant is most sensitive for changes in  $a_K$ , and slightly less sensitive for changes in  $a_S$ .  $\alpha$  has less influence. As the surface area of the interrills in the rill-interrill variant forms the largest part of the total surface area, the sensitivity for the interrill parameters is much the same as in the lumped variant. The rill parameters  $a_K$  and  $a_S$  have much less influence, because the rill surface is much smaller than the interrill surface, but the sensitivity of TANKFLOW peak discharge for changes in  $\alpha$  for the rills is only slightly less than for the interrills. Also, it appears that the sensitivity of TANKFLOW peak discharge for changes in its input parameters generally decreases with increasing rainfall intensity and discharge. This effect is less clear for  $\alpha$ . It can be concluded that  $a_K$  and  $a_S$  (in the rill-interrill variant: for interrills) are the most important parameters to be determined accurately with respect to

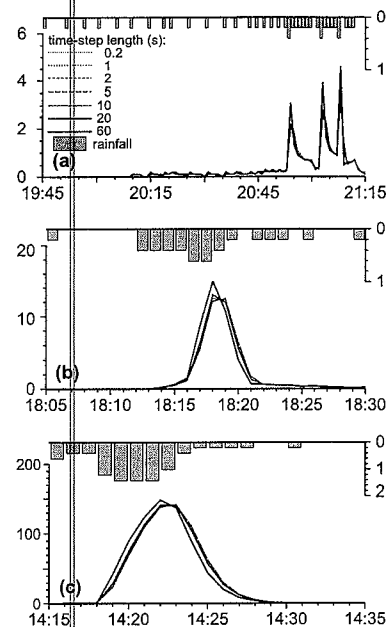


Figure 7.11 Effect of time-step length on TANKFLOW 'lumped' discharge at: (a) low (1 July 1993); (b) intermediate (6 June 1993); (c) high discharge (5 August 1993). Horizontal axis: time; left axis: discharge (l/min); right axis: rainfall (mm).

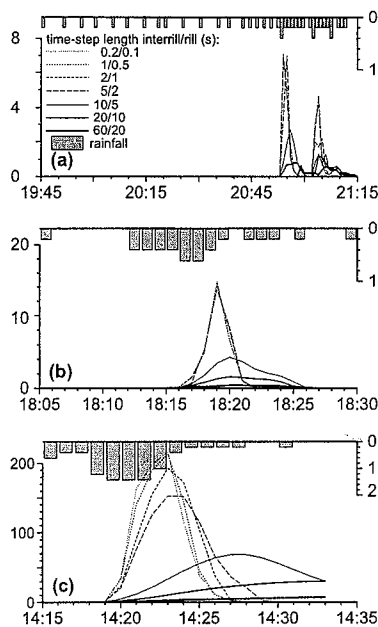


Figure 7.12 Effect of time-step length on DINOFLOW discharge at: (a) low (1 July 1993); (b) intermediate (6 June 1993); (c) high discharge (5 August 1993). Horizontal axis: time; left axis: discharge (l/min); right axis: rainfall (mm).

TANKFLOW peak discharge, followed by  $a_K$  and  $a_S$  for the rills and  $\alpha$ . If the fraction of the surface area occupied by the rills is larger, the sensitivity of TANKFLOW peak discharge for the rill parameters  $a_K$  and  $a_S$  will increase.

Figure 7.14 shows the sensitivity of DINOFLOW peak discharge for the parameters  $a_K$ ,  $a_S$ ,  $\alpha$ ,  $\eta_{max}$ ,  $\rho_{of}$ ,  $OFC$  and Manning's  $n$ . Manning's  $n$  appears to have very little influence on the discharge peaks, so it was fixed at  $n = 0.10$ . Apparently the high viscosity of the overland flow suppresses turbulence and flow conditions remain laminar. Changes in  $\eta_{max}$  also seem to have little effect, but it must be borne in mind that this parameter may vary by several orders of magnitude. At low and intermediate discharges,  $\alpha$ ,  $\rho_{of}$  and  $OFC$  have some influence on peak discharge, but at high discharges, their effect is minor. DINOFLOW peak discharge is most sensitive to  $a_K$  and  $a_S$ . Their effect is strongest at low and intermediate discharges and less strong at high discharges. The sensitivity of DINOFLOW peak discharge for changes in the input parameters generally decreases with increasing peak discharge; at high discharges DINOFLOW peak discharge is nearly insensitive to all parameters except  $a_K$  and  $a_S$ . To conclude,  $a_K$  and  $a_S$  are the most important parameters to be determined for modelling peak discharge with DINOFLOW, and probably  $\eta_{max}$  as well. At lower discharges,  $\alpha$ ,  $\rho_{of}$  and  $OFC$  should also be determined accurately.

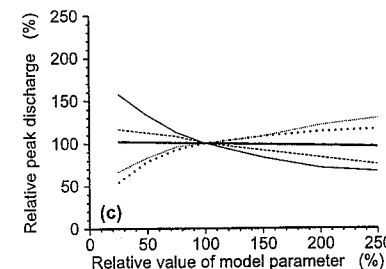
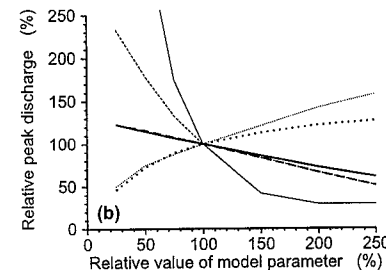
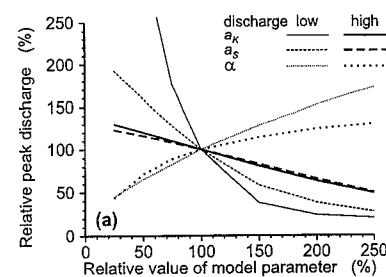


Figure 7.13 Sensitivity of TANKFLOW at low and high discharges: (a) lumped; (b) rill-interrill, interrill parameters; (c) rill-interrill, rill parameters.

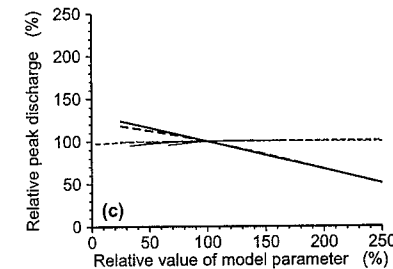
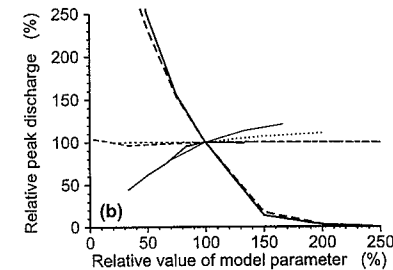
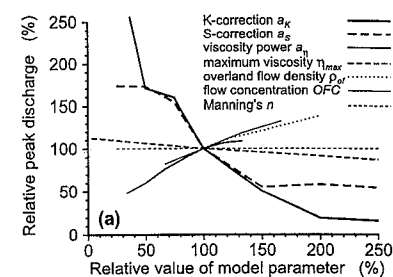


Figure 7.14 Sensitivity of DINOFLOW discharge at: (a) low; (b) intermediate; (c) high discharge.

#### 7.4.7 Accuracy of the discharge models

Figure 7.9a also gives an indication of the uncertainty in discharge caused by the uncertainty in the rainfall measurements. For the 23 July 1991 rainstorm, discharges have been calculated for rainfall data from both raingauges at the TCP site. The difference between the rainfall registered by the two raingauges on peak discharge for the second peak is quite strong in both models. As it is not known which of the two raingauges has provided the most reliable rainfall record for this rainstorm, and as the discharge peak from this rainstorm was the most important one used for calibration of the models, it must be concluded that neither TANKFLOW nor DINOFLOW could be calibrated accurately. The discharge record also has its uncertainties, but no data are available to quantify this uncertainty.

second discharge peak which is either 50% higher or lower than the measured discharge (fig. 7.9a). Combination with the peak discharge sensitivity curves for intermediate discharges from the lumped variant (fig. 7.13a) shows that 50% lower discharges are obtained with for example 40% higher  $a_K$ , 50% higher  $a_s$  or 70% lower  $\alpha$  values, whereas 50% higher values are obtained for 20% lower  $a_K$ , 35% lower  $a_s$  or 100% higher  $\alpha$  values. In the light of the uncertainty in the rainfall inputs, the ranges of parameter values that might give acceptable peak discharges appears to be very wide. In table 7.1 these acceptable ranges of values are indicated as well.

DINOFLOW is even more sensitive for the uncertainties in the rainfall records, as figure 7.9a shows. Here the calculated peak discharges for the second discharge peak are either 60% lower or 110% higher than the measured peak discharge. Combination with figure 7.14b (intermediate discharge) shows that 60% lower peak discharges can be obtained for 70% lower  $a_K$  or OFC values or 30% higher  $a_K$  or  $a_s$  values. 100% higher discharges are only obtained for 35-40% lower  $a_K$  or  $a_s$  values and for extremely large changes in any of the other parameters. The resulting acceptable ranges of values for the parameters are also very wide (table 7.2).

## 7.5 Discussion and conclusions

The calibration of TANKFLOW and DINOFLOW shows that  $K$  and  $S$  values are indeed overestimated by the rainfall simulation method, as was mentioned in chapter 6. Rough estimates of overestimation ratios from tables 7.1 and 7.2 are about 2.5 (range 1.8-4) for  $K$  and about 2.1 (range 1.7-4) for  $S$ . The fact that Manning's  $n$  has no influence on DINOFLOW discharge suggests predominantly laminar flow conditions, caused by the increased viscosity in DINOFLOW which yields very low  $Re$  values compared to pure water. However, the acceptable range for the maximum viscosity  $\eta_{max}$  in DINOFLOW is very wide, so actual flow conditions of the sediment-rich overland flow may still be turbulent.

At this point, a general a priori comparison can be made between the different models presented in this chapter. Hortonian overland flow is supposed to be the direct trigger mechanism for debris flows. As Hortonian overland flow is triggered by rainfall, rainfall indirectly triggers debris flows. Thus, if the discharge models are accurate, they can be expected to yield more clearly defined thresholds for debris-flow occurrence than models based on rainfall only.

However, TANKFLOW and DINOFLOW both suffer from uncertainties in the model parameters caused by variability and uncertainty in input data and the lack of reliable discharge records for calibration. Considering these problems, TANKFLOW and DINOFLOW peak discharges have uncertainties in the order of at least 50%, and this may very well obscure the relation between modelled peak discharges and debris-flow triggering. For the same reason, the high number of model parameters and input data demanded by DINOFLOW result in more uncertain peak discharges than in TANKFLOW, even though the physical basis of DINOFLOW is more sound.

Related to this is the issue of the identifiability of parameters in models in relation with model complexity. The more complex a model becomes, the more accurate the model may describe the observed variation of a certain phenomenon. However, the increasing complexity of the model also causes a loss in degrees of freedom. The net effect is that the addition of more parameters to the model will result in a significant increase of the explained variation only up to a certain level of model complexity, after which the addition of any more parameters will no longer increase the explained variation significantly. As more parameters are used in the model, more control buttons may be adjusted and correlation between the model parameters will result in the same model outcome for many combinations of parameter settings. This means that the identification of model parameters becomes more and more difficult as their number increases, and therefore the processes represented by the parameters also become less identifiable, as has been mentioned by e.g. Van der Perk (1996, 1997) in the field of water quality modelling.

## 8.1 Introduction

In this chapter the results of debris flows triggered at the Tête du Clot des Pastres (TCP) debris-flow trigger zone and their controlling factors are dealt with. First, the identification of debris flows that have occurred in the period 1991-1995 will be discussed (section 8.2) and will be related to rainstorms. Next, the effect of different rainfall and runoff factors on debris-flow triggering will be quantified, and from this the most important factors controlling debris-flow triggering will be identified. From these, the most efficient factor or combination of factors explaining debris-flow occurrence will be determined (section 8.3). Finally (section 8.4) debris-flow frequency at TCP will be modelled using only rainfall data.

## 8.2 Debris flows at Tête du Clot des Pastres site between June 1991 and June 1995

During the field campaigns in the 'study period' (June 1991 - June 1995) the TCP site was visited frequently in summer (June and July) and early autumn (late September - mid October), allowing the identification of at least six or seven debris flows occurring in this period. Figure 8.1 shows the debris-flow tracks formed during this period. Two debris flows occurred during the field campaigns and could be linked uniquely to rainstorms (see table 8.1): The 12 July 1991 and 26 June 1994 debris flows. The other (at least) four debris flows have occurred between the field campaigns and therefore they could not be linked to any particular rainstorm with absolute certainty. Usually more than one rainstorm could be found which could have triggered a debris flow (table 8.1, appendix A2). Table 8.1 also shows that there is very little evidence of debris-flow activity during the months October - May.

It seems likely that sometimes more than one debris flow had occurred, although only a single 'fresh' deposit could be identified. This is the case for the surveys of autumn 1992 (2 debris flows are very likely), autumn 1993 (3 are very likely) and autumn 1994 (2 are very likely and another 2 are likely). The debris flow mapped in the summer of 1994 (before 26 June), had possibly occurred on 7 October 1993 (based on Barcelonnette rainfall records). The probable debris flow that was mapped in autumn 1991 could only be linked to one rainstorm, on the 9<sup>th</sup> August 1991. Thus, although at least 6 debris flows have occurred in the study period, a number of 8-12 seems more realistic.

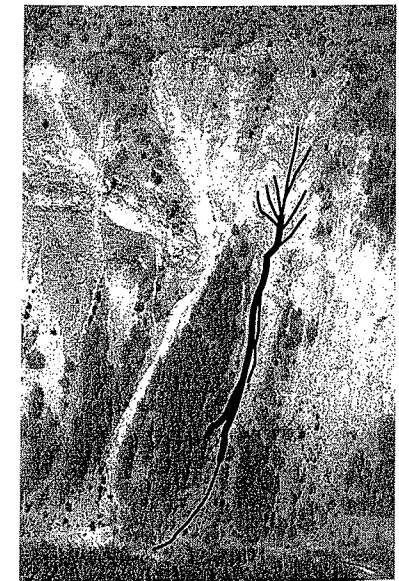


Figure 8.1 Debris-flow tracks originating from the debris-flow trigger zone TCP from June 1991 until June 1995.

Rainstorms triggering debris flows at the TCP site in the period June 1991 - June 1995.									
Survey	Number of debris flows identified	Ranking of rainstorm with regard to debris-flow triggering							
		Certain		Very likely		Likely		Possible	
summer 1991	1	12 July 14:07							
autumn 1991	1*								
summer 1992	0	9 August 5:03							
autumn 1992	1	19 August 17:38							
		29 August 12:47							
		22 September 11:52							
		22 September 13:06							
		27 September 18:01							
summer 1993	0								
autumn 1993	1	5 August 14:15							
		15 August 13:38							
		15 August 14:31							
summer 1994	2	26 June 15:01 or 17:01							
		7 October 1993							
		22 September 1993							
		23 September 1993							
		30 September 1993							
autumn 1994	1	11 July 22:34							
		27 July 18:43							
		8 September 9:36							
		8 September 14:17							
		22 July 15:25							
		8 September 15:41							
summer 1995	0	14 September 9:46							

\* Probable debris flow.

\* Probable debris flow.

### 8.3 Factors affecting debris-flow triggering

#### 8.3.1 Describing debris-flow triggering: the logistic regression model

In order to identify the most important factors from the rainfall and discharge factors with regard to debris-flow triggering, two methods can be used. The first is simply to find for each factor the minimum value having triggered a debris flow,  $DF_{min}$ , and the maximum value not having triggered a debris flow,  $NDF_{max}$ . This gives some information on debris-flow thresholds and on the width of the 'grey' zone in which both triggering and non-triggering of debris flows can occur ( $NDF_{max} - DF_{min}$ ). However, this method needs abundant input data for both debris-flow triggering and non-triggering situations, otherwise the values of  $DF_{min}$  and  $NDF_{max}$  are strongly influenced by chance. Therefore, a regression method making use of all available data seems better. The logistic regression method, which expresses the probability of occurrence of a phenomenon,  $p$ , as a function of the value(s) of one or more independent variables, seems to be a suitable regression technique. This non-linear regression method is well-known in medicine (e.g. Green and Symmons 1983) and in ecology (e.g. Ertsen 1995). A detailed description of the logistic regression method is given by Hosmer and Lemeshow (1989). The linear logistic function is a sigmoidal curve (see fig. 8.2) given by:

$$p = \frac{e^{a_0 + a_1x_1 + a_2x_2 + \dots + a_Nx_N}}{1 + e^{a_0 + a_1x_1 + a_2x_2 + \dots + a_Nx_N}} \quad 8.1$$

where:  $p$  = probability of occurrence;  $x_1 \dots x_N$  are  $N$  variables;  $a_0 \dots a_N$  are  $N+1$  function parameters. The number of parameters in this linear logistic regression function exceeds the number of variables by one. It is called 'linear' because the logit transformation results in a linear equation:

$$\text{logit}(p) = \ln\left(\frac{p}{1-p}\right) = a_0 + a_1x_1 + a_2x_2 + \dots + a_Nx_N \quad 8.2$$

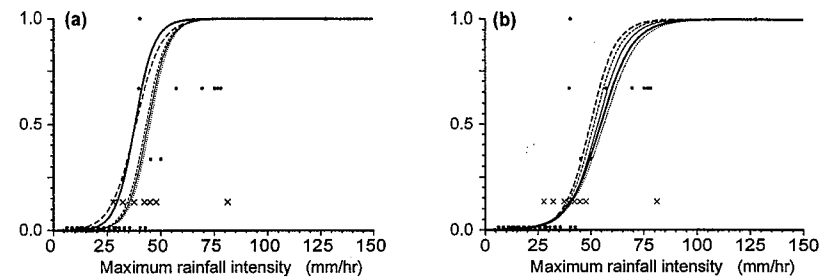


Figure 8.2

Logistic-regression relations between maximum 5-minute rainfall intensity,  $i_s$ , and debris-flow probability for different curve-fitting methods: (a) category possible assigned to group debris flow present; (b) category possible assigned to group debris flow absent.

In order to use logistic regression for the analysis of debris-flow occurrence, the data for all rainstorms (in case of total daily rainfall: for all days) had to be divided in two groups: *debris flow present* (with debris-flow probability  $p = 1$ ) and *debris flow absent* ( $p = 0$ ). To begin with, each rainstorm was assigned to one of the four 'debris-flow triggering' categories mentioned in table 8.1 (*certain*, *very likely*, *likely* and *possible*) or in one of the categories *very unlikely* and *certainly not*. Figure 8.3 shows the flow chart for this classification. If more than one rainstorm could have triggered a debris flow, independent data were used as much as possible to link each rainstorm to a certain debris-flow likelihood category. Videotapes showing runoff and sediment content characteristics at high rainfall intensities and debris-flow deposit 'freshness' characteristics, such as water content, amount of silt and fine sand on stones at the surface of the deposit or the condition of the vegetation have been used. Another source of information came from the discharge measurements at the TCP site: unexpected (changes in) amounts of discharge might be caused by sediment displacement. If the above mentioned data were insufficient, rainfall characteristics (rainfall intensity, total rainfall amount and rainfall history) have also been used. However, as the intention was to examine the influence of these rainfall factors on debris-flow triggering, they were used as little as possible to avoid circular reasoning. Table 8.2 shows the number of rainstorms associated with each of these categories.

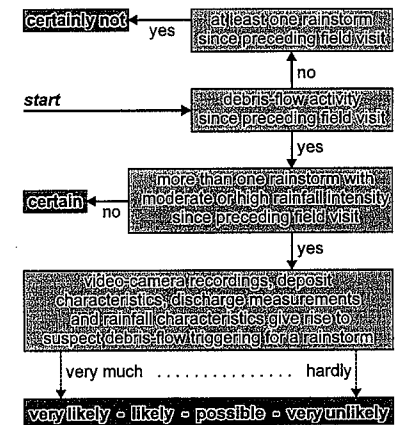


Figure 8.3

Flow chart for the identification of 'debris-flow triggering likelihood' categories for rainstorms at TCP.

Debris-flow likelihood category	Number of rainstorms	Allocated probabilities		
		Low	Best Guess	High
certain	2	1	1	1
very likely	8	0.5	0.666...	0.75
likely	2	0.25	0.333...	0.5
possible	10	0.1	0.1333...	0.2
very unlikely	59	0.01	0.01333...	0
certainly not	50	0	0	0
Total <sup>a</sup>	131	8.09	10.12	12.2

<sup>a</sup> Total predicted number of debris flows = Sum of probabilities for all rainstorms.

debris flows that have occurred (see table 8.2). *Low* represents a conservative approach, for which the total number of debris flows (8) exceeds the minimum number of debris flows identified in the field only slightly. *Best guess* is based on the best-guess of the number of debris flows (10) based on the evidence from videotapes, deposit characteristics and from runoff and rainfall data. A third approach, *high*, corresponds with a total of just over 12 debris flows. This seems to be about the maximum number of debris flows that have occurred in the period 1991-1995.

In order to assess the effects of these uncertainties, several variants of logistic regressions were performed. The variants were based on:

- 1 the type of estimator: maximum likelihood or least squares,
- 2 the category *possible* being added to either *debris flow present* or *debris flow absent*,
- 3 either or not using weights for the data points, and
- 4 the *low*, *best guess* and *high* approaches of probabilities in table 8.2, if weights were used.

The relations resulting from these variants were calculated for the maximum 5-minute rainfall intensity  $i_{5s}$  (fig. 8.2) and for TANKFLOW peak discharge (rill-interrill variant with antecedent rainfall; fig. 8.4). 'Validation' of the relations was carried out by calculating the total (cumulative) number of debris flows predicted for the total data set by each of the relations, which should ideally be the actual total number of debris flows that have occurred (about 8-12; see section 8.2). Table 8.3 shows that only the relations based on *possible* assigned to the group *debris flow absent* give reasonable predictions.

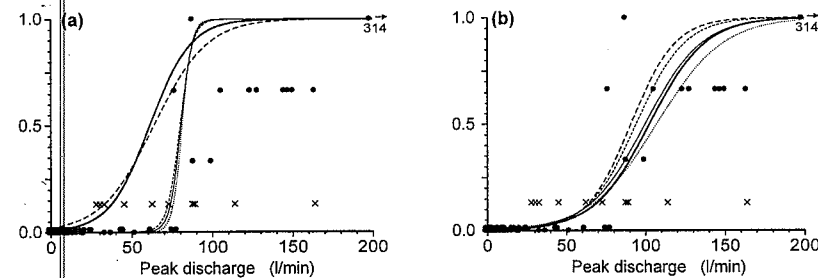


Figure 8.4 Logistic-regression relations between TANKFLOW peak discharge (rill-interrill variant; accounting for antecedent precipitation) and debris-flow probability for different curve-fitting methods: (a) category *possible* assigned to group *debris flow present*; (b) category *possible* assigned to group *debris flow absent*. Legend: see figure 8.3.

Table 8.3 Number of debris flows predicted for data set by logistic relations between probability of debris-flow occurrence and rainfall intensity  $i_{5s}$ .

'Possible' added to group	Number of events in group		Maximum-likelihood estimates	Least-squares estimates			
	Debris flow present	Debris flow absent		No weights	Weights based on		
				No weights	Low	Best Guess	High
Debris flow present	22	109	22	23.06	15.74	17.14	16.4
Debris flow absent	12	119	12	13.34	11.57	12.69	12.1

Figures 8.2b and 8.4b show that the remaining curves do not show very large differences. From these, the maximum-likelihood variant was chosen because:

- 1 it does not need any additional assumptions concerning the weights of the data points, and
  - 2 it produces a good estimate of the total number of debris flows.
- Using maximum-likelihood estimation yields a  $\chi^2$ -value for the regression which can be compared to a critical  $\chi^2$ -value to test the significance of the relation: the strength of the relation rises with increasing  $\chi^2$ .

### 8.3.2 Logistic regression models for debris-flow triggering

#### Single-variable models

The next step in the analysis of the data was the determination of those factors that contribute most to debris-flow triggering. Table 8.4 presents the results of the analysis of debris-flow occurrence with respect to meteorological and hydrological factors. It shows that debris-flow triggering is strongly correlated with both maximum short-duration rainfall intensity and (short-duration) peak discharge; these factors give  $\chi^2$ -values of over 50, where the critical  $\chi^2$  for degrees-of-freedom  $df = 1$  and a confidence level of 95% is  $\chi^2 = 3.84$ . From the rainfall intensities, especially the maximum 2-15 minute rainfall intensities are strongly correlated with debris-flow triggering. The correlation quickly decreases as the time interval over which the maximum rainfall intensity is averaged rises: the maximum 24-hour rainfall intensity hardly shows any correlation with debris-flow triggering (barely significant at the 95% confidence level). Also, total daily rainfall and total rainstorm rainfall can hardly account for debris-flow triggering, so normal daily rainfall records are of no use in trying to explain debris-flow occurrence. Figures 8.5a-c show the debris-flow probability curves for rainfall intensities and rainfall totals obtained from the logistic regressions. For each variable, the curves have been drawn for values from 0 to 110% of the maximum measured or calculated value, which is believed to be a realistic range of values. Table 8.4 also shows that a logarithmic data transformation generally increases the correlation with debris-flow triggering. Figure 8.6a shows the corresponding debris-flow probability curves for the logarithmic logistic function which is given by:

$$\text{logit}(p) = a_0 + a_1 \log x_1 \quad 8.3$$

The peak discharges also show high correlations with debris-flow triggering, comparable with the maximum 2-15 minute rainfall intensities. Peak discharges were calculated with TANKFLOW and DINOFLOW and either (*history*) or not (*single*) accounting for the rainfall history in the last day before the rainstorm under consideration. For TANKFLOW, both the lumped and rill-interrill variants were used. It appears that DINOFLOW performs less well than TANKFLOW (see  $\chi^2$  in table 8.4). This may probably be attributed to the uncertainties concerning both the spatial distribution of model input values and the relation between rainfall intensity, discharge, sediment content, fluid density and fluid viscosity in the DINOFLOW model, as noted in chapter 7.

Table 8.4 Hydrological factors and debris-flow triggering: single-variable models.

Factor	Logistic regression results <sup>a</sup>						$DF_{min}$ $NDF_{max}$ <sup>c</sup>		
	$\chi^2$ <sup>d</sup>	$\alpha$ <sup>e</sup>	Regression constants <sup>f</sup>		Value for preset probability <sup>g</sup>				
			$a_0$	$a_1$	$p = 0.1$	$p = 0.5$	$p = 0.9$		
Rainfall duration $t_r$	0	0.873	-2.34	0	300	5100	9900	18	647
Total rainfall									
Day $I_{r,day}$ <sup>d</sup>	13.3	0.000 <sup>h</sup>	-3.56	0.048	28.4	74.4	120	9.3	103.4
Rainstorm $I_{r,rs}$	11.8	0	-3.27	0.074	14.4	44	73.7	9.3	52
Rainfall intensity									
$i_{r,1}$	45.6	0	-7.1	0.086	57.3	82.9	109	60.6	102
$i_{r,2}$	51.5	0	-8.06	0.113	52	71.5	91	54.6	97.2
$i_{r,3}$	50.6	0	-7.63	0.118	46.1	64.8	83.5	48.6	93
$i_{r,5}$	52.2	0	-7.22	0.131	38.2	54.9	71.1	40.8	82.6
$i_{r,10}$	52.8	0	-7.26	0.172	29.5	42.3	55.1	28.6	68
$i_{r,15}$	51.2	0	-7.45	0.223	23.6	33.5	43.3	23.6	55
$i_{r,30}$	41.8	0	-6.46	0.279	15.3	23.1	31	18.2	42.5
$i_{r,60}$	36.3	0	-6.01	0.358	10.7	16.8	23	9.3	24.1
$i_{r,120}$	28.5	0	-5.27	0.434	7.1	12.1	17.2	4.6	12.8
$i_{r,1440}$	3.9	0.05	-2.95	0.617	1.2	4.8	8.3	0.4	4.3
Antecedent rainfall									
at start of event: $API_{0,10}$	1.1	0.29	-2.5	0.076	4	33	62.1	0	20.6
at start of event: $API_{0,140}$	4.4	0.036	-2.62	3.453	0.1	0.8	1.4	0	0.6
at maximum $i_{r,5}$ : $API_{5,4}$	10.9	0	-3.58	0.104	13.4	34.5	55.7	6.8	38.8
at maximum $i_{r,5}$ : $API_{5,400}$	50.1	0	-7.23	3.063	1.6	2.4	3.1	1.8	3.6
Peak discharge									
TANKFLOW Lumped									
single $Q_{T,L,s}$	53.5	0	-5.13	0.053	55.2	96.6	138	56.4	177.6
history $Q_{T,L,h}$	54.2	0	-5.99	0.055	68.6	108	148	88.9	177.6
TANKFLOW Rill-Interrill									
single $Q_{T,RIR,s}$	53.5	0	-5.04	0.056	50.9	90.2	130	56	165.6
history $Q_{T,RIR,h}$	54	0	-5.86	0.057	64	102	141	77.5	165.6
DINOFLOW									
single $Q_{D,s}$	50.8	0	-5.26	0.04	76.1	131	186	75.4	226.5
history $Q_{D,h}$	41.5	0	-5.66	0.034	103	168	233	115	226.5
<sup>10</sup> LOG-TRANSFORMED DATA									
Rainfall intensity									
$i_{r,2}$	53	0	-28.6	15.5	50.5	70	96.9	54.6	97.2
$i_{r,3}$	52.8	0	-26.8	14.9	44.9	63.1	88.6	48.6	93
$i_{r,5}$	55.1	0	-24.6	14.3	36.9	52.6	74.9	40.8	82.6
$i_{r,10}$	56.5	0	-22.9	14.3	28.1	40.1	57.2	28.6	68
$i_{r,15}$	55.3	0	-22.4	14.9	22.8	32.1	45	23.6	55
$i_{r,30}$	48.7	0	-17.7	13.3	14.8	21.7	31.8	18.2	42.5
Peak discharge									
TANKFLOW Lumped									
single $Q_{T,L,s}$	58.8	0	-16.4	8.47	47.2	85.7	156	56.4	177.6
history $Q_{T,L,h}$	57.5	0	-23.2	11.5	66.5	103	160	88.9	177.6
TANKFLOW Rill-Interrill									
single $Q_{T,RIR,s}$	59.4	0	-15.8	8.32	42.7	78.5	144	56	165.6
history $Q_{T,RIR,h}$	57.3	0	-21.5	10.8	60.7	96.9	155	77.5	165.6
DINOFLOW									
single $Q_{D,s}$	55.2	0	-17.9	8.61	66.9	120	217	75.4	226.5
history $Q_{D,h}$	44.5	0	-21.5	9.72	97.9	165	277	115	226.5

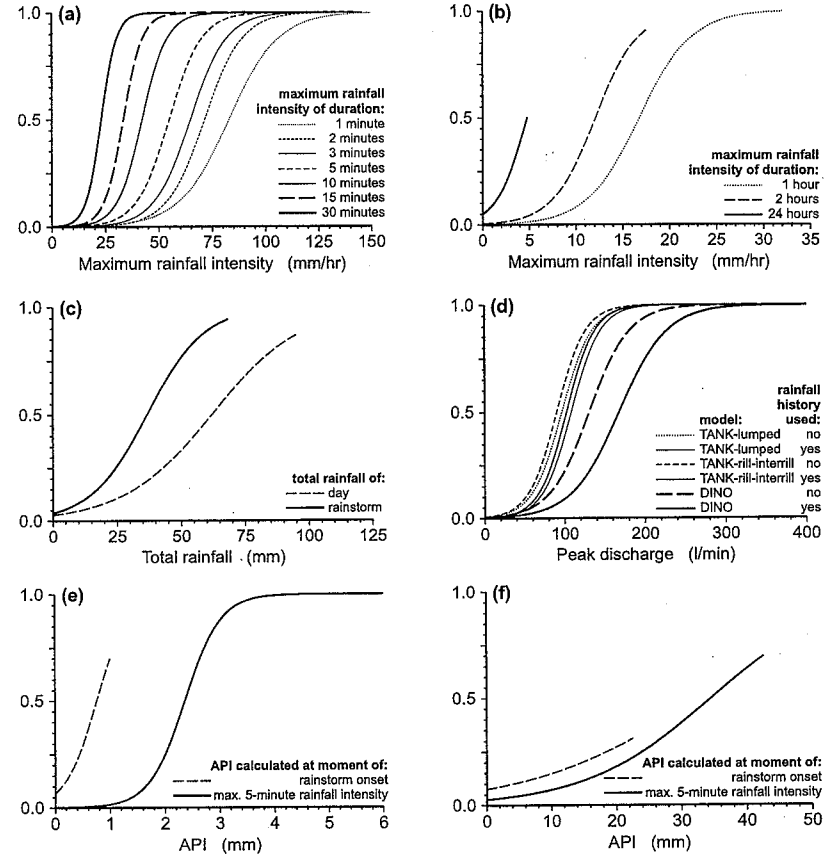
<sup>a</sup> Logistic regression with maximum-likelihood estimator and with 'possible' assigned to group 'debris flow absent'.<sup>b</sup>  $DF_{min}$  = minimum value of variable in group 'debris flow present'.<sup>c</sup>  $NDF_{max}$  = maximum value of variable in group 'debris flow absent'.<sup>d</sup> All rainstorm-based measures have  $N = 12$  in the group 'debris flow present' and  $N = 119$  in 'debris flow absent', with  $\chi^2 = 80.2$  for the average only. For total daily rainfall, these numbers are respectively  $N = 10$ ,  $N = 144$  and  $\chi^2 = 74.0$ .<sup>e</sup> Significance level of logistic regression relation.<sup>f</sup> Constants in logistic regression function (eq. 8.1).<sup>g</sup> Value of the variable which gives the given probability of debris-flow occurrence (0.1, 0.5 or 0.9).<sup>h</sup> Bold value indicates significant logistic relation at the 95% confidence level.

Figure 8.5 Probability of debris-flow triggering in relation to hydrological factors (linear models): (a) maximum 1-, 2-, 3-, 5-, 10-, 15- and 30-minute rainfall intensities; (b) maximum 1-, 2- and 24-hour rainfall intensities; (c) total rainstorm rainfall and total daily rainfall; (d) TANKFLOW and DINOFLOW peak discharges; (e) antecedent precipitation indexes (from single-parameter regression); (f) antecedent precipitation indexes (from 2-parameter models). Vertical axis: probability of debris-flow triggering.

The TANKFLOW model results are slightly better in predicting debris-flow triggering than the best of the maximum rainfall intensities. The two TANKFLOW variants, *lumped* and *rill-interrill* perform equally well with respect to debris-flow triggering. As the *lumped* variant needs less input data, this variant seems preferable over the *rill-interrill* variant. It seems that the influence of rills and gullies on peak discharges is small due to the small surface area occupied by rills and gullies, about 5% of the total area. Also, the difference in overland flow production between rill/gully and interrill surfaces may be negligible at high peak discharges. The effect of antecedent rainfall on runoff production and peak

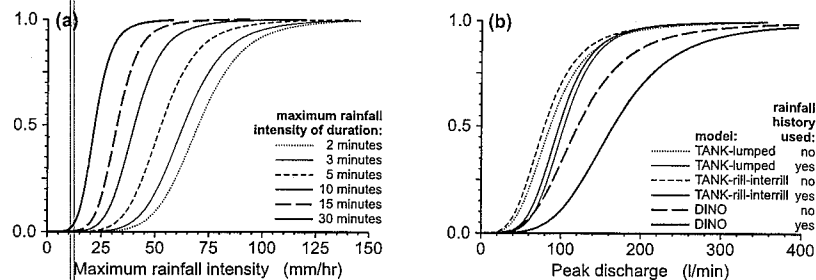


Figure 8.6 Probability of debris-flow triggering in relation to hydrological factors (logarithmic models): (a) maximum 2-, 3-, 5-, 10-, 15- and 30-minute rainfall intensities; (b) TANKFLOW and DINO peak discharges. Vertical axis: probability of debris-flow triggering.

discharges also appears to be small. Figure 8.5d shows the debris-flow triggering probability curves for peak discharges obtained from the hydrologic models. For peak discharges, the logarithmic logistic functions (fig. 8.6b) also give better results (table 8.4). Curiously enough, for the logarithmic logistic functions, accounting for antecedent rainfall decreases the correlation between debris-flow triggering and peak discharge compared to not accounting for antecedent rainfall.

Antecedent precipitation indexes in table 8.4 show widely varying correlations with debris-flow triggering.  $API_{0,140}$ , calculated at the start of the rainstorms with  $\alpha = 140 \text{ day}^{-1}$ , can hardly explain any debris-flow triggering, but the correlation between debris-flow triggering and  $API_{5,400}$ , calculated at the time of the maximum 5-minute rainfall intensity with  $\alpha = 400 \text{ day}^{-1}$ , is comparable with the short-duration maximum rainfall intensities. Actually,  $API_{5,400}$  is merely a 'disguised' measure of short-duration maximum rainfall intensity: with  $\alpha = 400 \text{ day}^{-1}$ , the influence of rainfall in the  $API$  quickly decreases. After 5 minutes, its influence is down to 25% of the original value, and another 5 minutes later it is down to 6%. The debris-flow probability curves for  $API$ 's are shown in figure 8.5e.

Table 8.5 Rainfall intensity, antecedent precipitation index and debris-flow triggering.

Rainfall intensity	Antecedent precipitation index	Logistic regression results <sup>a</sup>				
		$\chi^2$ <sup>c</sup>	$\alpha$ <sup>d</sup>	Regression constants <sup>e</sup>		
				$a_0$	$a_1$	$a_2$
<i>Antecedent precipitation at start of rainstorm</i>						
$i_{r,3}$	$API_{0,15}$	51.7	15	-7.99	0.117	0.12
$i_{r,5}$	$API_{0,10}$	53.7	10	-7.77	0.132	0.11
<i>Antecedent precipitation at moment of maximum rainfall intensity</i>						
$i_{r,2}$	$API_{2,5}$	56.2	5	-10.42	0.126	0.11
$i_{r,3}$	$API_{3,3}$	56.1	3	-10.31	0.134	0.1
$i_{r,5}$	$API_{5,4}$	58.4	4	-10.47	0.145	0.13
$i_{r,10}$	$API_{10,5}$	56.6	5	-9.28	0.17	0.12
$i_{r,15}$	$API_{15,15}$	52.4	15	-7.83	0.186	0.13

<sup>a</sup> Logistic regression with maximum-likelihood estimator and with 'possible' assigned to group 'debris flow absent'.

<sup>b</sup> Variation explained by logistic regression using least-squares estimator on non-weighted data and with 'possible' assigned to group 'debris flow absent'. Values added to allow for a rough comparison of  $\chi^2$  and  $r^2$ .

<sup>c</sup> Average only:  $\chi^2 = 80.2$ . All logistic regressions are significant at the 95% confidence level ( $\alpha < 0.001$  for all).

<sup>d</sup> Decrease coefficient in antecedent precipitation index function in [ $\text{day}^{-1}$ ] (eq. 7.10).

<sup>e</sup> Constants in logistic regression function (eqs. 8.1, 8.2).

## Multiple-variable models

After the identification of the main factors influencing debris-flow triggering, the logistic function was fitted for combinations of maximum short-duration rainfall intensity (over intervals of 2-30 minutes) and antecedent precipitation index. The best combinations appeared to be  $i_{r,5} - API_{0,10}$  (for  $API$  at the start of the rainstorm) and  $i_{r,5} - API_{5,4}$  (for  $API$  at the time of maximum rainfall intensity), as table 8.5 shows. The combination  $i_{r,5} - API_{0,10}$  hardly raises the 'explained'  $\chi^2$  above the level explained by  $i_{r,5}$  alone (53.7 versus 52.2). This leads to the conclusion that rain that has fallen during earlier rainstorms does not decrease the threshold rainfall intensity causing a debris flow. However, the combination  $i_{r,5} - API_{5,4}$  does increase the explained  $\chi^2$  (58.4) significantly above the level explained by  $i_{r,5}$  alone. As the difference between these two  $API$ 's can only be attributed to rainfall that has fallen during the rainstorm under consideration prior to reaching the maximum rainfall intensity, the conclusion must be that only such antecedent rainfall has some influence. With  $\alpha = 4 \text{ day}^{-1}$  in  $API_{5,4}$ , the influence of antecedent rainfall decreases rapidly: After 4 hours to 50%, after half a day to 14% and after one day to only 2%, from which it must be concluded that rainfall influence lasts for 1/2-1 day. This agrees with field observations, which showed that the effect of a rainstorm on the regolith surface had generally disappeared the next day. Finally,  $i_{r,5}$  appears to be

Table 8.6 Hydrological factors and debris-flow triggering: multiple-variable models.

Model parameters				Logistic regression results <sup>a</sup>					
1	2	3	4	$\chi^2$ <sup>c</sup>	Regression constants <sup>d</sup>				
					$a_0$	$a_1$	$a_2$	$a_3$	$a_4$
<b>2-parameter linear models</b>									
$i_{r,5}$	$i_{r,5}$			55.2	-8.71	0.147	0.0072		
$i_{r,5}$	$I_{r,10}$			56.4	-8.42	0.132	0.062		
$i_{r,5}$	$API_{0,10}$			53.7	-7.77	0.132	0.11		
$i_{r,5}$	$API_{5,4}$			58.4	-10.47	0.145	0.131		
$I_{r,10}$	$i_{r,5}$			38.9	-3.52	0.367	-0.049		
<b>3-parameter linear models</b>									
$i_{r,5}$	$I_{r,10}$	$i_{r,5}$		56.4	-8.43	0.132	0.061	0.0002	
$i_{r,5}$	$API_{5,4}$	$I_{r,10}$		59.5	-10.98	0.148	0.112	0.036	
$i_{r,5}$	$API_{5,4}$	$i_{r,5}$		59.7	-11.75	0.161	0.123	0.0063	
<b>4-parameters linear model</b>									
$i_{r,5}$	$API_{5,4}$	$I_{r,10}$	$i_{r,5}$	59.7	-11.7	0.16	0.122	0.0028	0
<b>2-parameter models with <sup>10</sup>log-transformed data</b>									
$i_{r,5}$	$i_{r,5}$			58.7	-35.21	17.66	2.76		
$i_{r,5}$	$I_{r,10}$			58.9	-28.76	14.35	3.47		
$i_{r,5}$	$API_{5,4}$			59.9	-34.66	16.94	4.59		
$I_{r,10}$	$i_{r,5}$			49.4	-0.01	15.27	-10.62		
<b>3-parameter models with <sup>10</sup>log-transformed data</b>									
$i_{r,5}$	$I_{r,10}$	$i_{r,5}$		59	-32.09	15.89	2.12	1.297	
$i_{r,5}$	$API_{5,4}$	$I_{r,10}$		60.8	-35.61	16.78	3.71	1.94	
$i_{r,5}$	$API_{5,4}$	$i_{r,5}$		61.2	-41.16	19.25	3.5	2.2	
<b>4-parameter model with <sup>10</sup>log-transformed data</b>									
$i_{r,5}$	$API_{5,4}$	$I_{r,10}$	$i_{r,5}$	61.3	-46.19	21.64	3.69	-2.16	4.05
<b>2-parameter model with <sup>10</sup>log-transformed API</b>									
$i_{r,5}$	$API_{5,4}$			58.7	-14.37	0.144	5.33		

<sup>a</sup> Logistic regression with maximum-likelihood estimator and with 'possible' assigned to group 'debris flow absent'.

<sup>b</sup> Variation explained by logistic regression using least-squares estimator on non-weighted data and with 'possible' assigned to group 'debris flow absent'. Values added to allow for a rough comparison of  $\chi^2$  and  $r^2$ .

<sup>c</sup> Average only:  $\chi^2 = 80.2$ . All logistic regressions are significant at the 95% confidence level ( $\alpha = 0.000$ ).

<sup>d</sup> Constants in logistic regression function (eqs. 8.1, 8.3 and 8.4).

the maximum rainfall intensity variable best correlated with debris-flow triggering when used in combination with antecedent rainfall.

Other combinations of  $i_{r,5}$ ,  $API_{5,4}$ ,  $I_{r,n}$  and  $t_{r,n}$  were also investigated, using linear combinations of either the 'raw' variables or of their log-transformed values (table 8.6 and fig. 8.7). To reduce the number of models, the only maximum rainfall intensity used was  $i_{r,5}$ . The log-log logistic model is given by:

$$\text{logit}(p) = a_0 + a_1 {}^{10}\log(i_{r,5}) + a_2 {}^{10}\log(x_2) + \dots + a_N {}^{10}\log(x_N) \quad 8.4$$

As table 8.6 shows, the highest explained  $\chi^2$  for a given number of variables (2 or 3) always occurs for a combination of variables with at least  $i_{r,5}$  and  $API_{5,4}$ . Therefore, one more model was investigated:

$$\text{logit}(p) = a_0 + a_1 i_{r,5} + a_2 {}^{10}\log API_{5,4} \quad 8.5$$

None of the multiple variable models appears to give a large rise in the explained  $\chi^2$  over the single-variable model with  $i_{r,5}$ . This raises the question whether or not the rise in explained  $\chi^2$  by any additional variable is significant. Table 8.7 gives Akaike's (1973) Information Criterion,  $AIC$ , for the different models. The  $AIC$  can be used to find the model which forms the best compromise between the explained variation  $\chi^2$  and the number of variables used in the model. The  $AIC$  is defined as:

Table 8.7 Akaike's (1973) Information Criterion  $AIC$  for logistic-regression models.

Model parameters				Linear models		Logarithmic models					
1	2	3	4	$N^a$		$\chi^2$		$AIC$		$\chi^2$	
				Normal	Corrected <sup>b</sup>	Normal	Corrected <sup>b</sup>	Normal	Corrected <sup>b</sup>	Normal	Corrected <sup>b</sup>
<b>1-parameter models</b>											
$i_{r,2}$				2		51.5	32.7			53	31.2
$i_{r,3}$				2		50.6	33.6			52.8	31.4
$i_{r,5}$				2		52.2	32.0			55.1	29.1
$i_{r,10}$				2		52.8	31.4			56.5	27.7
$i_{r,15}$				2		51.2	33.0			55.3	28.9
$Q_{T,L,h}$				2	5	53.5	30.7	36.7		58.8	25.4
$Q_{T,L,h}$				2	5	54.2	30.0	36.0		57.5	26.7
$Q_{T,R,h}$				2	6	53.5	30.7	38.7		59.4	24.8
$Q_{T,R,h}$				2	6	54	30.2	38.2		57.3	26.9
$Q_{D,h}$				2	9 <sup>c</sup>	50.8	33.4	47.4		55.2	29.0
$Q_{D,h}$				2	9 <sup>c</sup>	41.5	42.7	56.7		44.5	39.7
<b>2-parameter models</b>											
$i_{r,5}$	$API_{5,4}$			3	4	58.4	27.8	29.8		59.9	26.3
$i_{r,5}$	$API_{0,10}$			3	4	53.7	32.5	34.5			
$i_{r,5}$	$I_{r,n}$			3		56.4	29.8			58.9	27.3
$i_{r,5}$	$t_{r,n}$			3		55.2	31.0			58.7	27.5
$i_{r,5}$	$t_{r,n}$			3		38.9	47.3			49.4	36.8
<b>3-parameter models</b>											
$i_{r,5}$	$API_{5,4}$	$I_{r,n}$		4	5	59.5	28.7	30.7		60.8	27.4
$i_{r,5}$	$API_{5,4}$	$t_{r,n}$		4	5	59.7	28.5	30.5		61.2	27.0
$i_{r,5}$	$I_{r,n}$	$t_{r,n}$		4		56.4	31.8			59	29.2
<b>4-parameter model</b>											
$i_{r,5}$	$API_{5,4}$	$I_{r,n}$	$t_{r,n}$	5	6	59.7	30.5	32.5		61.3	28.9
<b>2-parameter model with <sup>10</sup>log-transformed <math>API^d</math></b>											
$i_{r,5}$	$API_{5,4}$			3	4	58.7	27.5	29.5			

<sup>a</sup> Number of model parameters.

<sup>b</sup> Number of model parameters, corrected for 'hidden' parameters from underlying models.

<sup>c</sup> Some of the model parameters are constant throughout the catchment, others differ between cells.

<sup>d</sup> See equation 8.5.

Legend for figures 8.7-8.9

+ debris flow: certain, very likely, likely  
• no debris flow: possible, unlikely, certainly not

impossible combinations

probability contours:

—  $p = 0.5$   
- - -  $p = 0.25$   $p = 0.75$   
...  $p = 0.1$   $p = 0.9$   
- - -  $p = 0.05$   $p = 0.95$   
...  $p = 0.02$   $p = 0.98$   
- - -  $p = 0.01$   $p = 0.99$   
...  $p = 0.005$   $p = 0.995$

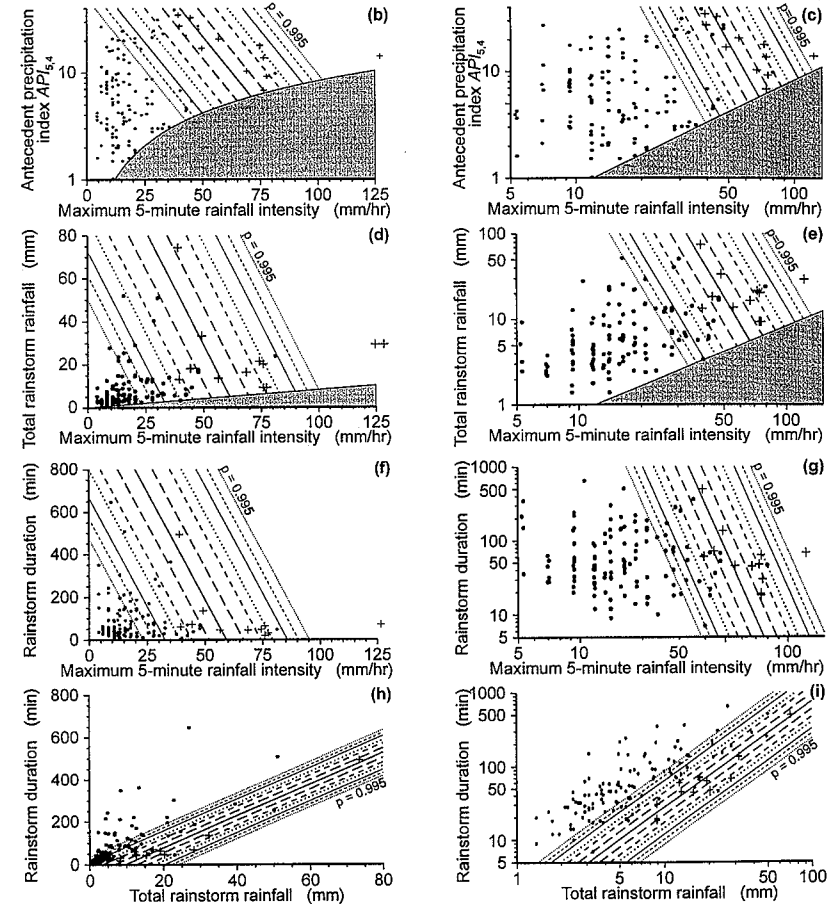


Figure 8.7 Relation between debris-flow triggering and hydrological factors: debris-flow triggering-probability contour plots for 2-parameter models: (a)  $i_{r,5}$  and  $API_{5,4}$ ; (b)  $i_{r,5}$  and  $\log(API_{5,4})$ ; (c)  $\log(i_{r,5})$  and  $\log(API_{5,4})$ ; (d)  $i_{r,5}$  and  $I_{r,n}$ ; (e)  $\log(i_{r,5})$  and  $\log(I_{r,n})$ ; (f)  $i_{r,5}$  and  $t_{r,n}$ ; (g)  $\log(i_{r,5})$  and  $\log(t_{r,n})$ ; (h)  $I_{r,n}$  and  $t_{r,n}$ ; (i)  $\log(I_{r,n})$  and  $\log(t_{r,n})$ .



where the number of parameters exceeds the number of variables by one for the models used in this study. The model with the minimum  $AIC$ -value is the optimal model. Webster and McBratney (1989) have used the  $AIC$  to compare the goodness-of-fit of different models for soil property variograms, in compliance with the number of model variables. Van der Perk (1996, 1997) used the  $AIC$  to compare phosphate concentration models with different degrees of complexity.

Using the  $AIC$ , table 8.7 (columns ' $AIC$  - normal') seems to suggest that the 2-variable model with  $i_{rs}$  and  $API_{5,4}$  is the best of the linear models ( $AIC = 27.8$ ) and that the best overall model is the single-variable model based on log-transformed  $Q_{T,RIR,s}$  ( $AIC = 24.8$ ). However, some of the variables used in these logistic regressions have been calculated from models which themselves have used parameters that had to be calibrated. For instance,  $Q_{T,RIR,s}$  appears as a single variable in the logistic regressions, but in its calculation (see Chapter 7) four parameters were involved: the correction factors for hydraulic conductivity,  $\alpha_K$ , and sorptivity,  $\alpha_S$ , and the catchment outflow constants for rills,  $\alpha_{Rr}$  and for interrills,  $\alpha_{IR}$ . These four parameters can be seen as parameters 'hidden inside' the variable  $Q_{T,RIR,s}$  and this raises the  $AIC$  of the seemingly best overall model from 24.8 to 32.8. When the  $AIC$  is corrected for such extra, 'hidden' parameters according to equation 8.6, the best linear models are the 2-variable models with  $i_{rs}$  and either  $API_{5,4}$  or  $I_{rs}$  ( $AIC = 29.8$ ; figs. 8.7a and d). The best overall model is now the 2-variable logarithmic logistic model with  $i_{rs}$  and  $I_{rs}$  ( $AIC = 27.3$ ; fig. 8.7e):

$$\log(p) = -28.76 + 14.35^{10} \log i_{rs} + 3.47^{10} \log I_{rs} \quad 8.7$$

closely followed by the 2-variable logarithmic logistic model with  $i_{rs}$  and  $t_{rs}$  ( $AIC = 27.5$ ; fig. 8.7g) and the 1-variable logarithmic model with  $i_{rs}$  ( $AIC = 27.7$ ; fig. 8.6a).

The results clearly show that (peak overland flow discharge caused by) maximum short-duration ( $\leq 15$ -minutes) rainfall intensity is the main factor controlling debris-flow triggering. A maximum 5-minute rainfall intensity of about 55 mm/hr has 50% probability of triggering a debris flow. Secondary factors are antecedent rainfall from the same rainstorm, total rainstorm rainfall and rainstorm duration. As the value of any of these secondary factors increases, the rainfall intensity needed to maintain a fixed level of debris-flow triggering probability decreases. For instance, if the antecedent precipitation index  $API_{5,4}$  rises from 6 to 26, the maximum 5-minute rainfall intensity  $i_{rs}$  with a 50% probability of debris-flow triggering decreases from about 68 mm/hr to 46 mm/hr in the logarithmic model (fig. 8.7c).

### 8.3.3 Other models for debris-flow triggering

In figure 8.7, the probability contours of the logarithmic logistic model appear as straight lines when plotted on log-log scale. Any of these contours can be described by a function  $x_2 = f(x_1)$ . By rewriting equation 8.4 in a form similar to that of equation 8.2 and rearranging the results, the following function is obtained:

$$x_1 = 10^{\left\{ \frac{a_0}{a_1} + \frac{1}{a_1} \ln \left( \frac{p}{1-p} \right) \right\}} \cdot x_2^{\left\{ \frac{a_2}{a_1} \right\}} = 10^{\left\{ \frac{a_0}{a_1} \right\}} \cdot \left( \frac{p}{1-p} \right)^{\left\{ \frac{\ln 10}{a_1} \right\}} \cdot x_2^{\left\{ \frac{a_2}{a_1} \right\}} \quad 8.8$$

For  $x_1 = I_{rs}$  and  $x_2 = t_{rs}$ , a formula similar to Innes' (1983a) debris-flow triggering threshold curve (eq. 2.5) is obtained (with  $t_{rs}$  in minutes and  $t_r$  in hours !):

$$I_{rs} = 1.0015 \left( \frac{p}{1-p} \right)^{\left( \frac{\ln 10}{15.27} \right)} \cdot I_{rs}^{0.695} = 17.24 \left( \frac{p}{1-p} \right)^{0.1508} \cdot t_r^{0.695} \quad 8.9$$

The power coefficient in these curves (0.695) is higher than the one in Innes' (1983a) equation (0.5041) and even slightly higher than the one in the equation derived from Caine's (1980) debris-flow

triggering threshold curve (eq. 2.4). As the power coefficient in this study differs from those of Caine and Innes, the debris-flow thresholds defined by them do not correspond to single, fixed levels of debris-flow triggering probability, but these levels vary with rainfall duration. From figure 8.8 it can be seen, that the debris-flow triggering threshold derived from Caine (1980) corresponds to 50% debris-flow triggering probability for short rainfall durations ( $\leq 20$  minutes), to 25% for medium rainfall durations (0.5 - 2 hours) and to 10% for longer durations ( $\geq 5$  hours). Looking at the 50% probability line, for short rainfall durations ( $\leq 30$  minutes) Caine's curve predicts the same threshold amount of rainfall to trigger debris flows, but for longer rainfall durations her curve predicts lower threshold amounts of rainfall. Only two debris-flow triggering rainstorms are situated below the threshold, and only few non-debris-flow rainstorms are situated above the threshold line. Thus Caine's (1980) curve describes debris-flow triggering conditions in the Tête du Clot des Pastres debris-flow trigger zone quite well. On the contrary, Innes' (1983a) curve describes threshold conditions for debris-flow triggering very poorly.

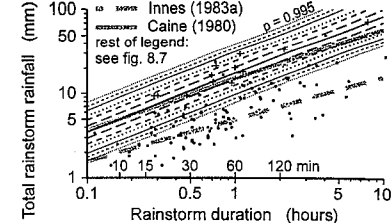


Figure 8.8 Comparison of Caine's (1980) and Innes' (1983a) debris-flow thresholds with debris-flow triggering probability curves.

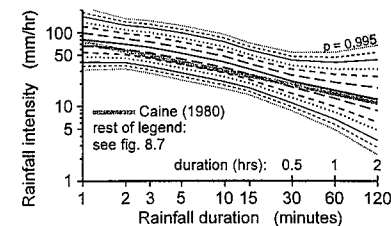


Figure 8.9 Comparison of debris-flow triggering-probability curves with Caine's (1980) debris-flow threshold.

Figure 8.9 shows the relation between Caine's (1980) original debris-flow threshold and the debris-flow probabilities obtained from the logarithmic logistic regression function. Caine's (1980) curve generally has the same slope as the probability contours. For durations of 2-15 minutes, her curve corresponds to a 15-20% probability of debris-flow triggering.

Figures 8.10a-h show the maximum intensity - duration curves for most of the rainstorms in the period June 1991 - September 1994, together with Caine's (1980) and Innes' (1983a) threshold curves. Each individual rainstorm is indicated by a letter. Once again, it shows that Caine's (1980) threshold is a far better indicator for conditions leading to debris-flow triggering than Innes' (1983a) threshold. All rainstorms from the group *debris flow present*, except for the 29 August 1992 rainstorm (fig. 8.10c), amply exceed Caine's threshold for durations between 3-15 minutes. On the contrary, only four rainstorms from the group *debris flow absent* also exceed Caine's (1980) curve over the range 3-15 minutes. One of these has behaved in an unexpected way: the 22 July 1994 rainstorm starting at 15:25 hr (fig. 8.10f). This rainstorm did not seem to have triggered a debris flow, yet it is situated well above the threshold. In fact it is the second most intense rainstorm recorded during the study. Although some activity (overland flow, some small debris surges) was observed on the videotapes, this seemed too limited to trigger a debris flow.

Altogether, 12 rainstorms from the group *debris flow absent* exceed Caine's (1980) curve somewhere in the range 1-120 minutes. The majority of these, 8, have occurred in September (67%). Comparison with the relative number of rainstorms in September (35 out of a total of 131 = 27%) seems to indicate that the debris-flow threshold increases slightly during summer. This may well be related to a deepening of rills and gullies in the debris-flow trigger zone during summer, and the consequential decrease of the amount of unconsolidated, readily available material at the surface (see section 3.3).

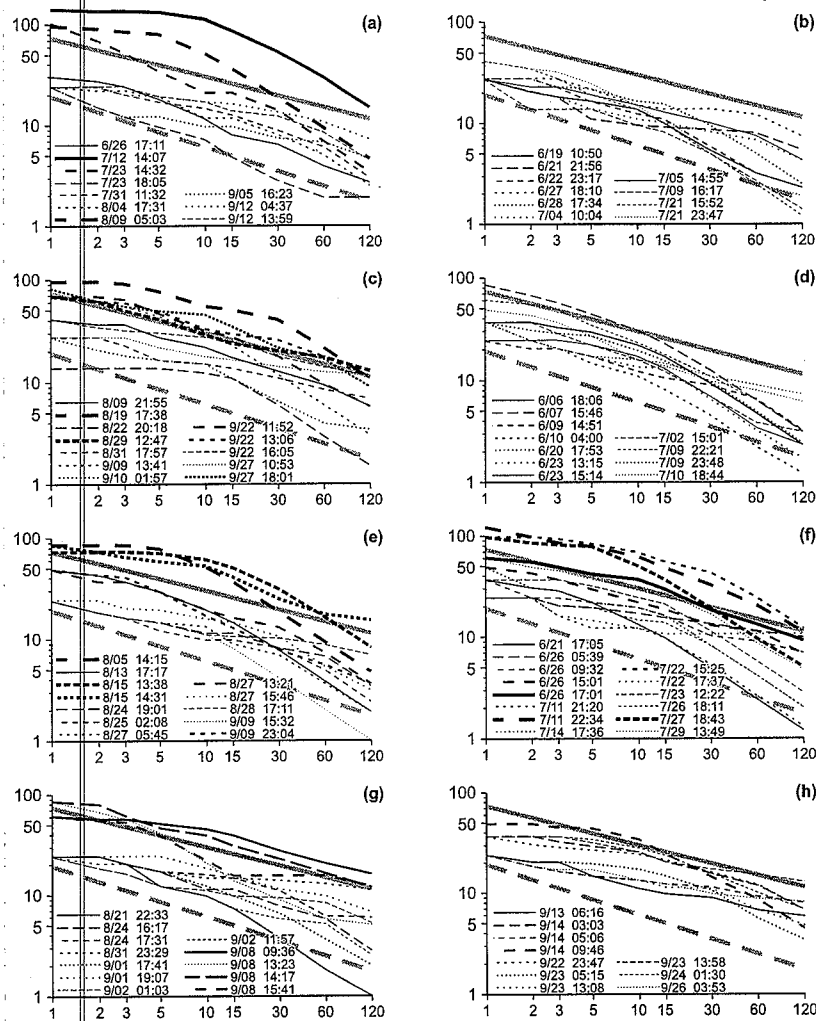


Figure 8.10 Comparison of individual rainstorms with Caine's (1980) and Innes' (1983a) debris-flow thresholds: (a) June-September 1991; (b) June/July 1992; (c) August/September 1992; (d) June/July 1993; (e) August/September 1993; (f) June/July 1994; (g) August/September 1994; (h) September 1994. Horizontal axis: rainfall duration (minutes); vertical axis: maximum rainfall intensity (mm/hr).

#### 8.4.1 The maximum 10-minute rainfall intensity frequency curve

The step from triggering to frequency of debris flows implies some knowledge of the frequency or the frequency distribution of the debris-flow triggering factor(s). In this section such a frequency distribution curve will be produced for the occurrence of maximum 10-minute rainfall intensities and this curve will be used to obtain some estimates of debris-flow frequency. The log-transformed maximum 10-minute rainfall intensity was used because it is the variable best correlated with debris-flow triggering. Also, frequency distributions are much more difficult to calculate for combinations of 2 or more variables. 10-minute rainfall intensities were extracted from the complete rainfall data set and show a bimodal distribution (fig. 8.11). For further analysis the data from the high peak at very low rainfall intensities ( $\leq 1.5$  mm/hr) were discarded because these data could strongly influence distributions fitted to the data. This seems to be justified, because in this study interest is mainly on high rainfall intensities, rainfall intensities that produce runoff and may trigger debris flows.

As figure 8.12 shows, the remaining log-transformed data are slightly positively skewed. A Gumbel type I distribution fits this distribution better than a log-normal distribution (Seyhan 1979), as is generally the case for distributions of extremes. Especially, the Gumbel distribution gives a more accurate description of the high-end tail of the distribution (Middelkoop and Van der Perk 1991), on which interest is focussed in this study. For these reasons, the Gumbel type I distribution has been widely used in flood frequency research (e.g. Coulson 1966, Viessman et al. 1989, Middelkoop and Van der Perk 1991). It has also been used to analyse rainfall data, for example by Cayla and Taibi (1990) for the frequency distribution of annual maxima of total rainstorm precipitation. Seyhan (1979) mentions the use of the Gumbel type I distribution for the frequency analysis of maximum daily rainfall amounts. The Gumbel type I probability density function PDF is given by:

$$PDF(x) = \alpha e^{-\alpha(x-\beta)} - e^{-\alpha(x-\beta)} \quad 8.10$$

and the cumulative distribution function CDF by:

$$CDF(x) = e^{-e^{-\alpha(x-\beta)}} \quad 8.11$$

with:

$$\alpha = \frac{\pi}{\sqrt{6}} s_x \quad 8.12$$

$$\beta = \bar{x} - \frac{C_E}{\alpha} \approx \bar{x} - 0.45 s_x \quad 8.13$$

where:  $x$  = value of variable  $X$ ;  $\bar{x}$  and  $s_x$  are the average and standard deviation of  $X$ ;  $\alpha$  and  $\beta$  are the Gumbel-distribution parameters ( $\beta$  has the same units as  $X$ ;  $\alpha$  has the units of  $1/X$ );  $C_E$  is Euler's constant ( $\approx 0.5572$ ).  $\alpha$  is a measure of the concentration (or conversely: the dispersion) of the distribution,  $\beta$  is the mode of the distribution. The standard error of the Gumbel estimate of the magnitude  $x_T$  for a given return period  $T$ ,  $se(x_T)$  can be calculated from (Seyhan 1979):

$$se(x_T) = \delta \sqrt{\frac{2}{N} s_x^2} \quad 8.14$$

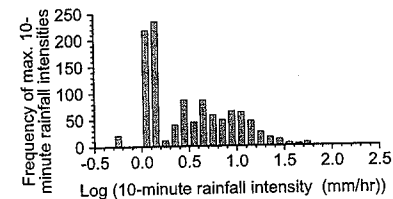


Figure 8.11 Frequency distribution of maximum 10-minute rainfall intensities.

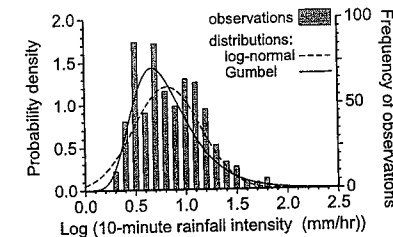


Figure 8.12 Frequency and probability density distributions for maximum 10-minute rainfall intensities  $>1.5$  mm/hr ( $N=623$ ).

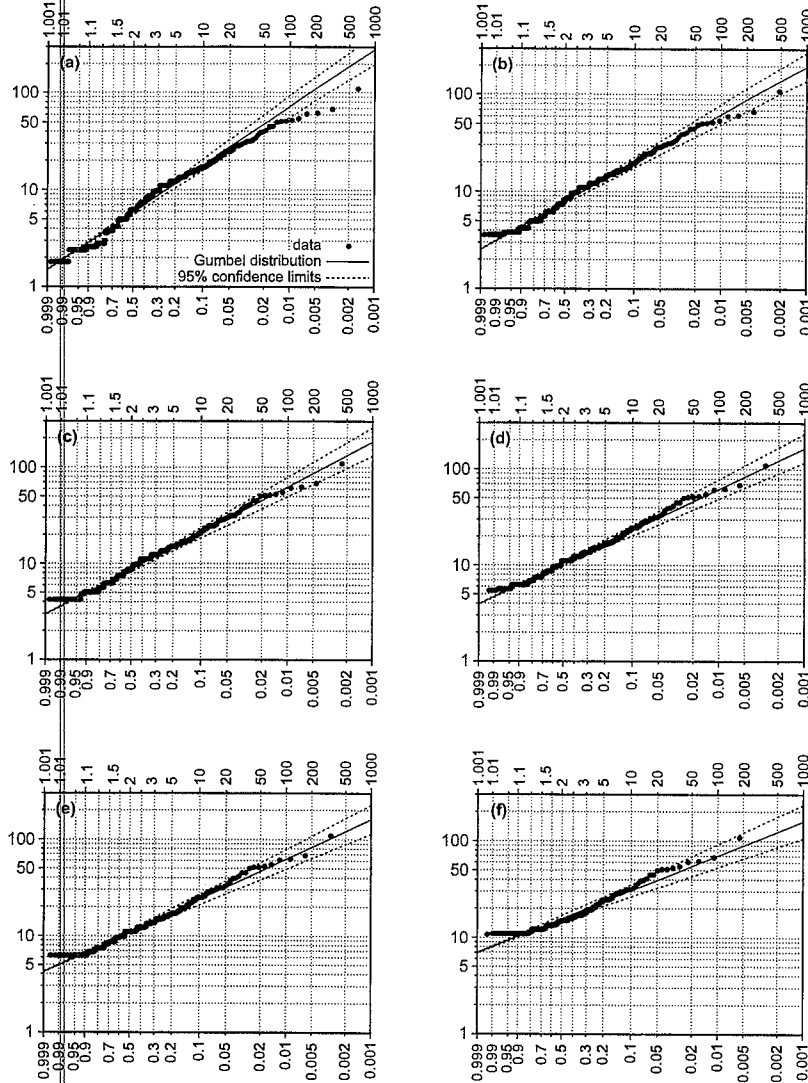


Figure 8.13 Gumbel distribution and 95% confidence limits of exceedance probabilities and return periods for 10-minute rainfall intensities: (a) data  $>1.5$  mm/hr ( $N = 623$ ); (b)  $>3$  mm/hr ( $N = 485$ ); (c)  $>4$  mm/hr ( $N = 440$ ); (d)  $>5$  mm/hr ( $N = 354$ ); (e)  $>6$  mm/hr ( $N = 333$ ); (f)  $>10$  mm/hr ( $N = 182$ ). Horizontal axis: top: return period (number of rainfall peaks), bottom: exceedance probability per rainstorm; vertical axis: maximum 10-minute rainfall intensity (mm/hr).

where:  $\delta$  is a parameter depending on  $T$  and on the number of observations  $N$ . The error of the estimate is normally distributed, so the confidence interval of the estimate can be obtained from multiplying the standard error by the standardized normal variate  $t_n$  corresponding to the desired confidence level. For the 95% confidence level,  $t_{n, 0.05} \approx 1.96$ .

To obtain a frequency measure for the data, the method of plotting positions was used (Seyhan 1979, Coulson 1966). Data were arranged from high to low, ranks  $M(1..N)$  were assigned to them and plotting positions were calculated with the Weibull method (Seyhan 1979, Coulson 1966) method:

$$P(x \geq x_M) = \frac{M}{N+1}$$

and

$$T(x \geq x_M) = \frac{1}{P(x \geq x_M)} = \frac{N+1}{M}$$

where:  $x_M$  = magnitude of observation with rank  $M$ ;  $P(x \geq x_M)$  and  $T(x \geq x_M)$  are the probability and the return period of an event of magnitude  $x_M$  or higher.

Figure 8.13a shows both the data plotting positions and the fitted Gumbel distribution with the 95% confidence limits, plotted on Gumbel-logarithmic extremal-probability paper. If the data are really Gumbel type I distributed, they should plot as a straight line. Figure 8.13a shows, that this is not the case. Especially at higher rainfall intensities, the data plot outside the 95% confidence interval. Therefore more low-intensity data were discarded, successively for rainfall intensities  $\leq 3$ ,  $\leq 4$ ,  $\leq 5$ ,  $\leq 6$  and  $\leq 10$  mm/hr, and Gumbel distributions were fitted to the remaining data (figs. 8.13b-f). It appeared that the best fit for the Gumbel distribution was obtained when all rainfall intensities  $\leq 5$  or  $\leq 6$  mm/hr were discarded (figs. 8.13d and e). It was decided to use the data  $>6$  mm/hr for further analysis (fig. 8.14). The discarded lower intensities are not relevant with respect to debris-flow triggering: a 10-minute rainfall intensity of 6 mm/hr has a probability  $<10^{-5}$  of triggering a debris flow.

At this point, a remark has to be made concerning the return periods in figures 8.13a-f. These are given in 'number of' rainfall peaks' and not in 'years'. This was done because the period of observations was discontinuous. However, using some assumptions, the unit 'rainfall peaks' can be converted to the unit 'years':

- 1 In the months November - May the area is snow-covered with precipitation in the form of snow.
- 2 In the months June - October the area is free of snow and precipitation is in the form of rain.
- 3 In the months June - October the rainfall regime does not change.

These assumptions effectively mean, that only the months June through October are presumed to be relevant with respect to debris-flow triggering and that debris flows should occur evenly throughout the period June - October (the active period). In reality, relatively many rainfall peaks with high rainfall intensities have occurred in September (see section 8.3.3), so the third assumption might lead to an overestimation of the annual number of rainfall peaks. For this reason May has been included in the non-active period, although field observations have shown generally snow-free conditions at the end of the month. The active period has a duration of 153 days. Over the course of four years, the field measurement periods counted altogether 450 days, so an 'expected average annual number of rainfall peaks',  $N_{\text{expected}}$  can be calculated:

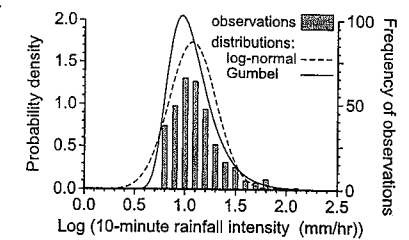


Figure 8.14 Frequency and probability density distributions for maximum 10-minute rainfall intensities  $>6$  mm/hr ( $N=333$ ).

$$N_{\text{expected}} = \frac{153}{450} N_{\text{observed}} = 0.34 N_{\text{observed}}$$

8.17

where:  $N_{\text{observed}}$  = total number of rainfall peaks (maximum 10-minute rainfall intensities) observed during the 450 days of the field measurement periods. By dividing all frequency estimates for the whole period of observations (450 days) by 0.34, frequency estimates on an annual basis are obtained and from these, return periods in years can be calculated easily.

#### 8.4.2 Debris-flow frequencies and return periods

Debris-flow frequencies and return periods have been calculated for the data set >6 mm/hr. Four methods were used by combining the maximum 10-minute rainfall intensity curve with:

- 1 Caine's (1980) threshold value for debris-flow occurrence,
- 2 as method 1, but now including the uncertainty in the rainfall intensity curve,
- 3 The debris-flow probability curve of figure 8.5,
- 4 as method 3, but now including the uncertainties in both curves.

Methods 1 and 3 each give a single value for debris-flow frequency,  $f_{df}$ , and return period,  $T$  (see table 8.8). In contrast, methods 2 and 4 yield frequency distributions of  $f_{df}$  and  $T$ . For these methods, the 95% confidence intervals are presented in table 8.8.

Equation 2.3 shows that Caine's (1980) 10-minute rainfall intensity threshold for debris-flow triggering is 29.8 mm/hr. Figure 8.13e shows that this value corresponds with a probability of exceedance  $P(i_{r,10} \geq 29.8) = 0.057$ , or  $T = 17.5$  rainfall peaks (method 1). This can also be calculated from equation 8.11, but now the probability of non-exceedance,  $P(i_{r,10} \leq 29.8) = 0.945$ , must be used. The 95% confidence interval in method 2 was obtained by calculating the exceedance probabilities for both 95% confidence limits of the maximum 10-minute rainfall intensity Gumbel curve at  $i_{r,10} = 29.8$  mm/hr.

Figure 8.15 shows both the Gumbel curve of maximum 10-minute rainfall intensity and the debris-flow probability as a function of the maximum 10-minute rainfall intensity. By multiplying both curves, a new function,  $f$ , showing the relative contribution of different rainfall intensities to debris-flow triggering is obtained (fig. 8.16):

$$f = 5.59 e^{-5.59(i_{r,10} - 0.967)} - e^{-5.59(i_{r,10} - 0.967)} \times \frac{e^{-22.9 + 14.3 \log i_{r,10}}}{1 + e^{-22.9 + 14.3 \log i_{r,10}}} \quad 8.18$$

Table 8.8 Debris-flow frequencies and return periods for four different methods.

Method	Debris-flow frequency $f_{df}$		Return period $T$		Overestimation ratio of 'input' frequency (= 3 per annum)
	Period of observations <sup>a</sup>	per year	in rainfall peaks <sup>a</sup>	in years	
1 Gumbel curve + Caine (1980) threshold	19	6.45	17.5	0.155	2.2
2 95% Gumbel confidence limits + Caine (1980) threshold	12.6- 26.1	4.30-8.87	12.8-26.3	0.113-0.233	1.4-3.0 (2.2) <sup>b</sup>
3 Gumbel + debris-flow probability curves	12	4.09	27.7	0.244	1.4
4 Gumbel + debris-flow probability curves; accounting for uncertainty in both curves	5.28-26.4 <sup>c</sup> 7.13-22.5 <sup>d</sup>	1.80-8.97 <sup>c</sup> 2.43-7.64 <sup>d</sup>	12.6-63.1 <sup>c</sup> 14.8-46.7 <sup>d</sup>	0.111-0.556 <sup>c</sup> 0.131-0.412 <sup>d</sup>	0.6-3.0 (1.5) <sup>c</sup> 0.8-2.5 (1.5) <sup>d</sup>

<sup>a</sup> Number of observations (total number of rainfall peaks for period of observations) is 333.

<sup>b</sup> Values between brackets are averages.

<sup>c</sup> 2.5% and 97.5% values of Gumbel distribution of calculated debris-flow frequencies.

<sup>d</sup> As <sup>c</sup>, but after rejection of 8 extreme values (> 12 debris flows per annum).

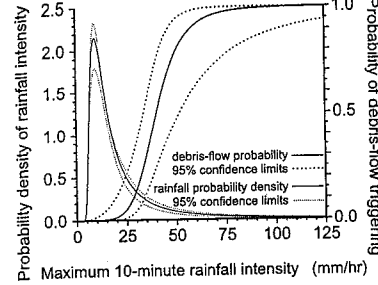


Figure 8.15 Gumbel probability curve of maximum 10-minute rainfall intensity (rainfall intensities >6 mm/hr) and debris-flow triggering probability curve as a function of 10-minute rainfall intensity (logarithmic logistic regression model) and the 95% confidence limits of these curves.

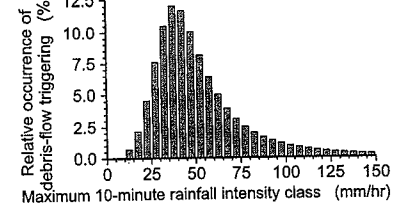


Figure 8.16 Relative occurrence of debris flows as a function of 10-minute rainfall intensity.

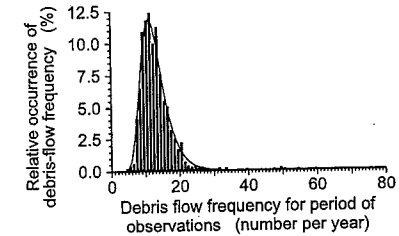


Figure 8.17 Distribution of debris-flow frequencies for the period of observation, obtained from the combination of 1000 pairs of debris-flow probability curves and maximum 10-minute rainfall intensity-frequency curves (method 4).

Figure 8.16 clearly shows that the largest number of debris flows is caused by 10-minute rainfall intensities of 35-45 mm/hr. At lower rainfall intensities, the larger number of rainstorms does not compensate for the very low probability of debris-flow triggering, whereas at higher intensities the increasing likelihood of debris-flow triggering by any rainstorm cannot compensate for the quickly decreasing number of rainstorms. By integrating the curve  $f$ , the total number of debris flows for the period of observations appears to be about 12 (method 3).

Figure 8.15 also shows the 95% confidence limits of the debris-flow probability and rainfall intensity probability functions. It clearly shows that the main source of uncertainty arises from the debris-flow probability curve. In method 4, the uncertainties in both curves were taken into account by randomly drawing curves from a known distribution of curves. For the Gumbel distribution, random curves were drawn from a normal distribution with average = calculated best-fit Gumbel curve and standard deviation given by equation 8.14. From the logistic regressions, the following parameters describing the debris-flow probability were derived: averages  $\bar{a}_0 = -22.86$  and  $\bar{a}_1 = 14.26$ ; standard errors  $se_{a_0} = 6.17$  and  $se_{a_1} = 3.94$ ; correlation coefficient between  $a_0$  and  $a_1$ :  $r_{a_0,a_1} = -0.996$ . Random logistic curves were constructed by first randomly drawing  $a_0$  from a normal distribution with average = -22.86 and standard deviation = 6.17. Next, the corresponding  $a_1$  was calculated from:

$$a_1 = \bar{a}_1 + \left( \frac{a_0 - \bar{a}_0}{se_{a_0}} r_{a_0,a_1} + \varepsilon(1 - r_{a_0,a_1}^2) \right) se_{a_1} = -0.293 - 0.636 a_0 + 0.0302 \varepsilon \quad 8.19$$

where:  $\varepsilon$  is a random term with standard normal distribution. For each pair of curves a debris-flow frequency was calculated in the way described for method 3. The distribution of debris-flow frequencies was calculated from 1000 pairs of curves. This distribution (fig. 8.17) is wide and slightly positively skewed, with a few extreme values (up to 76 debris flows for the period of observations, or 26 debris

flows per annum!), average = 13.25 (4.51 debris flows per annum) and standard deviation = 5.43. The lower and upper 95% confidence limits from this method, 1.80 and 8.97 debris flows per annum respectively (see table 8.10), differ by a factor 5. The Gumbel curve in figure 8.17 has been fitted to the data after rejecting the eight most extreme values (predicting > 35 debris flows) and has the following distribution parameters (for the whole period of observations): average = 12.93 (4.40 debris flows per annum), standard deviation = 3.95, Gumbel  $\alpha$  = 0.3247 and Gumbel  $\beta$  = 11.15. The 95% confidence interval of this distribution is 2.43 - 7.64 debris flows per annum.

When the calculated debris-flow frequencies in table 8.8 are compared with the numbers mentioned in section 8.2, (probably 8-12 debris flows in the whole period of four years), they appear to be on the high side. Especially the methods using the Caine threshold (methods 1 and 2) result in high debris-flow frequencies: about 6 (4-9) per annum, which is about 2.2 times as much as the number of debris flows used as input to construct the debris-flow probability curve (12) and it is four times higher than the minimum number of six debris flows that were identified in the field over a period of four years. Methods 3 and 4 give slightly better results. Method 3 overestimates the most likely number of debris flows by a factor of about 1.4. For method 4, the average of the distribution overestimates the most likely number of debris flows slightly more, by a factor 1.5. When the 'input' number of debris flows used to construct the debris-flow probability curve, 12 (3 per annum), is compared with the confidence bands of methods 2 and 4, it appears that this value falls inside the 95% confidence band of method 4, but outside the 95% confidence band of method 2.

## 8.5 Discussion and conclusions

### 8.5.1 Debris-flow triggering

The logistic regression method has provided several simple, but powerful models explaining debris-flow triggering to a high degree. The factors which are most linked with the triggering of debris flows, are short-duration maximum rainfall intensities (measured over 2-15 minutes) and peak discharges. The best single-parameter model, the logarithmic logistic model, predicts that a 10-minute rainfall intensity of 40 mm/hr has a 50% probability of triggering a debris flow at the TCP site (table 8.4). This value is not very precise: the 95% confidence interval of 10-minute rainfall intensities having a 50% probability of triggering a debris flow is 33-52 mm/hr (fig. 8.15). This confirms the 50 mm/hr threshold intensity mentioned by Blijenberg (1993b), which was based on a preliminary, qualitative interpretation of field data. Blijenberg et al. (1996) mentioned an threshold rainfall intensity for triggering micro-scale debris flows under conditions of simulated rainfall of 60-70 mm/hr on slope angles of 55° or more. Such micro-scale debris flows could be an important mechanism in the triggering of debris flows. However, the threshold mentioned by Blijenberg et al. (1996) was not corrected for splash loss of water during the rainfall simulations. In section 6.4 it was shown that actual rainfall intensities of about 70 mm/hr might trigger micro-scale debris flows on the slopes in the marls at the TCP site, which are generally in the order of 45°. As micro-scale debris flows were only observed in the first few minutes after the start of rainfall simulations, they should be compared with maximum 3-minute rainfall intensities. The 3-minute rainfall intensity with 50% probability of debris-flow triggering is 63 mm/hr (table 8.4; logarithmic logistic model). This intensity is 10% less than the 70 mm/hr mentioned above, although it seems more plausible that the threshold rainfall intensity for the occurrence of micro-scale debris flows should be somewhat lower than the threshold for full-grown debris flows. Perhaps the difference may be attributed to boundary effects (other than splash loss) during the rainfall simulations, resulting in an overestimation of the 'effective' rainfall intensity in the simulations. On the other hand, it can be argued that the 50% probability-of-debris-flow rainfall intensity is not the one corresponding with a 'threshold'. For instance, a 3-minute rainfall intensity of 70 mm/hr has about 65% probability of triggering a debris flow, but it seems unlikely that such

a high probability would correspond with a *minimum* (threshold) value for micro-scale debris flows. Finally, although the micro-scale debris flows seem to be an important mechanism in debris-flow triggering, the conditions causing micro-scale debris flows and full-grown debris flows may well differ.

The logistic regressions have clearly shown that for the small TCP site, the rainstorm duration, total rainstorm rainfall, total daily rainfall and antecedent precipitation are only marginally important for debris-flow triggering. The best available rainfall data for Barcelonnette and the Bachelard Valley are daily totals. It must be concluded that these can hardly be used for the analysis of debris-flow triggering from small-scale (< 10 ha) trigger zones. For the larger debris-flow trigger zones (fig. 3.9), 30-120 minute rainfall intensities may be expected to be most relevant with respect to debris-flow triggering and daily rainfall totals will probably hardly be useful as well. Antecedent rainfall has little influence on debris-flow triggering. The effect of antecedent rainfall on debris-flow triggering appears to last for about half a day to a day, which agrees with Blijenberg (1993b) who mentioned that the effect of rainfall on regolith characteristics disappeared in about 1 day during generally dry periods. However, in the exceptionally wet period of June 1992, the regolith would not return to a dry state even after 2-3 days. The small effect of antecedent rainfall is somewhat surprising, as wet regolith has a lower sorptivity and therefore a shorter time to ponding than dry regolith. Thus more overland flow is generated on a wet regolith, and this should be positively correlated with debris-flow triggering. However, it could be that this effect is counteracted by a fixation of loose material on the slopes during prolonged wet conditions, resulting in a decreased sediment availability.

The multiple variable logistic models usually give only a slight improvement over the single-variable models. Several of the variables used in the logistic regressions have been calculated with the aid of underlying, hidden parameters and variables. This is the case for antecedent precipitation indexes and for TANKFLOW and DINOFLOW peak discharges. When such hidden parameters and variables are taken into account, a simple 2-variable model containing the 5-minute rainfall intensity  $i_{5r}$  and the total rainstorm rainfall  $I_{r,m}$  appears to be the optimal model explaining debris-flow triggering, using Akaike's (1973) information criterion *AIC* to compare the models.

For debris-flow triggering at the Tête du Clot des Pastres site, Caine's (1980) threshold curve appears to be much more meaningful than Innes' (1983a) threshold curve. Caine's threshold corresponds to a debris-flow triggering probability of 15-20% for rainfall intensities taken over intervals of 2-15 minutes. The apparent slight increase from spring to autumn of the threshold rainfall intensity for debris-flow triggering could well be related to a decrease in the availability of loose debris, which was observed in the field by Blijenberg (1993b), Blijenberg et al. (1996) and De Graaf et al. (1993).

### 8.5.2 Debris-flow frequency

The actual debris-flow frequency over a period of four years from June 1991 until June 1995 at the TCP site has been at least 1.5 per annum, most likely 2-3 per annum. Combining the maximum 10-minute rainfall intensity frequency curve with debris-flow occurrence indicators yields estimates of debris-flow frequency that are too high. This is not completely unexpected, because of the way in which the 10-minute rainfall intensities are obtained. The rainfall intensity frequency curve is based on all rainfall intensity peaks during the period of observations which exceeded 6 mm/hr. The debris-flow probability curve is based on maximum rainfall intensities of individual rainstorms; these individual rainstorms can have more than one rainfall intensity peak. Discarding of rainfall intensities of 6 mm/hr and less for the construction of the rainfall intensity frequency curve is justified because such low rainfall intensities do not produce overland flow and therefore they cannot trigger debris flows. Discharge data presented by Blijenberg (1993b) show that 10-minute rainfall intensities of less than 6 mm/hr never generated overland flow and that overland flow may occur for 10-minute rainfall intensities of 10-15 mm/hr or more. One exception is the occurrence of runoff after a 10-minute rainfall

caused by saturation overland flow. The exceptional meteorological conditions of June 1992 are reflected in the low number of dry days and the low number of hours of sunshine recorded at the meteorological station of Embrun, 30 km northwest of the Bachelard Valley. Both broke the previous records.

Using Chaine's (1980) threshold value as a debris-flow occurrence indicator, the debris-flow frequency is overestimated by a factor 2.2 (range 1.4-3.0, see table 8.8). A better result is obtained when the logarithmic logistic debris-flow probability curve is used. With this curve, the observed debris-flow frequency is less overestimated, on average by a factor 1.4. The incorporation of the uncertainty in both the rainfall intensity frequency curve and the debris-flow triggering probability curve yields a wide range for debris-flow frequency: the upper and lower 95% confidence limits of this range differ by a factor 5 (1.80 and 8.97 debris flows per annum). Still this is much less than the range that was expected beforehand: a factor 100 or more. The observed debris-flow frequency of 2-3 debris flows per annum corresponds with values inside the 95% confidence band near the lower confidence limit. The combination of the rainfall intensity frequency curve and the debris-flow probability curve has also shown that debris flows at the TCP site are most frequently triggered by rainstorms with maximum 10-minute rainfall intensities of 35-45 mm/hr, which is the result of the quickly decreasing frequency of rainstorms with higher rainfall intensities on the one hand and the quickly decreasing probability of debris-flow triggering with lower rainfall intensities on the other hand.

### 8.5.3 Performance of the discharge models

Conceptually, discharge should have a higher correlation with debris-flow triggering than rainfall intensity, as discharge has a more direct link with debris-flow triggering. One explanation for the lower-than-expected correlation between calculated discharges and debris-flow triggering is the fact that the discharge models have only been run on a part of the TCP site catchment. A large part of the trigger zone consists of the same type of regolith developed in the marls and should therefore react more or less the same to rainfall. The remainder of the TCP site consists of weathered or intact sandstones, and this part probably reacts differently to rainfall. The sandstone regolith probably conducts water better than the regolith developed in the marls, whereas the intact sandstones are probably less conductive. Unfortunately, the net effect of these two is unknown.

Even so, the more complex, physically-based model DINOFLOW should be expected to perform better than the simple tank model TANKFLOW. Still, the results clearly demonstrate that the complexity of a model is not the only factor determining the results, a fact which has also been noted by Hendriks (1990). Input data for the models are equally important. Each additional input parameter or variable introduces additional input errors in the model result. This applies to measurement errors, interpolation errors and spatial and temporal variations (De Roo et al. 1992, De Roo 1996, Van der Perk 1996). De Roo (1996) referred to this as the 'parameter crisis'. In a study of phosphate concentrations in the Biebrza River, Poland, Van der Perk (1996) concludes that an increasing number of input parameters increased the accuracy of the model (a better prediction of the actual value) at the cost of an increased uncertainty (a larger error band around the predicted value). The conclusion is that at any given level of data availability and data accuracy, there exists one best model that forms the optimal compromise an accurate description of the process (as detailed as possible) and a minimum of input errors (as few input parameters as possible).

The discharge models TANKFLOW and DINOFLOW in this study clearly suffered from a 'parameter crisis'. TANKFLOW generally performed better than DINOFLOW: the complexity of DINOFLOW resulted in even less accurate results than TANKFLOW and also the uncertainty in DINOFLOW discharges is greater than in TANKFLOW discharges. Still, not even TANKFLOW can improve the results of the simple 2-variable regression models based on relatively easy-to-measure rainfall characteristics. Thus, if a model were needed for an early warning system, the choice would be easy.

## 9.1

### Introduction

Traditional reconstruction of debris-flow activity and frequency generally relies on dating of debris-flow deposits by means of dendrogeomorphology, lichenometry or other methods such as clast weathering crusts,  $^{14}\text{C}$  dating (Rapp and Nyberg 1981) or direct observations (Rebetez et al. 1997). Often, dating of debris-flow deposits is inhibited by a lack of datable material on, in or under the deposits, or the deposits are reworked by subsequent processes, such as rock fall, and the datable material is damaged or lost. Convergence may be a problem when dendrogeomorphology is used: changes in tree-ring patterns may be caused by processes other than debris flow, such as rock fall, avalanches or storms. Where debris-flow deposits have been dated, generally very little is known about the relation between the number of deposits recovered in the field and the actual number of debris flows that have occurred in the time span covered by the deposits. Usually the assumption is used -although not always consciously- that all debris-flow events have left recognizable deposits in the field, except those that have been buried by younger deposits.

In this study, dendrogeomorphology and lichenometry were employed in order to date debris-flow deposits from five debris-flow systems in the upper Bachelard Valley and in the Vallon de la Moutière (see fig. 9.1). This chapter contains the results of these datings, which are interpreted in terms of average frequencies and return periods and long-term periodicities. In the next chapter, a comparison will be made with other methods of obtaining debris-flow frequencies.

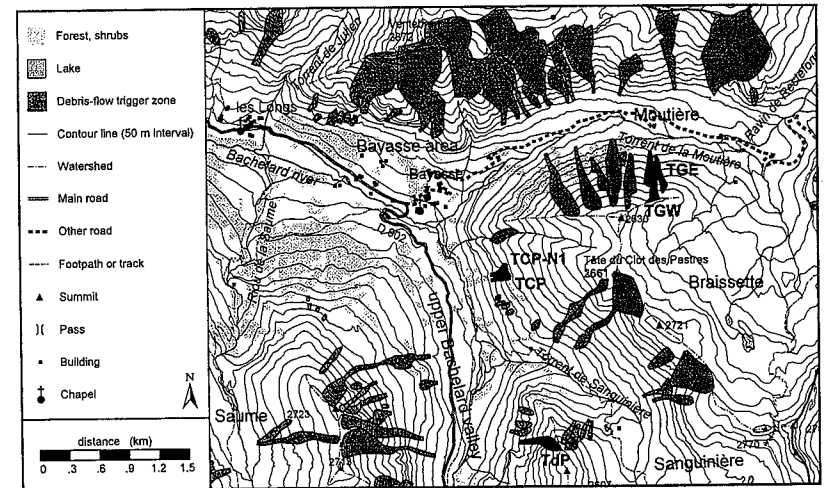


Figure 9.1 Location of debris-flow systems with dated deposits.

## 9.2.1 Dendrogeomorphological data: the Split-Moving Window test

Tree-ring widths and eccentricities were analysed with the Split-Moving Window (SMW) test, shown in figure 9.2 (Webster and Wong 1969, Webster 1973, Braam et al. 1987b). This test can be used on data which have been sampled at regular intervals in time or space. Two equally sized windows are moved over the data series, with a fixed distance (the *mullion* size  $M$ ) between them. For each position of the windows, the window averages are calculated and a measure called the generalized distance,  $D^2$ , is calculated for the difference between the windows:

$$D^2 = \frac{(\bar{x}_1 - \bar{x}_2)^2}{s_1^2 + s_2^2} \quad 9.1$$

where:  $\bar{x}_1$  and  $\bar{x}_2$  are the window segment averages;  $s_1^2$  and  $s_2^2$  are the window segment variances. The window averages can be tested for differences, because  $D^2$  is related to the Student's  $t$ -distribution by:

$$t = \sqrt{D^2 N} \quad 9.2$$

where:  $t$  = Student's  $t$ -statistic;  $N$  = sample size of each window. In fact, this is a difference-of-means test, which is carried out for each position of the windows. By comparing the  $t$ -value for each position of the windows with a critical  $t$ -value (with degrees of freedom  $df = 2N - 2$ ) for a chosen level of significance, the locations of statistically significant changes in tree-ring width or eccentricity can be found. Figure 9.2c shows that the SMW test is not capable of detecting changes near the start and end points of the data series (within a region of size  $N + \frac{1}{2}M$  for even  $M$  and  $N + \frac{1}{2}M - \frac{1}{2}$  for odd  $M$ ).

The SMW test can be adjusted for specific purposes by varying the sizes of the windows and the mullion. Long windows are less sensitive to a noisy data signal but may miss short intervals by averaging across small zones. On the other hand, short windows are more sensitive to short-range patterns and will identify small zones at the cost of a more irregular, possibly uninterpretable pattern of  $D^2$  (Davis 1986). Increasing the mullion size enhances the sensitivity of the technique whenever change takes place gradually. In this study attention is focussed on sudden changes in tree-ring patterns, so a narrow mullion was used:  $M = 1$ . After some experimenting, a window size  $N = 4$  seemed to give reasonable results. Input consisted of tree-ring width series for buried and inclined trees and tree-ring eccentricity series for inclined trees. Tree-ring eccentricities were calculated from equation 2.93 using the computer program CATIR (Braam et al. 1987a, 1987b). The significance level was chosen at 99% ( $\alpha = 0.01$ ), corresponding to a one-tailed critical  $t$ -value of 3.143 for  $df = 6$ . This study uses a one-tailed test, because it was expected that debris flows would only cause a decrease in general tree-ring growth after burial or exposure) or an increase in tree-ring eccentricity (after inclination).

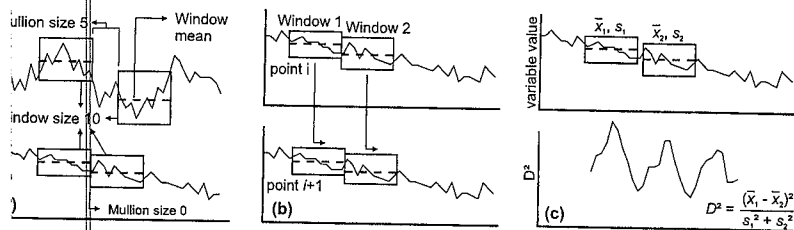


Figure 9.2 The Split-Moving Window (SMW) test: (a) general principles; (b) the test situation at points  $i$  and  $i+1$ ; (c) the test statistic  $D^2$ .

Initially, the lichenometrical datings were based on *Rhizocarpon geographicum* s.l. and *Xanthoria elegans*, but the *Xanthoria elegans* data were discarded because only very few lichens of this type were found. *Rhizocarpon geographicum* s.l. thalli were found in abundance. For deposits with *Rh. geographicum* s.l. thalli, Innes' (1984) rejection criterion for anomalously large thalli (eq. 2.95) was used, although this did not lead to a rejection of any thalli. The term *Rhizocarpon geographicum* s.l. is used to indicate that identification has been performed to *Rhizocarpon* subgenus level (fig. 2.29). Still, it seems likely that these thalli belong to *Rhizocarpon* section *Rhizocarpon* (the *Rhizocarpon Geographicum* group of Innes 1982b); section *Superficiale* and section *Viridiatrum* seem to be relatively rare species that are hardly ever reported in deposit dating studies. Also, although visual separation of section *Rhizocarpon* and section *Alpicola* is difficult, it is unlikely that the thalli belong to section *Alpicola*. First, Orombelli and Porter (1983) state that no *Rhizocarpon alpicola* have been reported growing in 'that part of the Alps' (the vicinity of the Aosta Valley, only 150 km NE of the study area). Second, Innes (1982b, 1983a, 1983d) found that the largest thalli growing on deposits which carry both section *Rhizocarpon* and section *Alpicola* thalli are most likely to belong to section *Rhizocarpon* when they are smaller than 50-60 mm (fig. 2.32). Similar observations were made by Bickerton and Matthews (1992). In a study on the accuracy of lichenometrical dates, they compared the sizes of the largest section *Alpicola* and the largest section *Rhizocarpon* thalli growing on moraines on the glacier foreland of Nigardsbreen, Norway. They found that the largest thalli always belonged to section *Rhizocarpon* for sizes up to about 60 mm (for the single largest thallus) or 85 mm (for the average of the 5 largest thalli). In this study, no largest thalli >40 mm have been found, so even if section *Alpicola* thalli were present, they were unlikely to be the largest thalli on the deposits. Another problem concerned the measured thalli diameters (fig. 2.35). It appeared that we had measured the longest diameter (diameter of the smallest enveloping circle) instead of the shortest diameter (diameter of the largest inscribing circle) which was used by Orombelli and Porter (1983) in the construction of their *Rhizocarpon* growth curve (fig. 9.3). According to them, thalli up to 150 years old (50-55 mm) tend to be reasonably circular, but this is contradicted by data from Innes (1983a) that clearly show a widely varying ratio of the shortest to the longest diameter over the whole range of thalli sizes (fig. 9.4). Thus the application of Orombelli and Porter's (1983) lichen-growth curve appears to be invalid for this study.

Fortunately, the presence of lichens on several debris-flow deposits that have also been dated with dendrogeomorphology made it possible to construct a growth curve for *Rhizocarpon geographicum* s.l. in the Bachelard Valley. These deposits were all located between 1800 and 2150 m elevation.

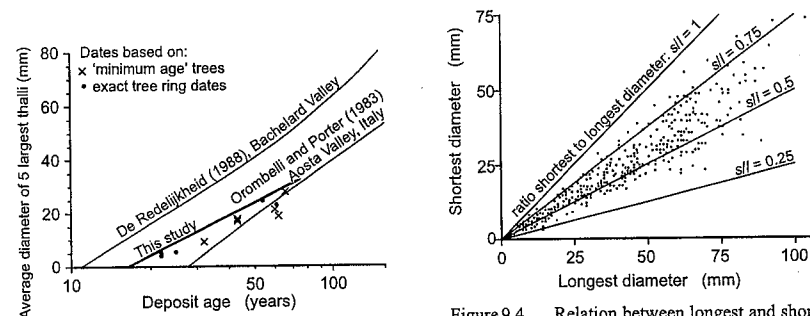


Figure 9.3 *Rhizocarpon geographicum* s.l. growth curves for the Bachelard Valley and the Aosta Valley.

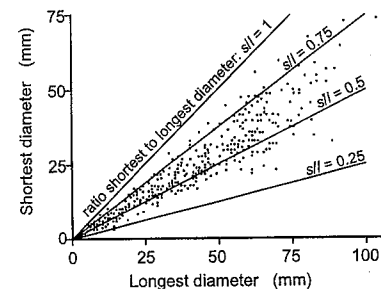


Figure 9.4 Relation between longest and shortest diameters of section *Rhizocarpon* thalli at Storbreen, south Norway (after Innes 1983a).



Number of debris-flow deposits and debris flows dated by lichenometry and dendrogeomorphology.							
Debris-flow system	Number of deposits						Number of dated debris flows
	Total	Undated	Dated with				
			Total	Lichenometry only	Dendrogeomorphology only	Lichenometry and dendrogeomorphology	
II	117	47	70	49	9	12	76
CP	29	9	20	12	2	6	21
CP-N1	30	8	22	10	6	6	27
3E+TGW	34	17	17	16	1	0	17
IP	24	13	11	11	0	0	11

Dated debris-flow deposits.										
Deposit	TCP			TCP-N1			TGE + TGW *			TdP *
	Lichens <sup>c</sup>	Dendro <sup>d</sup>	Visits <sup>e</sup>	Lichens	Dendro	Visits	Lichens	Dendro	Visits	Lichens Visits
1969	1968			1974						
1951	1952									1938
					1972, 1983					1927
					1972, 1988				1969	1935
1955					1971, 1988	1992	1971			1955
1958						1994	1969			1957
1948				1974						1970
1950							1970			1955
1973				1974	1972		1971			1942
1974							1962			1930
	1979						1968			1933
	1990									
1949				1973	1969		1966			
1947				1973	1972		1948			
					1975, 1985		1949			
1945				1961			1939			
1956	1951			1954	1954		1917			
1974					1984, 1986		1946			
		1992		1969	1962					
1949	1938			1958	1951					1972
1942	1940			1954						
1933	1928			1961						
1946				1947						
	1987	1994		1940			1945			
1974					1918		1948			
							1950			
				1948						
				1969						
				1975						
							1930			

Deposits 1-20 probably originate from TGE, deposits 21-34 from TGW. Some doubt remains over deposits 19-22.  
 Dendrochronological datings were made at TdP.  
 Lichenometrical dates.  
 Dendrogeomorphological dates.  
 Dates obtained from 'direct' field observations.

Figure 9.3 also shows these data and the corresponding *Rh. geographicum* s.l. growth curve. This minimum-age curve appears to be linear on a size - log(age) plot and is given by:

$$age = 16.5 \cdot e^{\left(\frac{d_{max,5}}{21.5}\right)} = 16.5 \times 1.0476^{d_{max,5}} \quad 9.3$$

where: 16.5 = colonization period in years;  $d_{max,5}$  = average diameter of the five largest thalli (in mm).

A comparison of the dates obtained from sudden changes in overall growth or eccentricity (*exact ages*) with those obtained from *minimum-age* trees in figure 9.3 shows that these *minimum-age* trees must have colonized the deposits within a few years after deposition took place. If the delay had been longer, the envelope curve for the *exact age* points would not have been the same as for the *minimum-age* points: *minimum-age* points would have appeared more to the left in this figure. For average sizes of the 5 largest thalli per deposit, the largest value used in the construction of the growth curve was 28 mm, which covers the range of all thalli sizes in this study quite well: only 5 deposits had larger average thalli sizes (up to 33 mm). The constructed lichen-growth curve shows that *Rh. geographicum* s.l. has a much shorter colonization period in the Bachelard Valley (16-17 years) than in the Aosta Valley (28 years). On the other hand, the growth in the first 50 years following the colonization period is faster in the Aosta Valley (33 mm; lichen factor 66 mm/century) than in the Bachelard Valley (30 mm; lichen factor 60 mm/century).

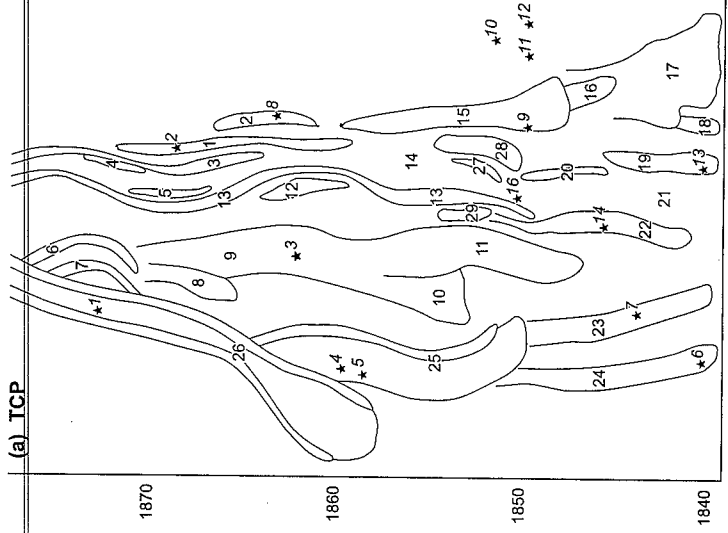
De Redelijkheid (1988) has also constructed a *Rh. geographicum* s.l. growth curve for the Bachelard Valley. He used deposits containing both *Rh. geographicum* and *Xanthoria elegans* and, assuming that his *Xanthoria* dates were more or less exact, corrected the obtained *Rhizocarpon* dates to produce the *Rhizocarpon geographicum* s.l. growth curve shown in figure 9.3. However, this assumption and the procedure described by De Redelijkheid (1988) to correct the *Rh. geographicum* s.l. growth curve seem questionable, especially as it was based on only 7 data points. Figure 9.3 seems to confirm that his procedure has led to a strong overestimation of *Rhizocarpon geographicum* s.l. growth.

### 9.3 Occurrence and frequency of debris flows

Table 9.1 shows the number of debris-flow deposits dated for each of the debris-flow systems investigated and table 9.2 gives the dates obtained for individual deposits shown in figure 9.5a-d. Data from TGE and TGW have been combined, because it was not possible to separate the deposits from both debris-flow systems with certainty. Frequency histograms of debris-flow occurrence are shown in figures 9.6a-g. All together, 76 debris flows have been dated from the deposits. The majority of these have occurred between 1940 and 1975, with two activity peaks: in the late forties to early fifties and in the late sixties to mid seventies. Deposits formed after 1975 were less likely to be dated, because *Rh. geographicum* s.l. lichens on those deposits were still in their colonization phase and therefore invisible or still too few and too small to detect (fig. 9.6f). Such recent deposits could only be dated if they had influenced tree growth (fig. 9.6g). An analysis of the undated deposits also shows that the apparent decrease in dated deposits after 1975 is (at least partly) caused by the absence of dating possibilities. Based on the appearance of the undated deposits and the position of these deposits relative to dated deposits it seems likely that 37 of the 47 undated deposits are quite recent (dating from the seventies, the eighties or the nineties), and only 6 appear to be older. Figures 9.5a-d show that the debris-flow deposits cover large parts of the surface, so it follows that deposits older than 1940 are likely to be buried by more recent ones, which explains the scarcity of deposits older than 1940. For each of the debris-flow systems, the debris-flow frequency has been calculated for the period 1940-1994 (table 9.3). Figure 9.6 shows that the debris-flow systems TCP, TCP-N1, TGE and TGW have only few deposits older than 1940 that have not been buried. Only for TdP has the full data range (1927-1994) been used. A clear difference between the debris-flow systems is present with regard to their activity. TCP-N1 is the most active debris-flow trigger zone with an average debris-flow frequency



(a) TCP



(b) ICP-N1

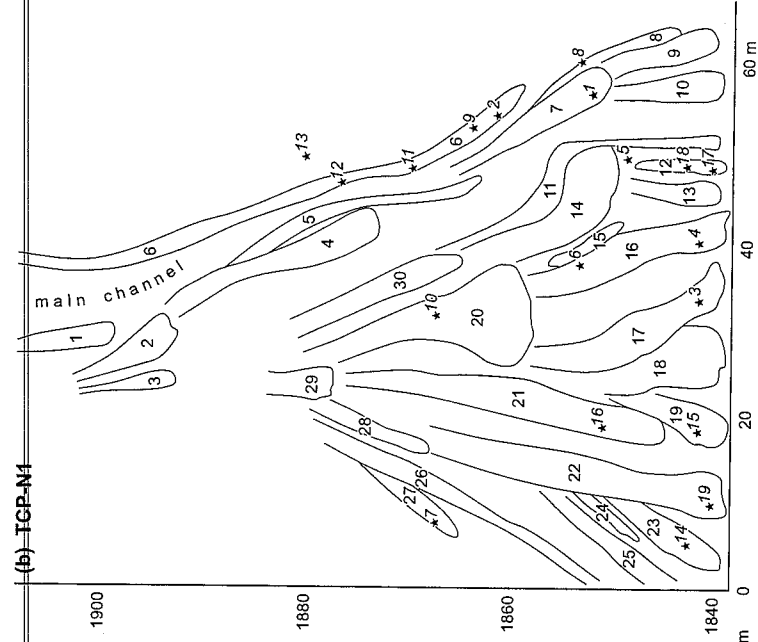
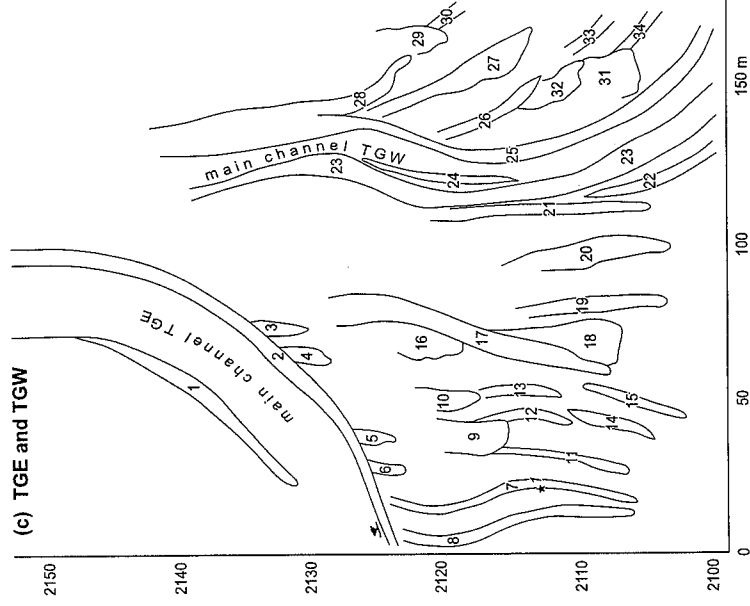


Figure 9.5 Debris-flow deposits from the debris-flow systems TCP and TCP-N1. Vertical axis: elevation; horizontal axis: distance; stars indicate trees used for dating. (after Overbeek and Wiersma 1996)

(c) TGE and TGW



(d) TdP

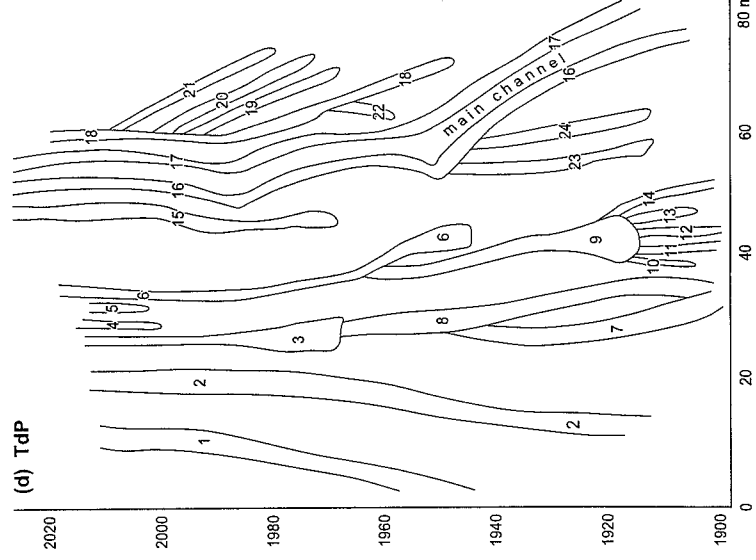


Figure 9.5 (continued)

Debris-flow deposits from the debris-flow systems TG (TGE and TGW) and TdP. Vertical axis: elevation; horizontal axis: distance; stars indicate trees used for dating. (after Overbeek and Wiersma 1996)

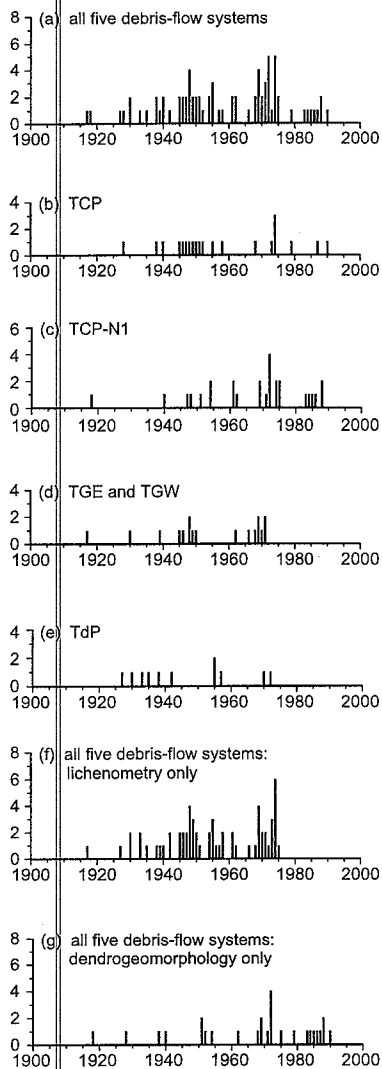


Figure 9.6 Temporal distribution of debris flows obtained from lichenometry and/or dendrogeomorphology. Horizontal axis: year; vertical axis: number of debris flows.

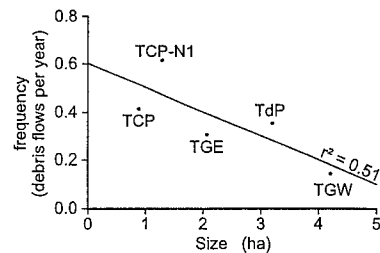


Figure 9.7 Relation between size of trigger zone and activity of debris-flow systems.

of 0.62 df/yr (debris flows per year) and TGW is the least active one with 0.15 df/yr. Figure 9.7 suggests that the activity of a debris-flow system is related to its size. The relation is not statistically significant ( $p = 0.107$ ) at the 95% confidence level, probably due to the small number of data points on which the relation is based.

When the date of a debris-flow deposit is plotted against the relative lateral position of the deposit within the deposition zone, a spatio-temporal pattern of deposition becomes apparent. Figure 9.8 shows the approximate lateral locations of successive debris-flow deposits within their deposit zones. It appears that successive debris flows do not choose their tracks in a random way, but their activity gradually shifts within the deposition zone. Such shifting patterns of activity are obvious for TCP, TCP-N1, TGE and TGW. At TdP the pattern appears to be more random.

In this study, all deposits have been treated independent of each other. However, it is likely that some of the deposits were formed during the same events and form matching pairs, for example a pair of levees formed by a debris flow. From figure 9.5 it appears that this may be true for deposits 4+5, 6+7 and 23+24 at TCP, deposits 5+6 and 23+25 at TCP-N1, deposits 1+2, 3+4, 5+6, 7+8, 12+13, 14+15 and 19+20 at TGE, deposits 23+25 and 33+34 at TGW and deposits 1+2, 3+6, 4+5, 8+9, 10+11 or 11+12 or 12+13 or 13+14, 16+17, 19+20 or 20+21 and 23+24 at TdP. Only a few of these pairs had both deposits dated by lichenometry or dendrochronology (see table 9.4). Table 9.4 has two possible interpretations. First, assuming the dates to be correct, the table shows which deposits actually

Table 9.3 Activity of five debris-flow systems in the period 1940-1994.

Site	Deposits			Average activity		Corrected activity	
	Total	Dated	Undated	Frequency (debris flows / year)	Return period (years)	Frequency (debris flows / year)	Return period (years)
All	111	70	41	2.02	0.5	1.93	0.52
TCP	27	19	8	0.49	2	0.48	2.1
TCP-N1	34	26	8	0.62	1.6	0.61	1.6
TGE	17	10	7	0.31	3.2	0.3	3.3
TGW	8	3	5	0.15	6.9	0.13	7.5
TdP*	24	11	13	0.35	2.8	0.32	3.1

\* Period 1927-1994.

Table 9.4 Possibly matching debris-flow deposits of dated debris-flow systems in the Bachelard Valley.

Site	Deposit pairs
TCP	23 (1940) - 24 (1928)*
TCP-N1	23 (1954) - 25 (1947)
TGE	7 (1969) - 8 (1971)*; 12 (1971) - 13 (1962); 14 (1968) - 15 (1966); 19 (1917) - 20 (1946)
TdP	3 (1938) - 6 (1927); 8 (1955) - 9 (1957); 10 (1970) - 11 (1955); 11 (1955) - 12 (1942); 12 (1942) - 13 (1930); 13 (1930) - 14 (1933)

\* numbers indicate deposit numbers for first and second deposit with corresponding dates between brackets.

<sup>b</sup> Bold values are matching deposits: age difference  $\leq 5$  yrs.

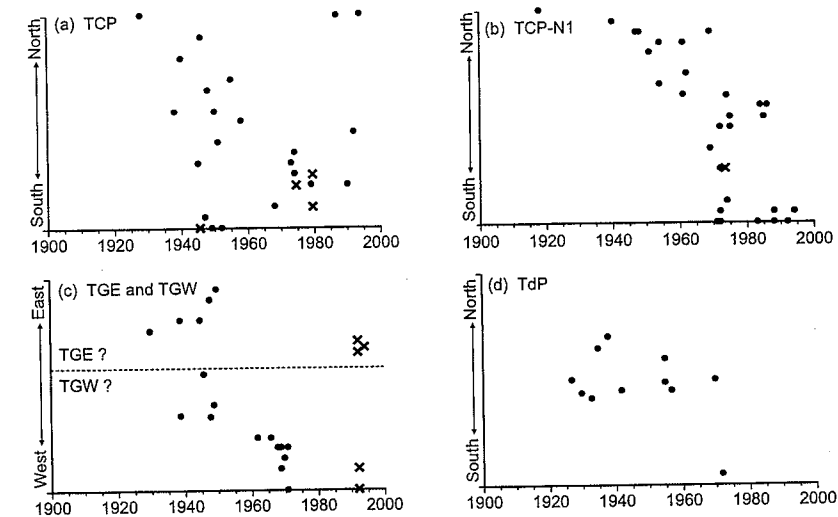


Figure 9.8 Spatial patterns of activity within debris-flow deposition zones. Horizontal axis: year; vertical axis: relative lateral position within deposition zone (the left and right sides of each diagram correspond with the lateral borders of the deposition zone); crosses are deposits with estimated ages.

by the same debris-flow event, the table would show the reliability and accuracy of the datings. Here the first interpretation is used. Using an arbitrary maximum difference of five years between the dates of both deposits indicating that the deposits really form matching pairs, only 4 out of the 12 pairs appear to be matching: 7+8 and 14+15 at TGE/TGW and 8+9 and 13+14 at TdP. By making the assumption that the same ratio (1 in 3) applies to the deposit pairs that were not (both) dated, the calculated frequencies and return periods in table 9.3 were corrected, as also shown in table 9.3. The corrected frequencies are only slightly less than the uncorrected ones. As the difference is only small, and the assumptions in the correction procedure are far from certain, the uncorrected frequencies and return periods have been used for further analysis.

#### 9.4 Temporal variation in debris-flow activity

Spectral analysis is a method to detect the existence of regular temporal variations in a time series by estimating the power spectrum of that time series sampled. It is a modification of Fourier analysis to make it suitable for stochastic rather than deterministic functions of time (Chatfield 1984). Fourier analysis, or harmonic analysis, is concerned with the approximation of a function by a sum of sine and cosine terms, the Fourier series representation:

$$x_t = \sum_{j=0}^{\frac{N}{2}} \left[ a_j \cos\left(\frac{2\pi j t}{N}\right) + b_j \sin\left(\frac{2\pi j t}{N}\right) \right] \quad (t = 1, \dots, N) \quad 9.4$$

with:

$$a_j = \frac{2}{N} \sum_{t=1}^N x_t \cos\left(\frac{2\pi j t}{N}\right) \quad 9.5$$

$$b_j = \frac{2}{N} \sum_{t=1}^N x_t \sin\left(\frac{2\pi j t}{N}\right) \quad 9.6$$

where:  $N$  = number of observations;  $a_j, b_j$  are coefficients;  $j$  = harmonic number ( $= 0, 1, \dots, \frac{1}{2}N$ );  $t$  = time;  $x_t$  = observation at time  $t$ . Note that  $a_0$  equals the average,  $\bar{x}$ , of the time series values and  $b_0$  and  $b_{N/2}$  are zero. With  $N$  parameters to describe  $N$  observations, the Fourier series representation fits the data exactly and explains all of the data variation. Rewriting equation 9.4 as:

$$x_t = \sum_{j=0}^{\frac{N}{2}} (a_j \cos(\omega_j t) + b_j \sin(\omega_j t)) = \sum_{j=0}^{\frac{N}{2}} R_j \cos(\omega_j t + \phi_j) \quad 9.7$$

with

$$\omega_j = \frac{2\pi j}{N} \quad 9.8$$

$$R_j = \sqrt{a_j^2 + b_j^2} \quad 9.9$$

$$\phi_j = \arctan\left(-\frac{b_j}{a_j}\right) \quad 9.10$$

where:  $\omega_j$  =  $j^{\text{th}}$  harmonic or component frequency;  $R_j$  = amplitude of the  $j^{\text{th}}$  harmonic;  $\phi_j$  = phase of the  $j^{\text{th}}$  harmonic. The highest frequency that can be estimated from a series of observations is the Nyquist frequency, whose wavelength is twice the observation interval length  $\Delta t$ . On the other hand, the lowest frequency that can be reasonably fitted has a wavelength equal to the duration of the time series.

The total variance is defined by:

$$s^2 = \frac{1}{N} \sum_{i=1}^N (x_i - \bar{x})^2 \quad 9.11$$

and the contribution of the  $j^{\text{th}}$  harmonic to the variance is given by:

$$s_j^2 = \frac{1}{N} \sum_{i=1}^N (x_{i,j} - \bar{x})^2 = \frac{1}{N} \sum_{i=1}^N R_j^2 \cos^2(\omega_j t + \phi_j) = \frac{R_j^2}{2} \quad 9.12$$

Plotting this contribution against the harmonic number  $j$ , the frequency  $\omega_j$  or the wavelength  $N/j$  results in the so-called periodogram.

A test developed by Fisher (1970, in Davis 1986) can be used to test the significance of the dominant frequency. The test calculates the probability that the contribution  $s_j^2$  of this frequency exceeds the contribution of the dominant frequency in the case of a time series of independent random points. The test statistic  $g$  is given by:

$$g = \frac{s_j^2}{2s^2} \quad 9.13$$

and the critical value of  $g_{p,cr}$  for a specified probability level  $p$  is given by:

$$g_{p,cr} \approx 1 - e^{\left(\frac{\ln p - \ln m}{m-1}\right)} \quad 9.14$$

where:  $m = \frac{1}{2}N$  for even  $N$  and  $m = \frac{1}{2}(N-1)$  for odd  $N$ . If the critical value is exceeded, the periodic component can be presumed to exist.

Figure 9.9 shows the obtained periodograms. It appears that the debris-flow trigger zones each have different spectra. The Fisher test shows that none of the peaks in these spectra are significant at a 95% probability level, so they could have arisen purely by chance. The same applies to the lumped periodograms of figure 9.10. Still, the 2 activity peaks that were identified from the frequency histograms of figure 9.6a seem to correspond with the periodicity peak at 25 years in figure 9.10a. The fact that this peak is not significant in the Fisher test is probably related to the short length of the data series.

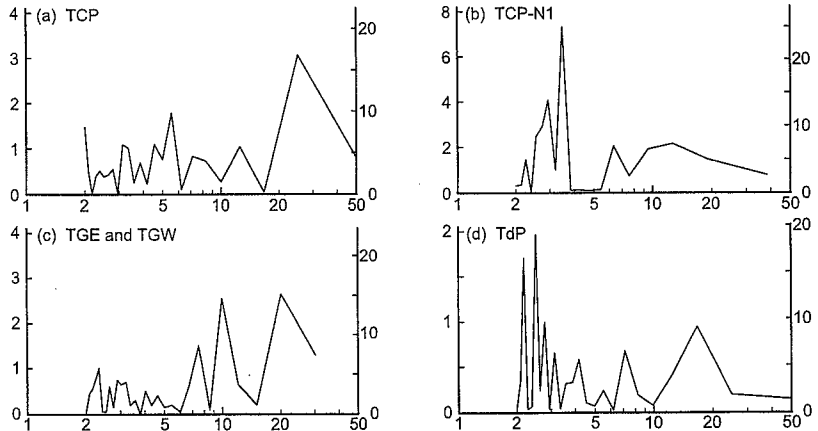


Figure 9.9 Periodicity of debris-flow activity in the five investigated debris-flow systems. Horizontal axis: period in years; left axis: periodogram value; right axis: explained variance in %.

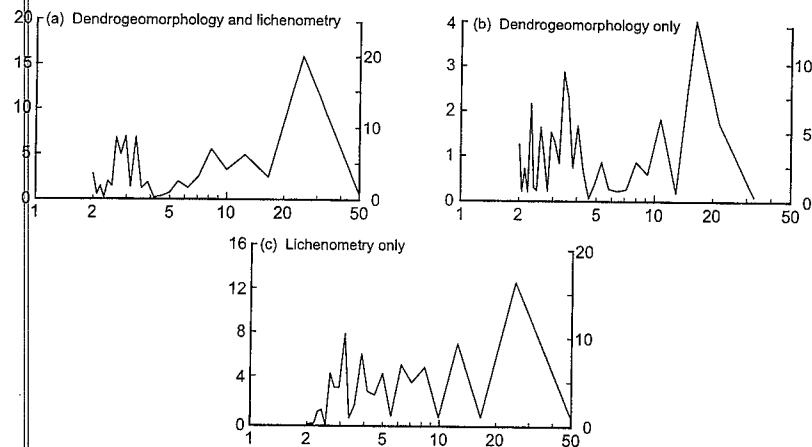


Figure 9.10 Periodicity of debris-flow activity in the Bachelard valley (all five debris-flow systems). Horizontal axis: period in years; left axis: periodogram value; right axis: explained variance in %.

## 9.5 Discussion and conclusions

It appears that both lichenometry and dendrogeomorphology are useful methods for dating debris-flow deposits in the Bachelard Valley, although they are not without problems. For dendrogeomorphological dating of debris-flow deposits in the Bachelard Valley, the number of debris-flow deposits that have actually hit trees and influenced tree growth is only a fraction of the total number of deposits. This problem becomes more severe for deposits at higher elevations, where tree growth is even less dense. In the Bachelard Valley, tree density rapidly decreases above about 2000 m. Also, the interpretation of tree-ring growth/eccentricity reactions can be problematic. Such reactions may also have been caused by processes other than debris flow. Rockfall and snow avalanches appear to be frequent phenomena on the steep slopes in the Bachelard Valley and on many occasions, they will affect debris-flow deposition zones, causing burial, inclination or wounding of trees. For this reason only the expected responses of trees based on their field situation were used. For example, a straight, non-curved, tree with a buried stem would only be analysed for changes in overall ring width growth, but not for changes in ring eccentricity. The problem gets more complicated when a tree reacted on more than one occasion. Usually there is little or no evidence that most or all of these reactions have been caused by a single process.

The application of lichenometry to the dating of debris flows or any other type of deposit depends strongly on the availability of a reliable lichen-growth curve. Usually it is quite difficult to obtain a reliable lichen-growth curve. This mainly relates to finding a large number of well-dated surfaces which also carry lichens and which are subject to the same environmental characteristics as the areas where the deposits to be dated are located. The calibration points are often located on gravestones, bridges or other anthropogenic structures, which are mainly located at lower elevations in the valleys. The deposits to be dated are often located several hundreds or even over a thousand metres higher up, although Innes (1982a, 1983b) recorded no variation in the growth rates of section *Rhizocarpon* thalli over an altitudinal gradient of 450 m in a study of debris flows in the Scottish Highlands. The reliability of the *Rhizocarpon geographicum* s.l. growth curve used in this study is still questionable as it is based on only 15 points.

The small number of deposits older than 1940 and the surface area covered by more recent deposit (fig. 9.5) show that deposits have a high probability of being buried by more recent deposits within 50-100 years after their formation. In these very active debris-flow systems, this strongly reduces the use of lichenometry as a dating method, as only deposits at the surface can be dated in this way. For less active debris-flow systems and debris-flow systems with larger deposition zones, deposits can remain at the surface for a longer time and lichenometry can be used up to several centuries back as shown by Innes (1983b, 1985b) and Van Steijn (1991, 1996). The systematic lateral shift of deposition activity within the deposition zones at TCP, TCP-N1, TGE and TGW remains to be explained. The activities of individual debris-flow trigger zones found in this study (table 9.3) exceed those mentioned by Van Asch and Van Steijn (1991) for the same area. The average return period for debris flows found in this study varies from 1.6 years (TCP-N1) and 2-3 years (TCP, TGE, TdP) to 6.9 years (TGW), whereas Van Asch and Van Steijn (1991) give average recurrence intervals of 10 years (and 4-5 years for the most active debris-flow trigger zones).

The relation between activity and size of a debris-flow system (fig. 9.7) may possibly be interpreted as follows. In small debris-flow trigger zones, small-sized debris flows are triggered relatively often and most of them can reach the deposition zone. In large debris-flow trigger zones the smaller debris flows may not always leave the trigger zone and only the larger, less frequently triggered debris flows reach the deposition zone. However this is only one possible explanation and other explanations cannot be ruled out, all the more since the relation in figure 9.7 is only weak. Differences in lithology between the debris-flow trigger zones could just as well be responsible for the variation in activity. Lithology is the same in TCP and TCP-N1 (limestones, marls and sandstones), but TdP (sandstones) and TGE and TGW (sandstones and blocky schists) are located in other rock types. Another possible explanation could be the presence of larger depth of accumulations of coarse debris in larger debris-flow trigger zones. With increasing depth of the coarse debris accumulation, the saturation level necessary to destabilize an accumulation of coarse debris increases linearly with the depth of the debris accumulation, so destabilisation could be more difficult in large debris-flow trigger zones.

On the basis of previous debris-flow deposit datings in the Bachelard Valley (De Redeljkheid 1988), we had expected to find an 11-year periodicity in debris-flow activity. Analysing tree-ring data, De Redeljkheid found a strong periodicity at about 11 years (fig. 9.11), which he attributed to a possible relation between debris-flow activity and variations in rainfall associated with the 11-year sun-spot cycle. Nearby, in Italy, Mazzarella and Palumbo (1992) showed a convincing direct relation between variations in annual rainfall and the sun-spot number (which represents sun-spot activity), so an 11-year periodicity in rainfall fluctuations is likely to exist in the study area as well. This does not necessarily imply that debris-flow activity must also show a periodicity at the same 11-year time scale: in chapter 8 it was already proven that even daily rainfall totals hardly correlate with the occurrence of debris flows, so it seems that annual totals are even more unlikely to correlate with debris-flow occurrence. Figure 9.10b presents the periodogram of dendrogeomorphological dates in this study, which only shows a (non-significant) peak at 16 years: there is no obvious relation with the sun-spot cycle. Thus, the results of this study do not support the conclusions drawn by De Redeljkheid (1988) and it seems that there is need for further investigations in order to resolve this matter.

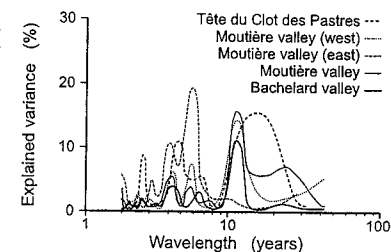


Figure 9.11 11-year periodicity of debris-flow activity in the Bachelard valley obtained through dendrogeomorphology (after De Redeljkheid 1988).

Papers dealing with the actual occurrence of debris flows are abundant. Most describe the occurrence of debris flows caused by particular, extreme meteorological situations. In the summer of 1987 the Alps were affected by extreme rainfall, triggering many water floods and mass movements like debris flows. In Switzerland, Zimmermann (1990), Haeblerli et al. (1991) and Rickenmann and Zimmermann (1993) have investigated the induced debris flows. In Italy this was done by Chardon (1990) and Pech (1990) and in France by Meunier (1990) and Ballandras (1993). Also, Clotet-Perarnau et al. (1989) have described debris flows in the Pyrenees Range resulting from an exceptional rainstorm in November 1982 and Bozonnet (1994) has described some exceptional debris flows occurring above 3500 m elevation in the Mont Blanc Massif in the summer of 1992. In the Bachelard valley, Hovius (1990), Blijenberg (1993b) and De Graaf et al. (1993) have investigated several debris flows in the period 1986-1991. Addison (1987) has investigated debris flows in north Wales, and for the central Karakoram, Hewitt (1993) has described debris flows resulting from torrential rains in September 1992. In the USA, Cenderelli and Kite (1998), Coe et al. (1998) and Wohl and Pearthree (1991) have described debris flows resulting from intense rainfall. Often, the return period for one or more rainstorm characteristics are mentioned (Brand 1993, Cenderelli and Kite 1998), but this does not necessarily represent the return period for debris flows, which might also be triggered by less intense rainfall or by different combinations of rainfall intensity and duration. Debris flows resulting from other causes have also been described, such as the debris flows resulting from the eruption of the 1980 eruption of Mount St. Helens in the USA (Cummans 1981).

Other researchers have investigated debris-flow occurrence to identify hazard and risk zones. Such investigations have been conducted by Pigeon (1991) in the northern French Alps, by Aulitzky (1994) in Austria, by Kienholz and Mani (1994) for the north face of the Rigi in Switzerland, by Lavigne and Thouret (1994) for the Merapi volcano in Indonesia, by Suzuki and Furuya (1992) for the Unzen Volcano in Japan and by Thouret and Laforge (1994) for the Rio Combeina valley and Ibagué City in Colombia. A theoretical approach using debris-flow movement and deposition models to identify hazardous zones was adopted by Takahashi (1981b) and Takahashi et al. (1981).

Debris-flow occurrence and frequency have also been the subject of research, using mainly methods such as dendrochronology and lichenometry, as was described in chapters 2 and 9. In contrast, very few papers deal with the actual spatio-temporal distribution of debris-flow occurrence. When field surveying techniques are used, the investigated area is usually small, such as a single slope or a small tributary valley. An example of such an investigation has been presented by Hétu et al. (1994), who have studied a single slope in Gaspésie (Quebec, Canada) nearly continuously over a period of more than half a year during the winter of 1989-1990. Within this period, at least 6 events producing frost-coated clast flows, a phenomenon related to debris flow (see table 2.2), were observed and accurately mapped. Whitehouse and McSaveney (1992) have used aerial photos of 5 different years covering the period 1938-1986. From these photos, debris-flow occurrence and other natural phenomena were mapped, resulting in a map of natural hazards and risks along State Highway 73 in New Zealand. Luckman (1992) has mapped relatively young (less than about 5 years old) debris-flow deposits in the Lairig Ghru in the Cairngorm Mountains of Scotland. He did this for both 1961 from aerial photos and for 1980 from a field survey. Probably the most elaborate spatio-temporal study on debris-flow occurrence concerns the Polish Tatra Mountains (Kotarba 1984a, 1989, 1992, 1997, Krzemień (1988), where regular and systematic investigations have been conducted ever since the mid-seventies. Krzemień (1988) has studied debris-flow occurrence in three deglaciated cirques in

the Polish Tatra Mountains in the period 1976-1986. He found that during those 10 years debris flows did occur, but debris-flow tracks hardly changed.

Field observations in 1991 and 1992 raised some doubt on the 'meaning' of debris-flow frequency obtained from dendrochronology and lichenometry. In just over one year of field investigations, 2 or 3 debris flows had been triggered in the TCP trigger zone. In the previous chapter, dendrochronological and lichenometrical dating of debris-flow deposits originating from the TCP site indicated that in the period 1940-1990 debris flows had occurred on average only every 2 years. Although these results are not necessarily conflicting, due to the irregularity of debris-flow activity (see fig. 9.6b), the rainfall data from 1991 and 1992 did not give any reason to expect an increased frequency of debris flows in these years, especially since the prolonged wet period in June had not produced any debris flows from the TCP debris-flow trigger zone.

Regular field surveys were started in 1992 in order to map the occurrence of 'fresh' debris flows in the Bachelard valley. They were carried out twice a year, in summer and in autumn. These surveys should give a better idea of the actual occurrence and frequency of debris flows and thus provide a check on the reliability, applicability and limitations of the debris-flow deposit dating methods used in chapter 9. Also, they should enhance the possibility to link debris-flow occurrence to rainstorms, thus allowing the possible recognition of relevant rainstorm characteristics, including spatial rainstorm aspects. In this way, detailed information concerning the temporal (year-to-year and seasonal) and spatial variability of debris-flow occurrence is obtained and the hypothesis formulated in chapter 1 can be checked.

In the surveys, no special attention was paid to the magnitude of debris flows. The only criterion used in the surveys was a minimum debris-flow length of about 50 m, which was the minimum size that could be mapped. Magnitude has two aspects, temporal variations and spatial variations. The spatial variation is largely a reflection of the characteristics of the debris-flow trigger zones involved. Where the temporal variation is concerned, the magnitude of a debris flow will probably reflect the magnitude of rainfall intensity of the rainstorm, which is intimately linked with its frequency (Van Steijn 1996). This may also have its influence in the dating of debris-flow deposits. For instance, smaller debris flows have more chance of being buried and less chance of affecting trees than larger debris flows, which occur less often. Magnitude has been left out of the investigations because there is no information on the spatio-temporal distribution of rainfall over the Bachelard Valley.

## 10.2 Occurrence of debris flows in the Bachelard valley in the period 1991-1995

Field surveys were carried out twice a year, in summer and in autumn, covering the period from June 1991 until June 1995. Systematic surveys were carried out between October 1992 and October 1994. Table 10.1 shows which regions of the Bachelard valley have been investigated in each survey. The regions are shown in figure 10.1. Debris-flow tracks were mapped as accurate as possible. Figures 10.2a-k show the distribution of debris flows in the Bachelard valley from 1991 until 1995. Based on rainfall measurements at the TCP site and on daily precipitation data from Barcelonnette, table 10.2 presents rainstorms, some of which must have triggered the debris flows.

In the summer of 1991 (fig. 10.2a), two fresh-looking debris flows were found in the Moutière valley. These had probably occurred shortly (several weeks ?) before the start of the field campaign. The debris flow at TCP occurred on 12 July and was triggered by a short-duration thunderstorm (table 10.2), the most severe short-duration rainstorm recorded during the whole period of investigations. The autumn 1991 debris flow from the TCP-N trigger zone (fig. 10.2b) was probably triggered by the 23 July or the 9 August rainstorm (see table 10.2). At TCP, another debris flow may have been triggered, but no conclusive field evidence was found to either accept or reject this possibility.

Table 10.1 Field surveys for mapping 'fresh' debris flows in the Bachelard Valley in the period 1991-1995.

Year	Season	Period		Systematic inventory	N <sup>a</sup>	N <sup>b</sup>	Inventory <sup>c</sup>
		From	Until				
1991	summer	6/1	7/19	no	5	1	only upper Bachelard Valley, Bayasse-Ventebrun area and Moutière, Braissette and Restefond Valleys
	autumn	9/21	9/22	no	1	3	only upper Bachelard Valley
1992	summer	5/31	7/22	no	3	1	only upper and lower Bachelard Valley and Petite Cayolle, Braissette and Restefond Valleys
	autumn	10/7	10/14	yes	28	12	except Petit Talon and Grand Talon Valleys and upper parts of Sanguinière and Pouterle Valleys
1993	summer	7/21	7/27	yes	20	11	complete
	autumn	9/18	9/22	yes	2	2	except Sanguinière and Julien Valleys
1994	summer	6/28	7/8	yes	89	33	complete
	autumn	10/4	10/12	yes	152 <sup>d</sup>	47 <sup>d</sup>	except Julien Valley
1995	summer	5/26	5/29	no	1	1	only upper, middle and lower Bachelard Valley

<sup>a</sup> Number of 'certainly new' debris flows.

<sup>b</sup> Number of 'probably new' debris flows.

<sup>c</sup> See figure 10.1.

<sup>d</sup> Of which 60 'certainly new' and 9 'probably new' debris flows occurred on 26 June.

The early summer of 1992 was generally a very wet period. On 15 May a prolonged period of rainfall started, only to end 8 weeks later on 12 July. In this period only 12 dry days were recorded at Barcelonnette. At TCP even less dry days must have occurred: only 3 days without any rainfall were recorded between 12 June and 12 July, against 7 in Barcelonnette in the same period. Although much rain fell in this period, rainfall intensities were relatively modest. Maximum 5-minute rainfall intensity  $i_{5,5}$  between 12 June and 12 July did not exceed 22 mm/hr at TCP (see table 10.2) and only a few debris flows were triggered (fig. 10.2c). The large debris flow in the lower Bachelard valley northeast of Uvernet occurred on 27 June during a 2-day long period of rainstorms and thunderstorms. Only on these two days did 5-minute rainfall intensities reach 22 mm/hr (table 10.2). Even though it is surprising that a debris flow was triggered by rainfall with such low intensities, it is not very surprising that it happened in just this debris-flow trigger zone, which is one of two debris-flow trigger zones situated in the relatively impermeable Terres Noires marls.

In the autumn of 1992 several debris flows were found in the Bachelard valley (fig. 10.2d). These debris flows show some degree of clustering. Many debris flows are situated in the Petite and Grande Cayolle valleys around the Trou de l'Aigle. Smaller clusters can be found in the Moutière and Tellière valleys. Figure 10.3 shows a debris flow in the upper Bachelard valley under the Tête de Peynier. According to TCP rainfall data, the debris flows may have occurred on 9, 19 or 29 August or on 9, 22 or 27 September (see table 10.2). On the first four of these dates thunderstorms occurred, on the last two dates prolonged rainfall occurred with short bursts of high-intensity rainfall. Video camera recordings have shown debris-flow-like surges occurring in the TCP trigger zone at least on 19 and 29 August. During the other four rainstorms, the video camera malfunctioned. It seems likely that such debris-flow-like surges have also taken place during the September rainstorms.

The debris flows mapped in the summer of 1993 are all located in the eastern part of the Bachelard valley (10.2e) in three well-defined clusters. The cluster with the most debris flows is situated around the Trou de l'Aigle and the Mont Pelat in the Grande and Petite Cayolle valleys. Nearby another cluster is situated in the Saume valley on the eastern slope of the Cimet. The third cluster is located in the Moutière valley, directly to the south of the Chevalier. Also, two debris flows were found in the upper Bachelard valley on the western slope of the Tête du clot des Pastres. The fact that debris-flow activity took place in well-defined clusters indicates that local rainstorms must have triggered the debris flows.

Table 10.2 Extreme rainstorms between June 1991 and September 1994 in the Bachelard Valley.

Year	Date	Tête du Clot des Pastres							Barcelonnette <sup>a</sup>
		Time	Duration minutes	$i_{r,3}$ mm/hr	$i_{r,5}$ mm/hr	$i_{r,30}$ mm/hr	$i_{r,rs}$ mm	$i_{r,day}$ mm	
1991	03/06								44.5
	03/08								34.5
	07/12	14:07	68	132	128.4	52.6	29.4	30.3	4.8
	07/23	14:32	29	52	33.6	13.8 <sup>b</sup>	6.9	16.7	13.5
	08/09	5:03	30	84	79.2	18.6	9.3	14.1	10.7
	09/26								42
	09/29								95.4
	10/06								52.7
	10/11								48.5
	11/13								34.3
1992	05/19								33.5
	06/27	18:10	65	27.2	21.7	13.6	12.5	16.8	10.8
	06/28	17:34	32	22.8	21.8	9.5	5	7.7	7.1
	08/09	21:55	82	36.4	27.2	12.7	10.7	11.6	5.8
	08/19	17:38	47	90.8	76.2	40	21.3	22	0
	08/29	12:47	493	49.8	40.8	20	74.5	75.4	31.9
	09/09	13:41	18	54.4	43.7	11.8	5.9	6.6	2.6
	09/22	11:52	36	63.6	46.3	17.7	9.5	82.9	42.3
		13:06	67	59	49.1	25.4	17.7		
		16:05	284	31.8	29.9	17.7	40.4		
		18:01	52	54.6	49.1	21.4	16.6	64.3	29.6
	09/27								29.6
	04/25								28.6
	05/20								29
	06/06	18:06	25	32.4	29.2	9.3	4.7	5.1	0
	06/07	15:46	22	56.8	43.8	12.5	6.3	7.1	21.5
	07/09	22:21	54	48.6	34.1	10.9	6.3	8.3	20.2
	07/10	18:44	117	36.4	26.8	9.7	12.1	34.6	17.1
	08/05	14:15	19	85	77.8	18.6	9.3	9.3	0.7
	08/13	17:17	18	36.6	29.2	7.7	3.8	6.3	0
	08/15	13:38	44	73	70.4	30.8	16.4	34.6	2.1
		14:31	45	64.8	58.3	24.7	13.6		
	08/27	13:21	40	36.4	29.2	13	7.3	23.7	19.4
	09/09	23:04	80	40.6	29.2	7.7	6.9	13.2	8.9
	09/22								30.4
	09/23								33.3
	09/30								32
	10/07								62.8
1994	06/26	15:01	70	36.4	29.2	12.9	12.5	68.8	41.5
		17:01	60	48.6	41.3	18.2	13.2		
	07/11	22:34	63	85	77.8	32	20.2	25.1	0
	07/22	15:25	46	93	82.6	42.5	23.9	36.2	10
	07/23	12:22	19	36.4	31.6	11.3	5.7	11.9	2.3
	07/27	18:43	18	81	77.8	19	9.3	12.1	0.9
	07/29	13:49	30	44.6	36.5	16.6	8.3	16	6.3
	09/08	09:36	135	56.6	51	27.5	33.4	67.2	31.4
		13:23	7	56.6	41.3	8.9	3.4		
		14:17	71	60.8	46.2	22.7	18.2		
		15:41	28	52.8	38.9	15.4	5.7		
	09/14	03:03	79	32.4	29.2	15.4	13.4	50.8	22.7
		09:46	68	44.6	43.7	14.2	8.7		
	09/23	13:58	253	36.4	31.6	17	51	103	33.2
	09/24	01:30	81	36.4	34	15.4	11.5	17.4	0

<sup>a</sup> Barcelonnette daily rainfall data are measured from 9 am on the preceding day until 9 am on the day concerned.

<sup>b</sup> Rainfall intensities are shown in *italics* if the rainfall-intensity interval exceeds the actual rainstorm duration. Dotted lines indicate field surveys.

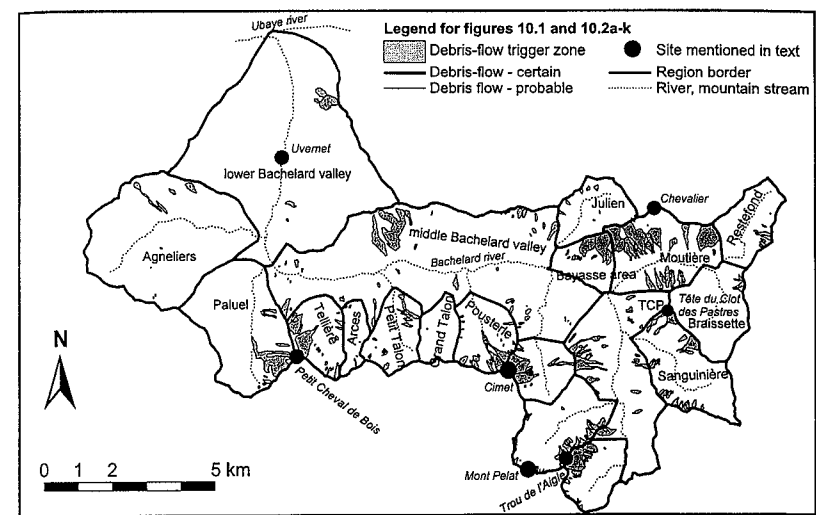


Figure 10.1 Regions in the Bachelard Valley.

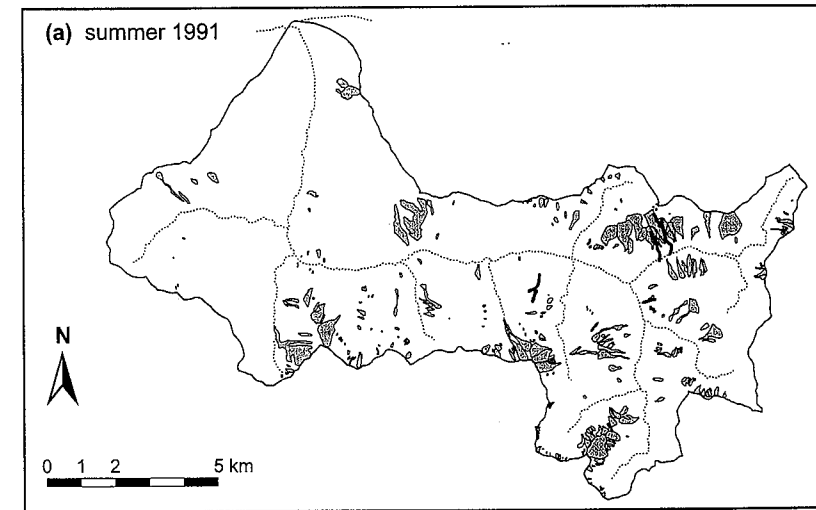


Figure 10.2 Debris flows in the Bachelard Valley in the period 1991-1995. Legend: see fig. 10.1.

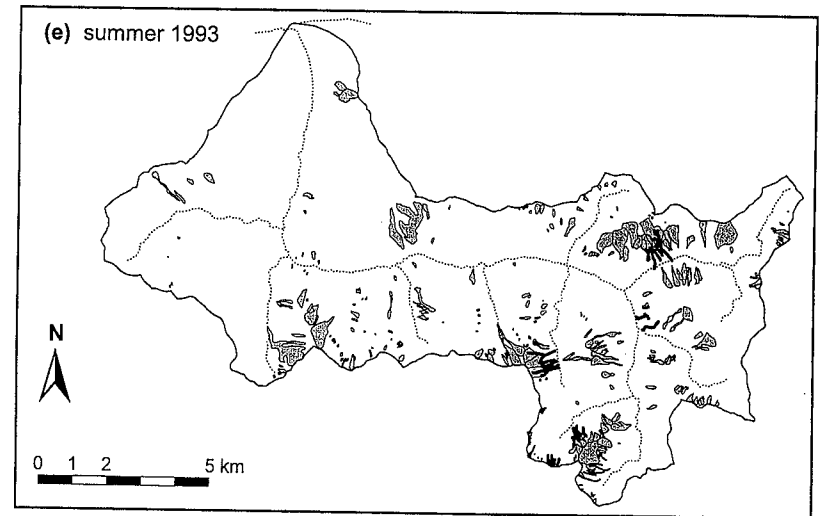
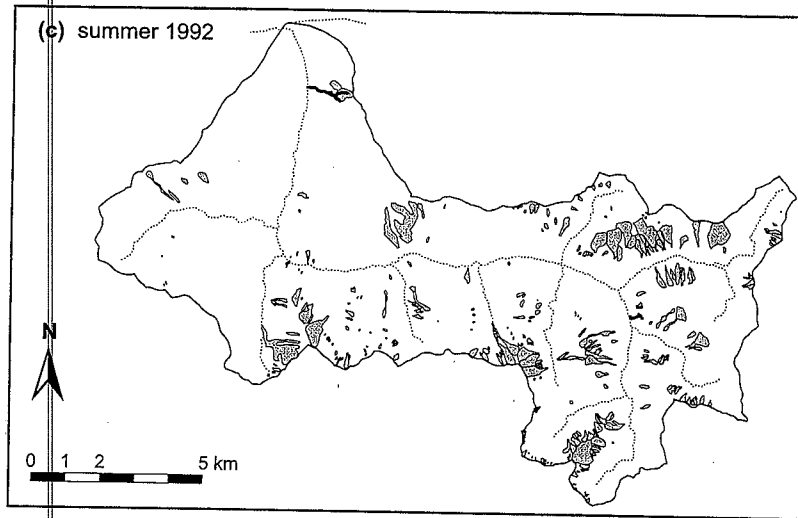
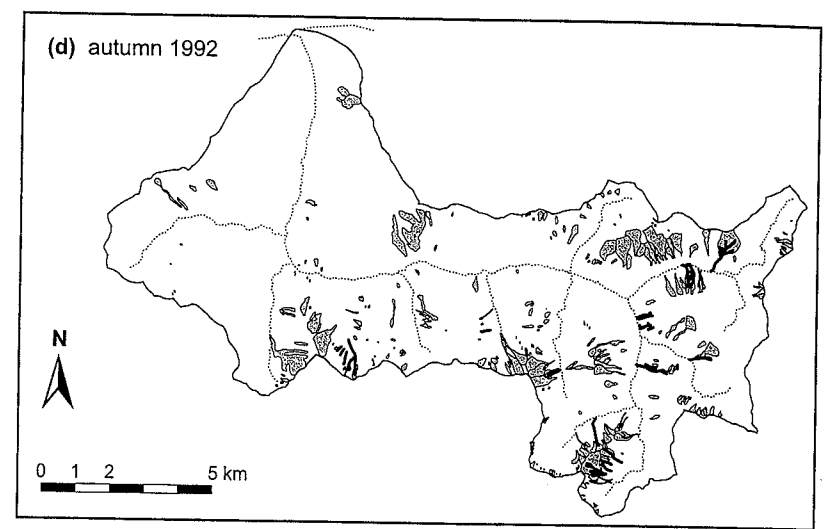
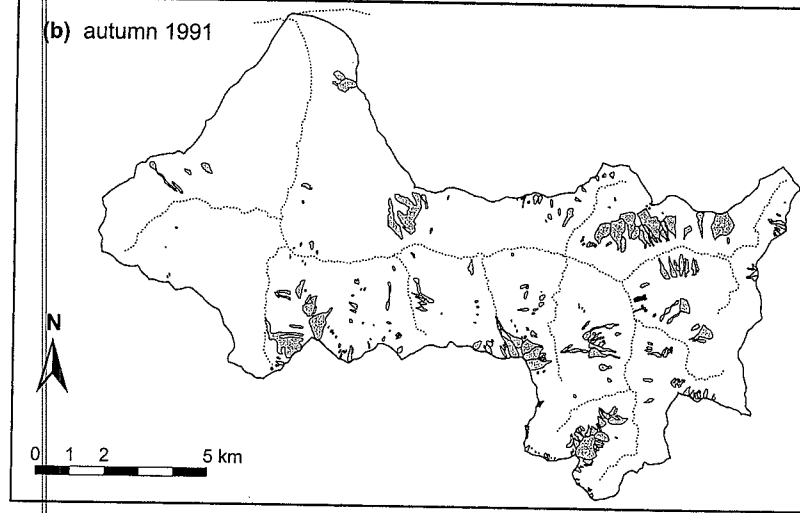


Figure 10.2(cont.) Debris flows in the Bachelard Valley in the period 1991-1995. Legend: see fig. 10.1.

Figure 10.2(cont.) Debris flows in the Bachelard Valley in the period 1991-1995. Legend: see fig. 10.1.



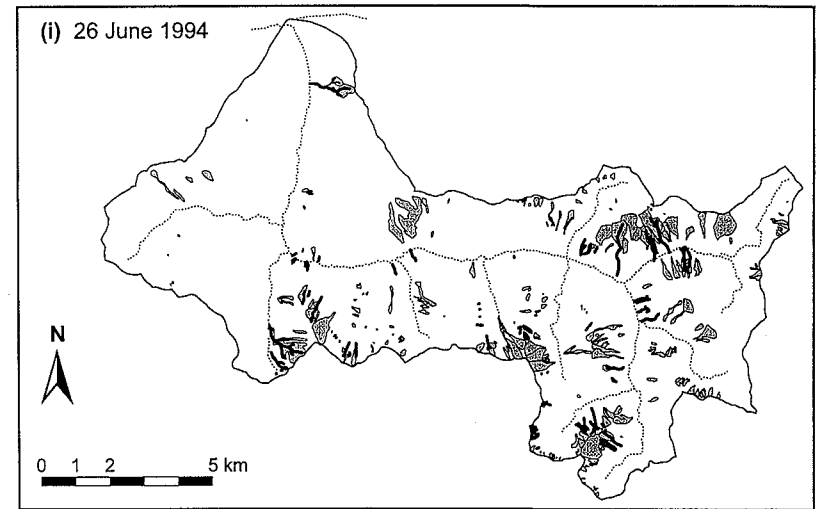
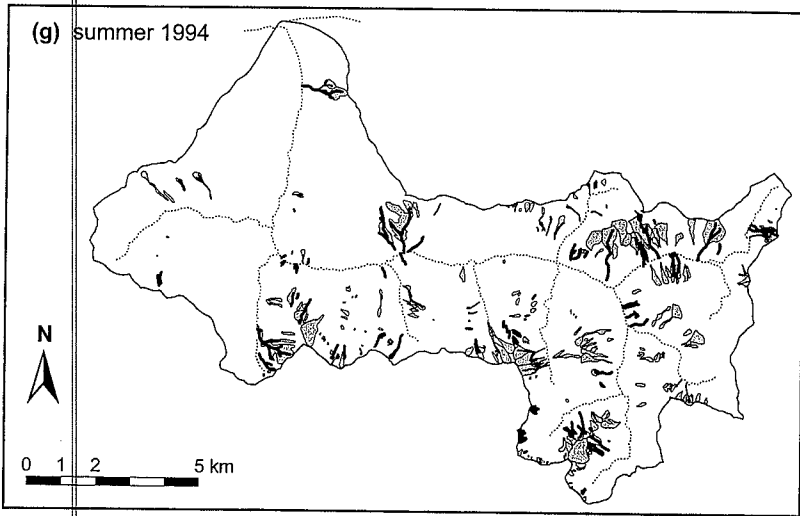
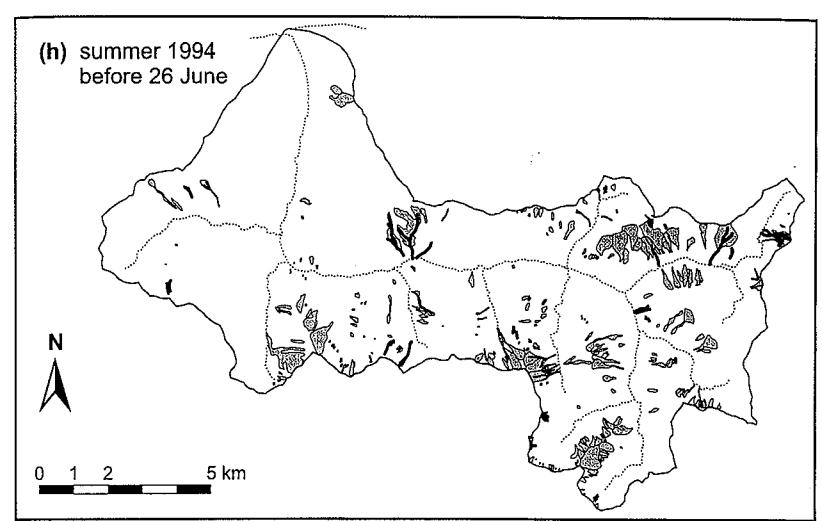
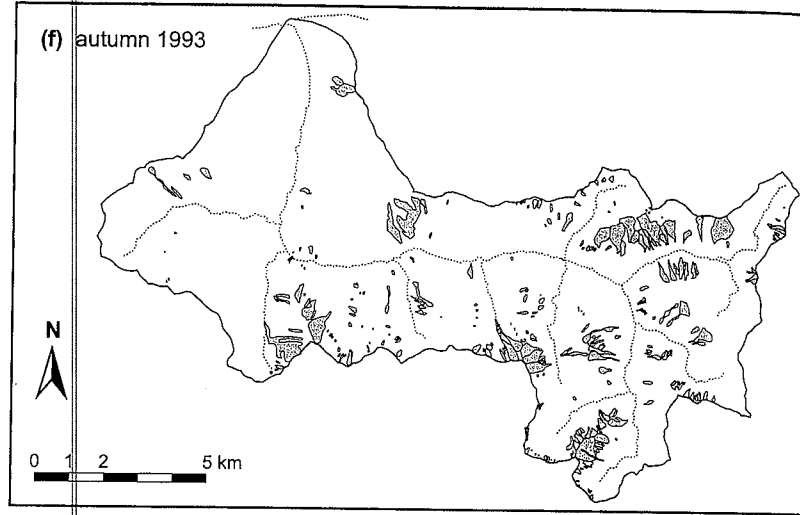


Figure 10.2 (cont.) Debris flows in the Bachelard Valley in the period 1991-1995. Legend: see fig. 10.1.

Figure 10.2 (cont.) Debris flows in the Bachelard Valley in the period 1991-1995. Legend: see fig. 10.1.

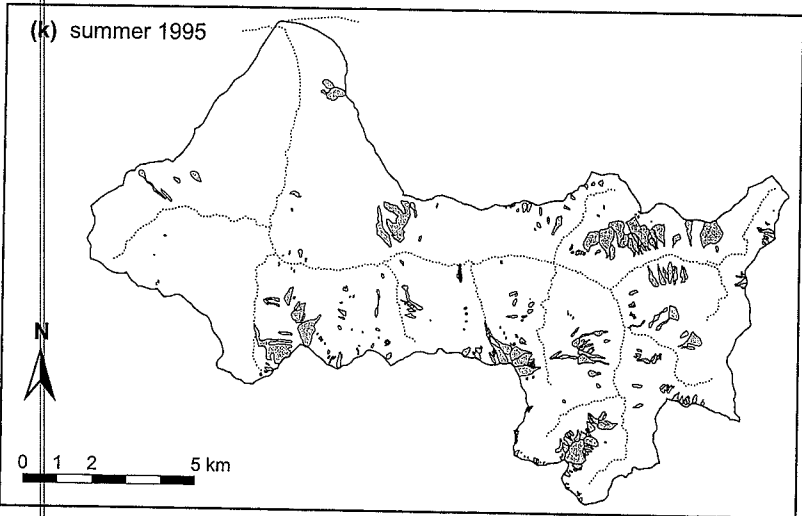
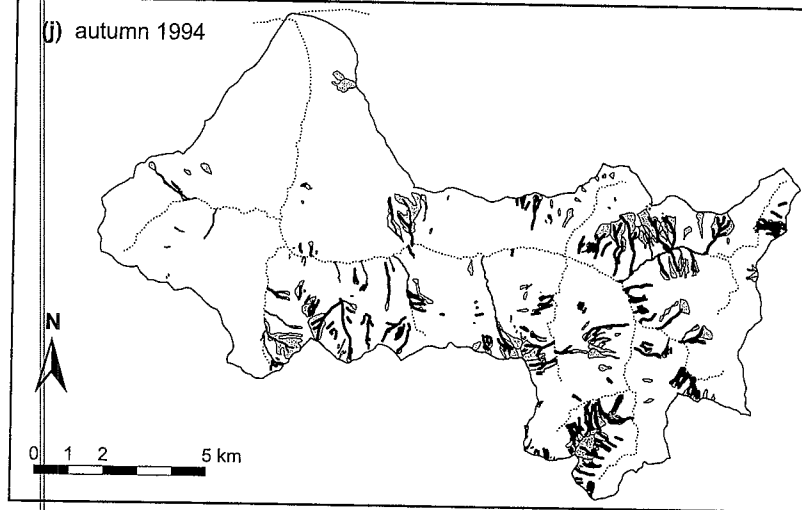


Figure 10.2 (cont.) Debris flows in the Bachelard Valley in the period 1991-1995. Legend: see fig. 10.1.

TCP rainfall data (table 10.2) show several moderate and severe rainstorms on 6-7 June and on 9-10 July. Barcelonnette rainfall data show the occurrence of thunderstorms in April and in May 1993 and rainy periods in October, November and December 1992. The October 1992 rainstorms seem less likely to have triggered the debris flows, as this was a period with prolonged rainfall of low to moderate rainfall intensities. Also, on a visit to the Moutière valley on 20 June, the debris flows located here still had a very fresh look. These may well have occurred on 6 or 7 June. On 10 July some debris-flow surges were recorded by the video-camera at the TCP site. However, these surges did not leave the debris-flow trigger zone and no debris flow was triggered.

Between late July and late September 1993 only few debris flows occurred in the Bachelard valley (fig. 10.2f), even though a number of severe rainstorms were recorded at the TCP site on 5, 13, 15 and 27 August and on 9 September (table 10.2). The debris flow originating from the TCP debris-flow trigger zone probably took place on 15 August, which is supported by the video-camera recordings. The video-camera also showed, that the rainstorm on 13 August certainly did not produce a debris flow at TCP.

The survey of late July 1994 revealed widespread debris-flow activity throughout the Bachelard valley (fig. 10.2g). A large number of these occurred on 26 June, as a result of the passage of a cold front accompanied by severe rainstorms and thunderstorms. The debris flows that occurred before 26 June are widespread throughout the whole Bachelard valley, with only weak clustering (fig. 10.2h). Most of these debris flows, such as those in the Saume valley, probably took place during the exceptionally wet period of 23 September until 14 October 1993 (table 10.2). Many of these were still partly covered with snow and must thus have been formed before the winter (fig. 2.4). The large amounts of rainfall recorded on 6-7 January (51.5 mm) and on 28 February (24.8 mm) in Barcelonnette probably did not trigger any debris flows in the Bachelard valley. On 6-7 January precipitation in the Bachelard valley must mainly have been in the form of snow. Also, during a short visit to the Bachelard valley in March no evidence was found for any debris-flow activity caused by the 28 February rainfall. Figure 10.2i presents the 26 June debris flows. Their spatial pattern also shows only weak clustering. Several debris flows in the Grande Cayolle valley and the large debris flow in the Paluel valley near the Petit Cheval de Bois had run over snowpatches in the gullies and couloirs (fig. 4.13). Therefore they must have been triggered after the winter season, most probably on 26 June. At the TCP site, video camera recordings indicate that a debris flow probably occurred at about 17:30 hr and/or at about 16:00 hr.

The largest debris flows and the largest number of debris flows were found during the survey in the autumn of 1994 (fig. 10.2j). At TCP, severe rainstorms or thunderstorms were recorded on 11, 22, 23, 27 and 29 July and on 8, 14, 23 and 24 September (table 10.2). The widespread occurrence of debris flows has most likely been caused by the rainfall on 8 September. On this day, prolonged rainfall

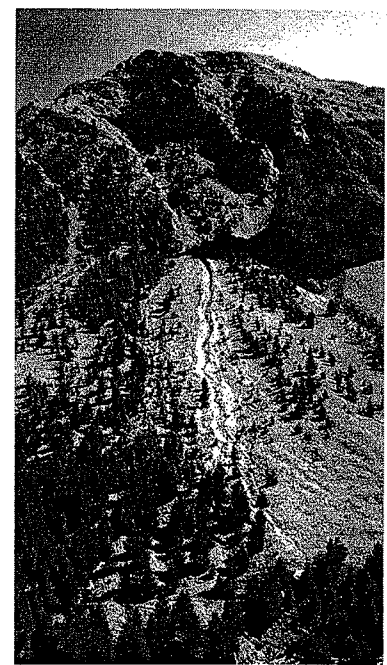


Figure 10.3 Debris flow on the west-facing slope of the Tête de Peynier (autumn 1992).

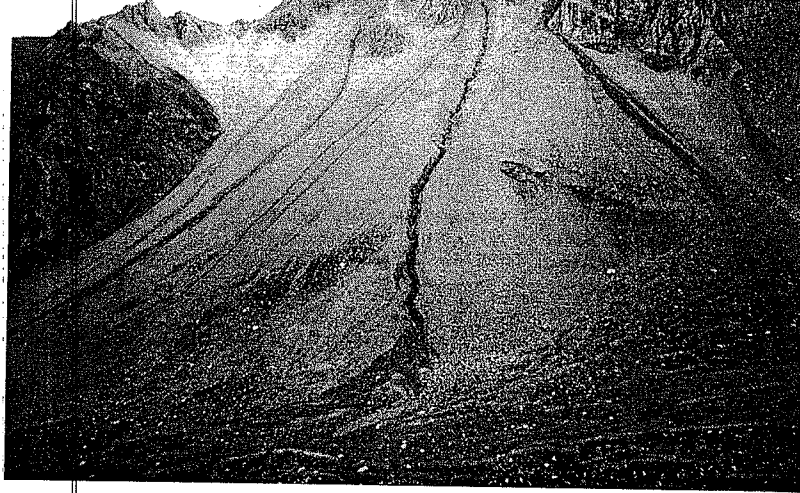


Figure 10.4 Debris flows in the Grande Cayolle Valley (autumn 1994).

occurred in combination with several bursts of high-intensity rainfall ( $i_{r,3}$  up to 53–61 mm/hr). The other rainstorms in September also show high amounts of rainfall, but lesser maximum rainfall intensities ( $i_{r,3}$  up to 36–45 mm/hr). Combining with Barcelonnette rainfall data shows that all these rainstorms were widespread. On the other hand, the 27 and 29 July rainstorms had high maximum intensities ( $i_{r,3}$  up to 45–81 mm/hr), but lesser rainfall amounts, and it seems that they were more localized. The rainstorms on 11 and 22 July also show a large spatial variation: at TCP, 25.1 mm and 36.2 mm of rainfall were recorded on these days with high rainfall intensities ( $i_{r,3}$  up to 85–93 mm/hr), whereas no rainfall was recorded on 11 July and only 10 mm on 22 July in Barcelonnette. Figure 10.4 shows some of the debris flows that occurred in the Grande Cayolle valley. The map of the summer of 1995 (fig. 10.2k) shows only two debris flows. A complete survey at this time was impossible, as a large part of the area above 2000 m was still covered with snow.

### 10.3 Discussion

#### 10.3.1 Temporal aspects

The following discussion on debris flows in the Bachelard valley will be restricted to the five systematic surveys, which cover the period from late July 1992 until mid-October 1994. In this period at least 291 debris flows were triggered for certain, and another 105 were possibly triggered. These numbers are minimum values, as more than one debris flow may have been triggered from any debris-flow trigger zone one between successive surveys. For each debris-flow trigger zone, only one debris flow was mapped if any fresh tracks or deposits were found, even when more than one track was present. This was done because it was hardly ever possible to find out whether or not the tracks were all formed during one rainstorm. On the other hand, multiple debris flows triggered by more than one rainstorm between two successive surveys may have followed the same tracks, leaving only a single track as evidence

of debris-flow activity. Similar observations were made by Krzemien (1988) for debris flows in the Polish Tatra Mountains. It is very unlikely that the large number of severe rainstorms and thunderstorms in July and September 1994 did not trigger more than one debris flow in at least some debris-flow trigger zones. There are some exceptions, where more than one debris flow could be identified between successive surveys. At the TCP site, this was made possible by regular field visits and video camera recordings. Also, for the summer of 1994, the debris flows occurring on 26 June could be separated from those occurring before 26 June, which showed that 2 debris flows had happened at TCP-N1 and at one of the trigger zones in the Moutière valley (see figs. 10.2h and i).

Debris-flow activity for each of the regions of figure 10.1 was characterized by calculating debris-flow frequency,  $f_{df,rv}$ , the average number of debris flows per trigger zone per year for a region obtained from regular surveys:

$$f_{df,rv} = \frac{N_{df,c} + 0.5 N_{df,p}}{N_{dfa} \Delta t_{fp}} \quad 10.1$$

where:  $N_{df,c}$  = total number of *certain*, fresh debris flows from the systematic surveys;  $N_{df,p}$  = total number of *probable*, fresh debris flows from the systematic surveys;  $N_{dfa}$  = number of debris-flow trigger zones in a region;  $t_p$  = time period covered by the surveys (in years). The upper Bachelard valley region was subdivided into the west slope of the Tête du Clot des Pastres and the rest of the upper Bachelard valley. The reason for this subdivision was the high frequency of visits to the west slope of the Tête du Clot des Pastres during the field campaigns which might influence the results. The probability that more than one debris flow has been triggered from a single debris-flow trigger zone increases directly with number of heavy rainstorms between successive surveys, which in turn depends on the time interval between successive surveys. Ideally, in order to identify all debris flows occurring, the study area would have to be surveyed after each heavy rainstorm, which is a time-consuming and therefore highly impractical task. The calculated debris-flow frequencies must therefore be regarded as minimum values.

The average debris-flow frequency varies from at least  $0.050 \text{ yr}^{-1}$  for the Braisette valley (average debris-flow return period of 20 years) to at least  $0.956 \text{ yr}^{-1}$  (average return period about 1 year) for the Tête du Clot des Pastres slope. For the TCP site, observed debris-flow frequencies were presented in sections 8.2 and 8.5.2, a minimum debris-flow frequency of  $1.5 \text{ yr}^{-1}$ , and a best guess of  $2\text{--}3 \text{ yr}^{-1}$  over the period of June-1991 until June 1995. Here a value of  $2.5 \text{ yr}^{-1}$  is assumed.

Some remarks can be made on the seasonal aspects of debris-flow occurrence in the Bachelard valley. It appears that debris flows are quite frequent in the months June–September. In October debris flows are probably not unusual. In April and May, roughly the snowmelt period, only few debris flows seem to occur, just as in November. Debris flows are unlikely in winter (December–March) when large parts of the area are covered with snow and most precipitation is snow.

#### 10.3.2 Spatial aspects

Figures 10.2d, e and h show that debris-flow activity often shows a clustered pattern. Such a clustered pattern seems to be indicative of debris-flow triggering by local rainstorms. High-intensity rainstorms and thunderstorms are often very local phenomena, with the diameter of the high-intensity rainfall cell in the order of several hundreds of metres, as can be seen in figure 10.5. The widespread patterns mapped for 26 June 1994 and in the autumn 1994 could be the result of widespread, long-duration rainfall, but it seems more likely that a larger number of local high-intensity raincells have passed through the study area, which has resulted in a coagulation of debris-flow clusters into an apparently non-clustered pattern. Rapp and Nyberg (1981) and Rapp and Strömquist (1976) also recognized that debris-flow distribution patterns reflected meteorological conditions.

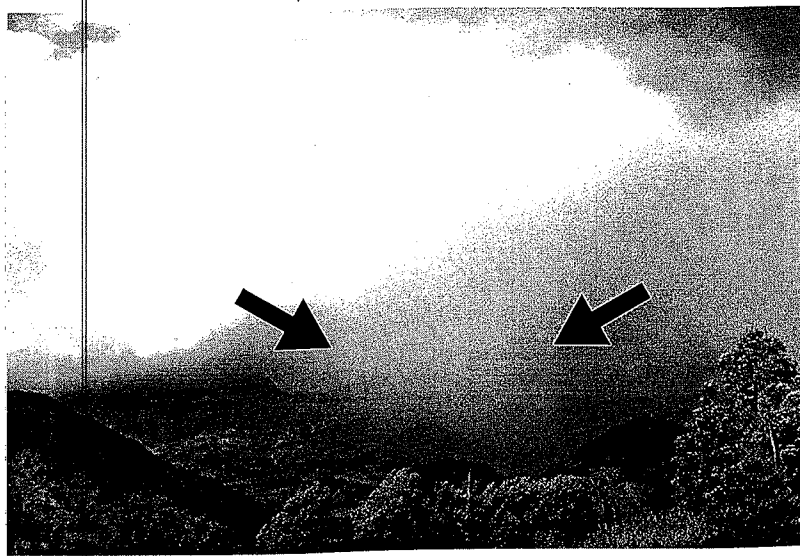


Figure 10.5 Local, high-intensity rainfall cell in a rainstorm. The arrows indicate the borders of the high-intensity rainfall cell (several hundred metres diameter).

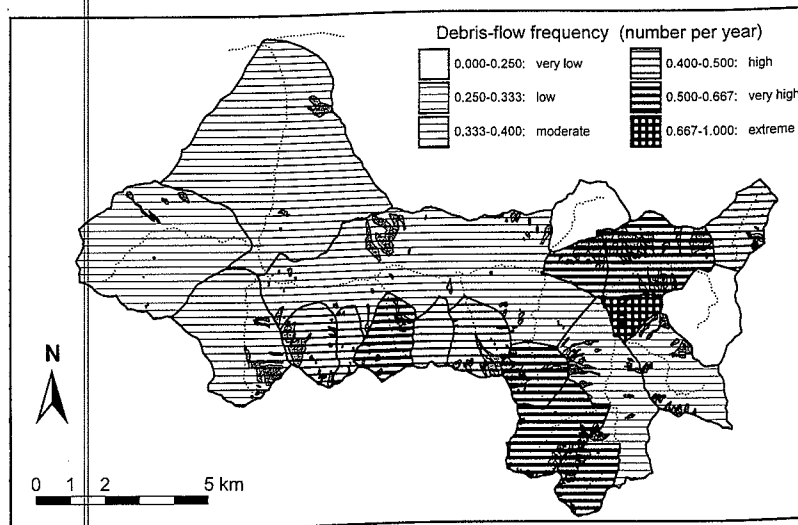


Figure 10.6 Debris-flow activity in the Bachelard Valley between July 1992 and October 1994.

Figure 10.6 shows the spatial variation of debris-flow frequency in the Bachelard valley in the period late July 1992 until mid-October 1994. The frequency is above average in the Bayasse area, the Moutière valley and the tributary valleys south of the Bachelard. No relation was found between the debris-flow frequency and elevation of the debris-flow trigger zones, although at first sight figure 10.6 seems to suggest such a relation. The frequency does show a significant ( $p = 0.05$ ), positive relation with the debris-flow trigger-zone density in the study area (see figs. 10.7a, b):

$$f_{df,fv} = 0.265 + 0.0449 \frac{N_{dfsa}}{A} \quad 10.2$$

or

$$f_{df,fv} = 0.734 + 0.281^{10} \log \left( \frac{N_{dfsa}}{A} \right) \quad 10.3$$

where:  $A$  = surface area of the region (in  $\text{km}^2$ );  $A_{dfm}$  = total surface area of debris-flow trigger zones in the region (in  $\text{km}^2$ );  $N_{dfsa}/A$  (in  $\text{km}^2$ ) and  $A_{dfm}/A$  ( $\text{km}^2/\text{km}^2$ ) are measures of debris-flow trigger-zone density. These relations explain respectively 32% and 38% of the variation in debris-flow frequency between the regions by their difference in debris-flow trigger-zone density. In these relations, only the regions with at least 10 debris-flow trigger zones were used. The results for regions with less debris-flow trigger zones were thought to be less reliable, as the influence of one debris flow more or less on the frequency is relatively large. Still, figures 10.7a and b show that this approach was too conservative, as only two regions form outliers. In both figures the west slope of the Tête du Clot des Pastres has a much higher frequency than any of the other regions. This supports the choice for a subdivision of the upper Bachelard valley. In figure 10.7b, the Grand Talon valley is the only other outlier. This is not surprising, as there is only a single debris-flow trigger zone in this region, which was formed in the autumn of 1994 when a small, surficial slide transformed into a debris flow (fig. 10.8).

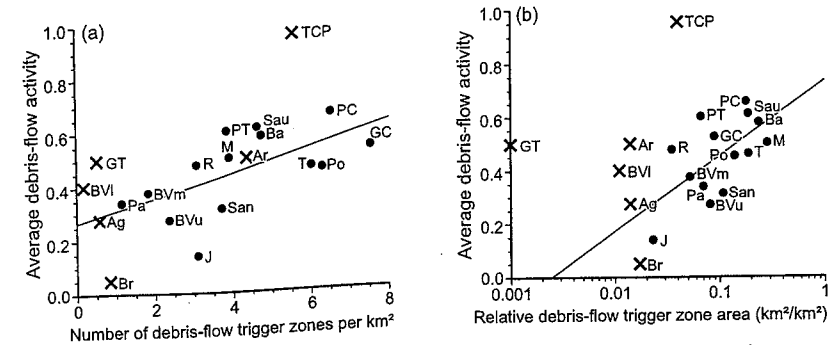


Figure 10.7 Relation between debris-flow activity and debris-flow trigger-zone density. Trigger-zone density expressed as: (a) number of debris-flow trigger zones per  $\text{km}^2$ ; (b) fraction of the total density expressed as: (a) number of debris flows per trigger zone per year. Crosses represent regions with 9 or less debris-flow trigger zones, dots regions with at least 10 trigger zones. Ag = Agneliers (8 debris-flow trigger zones), Ar = Arces (6), Ba = Bayasse (11), Br = Braissette (4), BVI, BVm, BVu = lower, middle and upper Bachelard Valley (4, 45, 11), GC = Grande Cayolle (39), GT = Grand Talon (1), J = Julien (10), M = Moutière (25), Pa = Paluel (10), PC = Petite Cayolle (20), Po = Poustierle (22), R = Restefond (10), San = Sanguinière (21), Sau = Saume (14), TCP = Tête du Clot des Pastres slope (9).

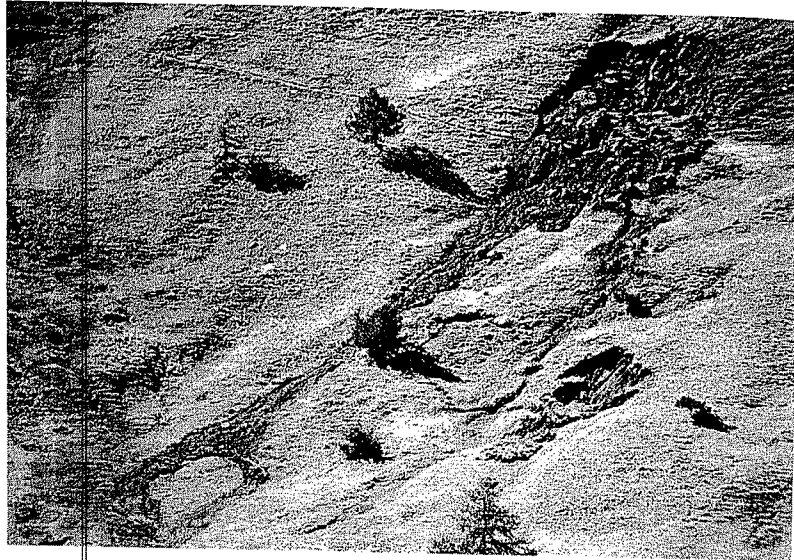


Figure 10.8 Small debris flow originating from the transformation of a small, surficial landslide in the Grand Talon Valley (autumn 1994).

The relation between the debris-flow frequency and debris-flow trigger-zone density is no surprise, but it is hard to say which of the two is the cause and which is the effect. In areas which are sensitive to the development of debris flows, debris-flow trigger zones will develop easily. This also implies that a large part of a certain area is occupied by debris-flow trigger zones, that area must have a high debris-flow frequency.

The relation between debris-flow frequency and debris-flow trigger-zone density suggests a relation between frequency and lithology. Yet only a weak relation was found. Regions with a high debris-flow frequency are mostly situated in flysch deposits (Tellière, Arces, Petit Talon, Grand Talon, Pousterle, and Cayolle, Petite Cayolle; see fig. 3.3) or rapidly alternating rocks with dense faulting (northern part of Moutière, Bayasse), but regions with relatively low debris-flow frequency can also be found in flysch deposits (Agneliers, Paluel, southern parts of the middle and lower Bachelard valley) and in rapidly alternating rocks (Julien, eastern part of the middle Bachelard valley, northwestern part of the lower Bachelard valley). Other regions with high debris-flow frequency are Restefond (schists), the northern part of Moutière (schists and sandstones) and Saume (mainly flysch and conglomerates). Other regions with low frequency are found in sandstones (Braissette, Sanguinière, southern and eastern parts of the upper Bachelard valley), in marls (northern part of the lower Bachelard valley) and in flysch and sandstones (northeastern part of the middle Bachelard valley).

Table 10.3 Comparison of debris flow frequencies obtained from field visits with frequencies obtained from dendrogeomorphology and lichenometry.

Location	$N_{dfn}$	Field visits (this study)				Dendrogeomorphology and lichenometry				
		Period	$\Delta t_{fo}$ <sup>a</sup>	$N_{df}$ <sup>b</sup>	$f_{df}$ <sup>c</sup>	Period	$\Delta t_{df}$ <sup>a</sup>	$N_{df}$ <sup>b</sup>	$f_{df}$ <sup>c</sup>	$f_{df}/f_{dfc}$ <sup>c</sup>
This study <sup>d</sup>										
TCP-N1	1	06/91 - 05/95	4	5	1.3	1940 - 1994	55	34	0.618	2.0
TdP	1	07/92 - 05/95	2.8	2	0.7	1927 - 1994	68	24	0.353	2.0
TGE	1	07/92 - 10/94	2.2	1.5	0.7	1940 - 1994	55	18	0.327	2.1
TGW	1	07/92 - 10/94	2.2	0.5	0.2	1940 - 1994	55	8	0.145	1.6
TGE+TGW	2	07/92 - 10/94	2.2	2	0.9	1940 - 1994	55	26	0.473	1.9
De Redelijkheid (1988) <sup>e</sup>										
Tête du Clot des Pastres	9	07/91 - 05/95	3.9	32	0.9	1889 - 1986	88	29	0.037	25
TCP-N2	1	07/91 - 05/95	3.9	2	0.5	1930 - 1986	57	2	0.035	15
TCP-N1	1	06/91 - 05/95	4	5	1.3	1911 - 1986	76	5	0.066	19
TCP	1	06/91 - 05/95	4	10	2.5	1909 - 1986	78	5	0.064	39
TCP-S1	1	07/91 - 05/95	3.9	7	1.8	1970 - 1986	17	1	0.059	30
TCP-S2	1	07/91 - 05/95	3.9	1	0.3	- 1986		0		
TCP-S3	1	07/91 - 05/95	3.9	4	1	1970 - 1986	17	2	0.118	8.7
TCP-S4	1	07/91 - 05/95	3.9	3.5	0.9	1889 - 1986	88	4	0.045	20
Vallon de la Moutière	12	07/92 - 10/94	2.2	17	0.6	1811 - 1986	176	102	0.048	13
GAW	1	07/92 - 10/94	2.2	1.5	0.7	1931 - 1986	56	23	0.41	1.6
GAC	1	07/92 - 10/94	2.2	2.5	1.1	1949 - 1986	38	7	0.18	6.0
CTS	1	07/92 - 10/94	2.2	1	0.4	- 1986		1		
CGAT	1	07/92 - 10/94	2.2	3.5	1.6	1865 - 1986	122	34	0.28	5.6
CTC	1	07/92 - 10/94	2.2	0	0	1918 - 1986	69	1	0.014	0
CTE	1	07/92 - 10/94	2.2	0.5	0.2	1901 - 1986	86	5	0.058	3.8
CE	1	07/92 - 10/94	2.2	1	0.4	1876 - 1986	111	16	0.144	3.1
TW	1	07/92 - 10/94	2.2	0	0	1916 - 1986	71	4	0.056	0
TE	1	07/92 - 10/94	2.2	0	0	1897 - 1986	90	3	0.033	0
CB	1	07/92 - 10/94	2.2	3	1.3	1811 - 1986	176	18	0.102	13

<sup>a</sup> Time in years.

<sup>b</sup> Number of debris flows. 'Probable' debris flows are counted for 50%.

<sup>c</sup> Frequency in debris flows per year per debris flow source area.

<sup>d</sup> Preliminary results were presented by Overbeek and Wiersma (1996).

<sup>e</sup> De Redelijkheid's (1988) tree-ring dates, *Xanthoria elegans* dates and uncorrected *Rhizocarpon geographicum* s.l. dates. Where tree-ring dates were used, each date was considered to be caused by a debris flow. Undated debris-flow deposits were assumed to be younger than the oldest dated deposit.

#### 10.4 Comparison of debris-flow frequencies from regular surveys and from deposit dating

It is interesting to compare the debris-flow frequencies obtained from regular field visits between 1991 and June 1995 for the TCP site (see section 8.2) with frequencies obtained from dendrochronology and lichenometry (chapter 9). It appears that the 'traditional' methods of estimating debris-flow occurrence and frequency, dendrochronology and lichenometry, greatly underestimate the debris-flow frequency (table 10.3). For the TCP site, the traditional methods have yielded a debris-flow frequency  $f_{df,df} = 0.49$  debris flows per year over a 55 year period, whereas the field visits have provided a minimum frequency  $f_{df,df} = 1.5 \text{ yr}^{-1}$  and a best-guess frequency of  $f_{df,df} = 2.5 \text{ (2-3) yr}^{-1}$ . The traditional methods thus appear to underestimate debris-flow frequency by a factor 5 ! For the other four debris-flow trigger zones for which debris-flow frequencies were obtained with the deposit dating techniques (figs. 9.1 and 10.9), similar comparisons can be made (table 10.3). Once again it is clear that debris-flow dating by dendrogeomorphology and lichenometry leads to an underestimation of the frequency of debris flows.

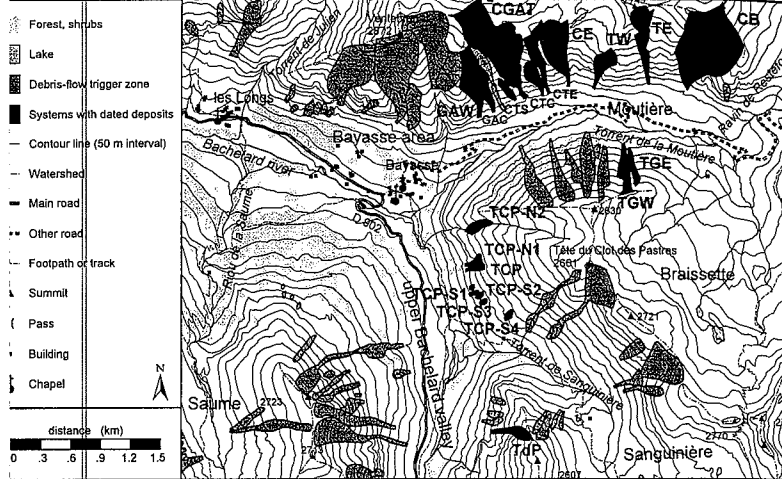


Figure 10.9 Location of debris-flow systems for which data are available on debris-flow occurrence from regular field visits as well as from dendrogeomorphology and lichenometry.

order to make a similar comparison with debris-flow frequencies obtained by De Redeljkheid (1988) th dendrogeomorphology and lichenometry, some assumptions had to be made. As mentioned in section 9.2.2, De Redeljkheid (1988) had used a questionable procedure in order to obtain a *Rhizocarpon geographicum* s.l. growth curve for the Bachelard Valley, resulting in an overestimation of the *Rhizocarpon geographicum* s.l. growth (fig. 9.3). Therefore his original dates as predicted by the ombelli and Porter (1983) *Rhizocarpon geographicum* s.l. growth curve were assumed to be correct. Comparing the frequencies obtained in this way with those from field visits in this study shows generally even larger differences between the two methods; for TCP and TCP-N1 the difference is in the order of 20-30 ! The large difference between the results of the deposit dating methods from this study with those of De Redeljkheid can probably be attributed to the more 'in-detail' survey carried out for this study (see also Overbeek and Wiersma 1996), where research was concentrated on only debris-flow systems. Due to the sporadic occurrence of debris flows in some debris-flow systems the Moutière Valley and the short time span of the regular surveys, the ratio  $f_{df,fo}/f_{df,al}$  shows large variations. The debris-flow return periods in the Bachelard Valley mentioned by Van Asch and Van Steijn (1991) and Van Steijn et al. (1988b) of 10-40 years for debris-flow systems with an average activity and 4-5 years for the most active systems also underestimate the actual activity by a factor 5-10.

The main explanation for the discrepancy between debris-flow frequencies obtained from dating of debris-flow deposits using dendrochronology and lichenometry on the one hand and debris-flow frequencies obtained from regular field surveys on the other hand has been briefly mentioned in section 3.1. Successive debris flows may follow the same track, reworking or burying previously deposited material. Thus the evidence of preceding debris flows is either destroyed or buried and cannot be dated, problem also noted by Van Steijn (1996). In period June 1991 - June 1995, debris flows at TCP have followed the same track until finally the lower part of the track shifted north on 26 June 1994. In

the autumn of 1994 the track shifted south again. De Redeljkheid (1988) has suggested the same mechanism and Krzemiński (1988) has similar observations of successive debris flows following the same tracks in the Polish Tatra Mountains. Two possible explanations can be given for the shift of the debris-flow track:

- If a low-magnitude debris flow comes to a stop in the track channel, a subsequent debris flow will encounter this obstruction and may be forced to change its course. At TCP, this seems to have occurred in the period between late June and mid October 1994.
- If a high-magnitude debris flow exceeds the capacity of the channel, the flow overtops the channel sides and the track can change its course. This was the 26 June 1994 situation at TCP.

Of course, when a debris flow chooses another track, this may well be an even older track which is reactivated and again the evidence of older deposits may be erased. These processes will lead to an underestimation of the actual debris-flow frequency by lichenometry. Bearing in mind that lichenometry only provides a minimum age for a deposit, the actual difference may be even larger. In contrast to the preceding, a single debris flow may also produce more than one deposit (see fig. 10.4). This occurred on 26 June 1994 at the TCP site. Although such a *single-rainstorm multiple-deposit* debris flow is not very common, its deposits have a higher probability of (partly) surviving without subsequent reworking or burial than the deposits of a *single-rainstorm single-deposit* debris flow. In dendrochronologically and lichenometrically dated deposits, single-rainstorm multiple-deposits will show up as two (or more) separate, apparently independent deposits occurring in about the same years. This results in a tendency to overestimate debris-flow frequency compared to a situation without single-rainstorm multiple-deposits.

Table 10.3 also shows that debris-flow frequencies obtained from regular field visits are generally higher on the western slope of the Tête du Clot des Pastres compared to the Vallon de la Moutière. This clearly shows that the possibility of identification of a debris-flow event increases with the intensity of field visits: the Tête du Clot des Pastres west slope was visited regularly in each field campaign. Within the debris-flow systems of the Tête du Clot des Pastres west slope, the most visited site, TCP, once more has the highest number of identified debris flows. This shows that debris-flow frequencies obtained from field visits are minimum values, so again the difference with the 'traditional' dating methods is probably larger. Due to the short period covered by the regular, systematic field surveys, it remains impossible to say whether or not 1994 has been an extreme year with regard to debris-flow occurrence. For the same reason, possible patterns of long-term variation in debris-flow activity cannot be detected. Such long-term variation was detected by De Redeljkheid (1988), Kotarba (1989, 1992, 1997), Rapp and Nyberg (1988), Strunk (1988, 1989, 1991) and Van Steijn (1991) with the use of lichenometrical and dendrogeomorphological methods.

## 10.5 Conclusions

At least 291 debris flows have occurred in the Bachelard Valley in the period end July 1992 until mid-October 1994. Most of the debris flows seem to occur in the months June-September, and October also seems to be a period of debris-flow occurrence. Only few debris flows seem to occur in April and May, the snowmelt period, and in November and hardly any debris flows occur in the winter months December-March, when the study area is covered with snow and most precipitation falls in the form of snow. The short period of regular, systematic surveys made the recognition of a possible pattern of long-term variation in debris-flow frequency impossible. For the same reason, it remains impossible to say whether or not 1994 has been an extreme year with regard to debris-flow occurrence. Spatial debris-flow occurrence patterns can give an indication of the type of rainstorms responsible for the triggering of the debris flow. Strongly clustered patterns indicate that local rainstorms were involved. A pattern showing evenly spread debris flows is more difficult to interpret. It can indicate both the occurrence of widespread rainfall or the occurrence of several local rainstorms.

The most active parts of the Bachelard Valley with regard to debris flows are the areas to the south of the Bachelard as well as the Moutière Valley and the Bayasse area. Absolute values of debris-flow frequency, expressed as the average number of debris flows per trigger zone per year for a region, range from 0.050 yr<sup>-1</sup> for the Braissette Valley to 0.956 yr<sup>-1</sup> for the west slope of the Tête du Clot des Pastres. The TCP site has a debris-flow frequency of at least 1.50 yr<sup>-1</sup>, but 2.50 yr<sup>-1</sup> seems to be a more realistic value. About one third of the variation in debris-flow frequency within the Bachelard Valley can be accounted for by differences in debris-flow trigger-zone density of the regions. Even when field visits are carried out once or twice a year, not all debris flows that have occurred are identified. Debris-flow frequencies obtained from regular field surveys are up to 30 times higher than those from dendrogeomorphologically and lichenometrically dated deposits. The most important causes are burial of older deposits and the use of the same track by successive debris flows, reworking previously deposited material and thereby destroying the evidence of former debris-flow activity. The deposits will be preserved only when the debris flow chooses a new track, caused by either an obstruction in the track channel or by exceedance of the channel capacity by a high-magnitude debris flow. Debris-flow deposit dates should therefore be interpreted with considerable care: the obtained dates often stand for debris-flow track *avulsion* rather than debris-flow *occurrence*. Therefore, debris-flow frequencies calculated from dendrogeomorphological and lichenometrical dates should be regarded as minimum values, and actual values can be an order of magnitude higher.

In this thesis temporal aspects and some spatial aspects concerning debris-flow occurrence have been investigated using different approaches: a physical, an empirical, a historical and a spatio-temporal approach. Many practical limitations have been encountered during the field investigations, most of which are strongly related to the nature of the terrain where most debris flows are triggered. Still, the study has provided new results regarding the conditions triggering debris flows.

### 11.1

#### Methodological considerations and the physical approach

The specific nature of the high-mountain environment of the Bachelard Valley with its steep slopes, high process activity, together with the remoteness of most debris-flow trigger zones, has a large influence on the methods that can be applied to obtain data. In addition, there are limitations imposed by transport of equipment and samples by car and by foot. Therefore it appears that simple equipment and simple field methods offer the best way to gather data under these circumstances. Yet such simple methods cannot be expected to deliver all necessary data.

The rainfall simulator experiments in chapter 6 are a good example of such a simple field method where other methods are difficult or impossible. First consider the constraints: steep slopes, rough surfaces with stones, limited availability of water within a reasonable distance of the test sites and a limited transportation capacity because all materials have to be transported by foot on steep slopes. Most other methods to measure infiltration characteristics are impossible to use under these circumstances or at least impractical. For instance, infiltrometers cannot be used on steep slopes and on rough surfaces. Taking (some) samples to the laboratory for testing might have been an option, but it is very hard to obtain undisturbed samples of the stony soils and keep them undisturbed during transport. The rainfall simulator on the other hand can be set up easily even on very steep slopes of 50-60° with rough surfaces without disturbing the soil surface. On the other hand, the small size of the rainfall simulator has some serious drawbacks, because boundary effects during the simulations are important. This resulted in an overestimation of both the infiltration parameters  $K$  and  $S$  by a factor 2-3. Although a larger simulator would suffer less from these boundary effects, the larger weight and water demand would make its transportation much less practical on the steep slopes. Thus it had to be taken for granted that the only practical method to measure the infiltration characteristics in the field suffered strongly from boundary effects.

Another example is the field method devised to measure the static and kinetic internal-friction angles of the cohesionless coarse debris that is present in most debris-flow trigger zones. It is both simple to carry out in the field and very little equipment is needed. However, during field experiments it appeared that the method was only feasible for the determination of the kinetic internal-friction angle, whereas the static internal-friction angle is the variable used in the physical models of debris-flow triggering. A subsequent literature study did not lead to a distinct, practical relation between these internal-friction angles. The results obtained for average kinetic internal-friction angles showed values ranging from 36-39°, with a strong dependence on stone size sorting and on stone shape.

A major problem proved to be the nature of the runoff within debris-flow trigger zones during high-intensity rainstorms. This runoff was found to contain high amounts of fine-grained sediment. Sometimes the amount was high enough to call it a micro-scale debris flow. The flow characteristics of such a runoff fluid are quite different from that of pure water, especially as a result of its higher density and much higher viscosity. As this runoff is able to transport small stones on the very steep



slopes, it cannot be predicted what exactly will happen when it meets an accumulation of coarse debris somewhere downslope in a channel. It has been shown that two extremes may occur for different grain-size compositions of the material transported by the runoff (assuming all other factors to be constant and the same for both extremes), resulting in strongly different safety factors from the infinite slope model. The runoff may behave as a fluid flowing *through* the coarse debris which can lead to complete saturation of the coarse debris mass, which yields a safety factor  $F = 0.94$ . On the other hand a complete blocking of the pores of the coarse debris mass by the stones in the runoff may occur, in which case the runoff behaves as a fluid flowing *over* the coarse debris. This yields  $F = 3.3$ , which is far from the point of failure. However, all other factors in the triggering models also showed variation, so the uncertainty is even worse. Using Takahashi's (1978, 1980) debris-flow triggering model, input data distributions obtained from measurements, and assuming a fully-saturated debris mass (the first extreme described above), the 95% probability range for the safety factor was found to be 0.42-0.94 from a Monte-Carlo type simulation. Yet another source of uncertainty results from the infiltration characteristics and the amount of water available for surface runoff during high-intensity rainstorms.

## 11.2 Debris-flow occurrence: the empirical approach

In view of both the limitations of data collection and the large variation and uncertainties of the input (mainly due to the complex nature of the runoff), it was concluded that a continuation of a physical approach of debris-flow triggering would be rather senseless. On the other hand, there were enough data to attempt an empirical approach. This consisted of quantifying the influence of several meteorological and hydrological factors on debris-flow triggering using logistic regression techniques based on recorded debris flows and using rainfall and runoff measurements for a representative debris-flow trigger zone, TCP. From these, the most important factors for debris-flow triggering on short time scales could be identified. In this analysis, the assumption was made that debris flows are triggered by rainfall only through the generation of runoff, and therefore runoff should be expected to be a better explaining factor in debris-flow occurrence than rainfall.

Based on rainfall and runoff measurements which were made every minute, several meteorological and hydrological parameters were calculated. The meteorological variables were the rainstorm maximum rainfall intensities over time intervals of 1 minute to 1 day, total rainstorm precipitation, total daily precipitation, rainstorm duration and several antecedent precipitation indices. From these, the rainfall intensities over short time intervals (2-15 minutes) appeared to be the most important factors determining debris-flow triggering. Unexpectedly, antecedent precipitation appeared to have only little influence on debris-flow triggering. The most likely explanation for this are two counteracting effects due to antecedent rainfall. On the one hand, with higher antecedent precipitation, the water content of the soil will be higher. This leads to a quicker and more intense generation of runoff when rainfall occurs, which rises the probability of debris-flow triggering. On the other hand, the wetting of the soil surface by antecedent rainfall more or less 'glues' loose particles to the surface, making their mobilization more difficult. Thus any runoff that is generated will contain less sediment and have lower density and viscosity, which decreases the probability of debris-flow triggering. Daily rainfall totals also proved to be of little use in the explanation of debris-flow occurrence. This severely restricts the use of -easily obtainable- daily rainfall records in investigations of debris-flow occurrence and other processes which depend on short-duration high-intensity rainfall. For debris flows depending on short-duration high-intensity rainfall, probably mainly those which have relatively small trigger zones of several hectares or less, such daily rainfall records are useless. For larger debris-flow trigger zones, they may be of more use, as indicated by Rebetez et al. (1997) who have found that extremes of total 3-day rainfall explained debris-flow occurrence in the 1.4 km<sup>2</sup> Ritigraben catchment in southern Switzerland.

These conclusions were clearly supported by the events during the generally wet period of May and June 1992. During most of this 8 week period, long-duration low-to-mid-intensity rainfall occurred. Soil conditions in the TCP debris-flow trigger zone were found to be near saturation most of the time and low-to-mid-discharge runoff, probably generated as saturation overland flow, often took place. Yet during this period only a few small debris flows were triggered (fig. 10.2c). The results of this study also support the threshold curve defined by Caine (1980) for the occurrence of debris flows at shallow landslides. This was somewhat surprising, as this curve is largely based on estimated rainfall intensities for many different regions and climates. On the other hand, Innes' (1983a) curve for debris flow triggering is inapplicable to the Bachelard Valley. Caine's (1980) threshold 10-minute rainfall intensity for triggering debris flows is about 30 mm/hr.

During rainfall simulations, micro-scale debris flows or debris slides were sometimes triggered, for which a threshold curve could also be constructed in terms of minimum slope angle and minimum rainfall intensity. The minimum rainfall intensity during 2-3 minutes in these experiments was found to be 60-70 mm/hr on steep slopes. However, due to splash losses during these simulations, the actual corrected minimum rainfall intensity was much lower, probably 40-50 mm/hr, which also compares well with Caine's (1980) curve. The occurrence of these micro-scale debris flows and slides may form an important link between rainfall and debris-flow triggering by delivering high amounts of sediment to the overland flow.

As mentioned, meteorological factors influence debris-flow triggering through runoff. In order to quantify the relations between runoff and debris-flow triggering, two runoff models were applied to a key area of the TCP site. A simple tank model, TANKFLOW, treats the whole catchment as one (lumped variant) or two (rill-interrill variant) stores, from which runoff is generated whenever the infiltration capacity of the catchment is exceeded by the rainfall intensity. Infiltration is based on Philip's (1957) equation, and runoff intensity in this model is directly proportional to the amount of water stored at the surface. DINOFLOW is more complex. It is a distributed model based on physical principles. It incorporates an infiltration module based on Philip (1957), effects of sediment on the density and viscosity of the runoff fluid, concentration of interrill flow along preferential paths, flow routing and both laminar and turbulent flow velocity equations. DINOFLOW contains more parameters and variables to describe the discharge than TANKFLOW.

The infiltration parameters, steady-state infiltration capacity  $K$  and sorptivity  $S$ , used to describe the Philip (1957) infiltration, were obtained from rainfall simulations. It has already been mentioned that the results obtained from this method overestimated the actual values of the infiltration parameters, so correction factors for  $K$  and  $S$  were introduced in the models. Average measured values for TCP were  $K = 53$  mm/hr and  $S = 0.14$ - $0.20$  cm/ $\sqrt{\text{min}}$  from the 'infiltration-envelope' method and  $K = 43$  mm/hr and  $S = 0.16$ - $0.18$  cm/ $\sqrt{\text{min}}$  from the 'constant-runoff' method. During model calibration the runoff models showed the overestimation of both parameters to be a factor 2-3. It also appeared that both runoff models are most sensitive to  $K$ ,  $S$  and their correction factors. Rainfall is also a sensitive factor in the models, but the uncertainty in the values of measured rainfall is much less than the uncertainty in  $K$  and  $S$  values. The lack of reliable discharge measurements, caused by the blocking of the discharge flume particularly at high discharges, resulted in calibrated models which have a large uncertainty in modelled discharges. To account for the variation in input data during simulation runs Monte Carlo simulations were performed for both TANKFLOW and DINOFLOW. For each simulation and in the case of DINOFLOW for each gridcell of each simulation, the input values of steady-state infiltration capacity  $K$ , sorptivity  $S$ , field water content  $\theta_r$ , porosity  $\theta$ , and regolith depth  $z_{reg}$  were drawn randomly from known distributions.

Due to the uncertainties in model calibration, the variation in input values and the fact that the runoff was modelled for a key area instead of the whole catchment, the calculated discharges from both TANKFLOW and DINOFLOW do not correlate better with debris-flow triggering than simple meteorological parameters. DINOFLOW peak discharge always correlates worse with debris-flow occurrence



than the maximum 10-minute rainfall intensity. At best, TANKFLOW peak discharge correlates slightly better with debris-flow occurrence than the maximum 10-minute rainfall intensity of the rainstorm. However, this takes place at the cost of a much higher number of input and calibration parameters, for example the antecedent precipitation index actually uses 2 input parameters and DINOFLOW peak discharge needs 13 input and calibration parameters for its calculation. Taking account of the amount of visible and hidden parameters by applying Akaike's (1973) Information Criterion *AIC*, the simple meteorological models appear to be more efficient in explaining debris-flow occurrence. The most efficient models were 2 two-parameter models with rainstorm maximum 5-minute rainfall intensity and either total rainstorm precipitation or antecedent precipitation, using log-transformed data.

### 11.3 Debris-flow frequency

Debris-flow frequency was obtained in three ways: from 'observed' debris-flow events, from debris-flow frequency modelling and from dated debris-flow deposits. The first two methods were based on debris-flow events during the period of investigations only: June 1991 until June 1995. The last method provided data on debris-flow frequency over a longer period, roughly the past 50-60 years. The second method was carried out for the TCP debris-flow system only. Observations were made for all debris-flow systems in the Bachelard Valley, although not always as frequently and for as long a period as for TCP. It was assumed that the results from these observations represented the 'true' activity of the debris-flow systems. Deposit dating was performed for 5 debris-flow systems. From 'direct' observations, including comparison of photos from successive years and video camera recordings, at least 6 debris flows could be identified at the TCP site, but 8-12 seems a more likely number. This yields an average frequency of (at least 1.5) 2-3 debris flows per year. Based on 10-minute rainfall intensities, debris-flow frequency was also modelled. A Gumbel type I curve was fitted to the distribution of 10-minute rainfall intensities over the period of rainfall measurements, 4 consecutive summers in the years 1991-1994. From this, the frequency of extreme 10-minute rainfall intensities could be obtained. Combination of this distribution with either Caine's (1980) threshold curve for debris-flow occurrence or with the debris-flow probability curve obtained from logistic regression analysis yielded estimates of debris-flow frequency which were generally a factor 1½-2½ too high. Accounting for the uncertainties in the rainfall intensity distribution curve and the debris-flow probability curve, it appeared that the observed frequency lies within the 95% confidence limits of the modelled frequency for the combination with the debris-flow probability curve, but outside the 95% confidence limits for the combination with Caine's (1980) threshold curve. Thus it can be stated that only for this last case the modelled frequency differs significantly from the observation frequency in a statistical sense. The combination of the rainfall distribution and debris-flow probability curves also shows that the highest amount of debris flows can be expected from 10-minute rainfall intensities around 40 mm/hr.

In contrast to the modelled debris-flow frequency, dating of debris-flow deposits with dendrogeomorphology and lichenometry produced debris-flow frequency estimates which were lower than the observed frequencies. For five debris-flow systems, frequency estimates from dated deposits in this study ranged from 0.15 to 0.49 debris flows per year in the period 1940-1994, at least twice as low as their observed frequencies. De Redelijkheid's (1988) debris-flow deposits dates showed an even stronger underestimation of the actual debris-flow frequency: on average a factor 10 (1.5-30). The underestimation is caused by three factors. First, when lichenometry is used, individual deposits have to be separated based on field characteristics such as morphology, grain size, vegetation cover and lichen cover. When 2 or more adjacent deposits have occurred within a few years and cannot be separated visually, they will be identified as a single deposit. The probability of such errors increases with deposit age, as morphological features will slowly fade and vegetation cover and lichen cover will become more and more the same. Second, smaller deposits have more chance of being completely

buried than larger deposits and they have less chance of affecting trees. Thus deposit dating is biased towards dating deposits formed by high-magnitude events. Finally, consecutive debris flows may follow the same track. While that track is active, material from levees and lobes can be reentrained successive debris flows. This ends when a debris flow chooses another track and only the traces of the last debris flow that has passed the track remain. This leads to the conclusion that in many cases debris-flow deposit dating using lichenometry does not show the actual occurrence of debris flow in the past, but only debris-flow track avulsion. On the other hand, multiple deposits may be deposited by a single debris-flow event: two levees and one or more terminal deposits. In the field, these are not always identified as matching deposits and also the lichenometrical dating will probably provide different dates for each of those deposits.

Most of the dated debris-flow deposits dated from the period 1940-1975. More recent deposits could not be dated with lichenometry as a result of the colonization time of *Rhizocarpon geographicum* lichens. Only a few of the more recent ones could be dated by dendrogeomorphology, but a large number remained undated. Relative dating of the undated deposits revealed that most of these were recent, being formed after 1970-1975. This also leads to the conclusion that deposits formed before 1940 must nearly all be buried by younger ones in the five investigated debris-flow systems. Lichenometrical dates were based on the *Rhizocarpon geographicum* s.l. growth curve for the Bache Valley which was constructed with the aid of dendrogeomorphological data. This growth curve reveals a shorter colonization period (16-17 years) and a slower growth (30 mm in the first 50 years colonization) than Orombelli and Porter's (1983) growth curve from the nearby Aosta Valley. Deposit dates did not reveal any conspicuous cyclicity in debris-flow activity.

Regular surveys carried out twice a year in the whole Bachelard Valley indicated that debris flow are a much more frequent phenomenon in the Bachelard Valley than was previously thought. Asch and Van Steijn (1991) mentioned average debris-flow return periods of about 10 years, and years for debris flows from the most active systems, which was the starting-point for this study. Average return periods in this study for different sub-regions of the Bachelard Valley range from about 1½ years for the series of debris-flow trigger zones on the western slope of the Tête du Clot des Pastres to about 20 years for the Braissette Valley, the overall Bachelard Valley average being some 2-2½ years. This is as low as ½-½ year for the most intensively investigated site, TCP. As a positive relation was found between the frequency of field visits to a debris-flow system and the observed debris-flow frequency, most of the return periods are likely to be even shorter. This undermines the initial assumption that the results from these observations represented the 'true' activity of the debris-flow systems. Differences in lithology may also be responsible for differences in debris-flow activity, which seems to be high in debris-flow systems located in highly fractured rocks and in flysch deposits. Debris-flow occurrence often occurred in a clustered pattern reflecting the spatial distribution of local, high-intensity rainstorms. Most debris flows occurred in summer and early autumn, hardly any were triggered in winter or spring. Debris-flow trigger zones are mostly found above 2000 m in the Bachelard Valley.

### 11.4 General conclusions and recommendations for future research

One of the main conclusions from this study is the impossibility of using a fully physical approach to quantify debris-flow triggering conditions, one of the research aims defined in chapter 1. Due to the complex nature of overland flow in the debris-flow trigger zones, several models may apply to the triggering of debris flows. Figure 11.1 shows this complexity as an adaptation of Postma's (1988) debris-flow triggering model for the Bachelard Valley presented in figure 1.2. The adapted model incorporates runoff from the side slopes towards the accumulation of coarse debris in a central channel as overland flow transporting sediment or as a small-to-micro-scale debris flow and failure of the

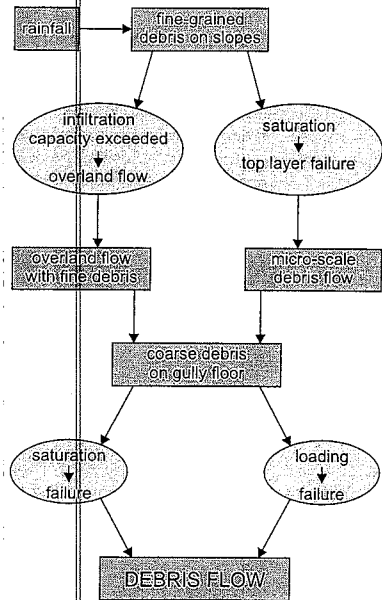


Figure 1.1 Revised debris-flow triggering hypothesis.

early-warning system for debris-flow hazard has to be installed. In view of the clustered pattern of debris-flow occurrence, rainfall measurements should be carried out as close as possible near the trigger zones of interest.

By obtaining several measures of debris-flow frequency, another research aim was met. All methods revealed that debris-flow frequency is higher than was believed until now. A comparison of the observed debris-flow frequency with the results of the debris-flow deposit dating led to the conclusion that the latter method only provides the dates of shifts in the location of debris-flow activity rather than dates of all debris-flow events. Long-term, regular, direct observations of debris-flow occurrence in other areas are needed to fill in the lack of data on actual debris-flow frequency: no other work concerning regular surveys of debris-flow occurrence in a larger area are known.

Another part of the research goals, finding the most important morphological and hydrological characteristics of debris-flow trigger zones with respect to debris-flow triggering and the prediction of debris-flow frequency on the basis of these characteristics has only partly been fulfilled. Some data on the location and activity of debris-flow trigger zones in terms of elevation and lithology have been gathered, but the relation with other topographic and geologic characteristics remains an interesting subject for study. Other topics on which future research might focus are the possible effects of climate change on debris-flow activity and (yet more) debris-flow deposits dating, including the construction of a reliable growth curve for *Rhizocarpon* in the Bachelard Valley. Such a study might clarify the contradictory results between this study and De Redelijkheid (1988) where deposits dates and cyclic variations in debris-flow activity are concerned.

debris mass can be achieved through saturation of that mass or by loading. The characteristics of the runoff fluid and its effect on debris-flow triggering proved to be impossible to forecast for given rainfall data. More research on this topic seems necessary. Also direct observations (laboratory, field camera) of the characteristics of runoff as a function of surface characteristics and rainfall intensity may reveal more about the expected type of runoff under different circumstances.

The empirical approach was successful. It clearly showed that Hortonian overland flow generated during short-duration high-intensity rainstorms is responsible for debris-flow triggering in the Bachelard Valley, thereby confirming the first part of the working hypothesis formulated in chapter 1. Antecedent rainfall only plays a minor role. A comparison of the performance of the hydrological models and the simple meteorological regression models shows that much more work has to be done concerning the hydrological behaviour of debris-flow trigger zones. This applies to infiltration characteristics as well as overland flow characteristics. On the other hand, it may be just as useful or more useful to improve rainfall measurements in debris-flow prone areas: this can be used in a simple but powerful model of debris-flow prediction and therefore seems to be more promising if an

## SAMENVATTING

### STROMENDE STENEN.

Initiatie en herhalingsfrequentie van hellingpuinstromen in het Bachelarddal, zuidelijke Franse Alpen.

#### 1 Introductie

Puinstromen vormen een belangrijk proces van sedimenttransport in vele bergachtige gebieden over de gehele wereld. De meeste puinstromen vinden min of meer onopgemerkt plaats in afgelegen gebieden, waardoor de belangstelling voor puinstromen in het verleden erg beperkt was. Met de toename van de economische druk in vele berggebieden neemt echter ook het risico van puinstromen voor de mens sterk toe, met name in dichtbevolkte gebieden zoals Japan. Ook het effect dat een verandering van het klimaat op het voorkomen van puinstromen zou kunnen hebben, leidt tot een grotere belangstelling voor het fenomeen puinstroom.

Dit proefschrift beschrijft de resultaten van het project "De Temporele Analyse van Puinstromen in een Alpien Milieu", dat van 1991-1995 plaatsvond en voortbouwt op eerdere onderzoeken van de vakgroep Fysische Geografie van de Universiteit Utrecht aan puinstromen in de zuidelijke Franse Alpen. Uit eerdere onderzoeken was een kwalitatief model voor het optreden van puinstromen in het Bachelarddal afgeleid. Centraal in dit project stond de vraag of, en zo ja, hoe de temporele aspecten van het optreden van puinstromen (initiatie en herhalingsfrequentie) konden worden gekwantificeerd op basis van neerslagkarakteristieken en morfologische en hydrologische kenmerken. Belangrijke onderzoeksdoelen hadden vooral betrekking op de puinstroominitiatie en de factoren die daarop van invloed zijn, de rol van water (karakteristieken van de neerslag en van oppervlakkige afstroming) en de herhalingsfrequentie van puinstromen (ruimtelijke en temporele variabiliteit van puinstroomactiviteit; vergelijking tussen herhalingsfrequenties verkregen door modellering op grond van neerslagkarakteristieken, door datering van oude puinstroomafzettingen en door kartering van actuele puinstromen). Het project werd gefinancierd door de Europese Unie (het EPOCH programma) en de Universiteit Utrecht.

#### 2 Puinstromen: een literatuurstudie

Puinstromen zijn snelle massabewegingen, waarbij een mengsel van vaste delen, water en soms lucht als één viskeuze massa beweegt. In een continuüm van droog naar nat bevinden puinstromen zich tussen aan de ene kant droge vormen van massabeweging, waarbij water slechts als smeermiddel dient, en aan de andere kant transport van sediment door stromend water. Typerend voor puinstromen zijn de afzettingen in de vorm van oeverwallen en eindlobben.

Puinstromen kunnen op diverse manieren ontstaan, zoals uit afglijdingen. Veelal speelt water een belangrijke rol bij de initiatie. Vooral regen en sneeuwsmeelt zijn vaak genoemde oorzaken van puinstroomactiviteit. Drempelwaarden voor het optreden van puinstromen als functie van neerslagtotalen en -intensiteiten zijn gegeven door Innes (1983a) en Caine (1980). Fysische modellen voor puinstroominitiatie worden gegeven door Johnson (1965, 1970) voor de vorming van puinstromen uit afglijdingen en door Takahashi (1978, 1980, 1981a, 1981b) voor spontane initiatie van puinstromen. Postma (1988) geeft voor puinstromen in het Bachelarddal een aangepast model voor puinstroominitiatie op basis van het model van Takahashi, waarbij een scheiding tussen grof puin en de toevoer van water met fijn materiaal wordt gemaakt.

Bewegingsmodellen voor puinstromen zijn ruwweg in twee groepen te verdelen: modellen die rekening houden met de interactie tussen individuele stenen en/of tussen stenen en vloeistof, en modellen die dat niet doen. Onder de eerste groep vallen onder andere de bewegingsmodellen van Takahashi en van Chen (1988a, 1988b), in de tweede groep vallen modellen op basis van Newton-

viskeus gedrag en Bingham- of Coulomb-viskopplastisch gedrag (bijvoorbeeld het model van Johnson). Zowel watergehalte als korrelgrootteverdeling hebben een sterke invloed op het bewegingsgedrag van puinstromen.

Om de risico's van puinstromen voor de mens te beperken zijn er zowel 'harde' als 'zachte' maatregelen mogelijk. Harde maatregelen betreffen vooral de aanleg van constructies; zachte maatregelen berusten vooral op het vermijden van door puinstromen bedreigde plaatsen, veelal aan de hand van risicokarteringen. Ook zijn maatregelen mogelijk die invloed hebben op de gevoeligheid voor het ontstaan van puinstromen, zoals drainage, aangepast landgebruik of herbebossing.

Veel puinstromen ontstaan tijdens hevige regen- en onweersbuien, waarbij de infiltratiecapaciteit van de bodem wordt overtroffen en Horton-type oppervlakkige afvoer optreedt. Green en Ampt (1911), Horton (1933, 1939) en Philip (1957) geven functies voor de infiltratiecapaciteit van de bodem indien de watertoevoer de infiltratie niet beperkt. Deze functies zijn monotoon dalend naar een asymptotische eindwaarde, de 'steady-state' infiltratiecapaciteit. Wanneer de watertoevoer aanvankelijk wel minder is dan de infiltratie, zal pas na enige tijd de infiltratiecapaciteit worden overschreden. Het deel dat niet infiltreert zal op steile hellingen direct oppervlakkig afstromen. Tussen de 'rills' zal de stroming meestal laminair zijn, in 'rills' veelal turbulent. In beide gevallen kan de snelheid van het afstromende water worden berekend. Het veelal hoge sedimentgehalte van afstromend water op steile hellingen vormt een complicerende factor.

Puinstromen kunnen op diverse manieren gedateerd worden. Een belangrijke methode om puinstromen te dateren is dendrogeomorfologie, gebaseerd op de groei van bomen en op veranderingen in patroon van de jaarringen van bomen, zoals plotselinge groeivermindering als gevolg van het deels begraven raken van de boomstam, plotselinge verandering in de excentriciteit van de jaarringen als gevolg van scheefstelling van de boom, of het plaatselijk ontbreken van jaarringen na een verwonding van de boom. Een andere belangrijke methode is lichenometrie, gebaseerd op de regelmatige groei van sommige korstmossoorten. Hierbij spelen vooral soorten van het genus *Rhizocarpon* een belangrijke rol.

### 3 Het onderzoeksgebied: het Bachelarddal

Het dal van de Bachelard, een zijrivier van de Ubaye, ligt in de zuidelijke Franse Alpen op een hoogte tussen 1100 en 3050 m. Een groot deel van het Bachelarddal ligt in een nationaal park, het Parc du Mercantour. Geologisch wordt het gebied gekenmerkt door de aanwezigheid van zowel autochtone gesteenten als dekbladen. De belangrijkste gesteentesoorten zijn flysch, zandsteen (Gres d'Annot), mergel (Terres Noires), kalksteen en schist. Morfologisch wordt het gebied sterk bepaald door glaciële relict, steile rotskliffen, puinhellingen en massabewegingen. Het klimaat is gematigd mediterraan-oceanisch met een neerslagmaximum in herfst. De jaarlijkse neerslag in Fours-St.-Laurent (1660 m) bedraagt 977 mm. Met name in de zomer en de vroege herfst kunnen hevige buien voorkomen. De 0°C-isotherm ligt op een hoogte van ongeveer 2400-2500 m, en op deze hoogte komt mogelijk sporadisch permafrost voor. De boomgrens ligt slechts weinig lager, op 2200-2400 m. De vegetatie bestaat voornamelijk uit alpenweiden en bossen, met name de boomsoorten *Larix decidua* en *Pinus sylvestris* komen veel voor. Het Bachelarddal is in de afgelopen eeuwen sterk ontvolkt, en tegenwoordig leven er nog slechts enkele tientallen mensen stroomopwaarts van Uvernet-Fours.

In het Bachelarddal bevinden zich meer dan 300 puinstroomsystemen, waarvan de bronzones een gemiddelde grootte hebben van 3 hectare. De bronzones komen vooral voor boven de 2000 m en hun voorkomen neemt toe met de hoogte. Op deze hoogten spelen periglaciële condities mogelijk een belangrijke rol bij de productie van grof puin. Bronzones blijken een voorkeur te hebben voor locaties met qua resistentie sterk afwisselende gesteentesoorten; bovendien blijkt dat veel bronzones in clusters liggen. De meeste bronzones bevatten nauwelijks of geen vegetatie. Twee hoofdtypen

bronzones kunnen van elkaar worden onderscheiden: couloir-puinhelling bronzones en kom- of trechtervormige bronzones. In het eerste type bronzone bestaat een duidelijke scheiding tussen de delen die water leveren en de delen waar het puin ligt. Kom- en trechtervormige bronzones bevinden zich vooral op locaties met sterk wisselende gesteentesoorten en op puinhellingen, en hier is het puin in gehele bronzone aanwezig; wel is er vaak een scheiding tussen delen waar grof puin ligt, vaak een centrale afvoergeul, en delen waar fijn materiaal aanwezig is. Dit type bronzone heeft hellingen van gemiddeld 38° en geulen van 30° of steiler. Puinstroomafzettingen komen in het Bachelarddal voor tussen 1700 en 2400 m, hebben een lengte van enkele honderden tot meer dan 1000 m en een volume van 1-1000 m<sup>3</sup>).

Het onderzoek heeft zich grotendeels geconcentreerd op de trechtervormige bronzone TCP (Tête du Clot des Pastres), welke op een hoogte van 1975-2150 m is gelegen op de westelijke helling van de Tête du Clot des Pastres. De geulen in dit brongebied hebben hellingshoeken van 35-38°, de zijwanden 45-50°. Boven 2060 m komt zandsteen (Gres d'Annot) aan het oppervlak, welke de leverancier is van het grove puin in de brede, ondiepe centrale geul. Onderin het brongebied is dit puinpakket 1 à 2 m dik. Tussen 2015 m en 2060 m liggen verweerde mergels aan het oppervlak, en onder 2015 m ligt een laag kalksteen welke verder naar onder toe verdwijnt onder een puindek. De mergels zijn sterk versneden door rills en gullies. Deze gullies zijn zeer steil: gemiddeld 42° en de zijwanden van de gullies hebben hellingen van zo'n 50°. Het verweringsdek dat de mergels bedekt is zeer gevoelig voor erosie door Horton oppervlakkige afstroming welke optreedt tijdens hevige buien. Dit leidt tot een sterke insnijding van de rills en de gullies in de zomer. In de winter wordt deze insnijding grotendeels tenietgedaan doordat solifluctiemateriaal de rills en gullies weer opvult. In het brongebied TCP komt nauwelijks vegetatie voor.

### 4 Onderzoeksmethoden

De te gebruiken veldmethoden werden sterk bepaald door de praktische problemen die het moeilijk toegankelijke terrein opwierp. Er is onder andere een nieuwe testmethode voor de bepaling van de hoek van inwendige wrijving van cohesieloos (grof) puin. Hiertoe werden in-situ metingen gedaan op plekken waar grof puin was geaccumuleerd en bovendien de hellingshoek van het terrein vrijwel gelijk was aan de hoek van inwendige wrijving van het materiaal. De methode bestaat uit het weggraven van puin totdat het erboven gelegen pakket in beweging komt. Deze methode bleek voornamelijk praktisch voor bepaling van de kinetische hoek van inwendige wrijving, niet voor bepaling van de (in het puinstroominitiatie benodigde) statische hoek van inwendige wrijving. Voor de bepaling van de infiltratiekarakteristieken van verweringsdekken en puindekken in de bronzones van puinstromen is gebruik gemaakt van een kleine (24,5×24,5 cm<sup>2</sup>) regensimulator. Verder zijn porositeiten, veldvochtgehaltes, pF-karakteristieken, korrelgrootteverdelingen en diktes bepaald voor deze verweringsdekken.

In het brongebied TCP is een afvoergoot geplaatst, waar afvoeren werden gemeten van een 30 m lange, 10 m brede gully. Twee regenmeters registreerden de neerslag en een videocamera registreerde de gebeurtenissen tijdens hevige buien. De afvoermetingen bleken zeer problematisch doordat de goot telkens verstopt raakte door de grote hoeveelheden sediment die met de afvoer werden meegevoerd. Ook zijn ten behoeve van de hydrologische modellering geodetische metingen uitgevoerd, waarmee een DEM is gemaakt van het brongebied.

Van vijf puinstroomsystemen zijn de afzettingen gedateerd met behulp van dendrogeomorfologie en lichenometrie. Dendrogeomorfologische bepalingen betroffen de datering van wonden bij gewone bomen, de minimale leeftijd van afzettingen aan de hand van de leeftijd van bomen die pas later op de afzettingen zijn gaan groeien, en dateringen van plotselinge groeiveranderingen (ringdikte

onderzocht de afstromingsmetingen met de grootst mogelijke nauwkeurigheid (korstmoslichamen) van de soort *Rhizocarpon geographicum*. Ter vergelijking zijn twee maal per jaar, in de zomer en in de herfst, alle nieuw gevormde puinstroomafzettingen in het Bachelarddal gekarteerd.

**5 Fysische kwantificatie van de condities die leiden tot het ontstaan van puinstromen**  
Het puinstroominitiatie-model van Takahashi (1978, 1980, 1981a, 1981b) bevat de volgende variabelen: cohesie, statische hoek van inwendige wrijving, de dichtheid en de concentratie van de vaste delen, de dichtheid van de vloeistof in de poriën en de hellingshoek. Enkele hiervan zijn gekwantificeerd: de cohesie ( $= 0$ ), de hellingshoek ( $30-35^\circ$ ; bepaald uit het DEM) en de dichtheid ( $2200-2700 \text{ kg/m}^3$ ) en concentratie van de vaste delen. Deze concentratie is gemiddeld 0.55, is niet afhankelijk van de gemiddelde steengrootte, maar wel van de zettingsgraad en de korrelgrootteverdeling. De statische hoek van inwendige wrijving kon niet worden gemeten, maar wel de kinetische hoek van inwendige wrijving: deze varieerde tussen  $31^\circ$  en  $43^\circ$  voor 250 bepalingen. De gemiddelde waarden per puinpakket (50 metingen per puinpakket; kalksteenpuin, zandsteenpuin, flijschpuin en twee puinmengsels van meerdere gesteentesoorten) varieerden van  $36.0^\circ$  voor kalkpuin tot  $38.7^\circ$  voor een mengsel van gesteentesoorten. De verschillen in kinetische hoek van inwendige wrijving tussen de puinpakketten is voornamelijk afhankelijk van de sortingsgraad ( $r^2 = 0.71$ ) en van de steenvorm (beide samen:  $r^2 = 0.99$ ). De statische hoek van inwendige wrijving is waarschijnlijk enkele graden meer, mogelijk  $40-42^\circ$ .

De dichtheid van de vloeistof in de poriën is niet bepaald, deze is namelijk sterk afhankelijk van het sedimentgehalte. Ook neemt de viscositeit van de vloeistof sterk toe met een toename van het sedimentgehalte en de korrelgrootteverdeling van het meegevoerde sediment speelt een belangrijke rol bij het al dan niet door de poriën stromen van de vloeistof, samen met de grootte van de poriën. Dit betekent dat niet van te voren te voorspellen is of de sedimentrijke vloeistof de poriën van het grove puin wel of niet zal binnendringen. Dit heeft een sterke invloed op de mogelijkheid om het grove puin te mobiliseren en een puinstroom te initiëren: het eerste geval geeft voor een typische situatie van grof puin op een helling een veiligheidsfactor  $F = 1.53$ , het tweede geval levert  $F = 0.44$  op. Bovendien resulteren het ontbreken van gegevens van enkele factoren in het model van Takahashi en de grote variatie in wel goed gemeten gegevens in een grote variatie van uitkomsten van het model. Een volledig fysische kwantificering van de condities die leiden tot de initiatie van een puinstroom is dus niet mogelijk.

**6 Regensimulaties in brongebieden van puinstromen**  
Regenintensiteit en oppervlakkige afstroming lijken een sleutelrol te spelen in puinstroominitiatie, dus is het nodig om een vergelijking te maken tussen het voorkomen van puinstromen en regen- en afvoergegevens. Om een empirisch verband tussen het optreden van puinstromen en afvoeren mogelijk te maken is het nodig om afvoeren te meten dan wel te berekenen. Voor de berekening van afvoeren moet de infiltratiekarakteristiek van de bodem bekend zijn. Hiertoe zijn in totaal 351 regensimulaties uitgevoerd op verweringsdekken in 6 puinstroom-bronzones, waaruit steady-state infiltratiecapaciteiten  $K$  en sorptiviteiten ( $=$  slurpfactor  $S$ ) uit de Philip-infiltratievergelijking zijn bepaald. 252 van deze regensimulaties zijn uitgevoerd in het brongebied TCP op zandig-siltig verweringsdek in mergels. De brongebieden Pra Bouréou Noord (PBN) en Zuid (PBS) hebben vrijwel dezelfde lithologische opbouw als TCP, verder zijn regensimulaties uitgevoerd in Les Longs (LL; verweringsmateriaal van zandsteen, kalksteen en flijsch), Bayasse-Bachelard (BB; siltig-kleifig verweringsmateriaal) en Combal du Menon (CdM; flijsch-verweringsmateriaal). Tijdens de

regensimulaties vindt infiltratie niet alleen plaats in verticale richting, maar ook in laterale richting. Dit betekent dat alle berekende  $K$  en  $S$ -waarden de werkelijke waarden overschatten.

Tijdens Constante Afstromingsproeven (Constant Runoff; CR) werd doorberegend totdat het debiet van het afstromende water constant was. De 154 simulaties resulteerden in log-normaal verdeelde  $K$ -waarden van  $17-128 \text{ mm/uur}$  bij regenintensiteiten van  $30-291 \text{ mm/hr}$  op hellingen van  $27-54^\circ$ . Deze  $K$ -waarden worden deels bepaald door de samenstelling van het verweringsdek; ook blijkt er een positief verband te bestaan met de gebruikte regenintensiteiten. Hiervoor zijn verschillende mogelijke oorzaken aan te wijzen, zoals een dikkere waterlaag op het oppervlak, een dikkere verzadigde laag in de bodem of verliezen door splash en bij het opvangen van het afstromende water. TCP heeft een gemiddelde  $K$ -waarde van  $43 \text{ mm/uur}$ . Per regensimulatie werd ook de sorptiviteit berekend. Sorptiviteiten zijn normaal verdeeld met waarden van  $0.09-0.38 \text{ cm}^2/\text{min}$  (gemiddelde voor TCP  $0.18 \text{ cm}^2/\text{min}$ ). Twee andere methoden, waarbij één enkele sorptiviteit wordt berekend voor een hele dataset op basis van de Smith en Parlange vergelijking geven ongeveer dezelfde waarden. Er blijkt slechts een zwak verband te zijn tussen  $S$  en  $K$ .

Bij 316 regensimulaties is gebruik gemaakt van de methode die het moment van plasvorming aan het oppervlak beschrijft als functie van de regenintensiteit,  $K$  en  $S$ . Gebruikte regenintensiteiten waren  $28-291 \text{ mm/uur}$  op hellingen  $27-54^\circ$ . Het berekenen van functies die de gegevens beschrijven volgens de vergelijkingen van Philip en Smith en Parlange bleek in veel gevallen niet op een zinnige wijze mogelijk. Een negatieve exponentiële functie paste wel beter door de gegevens, maar deze heeft geen duidelijke fysische basis. Deze functie verklaart  $23-96\%$  van de variatie binnen verschillende datasets, en levert voor gemiddeld  $22\%$  hogere  $K$ -waarden dan de CR-methode (voor TCP:  $56 \text{ mm/uur}$ ). De met de negatieve exponentiële functies bepaalde  $K$ -waarden zijn ingevuld in de Philip en Smith en Parlange vergelijkingen om sorptiviteiten te berekenen. Hierbij valt op dat de Philip vergelijking  $20\%$  lagere waarden oplevert dan de waarden uit de Constante Afstromingsproeven en  $30\%$  lagere waarden dan de Smith en Parlange vergelijking. Ook in deze proeven blijkt de samenstelling van het verweringsdek invloed te hebben op de infiltratie-eigenschappen, evenals het initiële vochtgehalte van de bodem.

Tijdens de regensimulaties zijn diverse processen geobserveerd die normaliter ook een rol spelen binnen de brongebieden van puinstromen, zoals splash en het verweken van de uitdrogingskorst aan het oppervlak. Een bijzonder proces zijn de micro-puinstromen, die soms optreden tijdens regensimulaties met hoge regenintensiteiten op steile hellingen. Dergelijke micro-puinstromen traden alleen op in de eerste minuten van een simulatie. De drempelwaarde voor hun optreden is een functie van de hellingshoek (minimaal  $34-36^\circ$ ) en de regenintensiteit (minimaal  $60-70 \text{ mm/uur}$ , gecorrigeerd minimaal  $45-55 \text{ mm/uur}$ ). Mogelijk spelen deze micro-puinstromen een belangrijke rol spelen bij puinstroominitiatie.

#### 7 Modellering van puinstroom en -frequentie: modellen

Voor de vergelijking tussen het optreden van puinstromen en neerslag- en afvoergegevens zijn eenvoudige neerslagkarakteristieken en zowel eenvoudige als complexe afvoermodellen gebruikt, welke allen gebruik maken van neerslaggegevens. De afvoermodellen gebruiken ook de infiltratie-eigenschappen van de bodem ( $K$ ,  $S$ , bergingscapaciteit  $STO$ , regoliëtdikte  $z_{reg}$ ; voor rills en voor interrills). De gegevens van de twee regenmeters tonen onderlinge verschillen tot zo'n  $20\%$ . De regenkarakteristieken zoals de maximale regenintensiteit per bui gemeten over tijdsduren van 1-30 minuten en 1, 2 en 24 uur, de duur van de bui, de totale neerslaghoeveelheid van de bui en per etmaal, en antecedente neerslag indexen, zijn eenvoudig af te leiden uit de regengegevens. Deze

regenkaracteristieken zijn (multiple) logistische regressies analyses vergeleken met het optreden van puinstromen.

Uit de regensimulaties is gebleken dat Horton-type oppervlakkige afstroming tijdens hevige regenbuien kan voorkomen in puinstroom-bronzones. De infiltratie in de hydrologische modellen is gebaseerd op Philip; hierbij zijn (te kalibreren) correctiefactoren voor  $K$  en  $S$  ingebracht in de modellen vanwege de verwachte overschatting van deze twee variabelen. Vanwege de korte duur van buien die puinstromen veroorzaken zijn subsurface flow en grondwaterstroming in de hydrologische modellering verwaarloosd. TANKFLOW is een eenvoudig tankmodel met een afvoer die recht evenredig is met de hoeveelheid water op het oppervlak. Dit model heeft de mogelijkheid om een onderscheid te maken tussen rills en interrills of alles op één hoop te gooien. Naast de invoervariabelen  $K$  en  $S$  en hun correctiefactoren gebruikt TANKFLOW alleen nog de uitstroomconstante als modelparameter.

DINOFLOW is een complexer afvoermodel dat gebruik maakt van een raster-GIS-achtige structuur en het verplaatsen van afstromend water volgens het reliëf. De stroming in DINOFLOW kan laminair zijn of turbulent (of iets er tussenin), afhankelijk van Reynoldsgetal, en wordt beschreven met de formules van Manning en van Robertson en Crowe. DINOFLOW houdt ook rekening met de concentratie van afvoer op de interrills en de dichtheid en viscositeit van de afstromende vloeistof. Naast de invoervariabelen  $K$ ,  $S$ , neerslag en bergingscapaciteit van de regoliet gebruikt het model 7 modelparameters voor welke gekalibreerd moet worden.

Voor beide modellen is een Monte Carlo procedure gebruikt (TANKFLOW  $N=500$ ; DINOFLOW  $N=10$ ) om de variatie in de waarden van de invoervariabelen te verwerken bij de kalibratie van de modelparameters van de modellen. Complicerende factoren bij de kalibratie waren de verschillen tussen de twee regenmeters en het gebrek aan betrouwbare afvoermetingen (een gevolg van het verstopt raken van de afvoergoot met sediment). De afvoermogelijkheden blijken vooral gevoelig te zijn voor de neerslag, voor  $K$  en  $S$  en hun correctiefactoren. Vanwege de onderlinge verschillen in de regengegevens zijn de modeluitkomsten niet erg betrouwbaar en de gekalibreerde waarden van de modelparameters niet erg stabiel: de range van acceptabele waarden is erg groot. Hierdoor neemt de identificeerbaarheid van de modelparameters af en dus ook het nut van modellen met (te) veel modelparameters. Uit de kalibratie blijkt dat de  $K$ -waarden bepaald met de regensimulaties de werkelijke  $K$ -waarden met een factor van ongeveer 2.5 overschatten; voor de sorptiviteiten is dit een factor 2.1.

## 8 Modellering van puinstroom en -frequentie: resultaten

Uit regelmatige veldbezoeken aan het brongebied TCP blijkt, dat hier in de periode Juni 1991 - Juni 1995 minimaal 6 à 7 puinstromen hebben plaatsgevonden, al lijkt een aantal van 8-12 waarschijnlijker. Slechts van twee van deze puinstromen is met zekerheid bekend door welke buien ze zijn veroorzaakt. Voor alle andere puinstromen geldt, dat ze met een wisselende mate van zekerheid aan bepaalde buien konden worden toegeschreven op grond van de karakteristieken van de buien zelf en, bij voorkeur, op grond van onafhankelijke informatie zoals veldkenmerken van de nieuwe afzettingen, opnames met de videocamera en afvoermetingen. De karakteristieken van de bui zelf zijn hiervoor zo weinig mogelijk gebruikt, aangezien dit leidt tot cirkelredeneringen wanneer het optreden van puinstromen vervolgens weer wordt gecorreleerd aan deze karakteristieken. Elke bui is ingedeeld in één van zes categorieën met betrekking tot de kans dat die bui een puinstroom heeft veroorzaakt: *zeker*, *zeer waarschijnlijk*, *waarschijnlijk*, *mogelijk*, *zeer onwaarschijnlijk* en *zeker niet*. In getallen uitgedrukt: *zeker*:  $p=1$ , *zeker niet*:  $p=0$ , de rest zit er tussenin. Het kwantificeren van de kans op het initiëren van een puinstroom als functie van neerslag- of afvoer karakteristiek(en) is gedaan door middel van logistische regressie met de maximum likelihood methode. Hiervoor werden de zes eerder genoemde categorieën teruggebracht tot twee

groepen: *wel puinstroom* (categorieën *zeker*, *zeer waarschijnlijk* en *waarschijnlijk*) en *geen puinstroom* (*mogelijk*, *zeer onwaarschijnlijk* en *zeker niet*).

De best met puinstroominitiatie correlerende variabelen zijn de maximale regenintensiteiten over korte tijdsintervallen (met name 2-15 minuten) en de piekafvoeren van TANKFLOW en DINOFLOW. Een maximale 10-minuten regenintensiteit van 40 mm/uur geeft 50% kans op puinstroominitiatie, een maximale 3-minuten regenintensiteit van 63 mm/uur eveneens. Deze laatste waarde is iets hoger dan de gecorrigeerde drempelwaarde van 45-55 mm/uur voor het optreden van micro-puinstromen tijdens regensimulaties. Neerslagtotalen van de buien en per etmaal correleren slechts gering met puinstroominitiatie, dus relatief gemakkelijk te verkrijgen gegevens zijn helaas slecht bruikbaar voor onderzoek aan dit soort puinstromen die worden geïnitieerd in kleine (<10 ha) brongebieden.

DINOFLOW piekafvoeren vertonen een wat lagere correlatie met puinstroomoptreden dan TANKFLOW piekafvoeren. Dit is waarschijnlijk het gevolg van het doorwerken van onzekerheden als gevolg van een groter aantal invoervariabelen en -parameters in DINOFLOW. Bij TANKFLOW blijken piekafvoeren van de lumped en de rill-interrill varianten vrijwel even goed te correleren met puinstroomoptreden. Ook het effect van antecedente neerslag op de piekafvoeren blijkt erg beperkt te zijn met betrekking tot de correlatie met puinstromen. Onder de gegeven omstandigheden varieert de onzekerheden met betrekking tot de invoervariabelen en -parameters blijken eenvoudige afvoermogelijkheden dus te prefereren boven complexe modellen.

Logaritmische transformatie van de invoervariabelen blijkt de correlaties in de logistische regressies te verhogen, zowel voor regen karakteristieken als voor piekafvoeren. Antecedente neerslag blijkt op zich slechts zeer laag te correleren met puinstroomoptreden. De invloed van neerslag blijkt een halve tot een hele dag stand te houden, en dit bevestigt eerdere veldwaarnemingen.

Modellen met 2 of meer variabelen geven hogere correlaties met het optreden van puinstromen, maar door het hogere aantal gebruikte variabelen hoeft de verklaarde variantie niet significant hoger te zijn. Door gebruik te maken van Akaike's Informatie Criterium  $AIS$ , welke laat zien of de toevoeging van extra variabelen al dan niet leidt tot een significant hogere verklaarde variantie, blijkt dat een simpel neerslagmodel met 2 parameters ( $\log-i_{r,3}$  en  $\log-I_{r,rn}$ ) het meest optimale model is. Blijkbaar zijn de onzekerheden in de invoervariabelen en -parameters zelfs voor het eenvoudige hydrologische tankmodel TANKFLOW al dermate groot, dat een eenvoudig regressiemodel met twee variabelen al beter voldoet.

Een vergelijking van de resultaten uit dit onderzoek met de drempelwaarden voor puinstromen volgens Innes (1983a) en Caine (1980) laat duidelijk zien dat de curve van Innes voor puinstromen in het Bachelarddal een veel te lage drempelwaarde geeft. De curve van Caine blijkt beter overeen te komen met de resultaten van dit onderzoek: voor tijdsintervallen van 1-120 minuten ligt deze curve in het bereik 15-50% kans op puinstroom. Op één na alle buien die in de groep *wel puinstroom* vallen, overschrijden Caine's drempelwaarde voor maximale regenintensiteiten in gemeten over 2-15 minuten. Uit buien in de groep *geen puinstroom* blijkt dat de drempelwaarde voor puinstroominitiatie gedurende de zomer enigszins toeneemt: de meeste buien in deze groep die de drempelwaarde van Caine overschreden, vonden plaats in september.

Om van puinstroominitiatie tot een puinstroomfrequentie te komen, is op de verdeling van maximale 10-minuten regenintensiteiten,  $i_{r,10}$ , een Gumbel type I verdeling gefit, waarbij Weibull's methoden van plotposities is gebruikt. Een goed passende Gumbel curve voor de extreme waarden van  $i_{r,10}$  werd pas verkregen nadat de lage regenintensiteiten ( $\leq 6$  mm/uur) werden verwijderd. Deze curve geeft de herhalingsfrequentie (of overschrijdingskans) als functie van de maximale 10-minuten regenintensiteit. Door combinatie van de curve met Caine's drempelwaarde (methode 1) of met de curve die de kans op puinstroominitiatie beschrijft als functie van de maximale 10-minuten

egenintensiteit (methode 3) kunnen puinstroomfrequenties worden berekend. Daarnaast kan ook og rekening worden gehouden met de betrouwbaarheidsintervallen van de herhalingsfrequentiecurve (methoden 2 en 4) en de puinstroomkanscurve (methode 4). Hierbij blijkt, at het betrouwbaarheidsinterval van de herhalingsfrequentiecurve veel nauwer is dan die van de uinstroomkanscurve. Methode 3 laat zien dat puinstromen het vaakst worden veroorzaakt door iaximale 10-minuten regenintensiteiten van 35-45 mm/uur. Alle 4 methoden overschatten de 'erkelijke puinstroomfrequentie van 3 ppj (factor 1.4-2.2). De werkelijke puinstroomfrequentie ligt 'el binnen de 95% betrouwbaarheidsgrenzen van methode 4. Om de puinstroomfrequentie in ppj uinstromen per jaar) te berekenen, waren enkele aannames nodig, aangezien neerslagmetingen, eldbezoeken en video-opnames alleen in de zomer en de herfst plaatsvonden. Deze aannames waren at (1) puinstromen alleen voorkomen in de periode van juni tot en met oktober, en (2) uinstroomactiviteit binnen deze periode niet varieert.

### Puinstromen in het Bachelarddal: datering van afzettingen

ateringen van puinstromen zijn uitgevoerd met behulp van dendrogeomorfologie en lichenometrie de depositiezones van 5 puinstroom-brongebieden. Boomringdikte- en -excentriciteitspatronen rden onderzocht met de Split-Moving Window test, waarmee plotselinge veranderingen in deze tronken kunnen worden opgespoord. De interpretatie van plotselinge groeiveranderingen is lastig, ook veroorzaakt kunnen zijn door andere geomorfologische processen. Ook werden enkele bomen ngetroffen waaruit de minimale ouderdom van de afzettingen waarop ze groeiden kon worden geleid, en twee bomen met een verwonding.

j de lichenometrische dateringen werd de soort *Rhizocarpon geographicum* gebruikt. *Xanthoria* 'gans bleek niet in voldoende mate aanwezig om ook te worden gebruikt. Een *Rhizocarpon* 'graphicum' groeicurve werd geconstrueerd aan de hand van afzettingen die zowel lichenometrisch dendrogeomorfologisch waren gedateerd, waarbij dendrogeomorfologische dateringen als erentiewaarden werden gebruikt. *Rhizocarpon geographicum* blijkt een kolonisatietijd van 16-17 r te hebben en een groeisnelheid van 30 mm in de eerste 50 jaar na de kolonisatietijd. Bovendien 'en de huidige resultaten een gegronde reden om de door de Redelijkheid (1988) geconstrueerde 'eicurve in twijfel te trekken.

meeste van de 76 gedateerde puinstroomafzettingen zijn lichenometrisch gedateerd, voornamelijk dat veel puinstromen geen bomen zijn tegengekomen op hun weg dalwaarts. De meeste eringen liggen tussen 1940 en 1975, met een piek in de activiteit rond het eind van de veertiger n tot het begin van de vijftiger jaren en een tweede piek aan het eind van de zestiger jaren 60 tot midden van de zeventiger jaren. Jongere afzettingen waren nog niet gekoloniseerd door *zocarpon*, maar voor een groot deel van deze afzettingen (37 van de 47) waren wel relatieve ringen mogelijk. Oudere afzettingen zijn grotendeels begraven onder jongere, dus lichenometrie oor de onderzochte puinstroomssystemen eigenlijk alleen bruikbaar voor de laatste 50-100 jaar. P-N1 (direct ten noorden van TCP) is het meest actieve systeem met een puinstroom- alingsfrequentie van 0.62 puinstromen per jaar (ppj), TGW (Tête de Glaudon West is het minst ef (0.15 ppj). De gevonden waarden zijn hoger dan de door van Asch en van Steijn (1991) oemde waarden (0.1-0.25 ppj); mogelijk vormen ze een overschatting aangezien in dit onderzoek puinstroom-afzettingen als onafhankelijke afzettingen beschouwd, terwijl ze in werkelijkheid r dezelfde puinstroom kunnen zijn gevormd. De puinstroomactiviteit lijkt een negatieve relatie ebben met grootte van de brongebieden. Bovendien blijkt de activiteit van puinstromen zich ematisch te verplaatsen binnen de depositiezones.

Fourier-analyse in combinatie met de Fisher test toont aan dat er geen significante periodieke aties in puinstroomactiviteit zijn. Dit ondersteunt de in eerdere onderzoeken gevonden 11-jarige

schommeling van de puinstroomactiviteit niet, welke aan klimaatschommelingen ten gevolge van variaties in zonnevlekactiviteit werd toegeschreven.

### 10 Puinstromen in het Bachelarddal: activiteit in de periode 1991-1995

De actuele ruimtelijke en temporele variatie van puinstroomactiviteit is een nog weinig onderzocht onderwerp, met name wanneer het een serie regelmatige inventarisaties betreft of gebieden groter dan een enkele helling of een eerste-orde dal. In het Bachelarddal is de ruimtelijke en temporele variatie van puinstroomactiviteit in de periode eind juli 1992 tot en met half oktober 1994 onderzocht door een combinatie van veld- en fotokarteringen. De aanleiding hiervoor was een groeiende twijfel aan de uit eerdere onderzoeken gevonden puinstroomfrequenties in vergelijking met de activiteit van het brongebied TCP. Het aspect van de magnitude van de puinstromen is in het huidige onderzoek niet aan bod gekomen. Alle puinstroomafzettingen werden als enkelvoudige puinstromen gekarteerd, tenzij bekend was dat er meerdere puinstromen langs dezelfde baan hadden plaatsgevonden. Naarmate de tijd tussen twee opeenvolgende karteringen toeneemt, neemt echter ook de kans toe om puinstromen te missen doordat in die tijd meerdere puinstromen dezelfde baan hebben gevolgd. Dit leidt dus tot een onderschatting van de werkelijke activiteit, die bovendien sterker wordt naarmate de tijd tussen twee opeenvolgende karteringen langer is.

Uit de karteringen blijkt, dat de natte periode van mei tot en met juli 1992 nauwelijks puinstromen heeft opgeleverd. Puinstroomactiviteit blijkt vaak een sterk geclusterd patroon te vertonen, met name vaak rondom één enkele bergtop. Dit wijst eens te meer op de rol van lokale, hevige buien. In de zomer en de herfst van 1994 heeft puinstroomactiviteit op grote schaal plaatsgevonden door gehele Bachelarddal. Een groot aantal puinstromen vond plaats op 26 juni ten gevolge van de passage van een koufront met onweersbuien. De puinstroomactiviteit van deze dag vertoont geen geclusterd patroon, maar is mogelijk toch veroorzaakt door (een groot aantal) lokale buien, zodat de individuele clusters samengeklonterd zijn. In de herfst van 1994 vond een zeer grote puinstroom plaats in het Vallon de la Moutiere; de puinstroom reikte tot aan de Bachelard. Met name voor de karteringen die zijn uitgevoerd in de zomer en in de herfst van 1994 lijkt het waarschijnlijk dat er puinstroom-brongebieden waren van waaruit meerdere puinstromen dezelfde baan hebben gevolgd.

Voor deelgebieden in Bachelarddal ligt de puinstroomactiviteit (= gemiddelde puinstroomfrequentie per brongebied) tussen 0.05 ppj (herhalingstijd 20 jaar) en minimaal 0.956 ppj (herhalingstijd 1 jaar). De laatste waarde geldt voor de westelijke helling van de Tête du Clot des Pastres, die vaker werd bezocht dan de meeste andere deelgebieden. Binnen deze helling heeft het brongebied TCP, het meest bezochte brongebied, de hoogste puinstroomfrequentie: minimaal 1.5 ppj, waarschijnlijk 2.5-3 ppj. Dit onderbouwt eveneens de genoemde relatie tussen de gevonden puinstroomactiviteit en de frequentie van veldbezoeken. De meeste puinstromen blijken te ontstaan in de zomerperiode van juni tot en met september. Er zijn nauwelijks aanwijzingen voor puinstroomactiviteit in de winter en in het voorjaar tijdens de periode van sneeuwsmelt. Puinstroomactiviteit bleek voor de deelgebieden een relatie te vertonen met de dichtheid van puinstroombrongebieden ( $r^2 = 0.32-0.38$ ). Ook lijkt een zwakke relatie met de lithologie te bestaan: actieve zones bevinden zich opvallend vaak in flysch of op plaatsen met qua resistentie sterk afwisselende gesteentesoorten of met een groot aantal breuken.

Een vergelijking van de verkregen puinstroomfrequenties uit actuele karteringen met die uit de datering van afzettingen laat zien dat de laatste methode de frequentie sterk onderschat. Voor de onderzochte brongebieden in Bachelarddal is dit een onderschatting met een factor 1.6-2.1 (gemiddeld 1.9) voor brongebieden met afzettingen gedateerd in dit onderzoek en een onderschatting met een factor 1.6-39 (gemiddeld 10-15) voor brongebieden gedateerd door de Redelijkheid (1988). Een mogelijke oorzaak is reeds genoemd: meerdere puinstromen kunnen dezelfde baan volgen en daarbij het sediment van vorige puinstromen bedekken of opnieuw in transport brengen.

Lichenometrische datering van zo'n afzetting is alleen mogelijk wanneer een volgende puinstroom een andere baan gaat volgen. Dit kan worden veroorzaakt door verstopping van de geul met een afzetting van een relatief kleine puinstroom, of door een overschrijding van de capaciteit van de geul door een grote puinstroom. De nieuw gekozen route kan evenzogoed een nog oudere puinstroombaan zijn. Lichenometrische datering van puinstroomafzettingen geeft dus eerder een indicatie van 'puinstroombaanverlegging' dan van het optreden van een puinstroom. In principe kan dendrogeomorfologie wel dateringen opleveren voor meer dan één of zelfs voor alle puinstromen die eenzelfde baan hebben gevolgd, mits de boom in het pad van de puinstromen staat.

## 11 Samenvatting en belangrijkste conclusies

Praktische mogelijkheden en onmogelijkheden vormen belangrijke overwegingen bij te kiezen/gebruiken methoden in steil, moeilijk begaanbaar terrein in de bergen. Voorbeelden hiervan zijn de keuze voor veldregensimulaties en voor in-situ puinsterkmetingen.

De aard van de oppervlakkige afstroming in de steile brongebieden van puinstromen is van groot belang met betrekking tot de initiatie van puinstromen. Deze oppervlakkige afstroming kan op de steile hellingen gemakkelijk sediment mobiliseren, waardoor de dichtheid en de viscositeit toenemen. Wat er vervolgens gebeurt wanneer deze oppervlakkige afstroming een pakket grof puin tegenkomt, is afhankelijk van het debiet, de dichtheid en de viscositeit van de afstromende vloeistof, en van de korrelgrootteverdeling van het meegevoerde sediment. Met name de laatste factor bepaalt in hoge mate of de oppervlakkige afstroming door de poriën van het grove puin zal gaan stromen dan wel deze poriën zal verstoppen en over het grove puin verder zal stromen. In combinatie met onzekerheden rond een grote variatie in invoerwaarden voor een fysisch model van puinstroominitiatie blijkt een kwantitatieve fysische benadering van puinstroominitiatie vooralsnog niet uitvoerbaar.

Daarentegen blijkt een empirische benadering wel goed te werken. Deze empirische benadering wordt gevormd door toepassing van logistische regressie om verbanden tussen het optreden van puinstromen en gemeten neerslag- en afvoercharacteristieken te achterhalen. Simpele neerslagmodellen (logistische regressie met 1 of 2 variabelen) blijken even goed of beter te corrélén met puinstroomoptreden dan de piekafvoeren berekend met een eenvoudig hydrologisch tankmodel (TANKFLOW), dat op zijn beurt weer beter werkt dan een gecompliceerd hydrologisch model (DINOFLOW). Dit is het gevolg van de toenemende mate van onzekerheid ten gevolge van het toenemend aantal invoervariabelen en -parameters gaande van de eenvoudige regenmodellen via TANKFLOW naar DINOFLOW en van een gebrek aan goede afvoergegevens om de hydrologische modellen op te kalibreren en te valideren. Elke extra invoervariabele of -parameter brengt extra onzekerheid in het model (kalibratie, -ruimtelijke- variatie), zodat modelkalibratie lastiger wordt. Uit de neerslagmodellen blijkt, dat vooral de maximale regenintensiteiten over korte tijdsduur (2-15 minuten) sterk corrélén met het optreden van puinstromen. Goed verkrijgbare gegevens zoals dagtotaal van de neerslag blijken nauwelijks te corrélén met het optreden van puinstromen en zijn dus niet of slechts beperkt bruikbaar voor onderzoek aan gelijksoortige puinstroomsystemen. Ook de invloed van het initieel vochtgehalte (antecedente neerslag) is beperkt.

De drempelwaarde voor de tijdens sommige regensimulaties waargenomen micro-puinstromen (voor splash gecorrigeerde 3-minuten regenintensiteit waarschijnlijk 45-55 mm/uur) blijkt goed overeen te komen met Caine's (1980) drempelwaarde voor puinstromen. Daarentegen geeft Innes' (1983a) curve een veel te lage drempelwaarde voor het onderzoeksgebied. Het optreden van micro-puinstromen is mogelijk een belangrijke schakel tussen het optreden van oppervlakkige afstroming en het ontstaan van een 'volgroeide' puinstroom. Dit wordt ondersteund door de maximale 3-

minuten regenintensiteit van 63 mm/uur die 50% kans op een puinstroom geeft, een waarde die slechts weinig hoger ligt dan de drempelwaarde voor het optreden van micro-puinstromen.

De frequentie van puinstromen is bepaald op drie verschillende wijzen. Voor puinstroomsystemen in het gehele Bachelarddal zijn van de zomer van 1992 tot en met de herfst van 1994 regelmatig karteringen uitgevoerd van nieuw gevormde puinstroomafzettingen. Voor vijf puinstroomsystemen, waaronder TCP, zijn bestaande afzettingen lichenometrisch en dendrogeomorfologisch gedateerd. Voor het puinstroomsysteem TCP zijn bovendien maximale 10-minuten regenintensiteiten gecorréléerd aan het optreden van puinstromen, zodat de puinstroomfrequentie gemodelleerd kon worden met behulp van de herhalingsfrequentie van maximale 10-minuten regenintensiteiten. De belangrijkste conclusies zijn:

- Datering van bestaande afzettingen met behulp van lichenometrie en dendrogeomorfologie levert een sterke onderschatting van de werkelijke puinstroomfrequentie op, waarschijnlijk doordat meerdere puinstromen dezelfde baan volgen totdat een 'puinstroombaanverlegging' plaatsvindt en de afzettingen niet meer verstoord worden. Bovendien worden met name de kleinere afzettingen in de loop van de tijd minder goed herkenbaar en raken eerder bedolven, zodat vooral de afzettingen van hoge-magnitude puinstromen bewaard blijven.
- De achterhaalde frequentie hangt af van het aantal herkende puinstroomafzettingen. Dit aantal neemt toe naarmate een gebied vaker wordt bezocht, zoals blijkt uit de toename van de gevonden puinstroomactiviteit voor achtereenvolgens het gehele Bachelarddal (0.4-0.5 ppj per puinstroomsysteem), de TCP helling (1.0 ppj per puinstroomsysteem) en het brongebied TCP (2-3 ppj).
- De frequentie van puinstromen in het Bachelarddal is aanzienlijk hoger dan tot nu toe werd gedacht.



## REFERENCES

- ADDISON, K. (1987), Debris flow during intense rainfall in Snowdonia, North Wales: A preliminary survey. *Earth Surface Processes and Landforms* **12**, pp. 561-566.
- AKAIKE, H. (1973), Information theory and an extension of maximum likelihood principle. In: B.N. Petrov & F. Csáki (Eds.): *Second International Symposium on Information Theory*. Budapest: Akadémia Kiadó, pp. 267-281.
- ALESTALO, J. (1971), Dendrochronological Interpretation of Geomorphic Processes. *Fennia* **105**.
- ANDERSEN, J.L. & J.L. SOLLID (1971), Glacial chronology and glacial geomorphology in the marginal zones of the glaciers Midtdalsbreen and Nigardsbreen, southern Norway. *Norsk Geografisk Tidsskrift* **25**, pp. 1-38.
- ANDRÉ, M.-F. (1995), Holocene climate fluctuations and geomorphic impact of extreme events in Svalbard. *Geografiska Annaler* **77A**, pp. 241-250.
- ANDREWS, J.T. & D.M. BARNETT (1979), Holocene (Neoglacal) moraine and periglacial lake chronology, Barnes Ice Cap, North West Territories, Canada. *Boreas* **8**, pp. 341-358.
- ARBOLEDA, R.A. AND R.S. PUNONGBAYAN (1991), Landslides induced by the 16 July 1990 Luzon, Philippines, earthquake. *Landslide News* **5**, pp. 5-7.
- ARGUDEN, A.T. & K.S. RODOLFO (1990), Sedimentologic and dynamic differences between hot and cold laharic debris flows of Mayon Volcano, Philippines. *Geological Society of America Bulletin* **102**, pp. 865-876.
- AULITZKY, H. (1994), Hazard mapping and zoning in Austria: Methods and legal implications. *Mountain Research and Development* **14**, pp. 307-313.
- AULITZKY, H., H. HEUBERGER & G. PATZELT (1994), Mountain hazard geomorphology of Tyrol and Vorarlberg. *Mountain Research and Development* **14**, pp. 273-305.
- AVOCAT, C. (1970), Premiers résultats du recensement de 1968 en Ubaye. *Revue de Géographie Alpine* **58**, pp. 435-451.
- AZIMI, C. & P. DESVARREUX (1974), A study of one special type of mudflow in the French Alps. *Quarterly Journal of Engineering Geology* **7**, pp. 329-338.
- BAGNOLD, R.A. (1954), Experiments on a gravity-free dispersion of large solid spheres in a Newtonian fluid under shear. *Proceedings of the Royal Society of London* **225A**, pp. 49-63.
- BAGNOLD, R.A. (1956), The flow of cohesionless grains in fluids. *Proceedings of the Royal Society of London* **249A**, pp. 235-297.
- BAILEY, R.W., C.L. FORSLING & R.J. BECRAFT (1934), Floods and accelerated erosion in northern Utah. United States Department of Agriculture, Miscellaneous Publication **196**.
- BAIRD, P.D. & W.V. LEWIS (1957), The Cairngorm flood 1956. *Scottish Geographical Magazine* **73**, pp. 91-100.
- BALLANDRAS, S. (1993), Les crues torrentielles de l'été 1987 dans les Alpes françaises. Interprétation et enseignements. *Revue de Géographie Alpine* **81**, pp. 13-32.
- BALLANTYNE, C.K. (1981), Periglacial landforms and environments on mountains in the northern highlands of Scotland. University of Edinburgh, unpublished PhD thesis.
- BALLANTYNE, C.K. (1991), Holocene geomorphic activity in the Scottish Highlands. *Scottish Geographical Magazine* **107**, pp. 84-98.
- BALTEANU, D. (1976), Two case studies of mudflows in the Buzau Subcarpathians. *Geografiska Annaler* **58A**, pp. 165-171.
- BEAUJEU-GARNIER, J. (1972), *Le Relief de la France. Regards sur la Géographie*. Roby: Paris.
- BEGÉT, J.E. (1994), Tephrochronology, lichenometry and radiocarbon dating at Gulkana Glacier, central Alaska Range, USA. *The Holocene* **4**, pp. 307-313.
- BENDA, L. (1990), The influence of debris flows on channels and valley floors in the Oregon Coast Range, U.S.A. *Earth Surface Processes and Landforms* **15**, pp. 457-466.
- BENDA, L. & T. DUNNE (1987), Sediment routing by debris flow. In: R.L. Beschta et al. (Eds.): *Erosion and Sedimentation in the Pacific Rim*. (Proceedings of the Corvallis Symposium, August 1987). IAHS Publications **165**, pp. 213-223.



- Establishing a lichen growth curve. *Journal of Glaciology* 6, pp. 817-832.
- BENEDICT, J.B. (1988), Techniques in lichenometry: identifying the yellow Rhizocarpons. *Arctic and Alpine Research* 20, pp. 285-291.
- BENEDICT, J.B. (1991), Experiments on lichen growth. II. Effects of a seasonal snow cover. *Arctic and Alpine Research* 23, pp. 189-199.
- BENEDICT, J.B. (1993), A 2000-year lichen-snowkill chronology for the Colorado Front Range, USA. *The Holocene* 3, pp. 27-33.
- BENISCHKE, R. & T. HARUM (1990), Determination of discharge rates in turbulent streams by salt tracer dilution applying a microcomputer system. Comparison with current meter measurements. In: H. Lang & M. Musy (Eds.): *Hydrology in Mountainous Regions. Part I: Hydrological Measurements; the Water Cycle*. (Proceedings of two Lausanne Symposia, August 1990). IAHS Publications 193, pp. 215-221.
- BENTLEY, S.P. (1979), Viscometric assessment of remoulded sensitive clays. *Canadian Geotechnical Journal* 16, pp. 414-419.
- BERTRAN, P. & J.-P. TEXIER (1994), Structures sédimentaires d'un cône de flots de débris (Vars, Alpes Françaises Méridionales). *Permafrost and Periglacial Processes* 5, pp. 155-170.
- BESCHEL, R.E. (1950), Flechten als Altersmasstab rezenter Moränen. *Zeitschrift für Gletscherkunde und Glazialgeologie* 1, pp. 152-161.
- BESCHEL, R.E. (1961), Dating rock surfaces by lichen growth and its application to glaciology and physiography (lichenometry). In: G.O. Raasch (Ed.): *Geology of the Arctic. Volume II*. University of Toronto Press: Toronto, pp. 1044-1062.
- BICKERTON, R.W. & J.A. MATTHEWS (1992), On the accuracy of lichenometric dates: an assessment based on the 'Little Ice Age' moraine sequence of Nigardsbreen, southern Norway. *The Holocene* 2, pp. 227-237.
- BICKERTON, R.W. & J.A. MATTHEWS (1993), 'Little Ice Age' variations of outlet glaciers from the Jostedalbreen ice-cap, southern Norway: a regional lichenometric-dating study of ice-marginal moraine sequences and their climatic significance. *Journal of Quaternary Science* 8, pp. 45-68.
- BIRKELAND, P.W. (1982), Subdivision of Holocene glacial deposits, Ben Ohau Range, New Zealand, using relative-dating methods. *Bulletin of the Geological Society of America* 93, pp. 433-449.
- BISHOP, A.W. (1948), A large shear box for testing sands and gravels. *Proceedings of the Second International Conference on Soil Mechanics and Foundation Engineering* 1, pp. 207-211.
- BISHOP, A.W. (1973), The stability of tips and spoil heaps. *Quarterly Journal of Engineering Geology* 6, pp. 335-376.
- BLACKWELDER, E. (1928), Mudflow as a geologic agent in semiarid mountains. *Bulletin of the Geological Society of America* 39, pp. 465-484.
- BLIJENBERG, H.M. (1993a), Debris flow measurement methods. In: J.C. Flageollet (Ed.): *Temporal Occurrence and Forecasting of Landslides in the European Community. Part I: Methodology (Reviews) for the Temporal Study of Landslides*, pp. 147-160.
- BLIJENBERG, H.M. (1993b), Results of debris flow investigations on the recent time scale. In: J.C. Flageollet (Ed.): *Temporal Occurrence and Forecasting of Landslides in the European Community. Part II: Case Studies of the Temporal Occurrence of Landslides in the European Community* 2, pp. 609-650.
- BLIJENBERG, H.M. (1995), In-situ strength tests of coarse, cohesionless debris on scree slopes. *Engineering Geology* 39, pp. 137-146.
- BLIJENBERG, H.M., P.J. DE GRAAF, M.R. HENDRIKS, J.F. DE RUITER & A.A.A. VAN TETERING (1996), Investigation of infiltration characteristics and debris flow initiation conditions in debris flow source areas using a rainfall simulator. *Hydrological Processes* 10, pp. 1527-1543.
- BOGUCKI, D.J. (1977), Debris slide hazards in the Adirondack Province of New York State. *Environmental Geology* 1, pp. 317-328.
- BONNEY, T.G. (1902), Moraines and mudstreams in the Alps. *Geological Magazine, Decade* 4, 9, pp. 8-16.
- BORNFELDT, F. & M. ÖSTERBERG (1958), *Lavarter som hjälpmedel för datering av ändmoräner vid norska glaciärer*. Unpublished report, Department of Geography, University of Stockholm.
- BOVIS, M.J. (1993), Hillslope geomorphology and geotechnique. *Progress in Physical Geography* 17, pp. 173-189.
- BOVIS, M.J. & B.R. DAGG (1987), Mechanisms of debris supply to steep channels along Howe Sound, southwest British Columbia. In: R.L. Beschta et al. (Eds.): *Erosion and Sedimentation in the Pacific Rim*. (Proceedings of the Corvallis Symposium, August 1987). IAHS Publications 165, pp. 191-200.
- BOVIS, M.J. & B.R. DAGG (1988), A model for debris accumulation and mobilization in steep mountain streams. *Hydrological Sciences Journal/Journal des Sciences Hydrologiques* 33, pp. 589-604.
- BOZONNET, R. (1994), Processus exceptionnels en haute montagne dans le Massif du Mont Blanc pendant l'été 1992. *Revue de Géographie Alpine* 82, pp. 85-92.
- BRAAM, R.R., E.E.J. WEISS & P.A. BURROUGH (1987a), Dendrogeomorphological analysis of mass movement: a technical note on the research method. *Catena* 14, pp. 575-589.
- BRAAM, R.R., E.E.J. WEISS & P.A. BURROUGH (1987b), Spatial and temporal analysis of mass movement using dendrochronology. *Catena* 14, pp. 573-584.
- BRADLEY, R.S. (1985), *Quaternary Paleoclimatology. Methods of Paleoclimatic Reconstruction*. Chapman & Hall: London.
- BRAND, E.W. (1993), Landslides in Hong Kong caused by the severe rainfall event of 8 May 1992. *Landslide News* 7, pp. 9-11.
- BRGM (1972), Notice Explicative à la Carte Géologique de la France à 1/50 000. Feuille XXXV-39 Barcelonnette, Bureau des Recherches Géologiques et Minières.
- BRUNSDEN, D. (1979), Mass movements. In: C.E. Embleton & J.B. Thornes (Eds.): *Process in Geomorphology*. Arnold: London, pp. 130-186.
- BUCHANAN, P. & K.W. SAVIGNY (1990), Factors controlling debris avalanche initiation. *Canadian Geotechnical Journal* 27, pp. 659-675.
- BULL, W.D., J. KING, F. KONG, T. MOUTOUX & W.M. PHILLIPS (1994), Lichen dating of coseismic landslide hazards in alpine mountains. *Geomorphology* 10, pp. 253-264.
- BULL, W.B., P. SCHLYTER AND S. BROGAARD (1995), Lichenometric analysis of the Kärkerieppe slush-avalanche fan, Kärkevage, Sweden. *Geografiska Annaler* 77A, pp. 231-240.
- CAILLEUX, A. & J. TRICART (1950), Une type de solifluction: les coulées boueuses. *Revue de Géographie Physique et Géologie Dynamique* 1, pp. 4-46.
- CAINE, N. (1980), The rainfall intensity - duration control of shallow landslides and debris flows. *Geografiska Annaler* 62A, pp. 23-27.
- CALKIN, P.E. & J.M. ELLIS (1980), A lichenometric dating curve and its application to Holocene glacial studies in the Central Brooks Range, Alaska. *Arctic and Alpine Research* 12, pp. 245-264.
- CAMPBELL, R.H. (1974), Debris flows originating from soil slips during rainstorms in southern California. *Quarterly Journal of Engineering Geology* 7, pp. 339-349.
- CAMPBELL, R.H. (1975), Soil slips, debris flows and rainstorms in the Santa Monica Mountains and vicinity, coastal southern California. *United States Geological Survey Professional Paper* 851.
- CAMUS, G., M. DIAMENT, H. GLOAGUEN, A. PROVOST & P. VINCENT (1992), Emplacement of a debris avalanche during the 1883 eruption of Krakatau (Sunda Straits, Indonesia). *Geojournal* 28, pp. 123-128.
- CARIS, J.P.T. & TH.W.J. VAN ASCH (1991), Geophysical, geotechnical and hydrological investigations of a small landslide in the French Alps. *Engineering Geology* 31, pp. 249-276.
- CARLING, P.A. (1986), The Noon Hill flash floods; July 17th 1983. Hydrological and geomorphological aspects of a major formative event in an upland landscape. *Transactions of the Institute of British Geographers, N.S.* 11, pp. 105-118.
- CARLING, P.A. (1987), Hydrodynamic interpretation of a boulder berm and associated debris-torrent deposits. *Geomorphology* 1, pp. 53-67.
- CASELDINE, C.J. (1983), Resurvey of the margins of Gílfjúrarárkjull and the chronology of recent deglaciation. *Jökull* 33, pp. 111-118.
- CASELDINE, C.J. (1990), Review of dating methods and their application in the development of a chronology of Holocene glacier variations in north Iceland. *Münchener Geographischen Abhandlungen Reihe B* 8, pp. 59-82.
- CAYLA, O. & M. TAIBI (1990), Synthèse régionale pluviométrique en région montagneuse. In: H. Lang & M. Musy (Eds.): *Hydrology in Mountainous Regions. Part I: Hydrological Measurements; the Water Cycle*. (Proceedings of two Lausanne Symposia, August 1990). IAHS Publications 193, pp. 357-364.

- CENDRERI, D.A. AND J.S. KITE (1998), Geomorphic effects of large debris flows on channel morphology at North Fork Mountain, eastern West Virginia, USA. *Earth Surface Processes and Landforms* **23**, pp. 1-19.
- CHAMLEY, H. (1977), *Sédimentologie*. Dunod: Paris.
- CHARDON, M. (1990), Les catastrophes naturelles de l'été 1987 en Lombardie. Crues, inondations, écroulement de Val Pola. *Revue de Géographie Alpine* **78**, pp. 59-87.
- CHARLES, J.A. (1991), Laboratory shear strength tests and the stability of rockfill slopes. In: E.M. Das Neves (Ed.): *Advances in Rockfill Structures. Proceedings of the NATO Advanced Study Institute on Advances in Rockfill Structures*. Kluwer: Dordrecht, NATO ASI Series E: Applied Sciences **200**, pp. 53-72.
- CHATFIELD, C. (1984), *The Analysis of Time Series. An Introduction*. Chapman and Hall: London.
- CHEN, C.L. (1986), Chinese concepts of modeling hyperconcentrated streamflow and debris flow. *Proceedings of the Third International Symposium on River Sedimentation*, Jackson, Mississippi, pp. 1647-1657.
- CHEN, C.L. (1988a), General solutions for viscoplastic debris flow. *Journal of Hydraulic Engineering* **114**, pp. 259-282.
- CHEN, C.L. (1988b), Generalized viscoplastic modeling of debris flow. *Journal of Hydraulic Engineering* **114**, pp. 237-258.
- CHIDA, H. AND I. HARIYONO (1995), Mt. Merapi pyroclastic flow and lahar disaster, Indonesia. *Landslide News* **9**, pp. 31-32.
- CHOW, V.T., D.R. MAIDMENT & L.W. MAYS (1988), *Applied Hydrology*. McGraw-Hill: Singapore.
- CLOTET-PERARNAU, N., J.M. GARCIA-RUIZ & F. GALLART (1989), High magnitude geomorphic work in the Pyrenees Range: unusual rainfall event, November 1982. *Studia Geomorphologica Carpatho-Balcanica* **23**, pp. 69-91.
- COE, J.A., P.A. GLANCY AND J.W. WHITNEY (1997), Volumetric analysis and hydrologic characterization of a modern debris flow near Yucca Mountain, Nevada. *Geomorphology* **20**, pp. 11-18.
- CONWAY, W.M. (1893), Exploration of the Mustagh Mountains. *Geographical Journal* **2**, pp. 289-303.
- CONWAY, W.M. (1894), Climbing and exploration in the Karakoram - Himalayas. Unwin: London.
- COOK-TALBOT, D.J. (1991), Sorted circles, relative-age dating and palaeoenvironmental reconstruction in an alpine periglacial environment, eastern Jotunheimen, Norway: lichenometric and weathering-based approaches. *The Holocene* **1**, pp. 128-141.
- COSTA, J.E. (1984), Physical geomorphology of debris flows. In: J.E. Costa & P.J. Fleisher (Eds.): *Developments and Applications of Geomorphology*, Springer Verlag: Berlin/Heidelberg, pp. 268-317.
- COULSON, A. (1966), Tables for Computing and Plotting Flood Frequency Curves. Department of Energy, Mines and Resources, Water Resources Branch, Ottawa, Technical Bulletin 3.
- COXSON, D.S. & K.A. KERSHAW (1983), The ecology of *Rhizocarpon superficiale* (Schaer.) Vain. II: The seasonal response of net photosynthesis and respiration to temperature, moisture and light. *Canadian Journal of Botany* **62**, pp. 3019-3030.
- CUMMANS, J. (1981), Mudflows resulting from the May 18, 1980 eruption of Mount St. Helens, Washington. United States Geological Survey Circular **850 B**.
- CURRY, R.R. (1966), Observation of alpine mudflows in the Tenmile Range, Central Colorado. *Bulletin of the Geological Society of America* **77**.
- DAVIS, J.C. (1986), *Statistics and Data Analysis in Geology*. Wiley: New York.
- DAVIS, R.H., J.-M. SERAYSSOL & E.J. HINCH (1986), The elastohydrodynamic collision of two spheres. *Journal of Fluid Mechanics* **163**, pp. 479-497.
- DE GRAAF, P.J., J.F. DE RUITER & A.A.A. VAN TETERING (1993), De Initiatie van puinstromen. Een onderzoek in het Bachelarddal, Alpes de Haute Provence. Unpublished report, Utrecht University, Department of Physical Geography.
- DE REDELIJKHEID, M. (1988), Datering van Puinstromen in de Franse Alpen met Lichenometrie en Dendrogeomorfologie. Unpublished report, Utrecht University, Department of Physical Geography.
- DE ROO, A.P.J. (1993), Modelling Surface Runoff and Soil Erosion in Catchments Using Geographical Information Systems. KNAG/Faculteit Ruimtelijke Wetenschappen Universiteit Utrecht: Utrecht. Netherlands Geographical Studies **157**. Also: PhD thesis, Utrecht University.
- DE ROO, A.P.J. (1996), Soil erosion assessment using G.I.S. In: V.P. Singh & M. Fiorentino (Eds.): *Geographical Information Systems in Hydrology*. Water Science and Technology Library **26**. Kluwer: Dordrecht, pp. 339-356.
- DE ROO, A.P.J., L. HAZELHOFF & G.B.M. HEUVELINK (1992), The use of Monte Carlo simulations to estimate the effects of spatial variability of infiltration on the output of a distributed hydrological and erosion model. *Hydrological Processes* **6**, pp. 127-143.
- DEBELMAS, J. (1983), *Alpes du Dauphiné. Guides Géologiques Régionales*. Masson: Paris.
- DEBELMAS, J. (1987), *Découverte Géologique des Alpes du Sud*. Editions du BRGM. Louis-Jean: Gap.
- DEBELMAS, J., A. PÉCHER & J.-C. BARFÉTY (1989), *Guide Géologique du Parc National des Écrins. Itinéraires de Découverte*. Editions du BRGM - Parc National des Écrins.
- DEGRAFF, J.V. (1994), The geomorphology of some debris flows in the southern Sierra Nevada, California. *Geomorphology* **10**, pp. 231-252.
- DOUGUÉDROIT, A. & M.F. DE SAINTIGNON (1970), Méthode d'étude de la décroissance des températures en montagne de latitude moyenne: exemple des Alpes françaises du Sud. *Revue de Géographie Alpine* **58**, pp. 453-472.
- DRAKE, T.G. & R.L. SHREVE (1986), High-speed motion pictures of nearly steady, uniform, two-dimensional, inertial flows of granular material. *Journal of Rheology* **30**, pp. 981-993.
- DUNIN, F.X. (1976), Infiltration: its simulation for field conditions. In: J.C. Rodda (Ed.): *Facets of Hydrology*. Wiley: London, pp. 199-227.
- EC (1994), Klimafaktoren und Natürliche Risiken im Alpenraum. European Commission.
- EINSTEIN, A. (1956), *Investigations on the theory of the Brownian movement*. Dover: New York.
- ELDER, K. & R. KATTELMANN (1993), A low-angle slushflow in the Kirgiz Range, Kirgizstan. *Permafrost and Periglacial Processes* **4**, pp. 301-310.
- EPSTEIN, S., C.J., YAPP & J.H. HALL (1976), The determination of the D/H ratio of non-exchangeable hydrogen in cellulose extracted from aquatic and land plants. *Earth Planetary Science Letters* **30**, pp. 241-251.
- ERTSEN, A.C.D. (1995), ITORS: Een Hydro-ecologisch Model voor Terrestrische Systemen in Noord-Holland. Department of Environmental Studies, Utrecht University.
- EVANS, D.J.A., C. BUTCHER & A.V. KIRTHISINGA (1994), Neoglaciation and an early 'Little Ice Age' in western Norway: lichenometric evidence from the Sandane area. *The Holocene* **4**, pp. 278-289.
- EVANS, S.G. (1986), Landslide damming in the Cordillera of western Canada. In: R.L. Schuster (Ed.): *Landslide Dams: Processes, Risk and Mitigation*. American Society of Civil Engineers, Geotechnical Special Publication **3**, pp. 111-130.
- EVANS, S.G. & G.R. BROOKS (1991), Prehistoric debris avalanches from Mount Cayley volcano, British Columbia. *Canadian Journal of Earth Sciences* **28**, pp. 1365-1374.
- EVIN, M. (1990), Les risques naturels dans un espace montagnard: la Haute Ubaye. *Revue de Géographie Alpine* **78**, pp. 175-192.
- EVIN, M. & A. ASSIER (1983), Mise en évidence de mouvements sur la moraine et le glacier rocheux de Sainte-Anne (Queyras, Alpes du Sud, France). Le rôle du pergélisol alpin. *Revue de Géographie Alpine* **71**, pp. 165-178.
- FAROUKI, O.T. & H.F. WINTERKORN (1964), *Mechanical Properties of Granular Systems*. Princeton Soil Engineering Research Series **1**.
- FERGUSON, C.W. JR. (1970), Concepts and techniques of dendrochronology. In: R. Berger (Ed.): *Scientific Methods in Medieval Archeology*. University of California Press: Berkeley.
- FISHER, R.A. (1970), *Statistical Methods for Research Workers*. Hafner: New York.
- FLAGEOLLET, J.C. (Ed.) (1993a), Temporal Occurrence and Forecasting of Landslides in the European Community. Part I: Methodology (Reviews), for the Temporal Study of Landslides.
- FLAGEOLLET, J.C. (Ed.) (1993b), Temporal Occurrence and Forecasting of Landslides in the European Community. Part II: Case Studies of the Temporal Occurrence of Landslides in the European Community. 2 volumes.
- FLEMING, R.W., S.D. ELLEN & M.A. ALGUS (1989), Transformation of dilative and contractive landslide debris into debris flows - an example from Marin County, California. *Engineering Geology* **27**, pp. 201-223.
- FOLLMANN, G. (1961), Estudios liquenométricos en los monumentos prehistóricos de la Isla de Pascua. *Revista Universitaria, Anales de la Academia Chilena de Ciencias Naturales* **24**, pp. 149-154.
- FRITTS, H.C. (1971), Dendroclimatology and dendroecology. *Quaternary Research* **1**, pp. 419-449.
- FRITTS, H.C. (1976), *Tree Rings and Climate*. Academic Press: London.
- GAGOSHIDZE, M.S. (1969), Mudflows and floods and their control. *Soviet Hydrology* **4**, pp. 410-422.
- GALLACHER, D. (1972), A Study of Plane Strain Tests on Granular Material. MSc thesis, Heriot Watt University, Edinburgh.
- GALLACHER, D. (1988), Asphaltic central core at the Megget Dam. *Transactions of the Sixteenth International Congress on Large Dams*, San Francisco, **2**, pp. 707-731.

- GALLART, F., N. CLOTET-PERANAU, O. BIANCIOTTI & J. PUIGDEFÀBREGAS (1994), Peat soilflows in Bàhia de Buen Suceso, Tierra del Fuego (Argentina). *Geomorphology* 9, pp. 235-241.
- GARCÍA-RUIZ, J.M., J. ARNÁEZ-VADILLO, L. ORTIGOSA-IZQUIERDO & A. GÓMEZ-VILLAR (1988), Debris flows subsequent to a forest fire in the Najerilla River Valley (Iberian System, Spain). *Pirineos* 131, pp. 3-24.
- GARDNER, J.S. (1989), High magnitude geomorphic events in the Canadian Rocky Mountains. *Studia Geomorphologica Carpatho-Balcanica* 23, pp. 39-51.
- GATES, W.L. (1985), The use of general circulation models in the analysis of the ecosystem impacts of climate change. *Climatic Change*, 7, pp. 267-284.
- GEES, A. (1990), Flow measurement under difficult measuring conditions: field experience with the salt dilution method. In: H. Lang & M. Musy (Eds.): *Hydrology in Mountainous Regions. Part I: Hydrological Measurements; the Water Cycle*. (Proceedings of two Lausanne Symposia, August 1990). IAHS Publications 193, pp. 255-262.
- GISPERT, C.-M. (1993), Les risques naturels dans les Pyrénées-Orientales: de l'inventaire au zonage, questions d'échelle et de méthode. *Revue Géographique des Pyrénées et du Sud-Ouest* 63, pp. 7-32.
- GIVONE, C. & X. MEIGNIEN (1990), Influence of topography on spatial distribution of rain. In: L. Molnar (Ed.): *Hydrology of Mountainous Areas*. (Proceedings of the Štrbské Pleso Workshop, Czechoslovakia, June 1988). IAHS Publications 190, pp. 57-65.
- GLOCK, W.S. & S. AGERTER (1963), Anomalous patterns in tree rings. *Endeavour* 22, pp. 9-13.
- GOLDIN, B.M. & L.S. LYUBASHEVSKIY (1966), Computation of the velocity of mudflows for Crimean rivers. *Soviet Hydrology* 2, pp. 179-181.
- GONTSCHAREV, E.P. (1962), Sjels in Tadshykistan. *Proceedings of the Fifth Symposium on Sjels, Baku*, pp. 109-114.
- GORDON, J.E. & M.J. SHARP (1983), Lichenometry in dating recent glacial landforms and deposits, southeast Iceland. *Boreas* 12, pp. 191-200.
- GREEN, M.S. & M.J. SYMMONS (1983), A comparison of the logistic risk function and the proportional hazards model in prospective epidemiologic studies. *Journal of Chronic Diseases* 36, pp. 715-724.
- GREEN, W.H. & G.A. AMPT (1911), Studies on soil physics. Part I: The flow of water and air through soils. *Journal of Agricultural Sciences* 4, pp. 1-24.
- GUDE, M. AND D. SCHERER (1995), Snowmelt and slush torrents - preliminary report from a field campaign in Kärkevagge, Swedish Lapland. *Geografiska Annaler* 77A, pp. 199-206.
- HÄBERLE, T. (1990), Spät- und postglaziale Gletscher-geschichte des Hörgárdalur-Gebietes, Tröllaskagi, Norrlandsland. PhD thesis, University of Zurich.
- HÄBERLE, W., D. RICKENMANN, M. ZIMMERMANN & U. RÖSLI (1990), Investigation of 1987 debris flows in the Swiss Alps: general concept and geophysical soundings. In: R.O. Sinniger & M. Monbaron (Eds.): *Hydrology in Mountainous Regions. Part II: Artificial Reservoirs; Water and Slopes*. (Proceedings of the two Lausanne Symposia, August 1990). IAHS Publications 194, pp. 303-310.
- HÄBERLE, W., D. RICKENMANN, M. ZIMMERMANN & U. RÖSLI (1991), Murgänge. In: *Ursachenanalyse der Hochwasser 1987. Ergebnisse der Untersuchungen. Mitteilung des Bundesamtes für Wasserversorgung*, 4; *Mitteilung der Landeshydrologie und -geologie* 14, pp. 77-88.
- HAINES-YOUNG, R.H. (1983), Size variation of *Rhizocarpon* on moraine slopes in southern Norway. *Arctic and Alpine Research* 15, pp. 295-305.
- HAMILTON, S.J. & W.B. WHALLEY (1995), Preliminary results from the lichenometric study of the Nautardalur rock glacier, Tröllaskagi, northern Iceland. *Geomorphology* 12, pp. 123-132.
- HANSEN, A. (1984), Landslide hazard analysis. In: D. Brunsden & D.B. Prior (Eds.): *Slope Instability*. Wiley: London, pp. 523-602.
- HANSEN, J.B. & H. LUNDGREN (1960), *Hauptprobleme der Bodenmechanik*. Springer: Berlin.
- HARP, E.L., R.W. JIBSON, W.Z. SAVAGE, L.W. HIGHLAND, R.A. LARSON & S.S. TAN (1995), Landslides triggered by January and March 1995 storms in southern California. *Landslide News* 9, pp. 15-18.
- HARRIS, S.A. & C.A. GUSTAFSON (1993), Debris flow characteristics in an area of continuous permafrost, St. Elias Range, Yukon Territory. *Zeitschrift für Geomorphologie Neue Folge* 37, pp. 41-56.
- HEINDRIKS, M.R. (1990), Regionalisation of Hydrological Data. Effects of Lithology and Land Use on Storm Runoff in East Luxembourg. KNAG/Geografisch Instituut Rijksuniversiteit Utrecht: Amsterdam/Utrecht. Netherlands Geographical Studies 114. Also: PhD thesis, Vrije Universiteit Amsterdam.
- HÉTU, B., H. VAN STEIJN & P. BERTRAN (1995), Le rôle des coulées de pierres sèches dans la genèse d'un certain type d'éboullis stratifiés. *Permafrost and Periglacial Processes* 6, pp. 173-194.
- HÉTU, B., H. VAN STEIJN & P. VANDELAC (1994), Les coulées de pierres glacées: un nouveau type d'écoulements de pierraille sur les talus d'éboullis. *Géographie Physique et Quaternaire* 48, pp. 3-22.
- HEWITT, K. (1993), Torrential rains in central Karakoram, 9-10 September 1992. *Geomorphological impact and implications for climatic change. Mountain Research and Development* 13, pp. 371-375.
- HORTON, R.E. (1933), The role of infiltration in the hydrologic cycle. *Transactions of the American Geophysical Union* 14, pp. 446-460.
- HORTON, R.E. (1939), Analysis of runoff plot experiments with varying infiltration capacity. *Transactions of the American Geophysical Union* 20, pp. 693-711.
- HOSMER, D.W. (JR.), & S. LEMESHOW (1989) *Applied Logistic Regression*. Wiley: New York.
- HOVIUS, N. (1990), Ontstaan van puinstromen. Een onderzoek naar de aard van ontstaansgebieden van puinstromen en naar de manier waarop puinstromen ontstaan, in het zuidelijk deel van de Franse Alpen. Unpublished report, Utrecht University, Department of Physical Geography.
- HSÜ, K.J. (1975), Catastrophic debris streams (Sturzstroms) generated by rockfalls. *Geological Society of America Bulletin* 86, pp. 129-140.
- HUNGR, O., G.C. MORGAN & R. KELLERHALS (1984), Quantitative analysis of debris torrent hazards for design of remedial measures. *Canadian Geotechnical Journal* 21, pp. 663-677.
- HUNT, B. (1994), Newtonian fluid mechanics treatment of debris flows and avalanches. *Journal of Hydraulic Engineering, American Society of Civil Engineers, Hydraulics Division* 120, pp. 1350-1363.
- IKEYA, H. (1981), A method of designation for area in danger of debris flow. In: *Erosion and Sedimentation in Pacific Rim Steeplands*. (Proceedings of the Christchurch Symposium, January 1981). IAHS Publications 132, pp. 576-588.
- IMESON, A.C. (1977), A simple field-portable rainfall simulator for difficult terrain. *Earth Surface Processes* 2, pp. 431-436.
- IMESON, A.C. & F.J.P.M. KWAAD (1982), Field measurement of infiltration in the Rif Mountains of northern Morocco. *Studia Geomorphologica Carpatho-Balcanica* 15, pp. 19-30.
- INNES, J.L. (1982a), Debris Flow Activity in the Scottish Highlands. PhD thesis, University of Cambridge.
- INNES, J.L. (1982b), Lichenometric use of an aggregated *Rhizocarpon* 'species'. *Boreas* 11, pp. 53-57.
- INNES, J.L. (1983a), Debris flows. *Progress in Physical Geography* 7, pp. 469-501.
- INNES, J.L. (1983b), Lichenometric dating of debris-flow deposits in the Scottish Highlands. *Earth Surface Processes and Landforms* 8, pp. 579-588.
- INNES, J.L. (1983c), Size frequency distributions as a lichenometric technique: an assessment. *Arctic and Alpine Research* 15, pp. 285-294.
- INNES, J.L. (1983d), Use of an aggregated *Rhizocarpon* 'species' in lichenometry: an evaluation. *Boreas* 12, pp. 183-190.
- INNES, J.L. (1984), The optimal sampling size in lichenometric studies. *Arctic and Alpine Research* 16, pp. 233-244.
- INNES, J.L. (1985a), A standard *Rhizocarpon* nomenclature for lichenometry. *Boreas* 14, pp. 83-85.
- INNES, J.L. (1985b), Lichenometric dating of debris-flow deposits on alpine colluvial fans in southwest Norway. *Earth Surface Processes and Landforms* 10, pp. 519-524.
- INNES, J.L. (1985c), Lichenometry. *Progress in Physical Geography* 9, pp. 187-254.
- INNES, J.L. (1985d), Moisture availability and lichen growth: the effects of snow cover and streams on lichenometric measurements. *Arctic and Alpine Research* 17, pp. 417-424.
- INNES, J.L. (1986a), Influence of sampling design on lichen size-frequency distributions and its effect on derived lichenometric indices. *Arctic and Alpine Research* 18, pp. 201-208.
- INNES, J.L. (1986b), The use of percentage cover measurements in lichenometric dating. *Arctic and Alpine Research* 18, pp. 209-216.
- INNES, J.L. (1989), Rapid mass movements in upland Britain: A review with particular reference to debris flows. *Studia Geomorphologica Carpatho-Balcanica* 23, pp. 53-67.
- IVERSON, R.M., J.E. COSTA AND R.G. LAHUSEN (1993), Large-scale debris-flow flume becomes operational in Oregon, USA. *Landslide News* 7, pp. 29-31.
- IVERSON, R.M. & R.P. DENLINGER (1987), The physics of debris flows - a conceptual assessment. In: R.L. Beschta et al. (Eds.): *Erosion and Sedimentation in the Pacific Rim*. (Proceedings of the Corvallis Symposium, August 1987). IAHS Publications 165, pp. 155-165.

- debris flows. Transactions of the American Geophysical Union 44, pp. 956.
- JACKSON, L.E., R.A. KOSTASCHUK & G.M. MACDONALD (1987), Identification of debris flow hazard on alluvial fans in the Canadian Rocky Mountains. In: J.E. Costa & G.F. Wieczorek (Eds.): *Debris Flow/Avalanches: Process, Recognition and Mitigation*. Reviews in Engineering Geology, Geological Society of America 7, pp. 115-124.
- JACOB, G.C. (Ed.). (1980) Proceedings of the International Meeting on Stable Isotopes in Tree-Ring Research. Carbon Dioxide Effects Research and Assessment Program, US Department of Energy.
- JOHNSON, A.M. (1965), A model for debris flow. PhD thesis, Pennsylvania State University.
- JOHNSON, A.M. (1970), Rheological properties of debris, ice and lava; Debris flow in channels. In: A.M. Johnson (Ed.): *Physical Processes in Geology*. Freeman Cooper: San Francisco, pp. 495-514.
- JOHNSON, A.M. & P.H. RAHN (1970), Mobilization of debris flows. In: P. Macar (Ed.): *New Contributions to Slope Evolution*. Zeitschrift für Geomorphologie Neue Folge Supplementband 9, pp. 168-186.
- JOHNSON, A.M. & J.R. RODINE (1984), Debris flow. In: D. Brunsten & D.B. Prior (Eds.): *Slope Instability*. Wiley: London, pp. 257-361.
- JOISEL, A. (1948), Crushing and Fragmentation of Rocks. *Annales de l'Institut Technique du Bâtiment et des Travaux Publics* 26.
- JONASSON, C., M. KOT & A. KOTARBA (1991), Lichenometrical studies and dating of debris flow deposits in the High Tatra Mountains, Poland. *Geografiska Annaler* 73A, pp. 141-146.
- JONES, F.O. (1973), Landslides of Rio de Janeiro and the Serra das Araras Escarpment, Brazil. United States Geological Survey Professional Paper 697.
- JORDAN, P. & O. SLAYMAKER (1991), Holocene sediment production in Lillooet River basin, British Columbia: a sediment budget approach. *Géographie Physique et Quaternaire* 45, pp. 45-57.
- JUSTO, J.L. (1991), Test fills and in situ tests. In: E.M. Das Neves (Ed.): *Advances in Rockfill Structures*. Proceedings of the NATO Advanced Study Institute on Advances in Rockfill Structures. Kluwer: Dordrecht, NATO ASI Series E: Applied Sciences 200, pp. 153-193.
- KANG ZICHENG & LI JING. (1987), Erosion processes and effects of debris flow. In: R.L. Beschta et al. (Eds.): *Erosion and Sedimentation in the Pacific Rim*. (Proceedings of the Corvallis Symposium, August 1987). IAHS Publications 165, pp. 233-242.
- KARLÉN, W. (1975), Lichenometrisk datering i norra Skandinavien - metodens tillförlitlighet och regionala tillämpning. Stockholm Universitet Naturgeografiska Institut Forskningsrapporter 22, pp. 1-70.
- KASZOWSKI, L. (1984), Vertical differentiation of the dynamics of the mountain relief in the Hindu Kush Munjan Mts., Afghanistan. *Studia Geomorphologica Carpatho-Balcanica* 18, pp. 73-94.
- KENNEY, C. (1984), Properties and behaviours of soils relevant to slope instability. In: D. Brunsten & D.B. Prior (Eds.): *Slope Instability*. Wiley: London, pp. 27-65.
- KERCKHOVE, C. (1979), Notice explicative de la feuille Gap à 1/250 000. Carte Géologique de la France à 1/250 000. Feuille 35 Gap.
- KEZDI, A. (1974), *Handbook of Soil Mechanics*. 1: Soil Physics. Elsevier: Amsterdam.
- KHEGAI, A.Y., N.V. POPOV, P.A. PLEKHANOV AND V.A. KEREMKULOV (1992), Experiments at the Chernomol debris-flow testing ground, Kazakhstan. *Landslide News* 6, pp. 27-28.
- KHERKHEULIDZE, I.I. (1967), Estimation of basic characteristics of mud flows ('sel'). In: Proceedings of the International Association of Scientific Hydrologists Symposium on Floods Computation, Leningrad 2, pp. 940-948.
- KIENHOLZ, H. & P. MANI (1994), Assessment of geomorphic hazards and priorities for forest management on the Rigi North face, Switzerland. *Mountain Research and Development* 14, pp. 321-328.
- KIENHOLZ, H., C. LEHMANN, C. GUGGISBERG, R. LOAT, U. RÖSLI & B. WOHLFAHRT (1991), Geschiebelieferung durch Wildbäche. In: Ursachenanalyse der Hochwasser 1987. Ergebnisse der Untersuchungen. Mitteilung des Bundesamtes für Wasserwirtschaft 4; Mitteilung der Landeshydrologie und -geologie 14, pp. 89-97.
- KJELLMAN, W. & B. JAKOBSON (1955), Some relations between stress and strain in coarse-grained cohesionless materials. Proceedings of the Royal Swedish Geotechnical Institute 9.
- KOBASHI, S. & M. SUZUKI (1987), The critical rainfall (danger index) for disasters caused by debris flows and slope failures. In: R.L. Beschta et al. (Eds.): *Erosion and Sedimentation in the Pacific Rim*. (Proceedings of the Corvallis Symposium, August 1987). IAHS Publications 165, pp. 201-211.
- KOTARBA, A. (1984a), Elevational differentiation of slope geomorphic processes in the Polish Tatra Mts. *Studia Geomorphologica Carpatho-Balcanica*, 18, pp. 117-133.
- KOTARBA, A. (1984b), Slope features in areas of high relief in maritime climate (with the Isle of Rhum as example). *Studia Geomorphologica Carpatho-Balcanica*, 17, pp. 77-90.
- KOTARBA, A. (1989), On the age of debris flows in the Tatra Mountains. *Studia Geomorphologica Carpatho-Balcanica* 23, pp. 139-152.
- KOTARBA, A. (1992), High-energy geomorphic events in the Polish Tatra Mountains. *Geografiska Annaler* 74A, pp. 123-131.
- KOTARBA, A. (1997), Formation of high-mountain talus slopes related to debris-flow activity in the High-Tatra Mountains. *Permafrost and Periglacial Processes* 8, pp. 191-204.
- KOWALKOWSKI, A. & L. STARKEL (1984), Altitudinal belts of geomorphic processes in the Southern Khangai Mts. (Mongolia). *Studia Geomorphologica Carpatho-Balcanica* 18, pp. 95-116.
- KRIEGER, I.M. & T.J. DOUGHERTY (1959), A mechanism for non-Newtonian flow in suspensions of rigid spheres. *Transactions of the Society of Rheology* 3, pp. 137-152.
- KRZEMIEN, K. (1988), The dynamics of debris flows in the upper part of the Starobociańska Valley (Western Tatra Mountains). *Studia Geomorphologica Carpatho-Balcanica* 22, pp. 123-144.
- KUGELMANN, O. (1990), Datierung neuerzeitlicher Gletschervorstöße in Svafadardalur/Skidadalur (Nordisland) mit einer neu erstellten Flechtenwachstumskurve. *Münchener Geographischen Abhandlungen Reihe B* 8, pp. 36-58.
- KWADIJK, J.C.J. (1991), Sensitivity of the River Rhine discharge to environmental change, a first tentative assessment. *Earth Surface Processes and Landforms* 16, pp. 627-637.
- KWADIJK, J.C.J. (1993), The impact of climate change on the discharge of the River Rhine. *KNAG/Faculteit Ruimtelijke Wetenschappen Universiteit Utrecht: Utrecht, Netherlands Geographical Studies* 171. Also: PhD thesis, Utrecht University.
- LAMBE, T.W. & R.V. WHITMAN (1969), *Soil Mechanics*. Wiley: New York.
- LAVIGNE, F. & J.C. THOURET (1994), Proposition d'une méthode d'évaluation et de cartographie des risques liés aux lahars sur le volcan Merapi (Java, Indonésie). *Revue de Géographie Alpine* 82, pp. 151-166.
- LEE, I.K., W. WHITE & O.G. INGLES (1983), *Geotechnical Engineering*. Pitman, Boston.
- LEFEBVRE, In: M. Meunier (1991) *Éléments d'hydraulique torrentielle*. Études du CEMAGREF, série Montagne 1, Louis Jean: Gap.
- LEHMKUHL, F. & LIU SHIJIAN. (1994), An outline of physical geography including Pleistocene glacial landforms of eastern Tibet (Provinces Sichuan and Qinghai). *Geojournal* 34, pp. 7-30.
- LEHMKUHL, F. & K.-H. PÖRTGE (1991), Hochwasser, Muren und Rutschungen in den Randbereichen des Tibetischen Plateaus. In: R. Mäkel (Ed.): *Aktuelle Geomorphodynamik und Angewandte Geomorphologie*. Zeitschrift für Geomorphologie Neue Folge Supplementband 89, pp. 143-155.
- LEMOINE, M. & P. TRICART (1988), Queyras: un Océan il y a 150 Millions d'Années. *Initiation à la Géologie sur les Sentiers du Queyras*. Éditions du BRGM - Parc du Queyras.
- LI JIAN & LUO DEFU. (1981), The formation and characteristics of mudflow and flood in the mountain area of the Dachao River and its prevention. *Zeitschrift für Geomorphologie Neue Folge* 25, pp. 470-484.
- LI JIAN, YUAN JIANMO, BICHENG & LUO DEFU. (1983), The main features of the mudflow in Jiang-Jia Ravine. *Zeitschrift für Geomorphologie* 27, pp. 325-341.
- LI LIE (1985), Debris flow hazards in mountainous areas of the northeastern part of Qinghai-Xizang Plateau. Reports on the northeastern part of the Qinghai-Xizang Plateau, Science Press: Beijing.
- LI, T. (1994), Landslide disasters and human responses in China. *Mountain Research and Development* 14, pp. 341-346.
- LOCKE, W.W. III, J.T. ANDREWS & P.J. WEBBER (1979), *A Manual for Lichenometry*. British Geomorphological Research Group Technical Bulletin 26.
- LUCKMAN, B.H. (1992), Debris flows and snow avalanche landforms in the Lairig Ghru, Cairngorm Mountains, Scotland. *Geografiska Annaler* 74A, pp. 109-121.
- LUN, C.K.K., S.B. SAVAGE, D.J. JEFFREY & N. CHEPURNIY (1984), Kinetic theories for granular flow: inelastic particles in Couette flow and slightly inelastic particles in a general flowfield. *Journal of Fluid Mechanics* 140, pp. 223-256.
- MAHANEY, W.C. & J.R. SPENCE (1989), Lichenometry of Neoglacial moraines in Lewis and Tyndall cirques on Mount Kenya, East Africa. *Zeitschrift für Gletscherkunde und Glazialgeologie* 25.

- MARCHI, L., A. PASUTO & P.R. TECCA (1993), Flow processes on alluvial fans in the Eastern Italian Alps. *Zeitschrift für Geomorphologie* 37, pp. 447-458.
- MARTINEZ, J.M., G. AVILA, A. AGUDELO, R.L. SCHUSTER, T.J. CASADEVALL AND K.M. SCOTT (1995), Landslides and debris flows triggered by the 6 June 1994 Paez earthquake, southwestern Colombia. *Landslide News* 9, pp. 13-15.
- MARTINS, R. (1991), Principles of rockfill hydraulics. In: E.M. Das Neves (Ed.): *Advances in Rockfill Structures. Proceedings of the NATO Advanced Study Institute on Advances in Rockfill Structures*. Kluwer: Dordrecht, NATO ASI Series E: Applied Sciences 200, pp. 523-570.
- MARUI, H., N. WATANABE, O. SATO AND H. FUKUOKA (1997), Gamahara Torrent debris flow on 6 December 1996, Japan. 1. Debris flow disaster. *Landslide News* 10, pp. 4-6.
- MASSON, D.G., Q.J. HUGGETT, P.P.E. WEAVER, D. BRUNSDEN AND R.B. KIDD (1992), The Saharan and Canary debris flows, offshore Northwest Africa. *Landslide News* 6, pp. 9-13.
- MATTHEWS, J.A. (1974), Families of lichenometric dating curves from the Storbreen gletschervorfeld, Jotunheimen, Norway. *Norsk Geografisk Tidsskrift* 28, pp. 215-235.
- MATTHEWS, J.A. (1980), Some problems and implications of 14C dates from a podzol buried beneath an end moraine at Haugabreen, southern Norway. *Geografiska Annaler* 62A, pp. 185-208.
- MAZZARELLA A. & F. PALUMBO (1992), Rainfall fluctuations over Italy and their association with solar activity. *Theoretical and Applied Climatology* 45, pp. 201-207.
- MCCARROLL, D. (1994), A new approach to lichenometry: dating single-age and diachronous surfaces. *The Holocene* 4, pp. 383-396.
- MEUNIER, M. (1990), La catastrophe du Grand Bormand: crue torrentielle du Borne le 14 juillet 1987. *Revue de Géographie Alpine* 78, pp. 103-114.
- MEUNIER, M. (1991), Éléments d'hydraulique torrentielle. *Études du CEMAGREF, série Montagne* 1. Louis Jean: Gap.
- MIDDELKOOP, H. & M. VAN DER PERK (1991), Een Reconstructie van de Opslibbing van Uiterwaarden. Utrecht University, Department of Physical Geography, Report GEOPRO 1991-06.
- MIDRIAK, R. (1984), Debris flows and their occurrence in the Czechoslovak Carpathians. *Studia Geomorphologica Carpatho-Balcanica* 18, pp. 135-149.
- MILES, M.J. & R. KELLERHALS (1981), Some engineering aspects of debris torrents. Canadian Society of Civil Engineering, Fifth Canadian Hydrotechnical Conference, New Brunswick, pp. 395-420.
- MILTENBURG, J.W. (1986), Verkenning naar de Toepasbaarheid van Lichenometrie in de Franse Alpen. Unpublished report, Utrecht University, Department of Physical Geography.
- MOONEY, M. (1951), The viscosity of a concentrated suspension of spherical particles. *Journal of Colloid Science* 6, pp. 162-170.
- MORA, S., C. MADRIGAL, J. ESTRADA AND R.L. SCHUSTER (1993), The 1992 Rio Toro landslide dam, Costa Rica. *Landslide News* 7, pp. 19-22.
- MORTON, D.M. & R.H. CAMPBELL (1974), Spring mudflows at Wrightwood, Southern California. *Quarterly Journal of Engineering Geology* 7, pp. 377-384.
- MULDER, H.F.H.M. (1991), Assessment of Landslide Hazard. KNAG/Geografisch Instituut Rijksuniversiteit Utrecht: Amsterdam/Utrecht. Netherlands Geographical Studies 124. Also: PhD thesis, Utrecht University.
- MULDER, H.F.H.M. & TH.W.J. VAN ASCH (1987), Quantitative approaches in landslide hazard zonation. In: *Géomorphologie et Risques Naturels. Travaux de l'Institut de Géographie de Reims* 69-72, pp. 43-53.
- MULDER, H.F.H.M. & TH.W.J. VAN ASCH (1988a), Risicokartering van massabewegingen in Alpine bosgebieden; een kwantitatieve aanpak. In: H.J.A. Berendsen & H. Van Steijn (Eds.): *Nieuwe Karteringsmethoden in de Fysische Geografie*. KNAG/Geografisch Instituut Utrecht: Amsterdam/Utrecht. Netherlands Geographical Studies 63, pp. 125-136.
- MULDER, H.F.H.M. & TH.W.J. VAN ASCH (1988b), Het gebruik van discriminantanalyse ten behoeve van een evaluatie van hellingstabiliteit. In: H.J.A. Berendsen & H. Van Steijn (Eds.): *Nieuwe Karteringsmethoden in de Fysische Geografie*. KNAG/Geografisch Instituut Utrecht: Amsterdam/Utrecht. Netherlands Geographical Studies 63, pp. 137-149.
- MULDER, H.F.H.M. & TH.W.J. VAN ASCH (1988c), On the nature and the magnitude of the variance of important geotechnical parameters, with special reference to a forest area in the French Alps. In: C. Bonnard (Ed.): *Landslides. Proceedings of the Fifth International Symposium on Landslides, Lausanne 10-15 July 1988*, pp. 239-244.
- MULDER, H.F.H.M. & TH.W.J. VAN ASCH (1987), The influence of forest on landslide activity. In: R.L. Beschta et al. (Eds.): *Erosion and Sedimentation in the Pacific Rim. (Proceedings Corvallis Symposium, August 1987)*. IAHS Publications 165, pp. 288-290.
- NAKADA, S. (1992), Volcanic hazard at Unzen, Japan. 1. 1990-1992 eruption of Unzen Volcano. *Landslide News* 6, pp. 2-4.
- NEALL, V.E. (1976), Lahars as geologic hazards. *Bulletin of the International Association of Engineering Geologists* 14, pp. 233-240.
- NIESSEN, A., P. VAN HORSEN & E.A. KOSTER (1992), Altitudinal zonation of selected geomorphological phenomena in an alpine periglacial area (Abisko, northern Sweden). *Geografiska Annaler* 74A, pp. 18-24.
- NIEUWENHUIZEN, M.E. & H. VAN STEIJN (1990), Alpine debris flows and their sedimentary profile. A case study from the French Alps. *Permafrost and Periglacial Processes* 1, pp. 111-128.
- NIYAZOV, B.S. & A.S. DEGOVETZ (1975), Estimation of the parameters of catastrophic mudflow basins of the Lesser and Greater Almatinka Rivers. *Soviet Hydrology* 2, pp. 75-80.
- OGURA, A.T. AND O.A. FILHO (1991), The Morin debris-flow disaster at Petropolis City, Rio de Janeiro, Brazil. *Landslide News* 5, pp. 22-24.
- OKUDA, S. (1989), Recent studies on rapid mass movements in Japan with reference to debris hazards. *Geomorphologica Carpatho-Balcanica* 23, pp. 5-22.
- OKUDA, S., H. SUWA, K. OKUNISHI, K. YOKOYAMA & M. NAKANO (1980), Observations on the motion of a debris flow and its geomorphological effects. In: O. Slaymaker, T. Dunne and A. Rapp (Eds.): *Geomorphic Experiments on Hillslopes. Zeitschrift für Geomorphologie Neue Folge Supplement* 1, pp. 142-163.
- OKUDA, S., H. SUWA, K. OKUNISHI, K. YOKOYAMA & K. OGAWA (1981), Synthetic observation of debris flow, part 7. *Annals of the Disaster Prevention Research Institute, Kyoto University* 24B, pp. 4-10.
- OKUNISHI, K. & H. SUWA (1985), Hydrological approach to debris flow. *Proceedings of the International Symposium on Erosion, Debris Flow and Disaster Prevention*, pp. 243-247.
- OKUNISHI, K., H. SUWA & S. HAMANA (1988), Hydrological controls of erosion and sediment transport in volcanic torrents. *Hydrological Sciences Journal/Journal des Sciences Hydrologiques* 33, pp. 5-14.
- OLYPHANT, G.A., C.P. CARLSON & D. HARPER (1991), Seasonal and storm-related aspects of sediment yield from a rapidly eroding coal refuse deposit in southwestern Indiana. *Water Resources Research* 27, pp. 2825-2833.
- OROMBELLI, G. & S.C. PORTER (1983), Lichen growth curves for the southern flank of the Monte Rosa Massif, western Italian Alps. *Arctic and Alpine Research* 15, pp. 193-200.
- OVERBEEK, J. & J. WIERSMA (1996), Puinstroomsystemen in de Franse Alpen. infiltratiekarakteristieken en dateringen. Unpublished report, Utrecht University, Department of Physical Geography.
- OWEN, L.A. (1991), Mass movement deposits in the Karakoram Mountains: their sedimentary characteristics, recognition and role in Karakoram landform evolution. *Zeitschrift für Geomorphologie Neue Folge* 45, pp. 401-424.
- OWEN, L.A., D.I. BENIN, E. DERBYSHIRE, D.J.A. EVANS, W.A. MITCHELL, D. THOMPSON & RICHARDSON, M. LLOYD & C. HOLDEN (1995), The geomorphology and landscape evolution of the Lahul Himalaya, Northern India. *Zeitschrift für Geomorphologie Neue Folge* 39, pp. 145-174.
- OWENS, I.F. (1973), Alpine mudflows in the Nigel Pass area, Canadian Rocky Mountains. Unpublished PhD thesis, Toronto.
- OWENS, I.F. (1974), Interrelationships between climatic and material characteristics in the occurrence of mudflows in the Nigel Pass area, Canadian Rocky Mountains. *Abhandlungen der Akademie der Wissenschaften in Göttingen, Mathematisch Physische Klasse* 29, pp. 313-318.
- PAIRIS, J.L. (1968), Nouvelles données sur le massif du Lan (Chapeau de Gendarme) au Sud de Barcelonnette (Basses-Alpes). *Géologie Alpine*, pp. 323-328.
- PECH, P. (1990), Les crues du 7 août 1987 dans l'Ossola. *Revue de Géographie Alpine* 78, pp. 89-94.
- PEDERSEN, K. (1976), Brigsdalsbreen, Vest Norge. *Glasiologiske og glacialgeologiske Undersøkelser*. University of Bergen.

- LEHRKE, F. (1994), L'initiative de modélisation des lahars induits à Quito (Equateur) par une éruption dendrovolcan du volcan Pichincha. *Revue de Géographie Alpine* 82, pp. 59-70.
- PENCK, W. (1924), Die morphologische Analyse. Engelhorn: Stuttgart. *Geographische Abhandlungen Reihe* 2.2.
- PHILLIP, J.R. (1957), The theory of infiltration. I. The infiltration equation and its solution. *Soil Science* 83, pp. 345-357.
- PHILLIPS, C.J. AND T.R.H. DAVIES (1991), Determining rheological parameters of debris flow material. *Geomorphology* 4, pp. 101-110.
- PIERSON, T.C. (1980), Erosion and deposition by debris flows at Mt. Thomas, North Canterbury, New Zealand. *Earth Surface Processes* 5, pp. 227-247.
- PIERSON, T.C. (1981), Dominant particle support mechanisms in debris flows at Mt. Thomas, New Zealand, and implications for flow mobility. *Sedimentology* 28, pp. 49-60.
- PIERSON, T.C. (1992), Rainfall-triggered lahars at Mt. Pinatubo, Philippines, following the June 1991 eruption. *Landslide News* 6, pp. 6-9.
- PIERSON, T.C. & J.E. COSTA (1987), A rheological classification of subaerial sediment-water flows. *Geological Society of America, Reviews in Engineering Geology* 7, pp. 1-12.
- PIGEON, P. (1991), Risques naturels et gestion communale: l'exemple de Bonneville (Haute Savoie). *Revue de Géographie Alpine* 79, pp. 55-68.
- PLAFKER, G. & G.E. ERICKSON (1978), Navados Huascaran avalanches, Peru. In: B. Voight (Ed.): *Rockslides and Avalanches. 1. Natural Phenomenon*. Elsevier: Amsterdam, pp. 277-314.
- PNM (1985), Voyages No. 2. Ubaye. Parc National du Mercantour. Serre: Nice.
- POBLT, J. (1988), *Rhizocarpon* Ram. em. Th. Fr. subgen. *Rhizocarpon* in Europe. *Arctic and Alpine Research* 20, pp. 292-298.
- POSITMA, R. (1988), Model voor de Initiatie van Debris Flows. Unpublished report, Utrecht University, Department of Physical Geography.
- PRIOR, D.B., N. STEPHENS & D.R. ARCHER (1968), Composite mudflows on the Antrim Coast of northeast Ireland. *Geografiska Annaler* 50A, pp. 65-78.
- PRIOR, D.B., N. STEPHENS & G.R. DOUGLAS (1971), Some examples of mudflow and rockfall activity in northeast Ireland. *Institute of British Geographers, Special Publication* 3, pp. 129-140.
- RAPP, A. (1963), The debris slides at Ulvadal, western Norway - an example of catastrophic slope processes in Scandinavia. In: *New International Contributions to the Morphology of Slopes*. Third report of the Committee on Slope Evolution, pp. 195-210.
- RAPP, A. & R. NYBERG (1981), Alpine debris flows in northern Scandinavia. *Geografiska Annaler* 63A, pp. 183-196.
- RAPP, A. & R. NYBERG (1988), Mass movements, nivation processes and climatic fluctuations in northern Scandinavian mountains. *Norsk Geografisk Tidsskrift* 42, pp. 245-253.
- RAPP, A. & L. STRÖMQUIST (1976), Slope erosion due to extreme rainfall in the Scandinavian mountains. *Geografiska Annaler* 58A, pp. 193-200.
- RAUDKIVI, A.J. (1979), *Hydrology: An Advanced Introduction to Hydrological Processes and Modelling*. Pergamon Press: Oxford.
- REBETZ, M., R. LUGON & P.-A. BAERISWYL (1997), Climatic change and debris flows in high mountain regions: the case study of the Ritigraben torrent (Swiss Alps). *Climatic Change* 36, pp. 371-389.
- REID, M.E., S.D. ELLEN, R.L. BAUM, R.W. FLEMING AND R.C. WILSON (1991), Landslides and debris flows near Honolulu, Hawaii, USA. *Landslide News* 5, pp. 28-30.
- RENLIN, Z. (1992), Preliminary report on the aerial photo interpretation of landslides and debris flows in southern China. *I.T.C. Journal* 3, pp. 254-256.
- RICHARDS, K. (1982), *Rivers. Form and Process in Alluvial Channels*. Methuen: London.
- RICKENMANN, D. (1990), Debris flows 1987 in Switzerland: modelling and fluvial sediment transport. In: R.O. Sinniger & M. Monbaron (Eds.): *Hydrology in Mountainous Regions. Part II: Artificial Reservoirs; Water and Slopes*. (Proceedings of the two Lausanne Symposia, August 1990). IAHS Publications 194, pp. 371-378.
- RICKENMANN, D. & M. ZIMMERMANN (1993), The 1987 debris flows in Switzerland: documentation and analysis. *Geomorphology* 8, pp. 175-189.
- RICKMERS, W.R. (1913), *The Duab of Turkestan*. Cambridge University Press: Cambridge.
- ROBERTSON, J.A. & C.T. CROWE (1975), *Engineering Fluid Mechanics*. Houghton-Mifflin: Boston.
- RODBELL, D.T. (1992), Lichenometric and radiocarbon dating of Holocene glaciation, Corallera Bianca, Peru. *The Holocene*, 2, pp. 19-29.
- RODINE, J.D. & A.M. JOHNSON (1976), The ability of debris, heavily freighted with coarse clastic materials, to flow on gentle slopes. *Sedimentology* 23, pp. 213-234.
- RÖSLI, U. & C. SCHINDLER (1990), Debris flows 1987 in Switzerland: geological and hydrogeological aspects. In: R.O. Sinniger & M. Monbaron (Eds.): *Hydrology in Mountainous Regions. Part II: Artificial Reservoirs; Water and Slopes*. (Proceedings of the two Lausanne Symposia, August 1990). IAHS Publications 194, pp. 379-386.
- ROSCOE, R. (1952), The viscosity of suspensions of rigid spheres. *British Journal of Applied Physics, Institute of Physics and Physical Society* 3, pp. 267-269.
- RUTGERS, I.R. (1962), Relative viscosity and concentration. *Rheologica Acta* 2, pp. 305-348.
- SALOMÉ, A.I. AND P.C. BEUKENKAMP (1989), Geomorphological mapping of a high-mountain area, in black and white. *Zeitschrift für Geomorphologie Neue Folge* 33, pp. 119-123.
- SAIJO, K. (1991), Slope evolution since Latest Pleistocene Time on the north slope of Chandragiri, Kathmandu Valley, the Middle Mountains of Nepal. *The Science Reports of the Tôhoku University 7th series (Geography)* 41, pp. 23-40.
- SASAHARA, K. AND R. TSUNAKI (1994), Landslide disasters triggered by heavy rainfall in Kagoshima Prefecture, July to September 1993. *Landslide News* 8, pp. 36-38.
- SASSA, K. (1985), The mechanics of debris flow. *Proceedings of the 11th International Conference on Soil Mechanics and Foundation Engineering* 3, pp. 1173-1176.
- SASSA, K., H. FUKUOKA AND F. WANG (1997), Gamahara Torrent debris flow on 6 December 1996, Japan 2. Possible mechanism of the debris flow. *Landslide News* 10, pp. 6-9.
- SAURET, In: M. Meunier (1991) *Éléments d'hydraulique torrentielle. Études du CEMAGREF série Montagne* 1. Louis Jean: Gap.
- SAVAGE, S.B. (1984), The mechanics of rapid granular flows. *Advanced applied mechanics* 24, pp. 289-366.
- SCHEIDEGGER, A.E. (1973), On the prediction of the reach and velocity of catastrophic landslides. *Rock Mechanics* 5, pp. 231-236.
- SCHLYTER, P., P. JÖNSSON, R. NYBERG, A. RAPP, C. JONASSON & J. REHN (1993), Geomorphological process studies related to climatic change in Kärkevagge, northern Sweden - status of current research. *Geografiska Annaler* 75A, pp. 55-60.
- SCHWEINGRUBER, F.H., TH. BARTHOLIN, E. SCHÄR & K.R. BRIFFA (1988), Radiodensitometric-dendroclimatological conifer chronologies from Lapland (Scandinavia) and the Alps (Switzerland). *Boreas* 17, pp. 559-566.
- SCHWEINGRUBER, F.H., H.C. FRITTS, O.U. BRÄKER, L.G. DREW & E. SCHÄR (1978), The x-ray technique as applied to dendroclimatology. *Tree-Ring Bulletin* 38, pp. 61-91.
- SCRIVENOR, J.B. (1929), The mudstreams ('lahars') of Gunung Keloet in Java. *Geological Magazine* 61, pp. 433-434.
- SELBY, M.J. (1993), *Hillslope Materials and Processes*. Oxford University Press: Oxford.
- SENGO, M. (1980), Rainfall conditions concerning the occurrence of debris flows. PhD thesis, Kyoto Prefectural University. (in Japanese)
- SEYHAN, E. (1979), *Application of Statistical Methods to Hydrology*. Institute of Earth Sciences, Free University, Amsterdam.
- SHAMOVA. In: B.M. Gol'din & L.S. Lyubashevskiy (1966): *Computation of the velocity of mudflows from Crimean rivers*. *Soviet Hydrology* 2, pp. 179-181.
- SHARP, R.P. & L.H. NOBLES (1953), Mudflow of 1941 at Wrightwood, Southern California. *Bulletin of the Geological Society of America* 64.
- SHRODER, J.F.JR. (1978), Dendrogeomorphological analysis of mass movement on Table Cliffs Plateau, Utah. *Quaternary Research* 9, pp. 168-185.
- SHRODER, J.F.JR. (1980), Dendrogeomorphology: review and new techniques of tree-ring dating. *Progress in Physical Geography* 4, pp. 161-188.
- SIGAFOOS, R.S. & E.L. HENDRICKS (1969), The time interval between stabilization of alpine glacial deposits and establishment of tree seedlings. *United States Geological Survey Professional Paper* 650-B, pp. 89-99.
- SKEMPTON, A.W. & R.D. NORTHIEY (1952), The sensitivity of clays. *Géotechnique* 3, pp. 30-53.

- CORDILERA. *Zeitschrift für Geomorphologie* 21, pp. 169-186.
- SMIRNOVA, T.Y. & A.A. NIKONOV (1990), A revised lichenometric method and its application: Dating great past earthquakes. *Arctic and Alpine Research* 22, pp. 375-388.
- SMITH, R.E. & J.Y. PARLANGE (1978), A parameter-efficient hydrologic infiltration model. *Water Resources Research* 14, pp. 533-538.
- SRIBNIY, In: B.M. Gol'din & L.S. Lyubashevskiy (1966): Computation of the velocity of mudflows for Crimean rivers. *Soviet Hydrology* 2, pp. 179-181.
- STARKE, L. (1972), The role of catastrophic rainfall in shaping the relief of the lower Himalaya (Darjeeling Hills). *Geogr. Pol.* 21, pp. 103-153.
- STATHAM, I. (1977), *Earth Surface Sediment Transport*. Clarendon Press: Oxford.
- STORK, A. (1963), Plant immigration in front of retreating glaciers with examples from Kebnekajse area, northern Sweden. *Geografiska Annaler* 45, pp. 1-22.
- STRUNK, H. (1988), Episodische Murschübe in den Pragser Dolomiten - semiquantitative Erfassung von Frequenz und Transportmenge. *Zeitschrift für Geomorphologie Neue Folge Supplementband* 70, pp. 163-186.
- STRUNK, H. (1989), Dendrochronological investigations on the frequency of debris flows in the Italian Alps. *Supplementi di Geografia Fisica e Dinamica Quaternaria* 2, pp. 13-17.
- STRUNK, H. (1991), Frequency distribution of debris flows in the Alps since the 'Little Ice Age'. In: J. De Ploey, G. Haase & H. Leser (Eds.): *Geomorphology and Geoecology. V. Geomorphological Approaches in Applied Geography. Proc. 2nd Int. Conf. Geom., Frankfurt/Main, 1989. Zeitschrift für Geomorphologie Neue Folge Supplementband* 83, pp. 71-81.
- SULEBAK, J.R. (1969), Mudflow in the low alpine region. *Norsk Geografisk Tidsskrift*, 23, pp. 15-33.
- SUWA, H. & S. OKUDA (1980), Dissection of valleys by debris flows. In: O. Slaymaker, T. Dunne and A. Rapp (Eds.): *Geomorphic Experiments on Hillslopes. Zeitschrift für Geomorphologie Neue Folge Supplementband* 35, pp. 164-182.
- SUWA, H. & S. OKUDA (1988), Seasonal variation of erosional processes in the Kamikamihori Valley of Mt. Yakedake, northern Japan Alps. *Catena Supplement* 13, pp. 61-77. Also in: A.M. Harvey & M. Sala (Eds.): *Geomorphic Processes in Environments with Strong Seasonal Contrasts, II: Geomorphic Systems*.
- SUZUKI, H. AND T. FURUYA (1992), Volcanic hazard at Unzen, Japan. 2. Hazard mapping at Unzen Volcano and the 1792 Mayuyama landslide. *Landslide News* 6, pp. 5-6.
- SWANSTON, D.N. & F.J. SWANSON (1976), Timber harvesting, mass erosion, and steepland forest geomorphology in the Pacific northwest. In: D.R. Coates (Ed.): *Geomorphology and Engineering*. Dowden, Hutchinson and Ross: Stroudsburg.
- SYANOZHETSKY, T.G.V., G.M. BERUCHASHVILI & N.B. KERESLIDZE (1973), Hydraulics of rapid turbulent and quasilinear (structural) mudstreams in deformed bed with abrupt slopes. *Proceedings of the Istanbul Conference of the International Association of Hydrological Scientists* 1, pp. 507-515.
- TAKAHASHI, T. (1978), Mechanical characteristics of debris flow. *Journal of the Hydraulic Division, Proceedings ASCE* 104 HY8, proceedings paper 13971, pp. 1153-1169.
- TAKAHASHI, T. (1980), Debris flow on prismatic open channel. *Journal of the Hydraulic Division, Proceedings ASCE* 106 HY3, proceedings paper 15245, pp. 381-396.
- TAKAHASHI, T. (1981a), Debris flow. *Annual Review of Fluid Mechanics* 13, pp. 57-77.
- TAKAHASHI, T. (1981b), Estimation of potential debris flows and their hazardous zones; soft countermeasures for a disaster. *Journal of Natural Disaster Science* 3, pp. 57-89.
- TAKAHASHI, T., K. ASHIDA & K. SAWAI (1981), Delineation of debris flow hazard areas. In: *Erosion and Sedimentation in Pacific Rim Steeplands. (Proceedings of the Christchurch Symposium, January 1981). IAHS Publications* 132, pp. 589-603.
- TAKAHASHI, T., H. NAKAGAWA, T. HARADA & Y. YAMASHIKI (1992), Routing debris flows with particle segregation. *Journal of Hydraulic Engineering* 118, pp. 1490-1507.
- TANG BANGXING, LIU SUGING & LIU SHIJIAN. (1994), Mountain disaster formation in Northwest Sichuan. *Geojournal* 34, pp. 41-46.
- THOMAS, D.G. (1965), Transport characteristics of suspension. VIII: A note on the viscosity of Newtonian suspensions of uniform spherical particles. *Journal of Colloid Science* 20, pp. 267-277.
- flow in the Rio Combeina Valley and Ibague City, Tolima Department, Colombia. *Geographical Journal* 41: 1-11.
- TRICART, J. (1957), Une lave torrentielle dans les Alpes Autrichiennes. *Revue de Géomorphologie Dynamique* 8, pp. 161-165.
- TSUBAKU, T., H. HASHIMOTO & T. SUETSUGI (1982), Grain stresses and flow properties of debris flow. *Transactions of the Japanese Society of Civil Engineers* 14, pp. 413-416. Also: *Proceedings of the Japanese Society of Civil Engineers*, 317, pp. 79-91. (in Japanese)
- VAN ASCH, TH.W.J. & J.T. BUMA (1997), Modelling groundwater fluctuations and the frequency of movement of a landslide in the Terres Noires region of Barcelonnette (France). *Earth Surface Processes and Landforms* 22, pp. 131-141.
- VAN ASCH, TH.W.J. & H. VAN STEIJN (1991), Temporal patterns of mass movements in the French Alps. *Catena* 18, pp. 515-527.
- VAN ASCH, TH.W.J., M.S. DEIMEL, W.J.C. HAAK & J. SIMON (1989), The viscous creep component in shallow clayey soil and the influence of tree load on creep rates. *Earth Surface Processes and Landforms* 14, pp. 557-564.
- VANDER PERK, M. (1996), Muddy Waters. Uncertainty Issues in Modelling the Influence of Bed Sediment on Water Composition. KNAG/Faculteit Ruimtelijke Wetenschappen Universiteit Utrecht: Utrecht Netherlands Geographical Studies 200. Also: PhD thesis, Utrecht University.
- VANDER PERK, M. (1997), Effect of model structure on the accuracy and uncertainty of results from water quality models. *Hydrological Processes* 11, pp. 227-239.
- VAN STEIJN, H. (1988), Debris flows involved in the development of Pleistocene stratified slope deposits. In: E.A. Koster & H.M. French (Eds.): *Periglacial Landforms and Processes. Zeitschrift für Geomorphologie Neue Folge Supplementband* 71, pp. 45-58.
- VAN STEIJN, H. (1989), Puinstromen. *Geografisch Tijdschrift* 23, pp. 119-128.
- VAN STEIJN, H. (1991), Frequency of hillslope debris flows in a part of the French Alps. *Bulletin of Geomorphology*, pp. 83-90.
- VAN STEIJN, H. (1996), Debris-flow magnitude-frequency relationships for mountainous regions of central and northwest Europe. *Geomorphology* 15, pp. 259-273.
- VAN STEIJN, H. & J.-P. COUTARD (1989), Laboratory experiments with small debris flows: physical properties related to sedimentary characteristics. *Earth Surface Processes and Landforms* 14, pp. 587-596.
- VAN STEIJN, H., J.-P. COUTARD, H. FILIPPO & C. MANDERSLOOT (1988a), Simulation expérimentale de laves de ruissellement: mouvement et sédimentation. *Bulletin de l'Association de Géographes Français* 1, pp. 33-40.
- VAN STEIJN, H., J. DE RUIG & F. HOOZEMANS (1988b), Morphological and mechanical aspects of debris flows in parts of the French Alps. *Zeitschrift für Geomorphologie Neue Folge* 32, pp. 143-161.
- VAN VLIET-LANOË, B. & B. VALLADAS (1992), Formations de pentes litées héritées, cryoreptation et illuviation de particules. *Mise au point. Quaternaire* 3, pp. 147-152.
- VARNES, D.J. (1978), Slope movement types and processes. In: R.L. Schuster & R.J. Krizek (Eds.): *Landslide Analysis and Control*, Washington, Transportation Research Board of the National Academy of Sciences special report 176, pp. 11-33.
- VARNES, D.J. (1984), *Landslide Hazard Zonation: A Review of Principles and Practice*. UNESCO: Paris.
- VISSMAN, W., G.L. LEWIS & J.W. KNAPP (1989), *Introduction to Hydrology*. Harper & Row: New York.
- WALDER, J.S. & C.L. DRIEDGER (1994), Rapid geomorphic change caused by glacial outburst floods and debris flows along Tahoma Creek, Mount Rainier, Washington, U.S.A. *Arctic and Alpine Research* 26, pp. 319-327.
- WALTHER, J. (1924), *Das Gesetz der Wüstenbildung*. Quelle und Meyer: Leipzig.
- WASSON, R.J. (1978), A debris flow at Reshun, Pakistan, Hindu Kush. *Geografiska Annaler* 60A, pp. 151-159.
- WEBSTER, R. (1973), Automatic soil-boundary location from transect data. *Journal of the International Association for Mathematical Geology* 5, pp. 27-37.
- WEBSTER, R. & A.B. MCBRATNEY (1989), On the Akaike Information Criterion for choosing models for variograms of soil properties. *Journal of Soil Science* 40, pp. 493-496.
- WEBSTER, R. & I.F. WONG (1969), A numerical procedure for testing soil boundaries interpreted from airphotographs. *Photogrammetria* 24, pp. 59-72.
- WEISS, E.E.J. (1988), Treering patterns and the frequency and intensity of mass movements (Structure de cernes et la fréquence et l'intensité des mouvements de terrain. In: C. Bonnard (Ed.): *Landslides - Glissement*



sheet 3540 est Entraunes - Col de la Cayolle (1990)



Date\* Time Dura- Debris Total rainfall<sup>a</sup> Rainfall intensity<sup>a</sup>

Antecedent Peak discharge<sup>c</sup>

Event Day

TANKFLOW

Date	Time	t <sub>r</sub>	DF cat.	I <sub>rec</sub>	I <sub>day</sub>	i <sub>t,1</sub>	i <sub>t,2</sub>	i <sub>t,3</sub>	i <sub>t,5</sub>	i <sub>t,10</sub>	i <sub>t,15</sub>	i <sub>t,30</sub>	i <sub>t,60</sub>	i <sub>t,120</sub>	i <sub>t,140</sub>	AP <sub>1,10</sub>	AP <sub>1,10</sub>	Lumped			Rill-interill			Single History	Single History	Single History	Single History	Single History	Single History	Single History	Single History	Single History	Single History	Single History	Single History	Single History	Single History	Single History	Single History	Single History	Single History	Single History	Single History	Single History	Single History	Single History	Single History	Single History	Single History	Single History	Single History	Single History	Single History	Single History	Single History	Single History	Single History	Single History	Single History	Single History	Single History	Single History	Single History	Single History	Single History	Single History	Single History	Single History	Single History	Single History	Single History	Single History	Single History	Single History	Single History	Single History	Single History	Single History	Single History	Single History	Single History	Single History	Single History	Single History	Single History	Single History	Single History	Single History	Single History	Single History	Single History	Single History	Single History	Single History	Single History	Single History	Single History	Single History	Single History	Single History	Single History	Single History	Single History	Single History	Single History	Single History	Single History	Single History	Single History	Single History	Single History	Single History	Single History	Single History	Single History	Single History	Single History	Single History	Single History	Single History	Single History	Single History	Single History	Single History	Single History	Single History	Single History	Single History	Single History	Single History	Single History	Single History	Single History	Single History	Single History	Single History	Single History	Single History	Single History	Single History	Single History	Single History	Single History	Single History	Single History	Single History	Single History	Single History	Single History	Single History	Single History	Single History	Single History	Single History	Single History	Single History	Single History	Single History	Single History	Single History	Single History	Single History	Single History	Single History	Single History	Single History	Single History	Single History	Single History	Single History	Single History	Single History	Single History	Single History	Single History	Single History	Single History	Single History	Single History	Single History	Single History	Single History	Single History	Single History	Single History	Single History	Single History	Single History	Single History	Single History	Single History	Single History	Single History	Single History	Single History	Single History	Single History	Single History	Single History	Single History	Single History	Single History	Single History	Single History	Single History	Single History	Single History	Single History	Single History	Single History	Single History	Single History	Single History	Single History	Single History	Single History	Single History	Single History	Single History	Single History	Single History	Single History	Single History	Single History	Single History	Single History	Single History	Single History	Single History	Single History	Single History	Single History	Single History	Single History	Single History	Single History	Single History	Single History	Single History	Single History	Single History	Single History	Single History	Single History	Single History	Single History	Single History	Single History	Single History	Single History	Single History	Single History	Single History	Single History	Single History	Single History	Single History	Single History	Single History	Single History	Single History	Single History	Single History	Single History	Single History	Single History	Single History	Single History	Single History	Single History	Single History	Single History	Single History	Single History	Single History	Single History	Single History	Single History	Single History	Single History	Single History	Single History	Single History	Single History	Single History	Single History	Single History	Single History	Single History	Single History	Single History	Single History	Single History	Single History	Single History	Single History	Single History	Single History	Single History	Single History	Single History	Single History	Single History	Single History	Single History	Single History	Single History	Single History	Single History	Single History	Single History	Single History	Single History	Single History	Single History	Single History	Single History	Single History	Single History	Single History	Single History	Single History	Single History	Single History	Single History	Single History	Single History	Single History	Single History	Single History	Single History	Single History	Single History	Single History	Single History	Single History	Single History	Single History	Single History	Single History	Single History	Single History	Single History	Single History	Single History	Single History	Single History	Single History	Single History	Single History	Single History	Single History	Single History	Single History	Single History
------	------	----------------	---------	------------------	------------------	------------------	------------------	------------------	------------------	-------------------	-------------------	-------------------	-------------------	--------------------	--------------------	--------------------	--------------------	--------	--	--	---------------	--	--	----------------	----------------	----------------	----------------	----------------	----------------	----------------	----------------	----------------	----------------	----------------	----------------	----------------	----------------	----------------	----------------	----------------	----------------	----------------	----------------	----------------	----------------	----------------	----------------	----------------	----------------	----------------	----------------	----------------	----------------	----------------	----------------	----------------	----------------	----------------	----------------	----------------	----------------	----------------	----------------	----------------	----------------	----------------	----------------	----------------	----------------	----------------	----------------	----------------	----------------	----------------	----------------	----------------	----------------	----------------	----------------	----------------	----------------	----------------	----------------	----------------	----------------	----------------	----------------	----------------	----------------	----------------	----------------	----------------	----------------	----------------	----------------	----------------	----------------	----------------	----------------	----------------	----------------	----------------	----------------	----------------	----------------	----------------	----------------	----------------	----------------	----------------	----------------	----------------	----------------	----------------	----------------	----------------	----------------	----------------	----------------	----------------	----------------	----------------	----------------	----------------	----------------	----------------	----------------	----------------	----------------	----------------	----------------	----------------	----------------	----------------	----------------	----------------	----------------	----------------	----------------	----------------	----------------	----------------	----------------	----------------	----------------	----------------	----------------	----------------	----------------	----------------	----------------	----------------	----------------	----------------	----------------	----------------	----------------	----------------	----------------	----------------	----------------	----------------	----------------	----------------	----------------	----------------	----------------	----------------	----------------	----------------	----------------	----------------	----------------	----------------	----------------	----------------	----------------	----------------	----------------	----------------	----------------	----------------	----------------	----------------	----------------	----------------	----------------	----------------	----------------	----------------	----------------	----------------	----------------	----------------	----------------	----------------	----------------	----------------	----------------	----------------	----------------	----------------	----------------	----------------	----------------	----------------	----------------	----------------	----------------	----------------	----------------	----------------	----------------	----------------	----------------	----------------	----------------	----------------	----------------	----------------	----------------	----------------	----------------	----------------	----------------	----------------	----------------	----------------	----------------	----------------	----------------	----------------	----------------	----------------	----------------	----------------	----------------	----------------	----------------	----------------	----------------	----------------	----------------	----------------	----------------	----------------	----------------	----------------	----------------	----------------	----------------	----------------	----------------	----------------	----------------	----------------	----------------	----------------	----------------	----------------	----------------	----------------	----------------	----------------	----------------	----------------	----------------	----------------	----------------	----------------	----------------	----------------	----------------	----------------	----------------	----------------	----------------	----------------	----------------	----------------	----------------	----------------	----------------	----------------	----------------	----------------	----------------	----------------	----------------	----------------	----------------	----------------	----------------	----------------	----------------	----------------	----------------	----------------	----------------	----------------	----------------	----------------	----------------	----------------	----------------	----------------	----------------	----------------	----------------	----------------	----------------	----------------	----------------	----------------	----------------	----------------	----------------	----------------	----------------	----------------	----------------	----------------	----------------	----------------	----------------	----------------	----------------	----------------	----------------	----------------	----------------	----------------	----------------	----------------	----------------	----------------	----------------	----------------	----------------	----------------	----------------	----------------	----------------	----------------	----------------	----------------	----------------	----------------	----------------	----------------	----------------	----------------	----------------	----------------	----------------

[illegible]

Harry Blijenberg werd geboren op 11 mei 1965 te Amersfoort. In mei 1983 behaalde hij het diploma Atheneum-B aan de Rijksscholengemeenschap "Thorbecke" te Amersfoort. In datzelfde jaar begon hij aan de studie Informatica aan de Rijksuniversiteit Utrecht. Zijn passie voor de bergen leidde ertoe dat hij het jaar daarop begon aan de studie Fysische Geografie aan diezelfde universiteit. Tijdens deze studie specialiseerde hij zich in de fysisch geografische proceskunde van reliëfrijke gebieden, met nadruk op grondmechanica. Tijdens de hierbij behorende veldwerken kwam hij voor het eerst terecht in de Franse Alpen. Eveneens tijdens zijn studietijd ontwikkelde hij een computerapplicatie voor het berekenen van grondwaterstanden op hellingen. Daarnaast deed hij stage bij de Dienst Getijdewateren van Rijkswaterstaat te Middelburg, waarbij de erosie van schorren in de Oosterschelde als gevolg van de aanleg van de Oosterschelddam centraal stond. Het doktoraal diploma Fysische Geografie behaalde hij in mei 1991.

Van oktober tot en met december 1990 werkte hij op projectbasis bij de Meetkundige Dienst van Rijkswaterstaat te Delft. Hier deed hij onderzoek naar de verspreiding van macro-algen in het Oosterscheldebekken, met name naar de veranderingen in ruimte en tijd sinds de aanleg van de Oosterschelddam.

Van mei 1991 t/m april 1995 was hij werkzaam als Assistent In Opleiding bij de vakgroep Fysische Geografie van de Universiteit Utrecht. Hier deed hij onderzoek aan puinstromen in de zuidelijke Franse Alpen, waarvan de resultaten in dit proefschrift zijn beschreven.

Sinds mei 1996 is hij weer werkzaam aan de Universiteit Utrecht op een project dat zich bezighoudt met mogelijke maatregelen ter vermindering van overlast door afstromend water vanuit landbouwgebieden in Zuid-Limburg. Zijdelings is hij betrokken bij een project dat de invloed van landgebruik op erosie op het Lössplateau in China onderzoekt en moet leiden tot het verminderen van de erosie.

